Institute of Physical Engineering, Faculty of Mechanical Engineering,
Brno University of Technology

Nanostructures for quantum information processing

Habilitation Thesis

Mgr. Vlastimil Křápek, Ph.D.

Brno 2020

Dedication

To all people who are filling
Plenty of Room at the Bottom.

Acknowledgment

My sincere appreciation goes to my colleagues and collaborators who created an inspiring research environment in Brno, Berlin, Dresden, Prague and elsewhere. Nature is acknowledged as the bottomless source of puzzles, and Physics as the ultimate tool that, with only a bit of ingenuity and imagination, allows to discover.

Author contribution statement

The thesis includes fifteen papers which I have coauthored. In all of them, I have been included to some extent in conceiving the research, data processing and data interpretation.

I have been responsible for most of the theory and numerical simulations. The following papers include a theoretical contribution of my co-authors. B: Ranber Singh and Gabriel Bester performed the atomistic simulations while I have contributed the continuum model. C, I, J: Petr Klenovský provided single particle states which I have used as a basis for the description of the exciton structure. N: Together with Martin Hrtoň we have programmed the EELS module for the software MNPBEM, which I have subsequently used to perform the simulations for the paper. D, O: I have only supervised the theoretical part.

The credit for the experimental work goes fully to my coauthors.

Abstract

The thesis is focused on some interesting aspects of semiconductor quantum dots and plasmonic antennas.

Excitonic fine structure splitting in quantum dots is closely related to the generation of polarization-entangled photon pairs for quantum information processing. I explain the relation of the fine structure to the symmetry of the wave function and related properties of quantum dots: morphology, strain field, and piezoelectric field. I discuss a possibility to tune the splitting by external strain field. Close-to-zero splitting required for the entangled photon pairs is experimentally demonstrated for ultrasymmetric quantum dots and quantum dots under external strain field, and predicted theoretically for quantum dots with the type-II confinement.

External strain can be used to engineer also other properties of quantum dots. Some of them are covered in the thesis, including the binding energies of excitons and their complexes, valence band mixing, polarization anisotropy of light emission, or tunneling rates in quantum dot molecules.

To complete the description of the exciton structure in quantum dots, I report the properties of the dark exciton pair, which does not exhibit linear optical response under standard conditions, but can be brightened near the cleaved edge of the sample.

Emission of light from quantum dots can be controlled and enhanced by plasmonic antennas – metallic nanostructures supporting localized plasmon resonance whose near field overlaps with the quantum dot. Within the thesis I report a study of the plasmon resonances in specific plasmonic antennas (gold crescents and discs) using electron energy loss spectroscopy.

Key words

Nanostructures, quantum dots, exciton, fine structure splitting, quantum information processing, quantum entanglement, polarization entanglement, entangled photon pairs, k·p theory, configuration interaction, plasmonic antennas, Purcell effect, electron energy loss spectroscopy.

Contents

1 Introduction

1.1 The splendors and miseries of nanostructures

The central point of this thesis are *nanostructures* – objects with the dimensions on the scale of nanometers (or up to hundreds of nanometers). The field of nanostructures is tremendously huge and I will cover only a small part here, based on my experience and preferences: Quantum dots and plasmonic antennas.

One thing all nanostructures have in common is that they are small. Miniaturization brings many advantages. It makes devices cheaper, portable, consuming less supplies or integrable into more complex functional units, all this while preserving the functionality. Many examples of successful miniaturization include cell phones, computers, transistors, or clockworks. Although it is common to consider the miniaturization a very modern trend, the last case shows that it is rather old, dating back to medieval times or even before.

In the aforementioned examples the smaller dimensions have not brought in the new functionality. Novel physics emerges when the dimensions of the nanoparticle become comparable with a characteristic length of some physical process, particle, or interaction. As the first example we will consider light. Its characteristic dimension is its wavelength (spatial periodicity) and for visible light in vacuum it ranges approximately from 400 nm to 750 nm. In the homogeneous medium, the vacuum wave length has to be divided by the refractive index, usually larger than one. When the medium is structured on the scale comparable with the light wave length, light behaves very differently than in the free space. A prominent example is a *photonic crystal* [1, 2, 3] formed by a periodic arrangement of building blocks with a contrast in the refractive index, such as a dielectric slab with drilled holes. A photonic band structure is formed in photonic crystals similar to the electron energy band structure in ordinary crystals, including the photonic band gaps – ranges of photon energies for which the absorption or emission of light (including spontaneous emission) is not allowed. On the other hand, for different photon energies the density of photon states can be considerably enhanced comparing to the free space case (described by Planck's law). In consequence, the emission of light can be enhanced. This effect was discovered by Edward Mills Purcell [4] (hence the name Purcell's effect) and is employed to improve the properties of light emitters [5, 6, 7]. *Photonic metamaterials* are periodic structures similar to photonic crystals but with subwavelength periodicity [8, 9, 10]. Building blocks represent artificial atoms, metaatoms, with engineerable properties. Metamaterial is perceived as a homogeneous environment by light as long as the wave length of light is much larger than the metaatom dimensions. It is thus well described by the local frequency-dependent electric permittivity and magnetic permeability. However, tremendous variability of metaatoms in comparison with atoms allows for extraordinary properties, a prominent example of which is a negative refractive index [8, 9, 11]. Metamaterial are also used for cloaking – making object invisible by allowing light to travel around the object instead of being scattered or absorbed [10, 12]. *Cavity quantum electrodynamics* [13, 14], another branch of photonics, focuses on light confined in a photonic cavity and interacting with a matter (an optical emitter). When the light is squeezed to sufficiently small volume (i.e., the cavity mode volume is comparable with λ^3 where λ denotes the wave length) and kept in the cavity for sufficiently long time (i.e., the cavity quality factor Q has to be large enough), then a coherent superposition of the light and matter states is formed, resulting in Rabi oscillations [15].

Plasmonic antennas are yet another kind of nanostructures confining light. In contrast to dielectric photonic structures discussed in the previous paragraph, plasmonic particles are metallic. The interface between the metal and dielectric hosts surface plasmon polaritons, which are electromagnetic waves coupled to the oscillations of free electron gas in the metal. The waves are evanescent: they decay

exponentially into both metal and dielectric. They can propagate along the interface. However, when the interface is enclosing the particle and is thus of finite size, standing waves are formed instead – localized surface plasmons. Due to their evanescent nature they can be confined on a subwavelength scale. Plasmonic modes have therefore a very small volume but their quality factor is lower than in the dielectric photonic structures due to ohmic losses in the metal.

Electrons experience more complex interaction with the environment than light. A discrete character of electric charge can be demonstrated in a device known as single electron transistor (SET). This is composed of a central capacitor of capacitance C connected via tunnel junctions to conducting electrodes (source and drain). With a large enough capacity, charging the capacitor with an extra electron costs almost no energy and the current flows through the transistor depending on the bias voltage and the resistivity of the device (mostly related to the tunnel junctions). However, when the charging energy of the capacitor, $E_C = e^2/2C$ (e denotes the elementary charge) becomes comparable with the thermal energy $E_T = k_B T$ (k_B is the Boltzmann constant and T is the temperature), the current is blocked for sufficiently small bias voltage – the effect is known as Coulomb blockade.The current can be restored, though, either by increasing the bias voltage above a certain threshold, or by gating the central capacitor and applying a gate voltage that compensates for the charging energy. Considering a spherical capacitor ($C = 4\pi\varepsilon R$), a characteristic dimension (the radius of the capacitor R) reads

$$R = \frac{e^2}{8\pi\varepsilon k_B T}$$

which, for $T = 300$ K and the dielectric constant ε of vacuum, takes the value $R = 39$ nm.

Electrons can also be confined in a way similar to light. Here, the characteristic length is de-Broglie wave length, reading $\lambda_{dB} = h/p$ (h is Planck constant and p is the momentum of the electron). For a non-relativistic electron with the kinetic energy E it reads $\lambda_{dB} = h/\sqrt{2mE}$. Inserting the thermal energy at 300 K and the effective mass of 0.067 of free electron mass m_e (corresponding to the edge of the conduction band in GaAs), one gets the de Broglie wave length of 30 nm. The nanoobjects of similar or smaller dimensions have the electron energy structure significantly different from extended objects which results into their non-classical properties.

1.2 Fabrication

The progress in the field of nanostructures is intimately related to the development of ingenious fabrication techniques. Traditionally, they fall into top-down and bottom-up approaches. In a *top-down* approach, the starting point is a bulk material that is processed (etched, milled, sputtered off, etc.) into a desired size and shape. Top-down techniques are usually deterministic and versatile, but on the other hand slow and limited to rather large objects. In a *bottom-up* approach, atoms, molecules, or other complexes are used as building blocks for more complex structures, put together e.g. by chemical reactions or by nanomanipulation. Bottom-up approaches are rather stochastic, difficult to control, and not so versatile, but they are fast, often scalable and suitable for mass production, and allow for smaller nanostructures than top-down approaches. We note that modern fabrication techniques are often composed of several steps combining both approaches. In the following, we present some of the basic fabrication techniques.

Electron beam lithography (EBL) is a technique capable to produce planar structures of arbitrary shape with the lateral resolution better than 10 nm. A substrate is first coated with an electron-sensitive resist. A focused electron beam is used to draw the desired structure, locally modifying the properties of the resist. Next, the development follows in which the exposed (positive lithography) or unexposed

(negative lithography) resist is removed. Finally, a layer of the desired material is deposited and the remaining resist is removed.

Focused ion beam milling (FIB) is a technique in which the desired structure is drawn with the focused beam of ions (most often Ga or Xe) directly into the thin layer of the target material. Contrary to electrons, massive ions are capable to sputter-off the target material so there is no need for the resist and development.

Nanoimprint lithography uses a solid stamp to structure the soft resist (by a mechanical pressure), which is then processed as in the case of EBL. In comparison with the previously mentioned lithographic techniques, nanoimprint lithography is low-cost and high-throughput technique suitable for industrial applications.

Nanomanipulation was enabled by the development of scanning probe microscopy. The objects (individual ions or larger particles) can be attached to the tip of the probe, dragged over the substrate, and detached at the desired position. The technique has been used e.g. to arrange 35 xenon atoms on nickel substrate to spell out the letters IBM or to place the plasmonic particles to the vicinity of self-organized quantum dots [16].

Chemical synthesis encompasses a broad class of chemical methods, in which nanostructures are produced through chemical reactions. The nanostructures prepared via chemical synthesis are usually of high quality (as no dirty or damaging processes are involved such as the resist deposition in EBL or the mechanical treatment in FIB). On the other hand, there is only a limited control over the process and its products, and also a limited versatility. Using chemical synthesis, it is possible to produce e.g. single crystal gold platelets for applications in plasmonics [17, 18], colloidal quantum dots [19], molecular nanomagnets [20, 21], etc.

Epitaxy refers to the ordered layer-by-layer growth of a crystalline film on a crystalline substrate. It produces high-quality thin films. The growth rate is rather small, between tenths of nanometer and units of micrometer per minute. In combination with using metallic nanoparticles as seeds (vapor-liquid-solid mechanism [22]), one-dimensional epitaxial growth can be realized producing nanowires. Quantum dots can be produced as well, either by self-assembly of the lattice-mismatched heterostructures, or by droplet epitaxy (see Sec. 1.4.1).

1.3 Characterization

The structural characterization of nanostructures relies on two main approaches: scanning probe microscopy and electron microscopy.

Scanning probe microscopy (SPM) is a class of methods in which the surface of the sample is scanned with a probe in a form of a sharp tip. Piezoelectric actuators allows for a precise control of the tip position. The methods differ by the physical quantity detected by the tip. *Atomic force microscopy* (AFM) relies on short-range mechanical force between the probe and the sample. It allows to image the surface profile with the sub-nanometer vertical resolution and can also be used for nanomanipulation. *Scanning tunneling microscopy* measures the tunneling current between the conductive tip and the sample. It is restricted to conductive samples. Due to the exponential dependence of the tunneling current on the tip-sample distance it provides a superb spatial resolution of 10 pm vertically and 100 pm horizontally [23]. Further, by varying the bias voltage the method enables to retrieve the energy-dependent local density of states. In *Scanning near-field optical microscopy*, the probe has a form of a tapered optical fibre that collects the near electromagnetic field (i.e., evanescent waves related e.g. to the quantum emitters or surface plasmons) present at the surface of the sample. The lateral resolution down to 20 nm has been demonstrated [23], well below the far-field diffraction limit.

Electron microscopy employs a beam of electrons to probe a sample. Owing to their short de Broglie wave length, electrons enable considerably better spatial resolution (several tens pm) than light (several hundreds of nm). The microscope is composed of an electron source (electron gun), a set of lenses, a sample stage, and a detector (usually a CCD camera), all mounted in evacuated electron column. There are two principal configurations of the electron microscope. In a *scanning electron microscope* (SEM), the focused electron beam is scanned over the sample and a reflected signal (secondary electrons, or possibly back-scattered electrons, X-rays, or light due to cathodoluminescence) is recorded. In a *transmission electron microscope* (TEM) a broad electron beam is transmitted through a sample. In addition to the unscattered electrons, the signal is composed of scattered electrons and cathodoluminescence. TEM requires thin samples (several tens of nanometers for the highest spatial resolution) and high-energy electrons that penetrate the sample (100–300 keV compared to less than 30 keV used in SEM). The scanning mode is also available for TEM, which is then known as scanning TEM (STEM).

Optical properties of nanoparticles and to some extent their electronic and quasiparticle structure are most conveniently studied by optical methods. Most prominent of them in the field of nanostructures are optical transmission and reflection spectroscopy and luminescence.

Optical transmission and reflection spectrometry is a quantitative method allowing to determine both the energy and the strength of various transitions (electronic, phononic, etc.) in a matter. White light from a source is either transmitted through or reflected from a sample, monochromatized or dispersed, and detected.

For the interaction of a matter with light, usually the Fermi golden rule and the electric dipole approximation are appropriate. The absorption transition rate (number of photons being absorbed per second) for the transition from the initial single electron state i to the final single electron state f then reads

$$W_{fi} = \frac{2\pi}{\hbar}\left(\frac{eE_0}{m_e\omega}\right)^2 |\langle f|\mathbf{e}\cdot\hat{\mathbf{p}}|i\rangle|^2\delta(E_f - E_i - \hbar\omega),$$

where $\hat{\mathbf{p}} = -i\hbar\nabla$ is the momentum operator, E_0, $\mathbf{e}$, and ω denote the amplitude, polarization vector, and frequency of the electric field, $E_{i,f}$ are the energies of respective states, and e, m_e, and $\hbar$ are the charge and mass of an electron, and reduced Planck constant. For more detailed discussion we refer to the standard textbooks, e.g., [24, 25]. Similar relations can be derived for other transitions related to the absorption of light (e.g. phononic or excitonic).

For a sample that is (at least piecewise) homogeneous it is customary to introduce the complex conductivity $\sigma(\omega) = \sigma_1(\omega) + i\sigma_2(\omega)$, whose real part reads

$$\sigma_1(\omega) = \frac{\pi e^2}{m_e^2\omega}\frac{2}{\Omega}\sum_{if}|\langle f|\mathbf{e}\cdot\hat{\mathbf{p}}|i\rangle|^2[f(E_i) - f(E_f)]\delta(E_f - E_i - \hbar\omega)$$

[$f(E)$ is the occupation number and Ω the volume of the system] and imaginary part is related through Kramers-Kronig relations. The (relative) complex dielectric function then reads $\varepsilon_d(\omega) = 1 - i\sigma(\omega)/\omega$, the refractive index is obtained as its square root, and finally the transmittance and reflectance can be calculated employing Fresnel relations.

However, for nanostructures the approach of homogeneous environment is often not appropriate. Instead, scattering and absorption of light are described by cross-sections C_{scat} and C_{abs}, defined as the power scattered and absorbed by the nanostructure when illuminated with a unit intensity. In the sparse system nanoparticles with the planar density n_S, the transmittance T is proportional to $1 - n_S(C_{scat} + C_{abs})$ and the reflectance R is proportional to $n_S C_{scat}$. When the nanostructures

are embedded in a homogeneous matrix (which is common), the relations above hold for a relative transmittance/reflectance with respect to an empty matrix.

Luminescence spectroscopy is a technique in which the luminescent light is observed. Luminescence is the light produced by the sample besides the thermal equilibrium (black-body) radiation. There are several mechanisms for the excitation of the sample out of the thermal equilibrium: external light (photoluminescence), injection of the carriers from conductive leads (electroluminescence), transfer of energy from high-energy beam of electrons passing through or near the excited structure (cathodoluminescence), etc. The photon energy of the luminescence is characteristic for the studied sample and independent of the parameters of excitation (e.g. the wave length of the exciting light).

The principle of the luminescence will be explained for the case of a semiconductor. An electron is excited from the valence to the conduction band, leaving a hole in the valence band. The system is now out of the thermodynamic equilibrium and will tend to restore it. The relaxation processes can be characterized as non-radiative (without the emission of photon) and radiative. Non-radiative processes (mostly phonon emission but also Auger processes, impurity scattering, etc.) are very efficient (time scale of ps or even fs) but allow only for a limited decrease of the electron's energy (tens of meV corresponding to a typical phonon energy). Radiative processes are generally much slower (time scale of ns) but allow for an arbitrary energy decrease (a photon of any energy can be emitted). Thus, the electron will first relax non-radiatively to the bottom of the conduction band (and the hole to the top of the valence band). The band edge presents so-called metastable state for which the non-radiative relaxation processes are no longer effective. The charge carriers dwell there for a comparably long time and eventually recombine through a radiative process, emitting a photon that contributes to the luminescence.

Luminescence spectroscopy is extremely sensitive technique, allowing in principle to register the emission of individual photons. It is however best suited for probing low-energy excitations, for which the non-radiative decay is hindered. It is also problematic to determine the strength of the transitions quantitatively because of complex relaxation effects influencing the recorded luminescence intensity.

1.4 Semiconductor quantum dots

Quantum dots (QDs) are semiconductor nanometer-sized heterostructures in which the electron motion is quantized in all direction and in consequence they exhibit discrete energy levels and wave functions confined to a finite volume. For that, QDs are also referred as artificial atoms. Quantum dots combine benefits of individual atoms (sharp density of states and slow decoherence) and solid state (easy integrability into more complex devices) and are therefore promising candidates for many applications such as lasers with low threshold current, single electron transistors, or single photon sources.

1.4.1 Fabrication

The methods for the fabrication of quantum dots can be divided into two classes – epitaxy and chemical synthesis.

Epitaxial quantum dots are prepared by depositing thin layers on a monocrystalline substrate. Two most common methods for the deposition are molecular beam epitaxy and metal-organic vapour phase epitaxy. [24] Typical growth is based on a strain-driven self-assembly and consists of several steps. On a substrate composed of a barrier material, a buffer layer of the same material is deposited to improve the quality of the surface. A thin layer (a few monolayers) of the QD material follows. Essentially, the two materials has to differ in the lattice parameter. The strain induced by the lattice mismatch is

relieved by the formation of islands (future QDs). Depending on the growth details a thin layer of QD material can be left below the islands (Stranski Krastanov growth mode) or the islands are located right at the substrate (Volmer-Weber growth mode). To facilitate the island formation, the growth can be interrupted for a short time (tens of seconds). Finally, the structure is terminated by the upper barrier layer.

The growth of lattice-matched quantum dots, e.g. GaAs dots with AlGaAs barrier, requires modified approaches. Droplet epitaxy is a modification of molecular beam epitaxy, in which metallic droplets (Al) are formed on the bottom barrier. The sample is then annealed and the droplets etch the underlying barrier. Nanoholes formed during this step are subsequently filled with the dot material (GaAs) and overgrown by the upper barrier. In this way, strain-free quantum dots are fabricated [26].

Chemically synthesized quantum dots are also known as colloidal quantum dots (for they are kept in solutions) or core-shell structures (for their characteristic shape of a core spheroid surrounded by spherical shell of the barrier material). They are mentioned here for completeness as the thesis deals solely with the epitaxial quantum dots.

1.4.2 Quantum confinement

QDs are composed of semiconductor crystals and electrons in them interact with a tremendous number of particles – lattice or other electrons. Therefore, we need a simplified view to describe quantum confinement in such a complex system in a comprehensible manner. The simplification is offered by the effective mass paradigm. Looking at the band structure of a bulk crystal we realize that the dispersion relation close to the band edges is parabolic, $E(k) = Ak^2$, and thus resembles the dispersion relation of free particles, $E(k) = (\hbar^2/2m_e) \cdot k^2$. The different slope can be treated as if the particles in crystal acquire effective mass m^* different from the mass of free electron m_e. The wave functions (Bloch waves) are composed of a plane wave part corresponding to the free particle and a periodic part. Taking these two facts into account it is natural to treat the crystal as a homogeneous environment of constant potential energy, in which electrons propagate as free particles. The effect of the complex crystal potential is hidden into modified effective mass and the modulation of the wave function by the periodic part of the Bloch wave. Such model constitutes the foundation for a description of heterostructures. Here, the band edge energies vary with the position and present a position-dependent effective confinement potential for the movement of the electrons with the (band dependent) effective mass. The confined wave functions have to be again multiplied by the periodic parts of the Bloch waves.

As an example, we can consider a quantum dot composed of GaAs (narrow band gap semiconductor, $E_g^{\mathrm{GaAs}} = 1.52$ eV at the temperature of 0 K) embedded in $Al_{40}Ga_{60}As$ (wide band gap semiconductor, $E_g^{\mathrm{AlGaAs}} = 2.06$ eV) [27]. The sum of the depths of potential wells for electrons (V_e) and holes (V_h) equals to the difference of band gaps, $V_e + V_h = E_g^{\mathrm{AlGaAs}} - E_g^{\mathrm{GaAs}} = 0.54$ eV. The determination of V_e and V_h is a tricky task and the data are usually not very reliable. Ref. [27] proposes $V_e = 0.34$ eV and $V_h = 0.21$ eV. The effective mass of the conduction band electrons in GaAs reads $m^* = 0.067 \cdot m_e$, the effective mass of the holes is anisotropic and cannot be described by a single value.

Two types of quantum dots are distinguished based on the band edge alignment of the inner (QD) and outer (barrier) material. For type-I QDs, both electrons and holes are confined inside the QD (V_e and $V_h > 0$). For type-II QDs, only one type of charge carriers is confined in QDs, while the other resides in the barrier and is only loosely bound to the QD by the electrostatic interaction with the former charge carrier, or by the inhomogeneous strain or piezoelectric field around the QD. Among QDs studied within the thesis, those based on GaAs/AlGaAs or InAs/GaAs materials belong to type I, Ge/SiGe are of

type II, and InAs QDs with GaAsSb capping are of transitional character with the type of confinement dependent of the thickness or composition of the GaAsSb layer.

Quantum confinement results into discrete energy spectrum and localized states. The former feature is related to narrow (in theory delta-function) density of states and thermal stability (low-energy thermal excitations are suppressed due to separation of energy levels). The latter feature results into rather strong Coulomb coupling between individual single-particle states and stable excitons and excitonic complexes.

1.4.3 Characterization

Quantum dots are typically embedded in the barrier region, which makes their structural characterization difficult. Further, the strain usually imposed by the capping layer causes pronounced morphological changes during the overgrowth which excludes the possibility to determine the shape and dimensions of quantum dots prior their embedding. Still, AFM provides a useful insight into the morphology of quantum dots. It was used for example to study the overgrowth of a QD with the capping layer [28], showing a clear flattening and lateral elongation of the studied QD. Direct determination of the QD size and shape is possible for the strain-free GaAs QDs in the AlGaAs barrier, for which the shape is not expected to change after the overgrowth [26, 29]. X-ray diffraction presents a powerful tool, but rather difficult to use [30, 31].

Photoluminescence is the primary method to study the electronic structure of quantum dots, in particular their low energy excitations. As a non-destructive and non-contact method it allows for plenty flavors, including the possibility to apply external electric, magnetic, or strain field, study thermal and pumping-intensity dependences, or perform time-resolved studies. The spectral resolution of the technique can be below several tens μeV (i.e., 10^{-5} on the relative scale). With the spatial resolution about 1 μm it is possible to study individual QDs. Photoluminescence together with the interpretation based on the theoretical modeling provides confinement energies of electrons and holes, binding energies of excitonic complexes, electric dipole moments, tunneling energies in quantum dot molecules, radiative lifetime of excitons, indications for the lateral symmetry breaking, and many others. Some of these cases are discussed further in this thesis. Less frequently, electronic structure of quantum dots is studied by optical absorbance measurements. Scanning tunneling spectroscopy allows to visualize the wave function of the bound states together with the determination of their energies [32, 33].

1.4.4 Theoretical methods

As the theoretical modeling of quantum dots constitutes substantial part of the thesis, I briefly review the involved methods. Typical procedure consists of four steps: calculation of fields, single particle states, multiparticle states, and optical properties. Except for the highly symmetric instances or simplified models, numerical solutions are necessary.

The first step consists in the calculation of fields that affect the band structure of solid: strain, electric, and magnetic field. Strain field is present either as built-in field due to lattice mismatch or as external field. It is obtained by minimizing strain energy within continuum elasticity model, or, less frequently, within atomistic model, e.g. valence force field. Electric field can be present due to piezoelectricity, pyroelectricity, or as external field. It is calculated from Laplace equation. I note that the electric field produced by occupied confined states is usually not considered in single-particle calculations.

Single particle states are most often obtained using $\mathbf{k} \cdot \mathbf{p}$ theory. With some simplification, this method represents a multiband extension of the effective mass theory. The wave function is expressed

as $\psi = \sum_b \chi_b u_b$, where the summation goes over a subset of energy bands, u_b is a periodic part of the Bloch wave at a specific point of Brillouin zone (usually Γ), and χ_b is a corresponding envelope function. Envelope functions are obtained from a set of Schrödinger-like differential equations and follow the normalization condition $\sum_b \langle \chi_b | \chi_b \rangle = 1$. Most frequently, eight bands are considered, two conduction and six valence (heavy hole band, light hole band, and spin-orbit split-off band, each doubled by a spin). The Hamiltonian is composed of Luttinger–Kohn Hamiltonian and Pikus–Bir Hamiltonian accounting for the effects of strain.

Alternatively, tight-binding or pseudopotential methods are used to obtain single-particle states.

In many quantum dots, including all instances considered here, Coulomb interaction between individual particles represents only a small correction to the confinement. It is thus appropriate to obtain multiparticle states (excitons and multiexcitonic complexes) by expanding the wave function into a series of limited set of Slater determinants formed from single particle states. This approach is named configuration interaction.

More details and references to this part is provided e.g. in [34, 35] and references therein.

1.5 Plasmonic antennas

Electrons, represented by plane waves in free space or by Bloch waves (modulated plane waves) in a bulk crystal, can be confined to a finite volume by the heterostructures with offsets in their band edges. Similarly, photons (light) represented by plane waves in free space can be confined to a finite volume by heterostructures with a contrast of their refractive indices. Such a heterostructure can be realized in small metal particles embedded in a dielectric environment, such as insulators, semiconductors, or air.

The mechanism of the light confinement in small metal particles is closely related to the quasiparticles called localised surface plasmons. Bulk metal supports collective oscillations of the free electron gas. Bulk plasmon is a quantum of such oscillations. On the boundary of the metal and a dielectric, the oscillating electrons produce a macroscopic electric field, evanescent waves that are free to move along the boundary and decay exponentially away from the boundary. The quasiparticles arising from the strong coupling between some excitation and the electromagnetic field are named polaritons. Here, so-called surface plasmon polaritons (SPP) are formed, referring to the coupling of the plasmon oscillations on a surface of metal to the evanescent wave propagating along the surface. Surface plasmon waves can be described by their frequency and by the in-plane component of the wave vector. The dispersion relation has two branches, whose asymptotes are the light dispersion line in the surrounding medium and two constant frequencies corresponding to the bulk plasmon and surface plasmon frequency [36]. The coupling is manifested by the avoided crossing of the lines. The electromagnetic field component of SPP is confined in the direction perpendicular to the metal surface but no in-plane confinement is observed.

When the metal surface is spatially restricted (such as in the case of metal nanoparticles), the interference of propagating surface plasmon waves gives rise to the standing waves; the related quasiparticle is called localised surface plasmon (LSP). The dispersion relation is now composed of discrete points, corresponding to the localized surface plasmon resonances (LSPR). Due to high losses in metal, the lifetime of the resonances is very short (femtoseconds) and their spectral width is thus rather large. Consequently, the response of the system supporting localised surface plasmons is spectrally continuous, with distinct peaks corresponding to different LSPR only if the frequency separation of the modes is larger than their spectral width (typically the case of several low-frequency LSPR in supported by small metal particles). The field related to LSPR is confined also in the in-plane directions.

For the experimental characterization of LSPR a variety of methods is employed. We describe here

two which are standardly used at the Institute of Physical Engineering BUT. Optical spectroscopy is one of the simplest and commonly used techniques. In the transmission mode it provides the extinction cross section of plasmonic particles and in the reflection dark-field field mode it allows to study the scattering cross section (a special dark-field objective is used to collect the scattered light while blocking the directly reflected light). Due to its far-field nature, the spatial resolution of the optical spectroscopy is set by the Abbe diffraction limit and is thus insufficient for the imaging of local LSPR properties (such as the plasmon's near field distribution). Further, the method is blind to so-called dark plasmons. The electric field of dark plasmons has a vanishing dipole moment which impedes their coupling to the far-field radiation. The electron energy loss spectroscopy allows to overcome both limits of the optical spectroscopy. In this technique, the sample in the form of a thin membrane (tens of nanometer) is scanned by a monochromated and focused beam of high-energy electrons (above 60 keV). The probe electrons interact with the electron gas in metal particles and can with some (very small) probability excite a LSPR. This is accompanied by a transfer of energy from the electron to a plasmon. If one detects the energy distribution of transmitted electrons, characteristic peaks at the energies corresponding to LSPR are observed. The spatial resolution of the method is better than 1 nm which allows for local imaging of LSPR. Further, the electrons interact also with dark plasmons. The spectral resolution of the method is about 0.01–0.1 eV – a fair value considering the energy of impinging electrons but naturally worse than the resolution of the optical spectroscopy. Further, the observation of the low-energy features (below 0.1–1 eV) is hindered by the strong zero-loss peak which corresponds to the electrons that pass through the sample without any inelastic scattering (it has a finite width due to a finite resolution of the monochromator).

The applications of localised surface plasmons are usually connected with their ability to focus and/or enhance the electromagnetic field. There are various plasmon-enhanced spectroscopic techniques, in which the studied sample is decorated with plasmon-supporting nanoparticles to enhance the measured signal. For example, plasmon-enhanced photoluminescence allowed to detect the fluorescence of individual molecules [37]. Another techniques comprise the tip or surface enhanced Raman scattering, surface enhanced infrared absorption, and others.

2 Quantum dot properties

This section is dedicated to general properties of quantum dots while more specific topics are discussed in the following sections. The research was triggered by design of complex quantum dot structures, development of a new tuning technique, or expanding the expertise gathered for standard InAs QDs to more exotic QDs. The studies have often introductory character, report rather basic properties of particular quantum dots, and their results are repeatedly used in the follow-up studies which pursue particular tasks of contemporary physics of semiconductor quantum dots.

2.1 Quantum dots with tunable thickness of the wetting layer

Strain-free GaAs quantum dots embedded in an AlGaAs barrier represent an unusual quantum dot system. The lattice parameter mismatch between both constituents is about 0.1 %, considerably smaller than e.g. in traditional InAs QDs embedded in GaAs (7 %). For simplicity and also for the sake of scientific marketing, the related low internal strain is advertised as zero internal strain, to which we will also adhere in the forthcoming discussion. In consequence, these QD are versatile as there is no strain-related restriction to their volume or shape. Further, the shape and composition of the QDs can

be experimentally retrieved with the accuracy and reliability impossible in any strained QDs: (1) There is negligible intermixing between the QD and barrier material during the growth. (2) Change of the QD shape during the growth of the capping layer (i.e., top barrier), in particular decrease of the height, which is common in strained QDs [28, 38], is absent here – this allows for easy determination of the QD morphology on uncapped samples. Together with simple form of the quantum confinement, which is not contributed by the strain or piezoelectric field, this facilitates the interpretation of the experimental data with reliable theoretical models. The GaAs/AlGaAs QDs are thus ideal testing system for new physical ideas and concepts. In particular, they are suitable for the studies of the excitonic fine structure splitting and its reduction towards zero (Sec. 3.1) as the total anisotropy of the QD is dominated by the structural anisotropy and the piezoelectric contribution is not present.

On the other hand, zero internal strain hinders the fabrication of the GaAs/AlGaAs QDs as the strain-driven self-assembly cannot be employed. Instead, complex growth procedures were developed including local droplet etching [39], modified droplet epitaxy [40], or hierarchical self-assembly [41].

In our study [29] the hierarchical self-assembly [41] was used for the GaAs/AlGaAs QD fabrication. In first step, InAs QDs were prepared by molecular beam epitaxy using the usual Stranski-Krastanov growth mode and capped by 10-nm thick GaAs layer. Next, strain-sensitive etching by $AsBr_3$ gas resulted in removal of InAs QDs and spontaneous formation of nanoholes in the GaAs layer at the place of InAs QDs. The bottom barrier layer of $\mathrm{Al_{0.45}Ga_{0.55}As}$ was deposited at low temperature so that the nanohole was transferred to AlGaAs surface. A thin layer of GaAs was deposited and the sample was annealed so that GaAs filled the nanohole. The excessive amount of GaAs, if present, formed a thin layer (an analogue of a wetting layer, WL) above the filled nanohole (quantum dot). The structure was completed with the top $\mathrm{Al_{0.35}Ga_{0.65}As}$ barrier. Due to anisotropic surface diffusion of Ga and Al atoms the resulting dots were strongly elongated along [110] direction, a fact which is important for the studies of fine structure splitting described in Sec. 3.1.

A series of samples with a different thickness of the wetting layer d (between 0 and 4 nm) was prepared and characterized by low-temperature photoluminescence with microscopic spatial resolution. Emission from quantum dots and a wetting layer was identified in the spectra, both exhibiting a pronounced red shift with increasing d (which corresponds to an increase of both the QD height and the WL thickness). With increasing excitation power, a shell-filling and the emission involving excited electrons and holes were observed.

The QD ground state emission was composed of several lines, a strong one at the high-energy side of the spectra and several weaker red shifted by ≥ 2 meV. With the help of polarization-resolved measurements and excitation-power-dependent measurements, the former was identified as neutral exciton (X) recombination, while the latter lines arose from the biexciton (XX, polarization doublet), positive trion (X^+, polarization singlet), or negative trion (X^-, polarization singlet). The discrimination between both trions was based on the background p-doping resulting in higher intensity of X^+ in comparison to X^-. The bonding nature of both trions and biexciton is rather uncommon in strained QDs and suggests a large overlap of electron and hole wave functions. This is facilitated by the absence of the piezoelectric field (which tends to separate the carriers with opposite charge) but still surprising due to a large effective mass difference between electrons and holes. We have used the concept of effective confinement potential [42] which is steeper for lighter electrons and shallower for heavier holes to show that in total the extension of both wave functions is comparable. Further, the biexciton and trion binding energies are only weakly dependent on d. As d the increases, the wave functions become more extended and the Coulomb interaction weakens (which tends to decrease the binding energies), but at the same time the correlation becomes more pronounced (which tends to increase the binding energies) and both the

effects almost cancel each other.

The measurements are well reproduced and interpreted with the numerical simulations combining the 8-band $k \cdot p$ theory for single particle states with the configuration interaction method for the excitonic complexes. In conclusion, a simple way to modify the height of the strain-free QDs and tailor their properties was demonstrated together with some peculiar properties such as the ultimate overlap of the electron and hole wave function and related bonding nature of all exciton complexes. These QDs were used in subsequent studies of the excitonic fine structure splitting [43, 44, 45] (see Sec. 3.1).

2.2 External strain as a tool for tuning QD properties

The strain field is an important ingredient in determining QD properties. Inhomogeneous internal strain is present in lattice-mismatched QDs with a magnitude up to several percent.External strain (usually homogeneous on a scale of QD dimensions) can be imposed to engineer the QD properties; the magnitude of such strain is considerably weaker than in the case of the internal strain and reaches usually up to 0.1 %. Unintentional external strain can result for example from the presence of defects in the barrier or vicinity of the cleaved edge of the sample.

The effect of the strain on the band structure is described by the Pikus-Bir Hamiltonian [46] and comprises the band shift and mixing. Elastic potentials are introduced to describe the magnitude of the shift. They refer to the shift per unit component of the strain tensor (or their linear combination) and their characteristic values range between 1 and 10 eV. For example, the heavy and light hole band in InAs QDs embedded in GaAs are split by about 0.4 eV and the fundamental band gap increases from 0.4 eV to more than 0.6 eV due to strong internal strain. The shifts induced by the external strain field are considerably smaller (up to several tens of meV) but still sufficiently large to induce observable effects e.g. in modifying the biexciton binding energy [47]. Band mixing is important in for the exciton polarization properties [45], exciton fine structure splitting [44], or making the dark exciton states optically active [48].

We have employed the external strain field in several studies aiming at the tuning of various quantum dot properties including the biexciton binding energy [47] (Sec. 2.2), the magnitude of fine structure splitting, polarization of the exciton transitions and the polarization anisotropy of QD photoluminescence [44, 45] (Sec. 3.1) or the tunneling energy in QD vertical molecules [49] (Sec. 4.2).

The principle of the strain application is common to all the studies, although details may differ due to technological progress over time. In the following we describe our state-of-the-art setup for strain application [50, 51]. The sample is prepared in a form of a nanomembrane containing the QDs, possibly embedded in a p-i-n diode structure if the simultaneous application of the external electric field is desired. The nanomembrane is integrated onto a lead magnesium niobate-lead titanate $[\mathrm{Pb}(\mathrm{Mg}_{1/3}\mathrm{Nb}_{2/3})\mathrm{O}_3]_{0.72} - [\mathrm{PbTiO}_3]_{0.28}$ (PMN-PT) piezoelectric actuator by gold-thermocompression bonding. PMMA resist used to bind the nanomembrane to the piezo-actuator in earlier works allowed to transfer only a limited strain and was prone to damage. The voltage applied on the piezo-actuator induces the in-plane biaxial strain field, either tensile or compressive depending on the sign of the electric field. The strain is transferred to the QD sample depending on its position on the actuator either as in-plane biaxial (the QD membrane on top of the actuator) or as uniaxial with the principal strain axis usually aligned with the QD $[110]$ direction (the QD membrane at the side of the actuator). In the latter case, denoting the strain along the principal axis ε, the strain along the perpendicular axis reads $-0.7 \times \varepsilon$ [52]. The method allows to impose the external strain up to 0.4 % [50].

In one of our early studies employing the external strain field we have addressed the binding energies of exciton species in InAs/GaAs QDs. Thin GaAs membranes (200 nm) with a single layer of self-

assembled InGaAs QDs were fabricated using molecular beam epitaxy, transferred onto piezo-actuators and characterized by low-temperature photoluminescence with the spatial resolution allowing to focus to individual QDs. Typical spectra consist of three sharp lines attributed to the recombination of the exciton (X), positive trion (X^+), and biexciton (XX). The assignment of the lines was based on the pumping-power and polarization dependent measurements. The transition energy of the neutral exciton was about 1.37 eV which gives evidence of rather small QDs. In different QDs, both red shift and blue shift of the biexciton with respect to the exciton was observed while the positive trion was consistently blue-shifted.

Binding energy E_B of the excitonic complex Y is the difference between the energy of complex components (a neutral exciton and a hole for the positive trion and two excitons for the biexciton) and the complex itself. The transition energy E_{tr} of that complex (i.e., the energy observed in the photoluminescence spectra) is the difference between the energy of the complex and the energy of the final state after the recombination of single electron-hole pair (i.e., an exciton for the biexciton and a single hole for the positive trion). The transition energy of the complex Y can be calculated by subtracting its binding energy from the transition energy of the neutral exciton, i.e.,

$$E_{tr}(Y) = E_{tr}(X) - E_B(Y).$$

The complexes with the positive/negative binding energy are called binding/antibinding and their spectral line is red-shifted/blue-shifted with respect to the neutral exciton line. In the studied QDs, the binding energy of the biexciton ranged from -2 meV to 2 meV and the binding energies of X^+ ranged from -8 meV to -3 meV. We note that the binding energy is not a measure of the complex stability – the components are held together by the quantum confinement, not by Coulomb interaction. In this aspect the exciton complexes in quantum dots differ considerably from those in a bulk crystal or quantum wells and wires.

The energies of exciton complexes can be estimated from the single particle energies (E_e for the ground electron state and E_h for the ground hole state) and the Coulomb integrals between those ground states (a negative J_{eh} describing the electron-hole attraction and positive J_{ee} and J_{hh} for the electron-electron and hole-hole repulsion, respectively). Such simple approach provides an elementary insight into the exciton complex properties, although it fully neglects the self-consistency (a modification of the wave functions due to the additional Coulomb potential) and correlation (a collective behavior of individual particles forming the complex) effects. For example, biexciton is composed of two electrons and two holes with four e-h attractions and one e-e and one h-h repulsions. Its energy reads

$$E(XX) = 2E_e + 2E_h + 4J_{eh} + J_{ee} + J_{hh}.$$

The energy of exciton reads

$$E(X) = E_e + E_h + J_{eh}$$

and for the binding energy of the biexciton we thus obtain

$$E_B(XX) = 2E(X) - E(XX) = -2J_{eh} - J_{ee} - J_{hh}.$$

Similarly, the binding energy of the positive trion reads

$$E_B(X^+) = -J_{eh} - J_{hh}.$$

Strongly antibinding positive trion therefore requires that the hole-hole repulsion is considerably stronger than the electron-hole attraction, $|J_{eh}| < J_{hh}$. This is possible when the hole wave function is more

compact than the electron wave function or when both particles are spatially separated (i.e., having different average coordinates). The latter case would result into strongly antibinding biexciton which is not observed. From the binding energies we therefore conclude that the hole is confined into a smaller volume than the electron (which is consistent with its larger effective mass).

When the external biaxial strain was applied to the QDs, the exciton transition energy $E_{tr}(X)$ was shifted up to several meV (blue-shifted for the in-plane compression and red-shifted for the in-plane expansion). Interestingly, the binding energies of XX and X^+ show a linear increase with $E_{tr}(X)$ with a slope

$$\gamma(Y) = \Delta E_B(Y)/\Delta E_{tr}(X)$$

(Y stays for XX or X^+), which for different QDs acquires values between $30\ \mu\mathrm{eV/meV}$ and $70\ \mu\mathrm{eV/meV}$, similar for both species.

The observations were explained with the help of theoretical modeling using the empirical pseudopotential calculations or the $k \cdot p$ calculations for single particles states combined with the configuration interaction calculations of the exciton states. The increase of the transition energies upon in-plane compression was explained by the shift of single particle energies. The observed changes in the binding energies were explained by the modification of the Coulomb integrals. The electron wave function tends to be more localized upon compression, which resulted in enhanced magnitudes of J_{ee} and J_{eh}. At the same time, the hole wave function becomes slightly less localized but the effect on J_{hh} was considerably weaker. Considering the weight J_{ee} and J_{eh} in the binding energy formulas, this explains the increase of the binding energies $E_B(XX)$, $E_B(X^+)$ upon compression.

For a QD with originally low biexciton binding energy it was demonstrated the the emission energies of X and XX can be tuned by the external strain to the same value. This has an interesting application in the production of polarization-entangled photon pairs utilizing so called time-reordering scheme proposed by Avron *et al.* [53].

2.3 Quantum dots between type I and type II confinement

The QDs with the type-II confinement (one type of the charge carriers is localized in the QD volume while the other in the barrier material, usually close to the QD) have considerably reduced overlap between the electron and hole wave functions. Consequently, the spontaneous emission rate is low and the radiative life time of excitations is high compared to type-I QDs [54]. This is for instance exploited in QD flash memories [55, 56]. In solar cells, QDs are used to enhance the infrared spectral response; the type-II QDs allow for an easier charge extraction [57, 58]. Even in purely optical applications such as lasers the InAs QDs with the GaAsSb overlayer close to the transition between type-I and type-II confinement are studied as their emission fits into the communication wavelengths of quartz optical fibers (1.3 and 1.55 μm) [59, 60]. Among several dot/barrier material combinations (e.g., Ge/Si, GaSb/GaAs, CdTe/CdSe, etc.), InAs QDs capped with a ternary $\mathrm{GaAs_{1-y}Sb_y}$ layer are particularly interesting because of the possibility to smoothly tune the QD confinement between type I and type II by setting a proper Sb content or the thickness of the GaAsSb layer. In this system, electrons are confined inside the QD and the holes reside in the GaAsSb layer.

Our interest in the GaAsSb capped QDs was originally triggered by the experimental effort to red-shift the emission wavelength of the standard InAs QDs towards the infrared telecommunication wavelengths of 1.3 and 1.55 μm. The role of the GaAsSb overlayer was to relieve the internal strain and to reduce the potential barrier. The reduced strain inside QDs results in a direct red shift of the emission and can allow for a growth of larger and taller QDs accompanied by additional redshift; the latter effect can be

considerably larger than the former one [61]. In our theoretical studies [62, 63], we have successfully reproduced previous experiments and interpreted the red shift of the emission with increasing Sb rate in the overlayer as a joint effect of the reduced strain field and a shifted band edge resulting in the reduced height of the confinement barrier in type I and reduced fundamental band gap in type II. In type I, both effects of the reduced strain and shifted band edges were equally important, in type II the latter prevails. Interestingly, no increase of the QD volume was found in contrast with the QDs with InGaAs overlayer [61]. This observation was attributed to the surfacting effect of antimony atoms which helps to preserve the shape and the height of the QDs during the overgrowth.

Type-II QDs exhibit unusual properties different from type I QDs which give rise to non-trivial physical phenomena such as the non-linear Stark effect, formation of molecular states, or vanishing fine structure splitting (see Sec. 3.2) despite the low symmetry of QDs. These phenomena are connected with the position and shape of the hole wave function. The hole confinement potential profile inside the GaAsSb overlayer is determined by the inhomogeneous elastic strain, piezoelectric potential, and, if present, composition and thickness fluctuations of the layer. The principal strain component contributing to the shift of the heavy-hole band edge is the biaxial strain B expressed in terms of the strain tensor components ε_{ij} as

$$B = \varepsilon_{zz} - (\varepsilon_{xx} + \varepsilon_{yy})/2$$

(z is perpendicular to the QD plane in accordance with the standard notation). The shift reads $\Delta E_{hh} = -b \cdot B$ where b is the biaxial deformation potential. Since b is negative, the holes are preferentially located in the regions with large positive B, i.e, in regions with the in-plane compression and the vertical expansion, which are located at the sides of a QD. A QD material has a largest lattice parameter of all the structure and acts therefore as a stressor. The overlayer at the sides of the QDs tends to be compressed vertically and stretched laterally. The vertical position of region of large positive B is rather sensitive to the In distribution inside the QD.

The piezoelectric field has an octopole form with the nodal plane slightly above the QD basis. Its magnitude is several tens meV, comparable with the strain-induced variations of the confinement potential. Exact position and shape of the hole wave functions therefore depends on the delicate interplay between both effects. In most cases, the piezoelectric field splits the hole wave function into two segments. The segments are either located at the dot basis and situated along [110] or located above the nodal plane of the piezoelectric field and situated along $[1\bar{1}0]$. The consequences of this unusual and intriguing hole wave function shape are discussed in the following.

Molecular states The confinement potential energy for electrons and holes is contributed by the piezoelectric potential energy, which exhibits four minima for the confinement of holes (along $[11\bar{1}]$, $[1\bar{1}1]$, $[\bar{1}11]$, and $[\bar{1}\bar{1}\bar{1}]$ direction from the center of a QD) and four minima for the confinement of electrons along the complementary directions. For electrons, the piezoelectric contribution means rather a small modification of the band-offset contribution and only contributes to a weak elongation of the electron wave functions. For the holes, the piezoelectric contribution is strong enough to split the wave function into two segments. Two lowest QD hole states then resemble bonding and antibonding molecular orbitals, although they can be in principle described as s and p atomic orbitals. The barrier between the minima of the potential energy is sufficient to produce true molecular states, with negligible probability density in the region between the segments. The width of the barrier can be adjusted at will by changing the lateral dimension of the QD. The (potential) height of the barrier is not tunable so easily but can be increased in some extent by increasing the height of the QD, which results into stronger strain field and thus stronger piezoelectric potential. Clear disadvantage of the concept resides in the impossibility to form the electron molecular states. Still, hole molecular states can be utilized in

the Burkard's proposal of quantum gate device [64].

Non-linear Stark shift The hole wave function is usually located at the bottom two minima of the confinement potential, i.e., below the electrons. Thus, the electric dipole moment is negative (pointing downwards). When the positive electric field is applied (with a positive potential at the bottom of the quantum dot), a linear Stark shift (an increase of the exciton transition energy) is observed with a weak quadratic part (due to a small polarizability of rather strongly confined charge carriers). For a certain critical value of the field (100 kV/cm for the case studied in Ref. [62]) the confinement energy minimum above the QD becomes more favorable and the hole is located there, above the electron. This is accompanied by an abrupt change in the electric dipole moment (which is now positive, i.e., pointing upwards) and the change in the slope of the energy-field relation. The Stark shift energy-field curve thus consists of two regions of ordinary, almost linear Stark shifts with an abrupt change of the slope at the boundary of the regions.

Tunable fine structure splitting Fine structure splitting in type-II QDs is in more detail covered in Sec. 3.2.

3 Excitonic fine structure

Single particle states in quantum dots are spin-degenerate doublets, unless a magnetic field is applied. This fact follows from Kramers theorem [65] which states that in any system with the half-integer total spin and underlying to the time reversal symmetry, the eigenstates are at least doubly degenerate. Time reversal symmetry is a symmetry of physical laws under the time reversal transformation $t \to -t$. Schrödinger equation fulfils the time reversal symmetry unless the magnetic field is applied. Thus, the single particle states in quantum dots form degenerate Kramers pairs (the states differing only in a spin projection). Similarly, trions (charged excitons, particles composed of two electron and one hole or one electron and two holes) form degenerate Kramers pairs. On the other hand, excitons are integer spin particles and as such they do not follow Kramers theorem. In Hartree approximation, where only a direct Coulomb interaction is considered, excitons are degenerate quadruplets. The exchange interaction between the electron and the hole splits the exciton levels, giving rise to a so-called fine structure. In common QDs, two of those levels are *bright* (with a short radiative lifetime and a strong optical response, e.g., photoluminescence) and two are *dark* (with a long radiative lifetime and a weak optical response, often below the experimental detection limit). The existence of such levels can be explained by a simple model. The conduction band electrons have the secondary (projection) total angular momentum quantum number $m_J^{(e)} = \pm 1/2$ while for the heavy hole states the number reads $m_J^{(h)} = \pm 3/2$. For exciton, $m_J^{(X)} = m_J^{(e)} - m_J^{(h)}$ holds, i.e., $m_J^{(X)} = \pm 1,\ \pm 2$. As the spin number of photon is 1, the selection rule for the single photon processes reads $\Delta m_J = 0,\ \pm 1$. The excitons with $m_J^{(X)} = \pm 1$ can recombine into the vacuum state ($m_J = 0$) producing single circular-polarized photon – they are therefore bright. On the other hand, excitons with $m_J^{(X)} = \pm 2$ cannot recombine by any single photon event (because the photon with a spin of 1 cannot carry the exciton momentum) – such excitons are dark. These simple rules are only approximate in the realistic QDs. For example, the heavy-hole – light-hole (hh-lh) mixing changes m_J of the hole states and makes the dark states optically active, although not as intense as the bright states. Such mixing is naturally present in QDs due to quantum confinement and can be also induced and tuned by the external strain field.

Considering the energy, the exciton quadruplet is split into dark and bright pairs. The dark pair has usually lower energy and is almost degenerate. The bright pair, usually of higher energy, is further split;

this splitting is known as fine structure splitting (FSS). Dark-bright splitting arises from the symmetric part of the exchange interaction and is thus a universal feature of quantum dots. FSS is attributed to the asymmetric part of the exchange interaction, it is thus present in QDs with reduced symmetry (lower than D_{2d} [66], an example is an elongated QD).

FSS was observed in various QD systems with the magnitude between zero [26] (which corresponds to values below a few μeV considering the experimental resolution) and 1 meV [67]. The theory of FSS was developed by Takagahara [68] soon after its discovery and further elaborated by numerous authors, our approach is briefly presented in Ref. [34]. The interest in FSS is both practical and fundamental. FSS helps to identify the optical transitions originating in the exciton, trion, and biexciton recombination. It plays an important role in the spin initialization e.g. in electron spin memories [69] or in exciton dynamics and dephasing. [70] It provides some insight into the size and shape of QDs. Benson's proposal of the source of entangled photon pairs relying on zero FSS [71] has called for the preparation of QD systems with low FSS. This issue was addressed in numerous studies either by sophisticated tailoring of the fabrication procedure to produce the desired high-symmetry QDs, or by applying a post-growth treatment or external field to tune the FSS.

Several our studies focused on FSS in various QD systemswith the aim to understand the fundamental properties of the bright exciton doublet and consider its utilization in the polarization-entangled photon pair source. GaAs QDs with AlGaAs barrier are addressed in Sec. 3.1, and type-II InAs QDs with a thin GaAsSb overlayer and a GaAs barrier in Sec. 3.2. Finally, a recent study on dark excitons is briefly described in Sec. 3.3.

3.1 Fine structure splitting of AlGaAs quantum dots

In a series of papers [43, 44, 45] we have studied elongated strain-free GaAs QDs with AlGaAs barrier described in more detail in Sec. 2.1. In the last paper, the quest for zero FSS was pursued by adjusting the growth process so that the resulting QDs have a symmetric (circular) shape.

In the first paper [43], we provided a direct quantitative comparison of measured and calculated FSS. This was enabled by using strain free QDs whose dimensions, shape, and composition were experimentally determined with then unprecedented accuracy. FSS was determined from the polarization-resolved photoluminescence of individual QDs. The spatial resolution of the setup allowed to collect the luminescence from as few as several tens of QDs. Since individual QDs emitted narrow lines (recorded linewidth of about 70 μeV is determined by the spectral resolution of a microphotoluminescence setup) and the ensemble emission covered the spectral range of about 10 meV (due to QD shape and size inhomogeneity), it was possible to resolve the emission of individual QDs. FSS was determined as the extent of characteristic wavy patterns formed by the peak energy of the emission plotted as a function of the polarization angle. The values determined for different structures ranged from 10 to 200 μeV. Simulations for realistic QD model (using as input scanning probe microscopy data of QD structures) reproduced both magnitude of FSS and polarization of both components of the emission with a reasonable accuracy.

Due to the elongation of QDs, the values of FSS are too large for the source of polarization-entangled photon pairs. For this reason, in our second study we explored the possibility to tune FSS by the external strain field [44]. Thin MBE-grown membranes (about 150 nm) containing GaAs/AlGaAs QDs were released from the substrate (by selectively etching off a sacrificial AlAs layer) and transferred onto a side face of a piezoelectric actuator (PMN-PT crystal). The voltage applied to the actuator results into strongly anisotropic biaxial strain with components $\varepsilon_{\parallel}$ and $\varepsilon_{\perp} \approx -0.7\varepsilon_{\parallel}$ along the direction parallel and perpendicular to the electric field, respectively. The membranes were oriented so that the

electric field direction was close to the $[1\bar{1}0]$ GaAs crystal direction, deviating by an angle up to 20°. When sweeping the strain $\varepsilon_{\|}$ in the range of few ‰(from negative to positive values), FSS first decreases and then increases. At the same time the polarization of the high-energy component of the excitonic emission changes by almost 90° (51–79° for different QDs), being almost perpendicular to the pulling direction for large strain. These observations are consistent with a strain-induced anticrossing of the bright exciton states.

The effect is reproduced and explained by a theoretical modelling. Strain field results into the mixing of heavy and light hole bands, yielding the bands with anisotropic effective mass. In turn, the elongation of the hole wave function significantly changes, becoming larger in the direction of the compressive strain. Strain can even compensate for or preponderate over the structural elongation, resulting into circular or inversely elongated hole wave functions in elongated QDs. At the same time, the electron wave function is only negligibly modified.

When a QD elongation axes coincide with the strain axes, a crossing of bright exciton states is predicted with a zero FSS and abrupt change in the polarization of the high-energy component's emission. For a tilt between both axes (and also in a realistic case of irregularly shaped QDs) there is an anticrossing with a finite minimum FSS and a smooth change in the polarization. The latter case corresponds to the experimental observations. Interestingly, in that case the hole wave function can be not only elongated, but also rotated.

In the third study the aspects of the strain-tunable FSS are discussed more thoroughly, including the relation between the heavy-hole–light-hole mixing, FSS, and polarization orientation and polarization degree of the excitonic emission [45].

3.2 Fine structure splitting of type-II quantum dots

Our theoretical study [34] dealt with the InAs QDs with a thin GaAsSb overlayer (GO) further embedded in GaAs. Depending on the thickness and the composition (Sb content) of the GO, the confinement can be continuously varied between type I and type II with the holes confined inside the GO in the vicinity of the QD. The transition between type I and type II is accompanied by a change in the hole wave function shape, in particular, in type II a two-segment hole wave function is formed. As we have learned in the foregoing, FSS is closely related to the elongation of the wave functions. These facts open an interesting prospect for tuning the FSS which is explored in the study. In particular, it is shown that small values of FSS comparable with the natural linewidth of the excitonic transitions are achievable for realistic quantum dots just by setting suitable GO properties.

We have studied the effect of the segmentation of the hole wave function with a toy model where the electron and hole probability densities were represented by anisotropic Gaussians. Splitting of the hole wave function into two segments resulted in a modification of its effective elongation with a possibility to compensate the electron elongation and achieve zero FSS for a range of parameters. The effective elongation is contributed by both the elongation of the segments and their mutual position.

Our inspection of the effective confinement potential identified the inhomogeneous strain field and the piezoelectric field as key ingredients determining the shape of the hole wave function. In particular, the piezoelectric field has a form of an octopole with a nodal plane slightly above the basis of a QD. Consequently, changing the vertical position of the hole shall result in a pronounced change in the position and shape of the segments.

In the next step we have attempted to vary the thickness of the GO to see whether we can vertically shift the hole wave function and modify the FSS. The electron wave function resided inside the QD and was almost unaffected. We indeed observed the expected effect (more complex than a simplified

explanation presented here) and for three considered model QDs (a lens, an elongated lens and a pyramid), zero FSS was achieved for a certain thickness of the GO.

Further, we have calculated the exciton radiative lifetime to see whether these type-II QDs are suitable for optical applications, in particular for the source of polarization-entangled photon pairs. In type-I QDs, typical lifetimes are about 0.5 ns. The zero FSS was obtained for the structures with the lifetimes of 0.9 ns and 2.2 ns (lens), 3.4 ns (elongated lens), and 4.8 ns (pyramid). Thus, these type-II QDs are still rather good emitters. We concluded that low natural FSS and efficient photoluminescence make the GaAsSb capped InAs QDs attractive as a possible source of entangled photon pairs.

In the follow-up study [72] we have shown that similar results can be obtained when the transition between type-I and type-II confinement is induced by the variation of the Sb content in the GaAsSb overlayer of constant thickness.

The experimental verification of our predictions was not possible so far and will be attempted in the ongoing research.

3.3 Spontaneous brightening of dark exciton

Although the dark pair of the exciton quadruplet attracts less attention than its bright sibling, it is still of considerable interest. Most importantly, it exhibits long radiative lifetime which makes it attractive for spin storage for quantum information processing [73]. Further, the knowledge of dark-bright energy splitting provides an insight into the nature of the exchange interaction (including e.g. screening) and helps to retrieve the QD size and composition.

Dark excitons are known to emit light due to the valence band mixing effects [74]. The factors promoting the mixing and making the dark excitons optically active include external magnetic field, external or built-in strain field, or shape asymmetries. The light propagates in the plane of a QD and is polarized along its vertical axis, different from in-plane polarized emission of bright excitons.

In our study [48] we reported the observation of dark exciton emission in strain-free GaAs/AlGaAs QDs with highly symmetric shape (identical to the last case of Sec. 3.1). The side emission from a cleaved facet of the sample was investigated by polarization-resolved micro-photoluminescence. Light was collected along $[1\bar{1}0]$ direction. Typical spectra consist of a strong [110]-polarized peak corresponding to one bright exciton and a weaker [001]-polarized peak corresponding to a dark exciton. The other bright exciton was observed indirectly due to total internal reflection within the sample and the second dark exciton remained dark.

In highly-symmetric QDs under no external field the brightening of dark exciton is not anticipated. The only symmetry-breaking factor is the presence of the cleaved facet. This may introduce a local electric field or an anisotropic strain field with major axis parallel to $[1\bar{1}0]$ direction. Our simulations have shown that it is this strain field (related e.g. to the oxidation of AlAs layer present below QDs) that is responsible for the brightening of the dark exciton. We also predict an increase of FSS (i.e., energy splitting of the bright exciton pair) in the vicinity of the cleaved edge due to the related strain, which was verified by subsequent measurements.

It is instructive to explain the mechanism of the brightening. As we have already mentioned, it is connected with the valence band mixing effect. The ground hole state is always dominated by the heavy hole band but it contains also a small contribution of light holes. Interestingly, there is a fair amount of light holes even in as-grown QDs. For a spin-up ground hole state, the weights of the light-hole-spin-up and light-hole-spin-down bands read 4.1 % and 0.7 %, respectively. However, in optical spectra there is no signature of light holes (such as the out-of-plane-polarized emission of the dark exciton). When the strain is applied (the magnitude of 0.1 % along the principal $[1\bar{1}0]$) axis has been set), the weight of

the light holes increases moderately to 5.0 % and 2.0 % for spin-up and spin-down band, respectively. Now, the dark exciton is brightened. The reason for such a behavior consists in the symmetry of the mixing terms and the related symmetry of the envelope functions. The mixing terms between the heavy-hole and light-hole bands in the kinetic Luttinger-Kohn Hamiltonian [75] are differential operators that results into light-hole envelope functions quasi-antisymmetric in two coordinates, with negligible contribution to the transition matrix elements. On the other hand, the mixing terms in the strain Pikus-Bir Hamiltonian [46] are numbers that result into quasi-symmetric light-hole envelope functions with substantial contribution to the transition matrix elements. More details are provided in our study [48].

Let us now discuss the practical implications of our study. We have shown that even a cleaved edge suffices to make a dark exciton optically active. On one hand, this allows a simple access to dark excitons. On the other hand, the effect has to be taken into account when a long lifetime of dark excitons is desirable. We also propose the possibility to have both optically active and inactive dark excitons on a single sample. Finally, we envision the possibility of dynamical brightening/darkening of a dark exciton via application of anisotropic stress pulses.

4 Quantum dot molecules

Similar to atoms, two or more quantum dots (artificial atoms) can be positioned close to each other so that their electron orbitals overlap forming joint molecular states. Unlike ordinary molecules, quantum dot molecules (QDMs) are held together by the embedding medium rather than by bonding electrons. This allows to tailor the strength of the interaction as well as to form unusual molecules, with e.g. partly molecular states, antisymmetric ground state, or molecular states for only one type of charge carriers (either electrons or holes).

QDMs find their application potential as quantum gates for quantum information processing. Here, individual QDs host qubits – two-state systems which, contrary to ordinary bits, can be in a state of a superposition of 0 and 1. Qubits are most often represented by a spin of a charge carrier confined in a QD, but can be also related to the properties of exciton. Quantum gates then allow to perform operations on qubits. Most prominent operation performed by a quantum gate is CNOT (controlled not or controlled negation). It takes two qubits as its input (control and target qubit) and reproduces or flips the target qubit on output depending on the state of the control qubit (the negation is performed when the state of the control bit is 1). CNOT is a universal gate (similarly to NAND and NOR gates in classical digital electronics) – any logical operation can be realized by combining CNOT gates. Various realizations of quantum gates relying on QDMs have been proposed [64, 76]. In addition, all-optical scheme for the initialization and readout of a spin qubit was realized with a QDM [77]. Outside the field of quantum information properties, QDMs (or double quantum dots) are studied for their unusual transport properties [78].

We have contributed to the field of QDMs by two distinct studies aimed at entanglement in lateral QDMs [63] (Sec. 4.1) and active tuning of the tunnel coupling strength in a QDM [49] (Sec. 4.2).

4.1 Entanglement in lateral quantum dot molecules

In this work we further elaborated Bayer's proposal of qubit formed by a charge carrier in a quantum dot molecule, with the carrier in a top/bottom QD representing 0/1. According to the proposal, a QDM can host two qubits (represented by an electron and a hole), for which an entangled state can be formed. Two drawbacks of the proposal limits the entanglement: (1) The QDs in a vertical arrangement are

always dissimilar. (2) The tunneling rate for electrons and holes is significantly different.

We studied theoretically a lateral QDM, in which both drawback are resolved. (1) The QDs in a lateral arrangement can be in principal identical. (2) The lateral tunneling rates for both types of charge carriers are not so different as the vertical ones. First, we employed a simple model (derived from a two-site Hubbard model) to study the effect of relevant parameters: The tunneling rates of electrons and holes t_E and t_H, the Coulomb coupling energy U, and the detuning Δ (a difference of the exciton energies in the left and right QD). We have come to the conclusion that for a large degree of the entanglement, $\Delta \ll t_E \approx t_H \ll U$ is required. The antisymmetric direct exciton offers a larger degree of entanglement than the symmetric direct exciton.

Next, we addressed realistic QDMs. For several distances between the QDs forming the QDM, the ratio t_E/t_H varied between 2 and 3, i.e., it was considerably smaller than in vertical QDMs. The entropy of entanglement $S = 0.99$ was predicted for the optimum case, but it was reduced to $S = 0.20$ even for a tiny difference between the QD radii of 1 % (0.2 nm of 14 nm). We proposed a strategy to increase the accessible entropy of entanglement consisting of the following steps: (1) Reducing the distance between the QDs in a QDM. (2) Reducing the lateral dimension of QDs and improving the barrier properties. (3) Minimization of the detuning by improving the homogeneity of QDs.

4.2 Active tuning of coherent tunneling in quantum dot molecules

In this work we demonstrate the possibility to manipulate the coupling strength in a QDM by using externally induced strain fields. Theory explains the effect in terms of modified weight of the light hole component mediating the coupling in the barrier.

The device consists of QDMs (two vertically stacked InGaAs QDs) embedded in the intrinsic region of n-i-p nanomembranes integrated onto piezoelectric actuators. It allows strain and electric field to be applied to single QDMs. Micro-photoluminescence measurements recorded while sweeping the external electric field applied to the molecule revealed characteristic anticrossing patterns [79], from which the tunnel coupling strength can be determined. The hole coupling strength can be modified by applying external biaxial strain: For a compressive (tensile) strain t_H decreases (increases). For the strain range between -0.04 % (compressive) and 0.02 % (tensile), t_H in different QDMs varies by 27–76 μeV, which is 15–30 % of the original value.

Our calculations reproduced well the observations and explained the tuning mechanism for t_H. Inspection of the wave functions reveals that, despite the overall heavy-hole character, the hole probability density in the barrier region is dominated by the light-hole component. The heavy-hole component penetrates the barrier region only by exponentially decaying tails at the QD boundaries, leaving negligible probability density in the barrier center. The compressive strain increases the energy of light holes with respect to the heavy holes, leading to a reduction of the light-hole component in the barrier and therefore the tunnel coupling.

The strain-tunability of the hole coupling can be exploited in the control of entanglement between spin-qubits in quantum dots.

5 Plasmonic nanostructures

5.1 Imaging of the plasmon resonances

We have employed EELS to image plasmons in gold crescent-shaped plasmonic nanoantennas [80]. These structures are highly tunable, support two non-degenerate dipolar (i.e., optically active) LSPR and are

compatible with infrared communication technology. Further, a particularly large field enhancement is expected close to their sharp tips. For these reasons, we considered them good candidates for plasmon-enhanced photoluminescence.

Metal nanoantennas of crescent shape were prepared by focused ion beam milling of a sputtered gold layer. The thickness of the antennas was 20 nm and the lateral dimensions ranged between several tens and a few hundreds nanometers. Silicon nitride membranes with the thickness of 40 nm were used as the substrate. The antennas were imaged by annular dark-field scanning transmission electron microscopy. EELS employed electrons with the energy of 300 keV and its spatial and spectral resolution was 0.3 nm and 0.2 eV, respectively. Our experimental research was accompanied by the numerical simulations based on the boundary element method (BEM) using a free software MNPBEM toolbox together with an in-house developed extension.

EEL spectra recorder for particular spots reveal several peaks corresponding to distinct LSPR. Maps of the loss probability for the loss energy corresponding to a particular peak reveal the spatial distribution of the plasmon near field. Depending on the size of the antennas we were able to resolve up to five LSPR.

From the fundamental point of view it is interesting to consider a transformation of a disk-shaped antenna into a crescent-shaped antenna, and related symmetry reduction. We have studied such a transformation and demonstrated splitting of the disk's dipolar mode into longitudinal and transverse dipolar modes of the crescent. Finally, we have demonstrated tunability of the LSPR energies by modifying structural parameters of crescents.

In the follow-up study, we addressed disk-shaped plasmonic antennas [81]. We discussed the influence of involved fabrication techniques (electron beam lithography and focused ion beam lithography) on the properties of plasmonic antennas and concluded that the former technique produces antennas of better quality.

6 Summary and Outlook

Benson's proposal [71] represents a major motivation for my research work over the last decade. In 2000, it opened the path towards the generation of polarization-entangled photon pairs and, at the same time, it raised the need for quantum dots with zero the fine structure splitting of the bright exciton pair. The FSS is related to the anisotropic exchange interaction; any effect that elongates the wave function of an electron or a hole forming the exciton results into finite FSS.

In 2008, when I entered the field, we were able to fabricate strain-free (and thus also piezoelectricity-free) AlGaAs quantum dots. We were able to reconstruct their structural parameters with a fair reliability and we understood well their optical properties [29]. Unfortunately, these QDs were strongly elongated and exhibited thus a large FSS [43]. We had at our disposal a powerful tuning technique based on the application of the external strain using in-house developed piezoelectric actuators [47]. It turned out to be very useful in reducing the FSS, although only a small part of QDs exhibited FSS values sufficient for the generation of entangled photon pairs [44]. Next progress was related to the improvements in the fabrication of quantum dots. With an improved growth protocol, it was possible to fabricate symmetric strain-free QDs with naturally low FSS [26]. Together with the new generation of the piezoelectric actuators, that allowed to independently control individual components of the applied strain tensor, the emission of entangled photon pairs has been experimentally demonstrated.

Along with the main research line, we tackled numerous related problems. In addition to the bright exciton pair, we studied also the dark exciton pair, which was made optically active by the strain present

near the cleaved edge of the sample [48] or higher charge and orbital excitation, including excitonic complexes and excited states of the exciton [29, 47]. The external strain field turned out to be a very useful tool for tuning and controlling various properties of quantum dots including the binding energies of excitons and their complexes [47], valence band mixing and polarization anisotropy of light emission [45], or tunneling rates in quantum dot molecules [49]. We have also addressed type-II quantum dots with spatially separated electrons and holes [62, 82]. Among others, we predicted the possibility to achieve zero FSS by adjusting the thickness of the capping layer.

Quantum dots determine the properties of excitons, the initial states for the generation of photons. However, as electronic elements, they have no or little influence on the generation process itself, which happens by means of spontaneous emission. Here, optical elements are required that influence the local photonic density of states and allow to control the rate and directionality of the emission. Plasmonic antennas represent an example of such optical elements. They are metallic nanostructures with dimensions comparable to quantum dots. They support localized plasmon resonance that allow to modify the photonic density of states at te nanoscale. When placed to a close vicinity of quantum dots they do not interfere with excitons except for controlling their spontaneous radiative decay. Our aim is to integrate the quantum dots with plasmonic antennas in order to controll the emission of photons. Our preliminary results in this direction include the fabrication of plasmonic antennas and characterization of their localized plasmon resonances using electron energy loss spectroscopy [80, 81].

After the decades of research, the field of semiconductor quantum dots is mature and ready for transfer of technology to industry. Quantum dot lasers are now commercially available [83], and quantum-dot-based single-photon sources or flash memories are expected to follow in the near future. The research in the field will mostly address novel materials, improvement of existing technologies, scalability necessary for mass industry, etc. Fundamentals of the quantum dot are in general well understood. Nevertheless, novel discoveries based on out-of-the-box thinking are still possible [84].

Quantum dots are one of the state-of-the-art light sources for quantum communications, both as single photon emitters and emitters of entangled photon pairs [85]. Our research substantially contributed to the understanding and optimization of the phenomena related to the latter point, in particular exciton fine structure splitting.

Despite the favourable properties, quantum dots do not represent an ideal source of quantum light for industrial applications. Most importantly, their fabrication is stochastic, which limits the uniformity of individual light sources and hinders their scalability. Next, low operation temperature is required for the emission of quantum light, at least for most widespread arsenide quantum dots. Further issues are related to the complexity of fabrication, difficult extraction of light from a material with the high refractive index, limited tunability, and environmental hazard.

A promising alternative quantum light source emerged recently: Two-dimensional (2D) single-layer semiconductors (hexagonal boron nitride or transition-metals dichalcogenides) exhibit single photon emission at room temperature [85]. The emitters can be prepared on-demand by local elastic strain [86] which offers unprecedented flexibility and controllability. 2D materials are flexible, offer wide-range tunability, and do not suffer from poor light extraction. While their current performance as light sources is in many aspects inferior to quantum dots, there is a substantial prospect for improvement. The field of light emission from 2D materials is fresh and still vastly unexplored. It is also the field into which we will direct our future research effort.

As excellent light sources, 2D materials are promising candidates for applications in the field of nanophotonics. 2D emitters are extremely compact and chemically stable and thus suitable for on-chip integration. Plasmonic antennas operate in deeply subwavelength regime and therefore also allow

high-density integration. It is the light itself and its wave length that limits the minimum accessible size of a photonic element. The time has come to harness the near electromagnetic field that beats the diffraction limit, allows for a subwavelength localization and thus open the path towards smaller photonic elements and higher density of integration. In our future research we will focus on integration of quantum light emitters with plasmonic antennas serving for enhanced light emission, steering the direction of the emitted light, or as waveguide couplers.

References

[1] E. Yablonovitch, Phys. Rev. Lett. **58**, 2059 (1987).

[2] S. John, Phys. Rev. Lett. **58**, 2486 (1987).

[3] T. F. Krauss, R. M. De La Rue, and S. Brand, Nature **383**, 699 (1996).

[4] E. M. Purcell, Phys. Rev. **69**, 674 (1946).

[5] H. Y. Ryu and M. Notomi, Opt. Lett. **28**, 2390 (2003).

[6] A. Badolato, K. Hennessy, M. Atatüre, J. Dreiser, E. Hu, P. M. Petroff, and A. Imamoğlu, Science **308**, 1158 (2005).

[7] D. C. Unitt, A. J. Bennett, P. Atkinson, D. A. Ritchie, and A. J. Shields, Phys. Rev. B **72**, 033318 (2005).

[8] D. R. Smith, W. J. Padilla, D. C. Vier, S. C. Nemat-Nasser, and S. Schultz, Phys. Rev. Lett. **84**, 4184 (2000).

[9] W. J. Padilla, D. N. Basov, and D. R. Smith, Mater. Today **9**, 28 (2006).

[10] D. Schurig, J. J. Mock, B. J. Justice, S. A. Cummer, J. B. Pendry, A. F. Starr, and D. R. Smith, Science **314**, 977 (2006).

[11] D. R. Smith, J. B. Pendry, and M. C. K. Wiltshire, Science **305**, 788 (2004).

[12] J. B. Pendry, D. Schurig, and D. R. Smith, Science **312**, 1780 (2006).

[13] H. Walther, B. T. H. Varcoe, B.-G. Englert, and T. Becker, Rep. Prog. Phys. **69**, 1325 (2006).

[14] R. Miller, T. E. Northup, K. M. Birnbaum, A. Boca, A. D. Boozer, and H. J. Kimble, J. Phys. B **38**, S551 (2005).

[15] H. J. Kimble, Phys. Scr. **1998**, 127 (1998).

[16] M. Pfeiffer, K. Lindfors, P. Atkinson, A. Rastelli, O. G. Schmidt, H. Giessen, and M. Lippitz, phys. status solidi (b) **249**, 678 (2012).

[17] J.-S. Huang, V. Callegari, P. Geisler, C. Brüning, J. Kern, J. C. Prangsma, X. Wu, T. Feichtner, J. Ziegler, P. Weinmann, M. Kamp, A. Forchel, P. Biagioni, U. Sennhauser, and B. Hecht, Nat. Commun. **1**, 150 (2010).

[18] B. Frank, P. Kahl, D. Podbiel, G. Spektor, M. Orenstein, L. Fu, T. Weiss, M. Horn-von Hoegen, T. J. Davis, F.-J. Meyer zu Heringdorf, and H. Giessen, Science Advances **3** (2017).

[19] C. R. Kagan, E. Lifshitz, E. H. Sargent, and D. V. Talapin, Science **353** (2016).

[20] N. Ishikawa, M. Sugita, T. Ishikawa, S.-y. Koshihara, and Y. Kaizu, J. Am. Chem. Soc. **125**, 8694 (2003).

[21] J.-Y. Ge, H.-Y. Wang, J. Li, J.-Z. Xie, Y. Song, and J.-L. Zuo, Dalton Trans. **46**, 3353 (2017).

[22] R. S. Wagner and W. C. Ellis, Appl. Phys. Lett. **4**, 89 (1964).

[23] A. F. Raigoza, J. W. Dugger, and L. J. Webb, ACS Appl. Mater. Interfaces **5**, 9249 (2013).

[24] J. H. Davies, *The Physics of Low-dimensional Semiconductors: An Introduction* (Cambridge University Press, 1997).

[25] P. Y. Yu and M. Cardona, *Fundamentals of Semiconductors: Physics and Materials Properties* (Springer, Berlin, 2005).

[26] Y. H. Huo, V. Křápek, A. Rastelli, and O. G. Schmidt, Phys. Rev. B **90**, 041304 (2014).

[27] I. Vurgaftman, J. R. Meyer, and L. R. Ram-Mohan, J. Appl. Phys. **89**, 5815 (2001).

[28] R. Songmuang, S. Kiravittaya, and O. Schmidt, J. Cryst. Growth **249**, 416 (2003).

[29] L. Wang, V. Křápek, F. Ding, F. Horton, A. Schliwa, D. Bimberg, A. Rastelli, and O. G. Schmidt, Phys. Rev. B **80**, 085309 (2009).

[30] M. Sztucki, T. Metzger, V. Chamard, A. Hesse, and V. Holy, J. Appl. Phys. **99** (2006).

[31] J. Stangl, V. Holý, and G. Bauer, Rev. Mod. Phys. **76**, 725 (2004).

[32] T. Maltezopoulos, A. Bolz, C. Meyer, C. Heyn, W. Hansen, M. Morgenstern, and R. Wiesendanger, Phys. Rev. Lett. **91**, 196804 (2003).

[33] M. Morgenstern, N. Freitag, A. Vaid, M. Pratzer, and M. Liebmann, phys. status solidi RRL **10**, 24 (2016).

[34] V. Křápek, P. Klenovský, and T. Šikola, Phys. Rev. B **92**, 195430 (2015).

[35] D. Bimberg, M. Grundmann, and N. Ledentsov, *Quantum Dot Heterostructures* (Wiley, 1999).

[36] S. Maier, *Plasmonics: Fundamentals And Applications* (Springer US, 2007).

[37] A. Kinkhabwala, Z. Yu, S. Fan, Y. Avlasevich, K. Müllen, and W. E. Moerner, Nat. Photonics **3**, 654 (2009).

[38] V. Křápek, K. Kuldová, J. Oswald, A. Hospodková, E. Hulicius, and J. Humlíček, Appl. Phys. Lett. **89**, 153108 (2006).

[39] C. Heyn, A. Stemmann, T. Köppen, C. Strelow, T. Kipp, M. Grave, S. Mendach, and W. Hansen, Appl. Phys. Lett. **94**, 183113 (2009).

[40] S. Sanguinetti, K. Watanabe, T. Tateno, M. Gurioli, P. Werner, M. Wakaki, and N. Koguchi, J. Cryst. Growth **253**, 71 (2003).

[41] A. Rastelli, S. Stufler, A. Schliwa, R. Songmuang, C. Manzano, G. Costantini, K. Kern, A. Zrenner, D. Bimberg, and O. G. Schmidt, Phys. Rev. Lett. **92**, 166104 (2004).

[42] A. Hospodková, V. Křápek, K. Kuldová, J. Humlíček, E. Hulicius, J. Oswald, J. Pangrác, and J. Zeman, Physica E **36**, 106 (2007).

[43] J. D. Plumhof, V. Křápek, L. Wang, A. Schliwa, D. Bimberg, A. Rastelli, and O. G. Schmidt, Phys. Rev. B **81**, 121309 (2010).

[44] J. D. Plumhof, V. Křápek, F. Ding, K. D. Jöns, R. Hafenbrak, P. Klenovský, A. Herklotz, K. Dörr, P. Michler, A. Rastelli, and O. G. Schmidt, Phys. Rev. B **83**, 121302 (2011).

[45] J. D. Plumhof, R. Trotta, V. Křápek, E. Zallo, P. Atkinson, S. Kumar, A. Rastelli, and O. G. Schmidt, Phys. Rev. B **87**, 075311 (2013).

[46] G. E. Pikus and G. L. Bir, Sov. Phys. – Solid State **1**, 1502 (1960).

[47] F. Ding, R. Singh, J. D. Plumhof, T. Zander, V. Křápek, Y. H. Chen, M. Benyoucef, V. Zwiller, K. Dörr, G. Bester, A. Rastelli, and O. G. Schmidt, Phys. Rev. Lett. **104**, 067405 (2010).

[48] Y. H. Huo, V. Křápek, O. G. Schmidt, and A. Rastelli, Phys. Rev. B **95**, 165304 (2017).

[49] E. Zallo, R. Trotta, V. Křápek, Y. H. Huo, P. Atkinson, F. Ding, T. Šikola, A. Rastelli, and O. G. Schmidt, Phys. Rev. B **89**, 241303 (2014).

[50] R. Trotta, P. Atkinson, J. D. Plumhof, E. Zallo, R. O. Rezaev, S. Kumar, S. Baunack, J. R. Schröter, A. Rastelli, and O. G. Schmidt, Adv. Mater. **24**, 2668 (2012).

[51] R. Trotta, E. Zallo, C. Ortix, P. Atkinson, J. D. Plumhof, J. van den Brink, A. Rastelli, and O. G. Schmidt, Phys. Rev. Lett. **109**, 147401 (2012).

[52] M. D. Biegalski, K. Dörr, D. H. Kim, and H. M. Christen, Appl. Phys. Lett. **96**, 151905 (2010).

[53] J. E. Avron, G. Bisker, D. Gershoni, N. H. Lindner, E. A. Meirom, and R. J. Warburton, Phys. Rev. Lett. **100**, 120501 (2008).

[54] Y. Jang, T. Badcock, D. Mowbray, M. Skolnick, J. Park, D. Lee, H. Liu, M. Steer, and M. Hopkinson, Appl. Phys. Lett. **92**, 251905 (2008).

[55] A. Marent, M. Geller, A. Schliwa, D. Feise, K. Pötschke, D. Bimberg, N. Akçay, and N. Öncan, Appl. Phys. Lett. **91**, 242109 (2007).

[56] M. Geller, A. Marent, T. Nowozin, D. Bimberg, N. Akçay, and N. Oncan, Appl. Phys. Lett. **92**, 092108 (2008).

[57] R. Laghumavarapu, A. Moscho, A. Khoshakhlagh, M. El-Emawy, L. Lester, and D. Huffaker, Appl. Phys. Lett. **90**, 173125 (2007).

[58] S. Itzhakov, H. Shen, S. Buhbut, H. Lin, and D. Oron, J. Phys. Chem. C **117**, 22203 (2013).

[59] K. Akahane, N. Yamamoto, and N. Ohtani, Physica E **21**, 295 (2004).

[60] M. Zíková, A. Hospodková, J. Pangrác, J. Oswald, P. Krčil, E. Hulicius, P. Komninou, and J. Kioseoglou, J. Cryst. Growth **414**, 167 (2015).

[61] K. Kuldová, V. Křápek, A. Hospodková, J. Oswald, J. Pangrác, K. Melichar, E. Hulicius, M. Potemski, and J. Humlíček, phys. status solidi (c) **3**, 3811 (2006).

[62] P. Klenovský, V. Křápek, D. Munzar, and J. Humlíček, Appl. Phys. Lett. **97**, 203107 (2010).

[63] V. Křápek, P. Klenovský, A. Rastelli, O. G. Schmidt, and D. Munzar, J. Phys. Conf. Ser. **245**, 012027 (2010).

[64] G. Burkard, D. Loss, and D. P. DiVincenzo, Phys. Rev. B **59**, 2070 (1999).

[65] H. A. Kramers, Proc. Amsterdam Acad. **33**, 959 (1930).

[66] M. Bayer, G. Ortner, O. Stern, A. Kuther, A. A. Gorbunov, A. Forchel, P. Hawrylak, S. Fafard, K. Hinzer, T. L. Reinecke, S. N. Walck, J. P. Reithmaier, F. Klopf, and F. Schäfer, Phys. Rev. B **65**, 195315 (2002).

[67] J. J. Finley, D. J. Mowbray, M. S. Skolnick, A. D. Ashmore, C. Baker, A. F. G. Monte, and M. Hopkinson, Phys. Rev. B **66**, 153316 (2002).

[68] T. Takagahara, Phys. Rev. B **62**, 16840 (2000).

[69] M. Kroutvar, Y. Ducommun, D. Heiss, M. Bichler, D. Schuh, G. Abstreiter, and J. J. Finley, Nature **432**, 81 (2004).

[70] T. Takagahara, Phys. Rev. B **60**, 2638 (1999).

[71] O. Benson, C. Santori, M. Pelton, and Y. Yamamoto, Phys. Rev. Lett. **84**, 2513 (2000).

[72] V. Křápek, P. Klenovský, and T. Šikola, Acta Phys. Pol. A **129**, A (2016).

[73] S. Lüker, T. Kuhn, and D. E. Reiter, Phys. Rev. B **92**, 201305 (2015).

[74] M. Korkusinski and P. Hawrylak, Phys. Rev. B **87**, 115310 (2013).

[75] J. M. Luttinger and W. Kohn, Phys. Rev. **97**, 869 (1955).

[76] M. Bayer, P. Hawrylak, K. Hinzer, S. Fafard, M. Korkusinski, Z. R. Wasilewski, O. Stern, and A. Forchel, Science **291**, 451 (2001).

[77] D. Kim, S. E. Economou, S. C. Bădescu, M. Scheibner, A. S. Bracker, M. Bashkansky, T. L. Reinecke, and D. Gammon, Phys. Rev. Lett. **101**, 236804 (2008).

[78] R. Hornberger, S. Koller, G. Begemann, A. Donarini, and M. Grifoni, Phys. Rev. B **77**, 245313 (2008).

[79] E. A. Stinaff, M. Scheibner, A. S. Bracker, I. V. Ponomarev, V. L. Korenev, M. E. Ware, M. F. Doty, T. L. Reinecke, and D. Gammon, Science **311**, 636 (2006).

[80] V. Křápek, A. L. Koh, L. Břínek, M. Hrtoň, O. Tomanec, R. Kalousek, S. A. Maier, and T. Šikola, Opt. Express **23**, 11855 (2015).

[81] M. Horák, K. Bukvišová, V. Švarc, J. Jaskowiec, V. Křápek, and T. Šikola, Sci. Rep. **8**, 9640 (2018).

[82] P. Klenovský, M. Brehm, V. Křápek, E. Lausecker, D. Munzar, F. Hackl, H. Steiner, T. Fromherz, G. Bauer, and J. Humlíček, Phys. Rev. B **86**, 115305 (2012).

[83] A. Sandhu and M. Sugawara, Nature Photonics **1**, 392 EP (2007).

[84] X. Yuan, F. Weyhausen-Brinkmann, J. Martín-Sánchez, G. Piredda, V. Krápek, Y. Huo, H. Huang, C. Schimpf, O. G. Schmidt, J. Edlinger, G. Bester, R. Trotta, and A. Rastelli, Nature Communications **9**, 3058 (2018).

[85] I. Aharonovich, D. Englund, and M. Toth, Nature Photonics **10**, 631 (2016).

[86] A. Branny, S. Kumar, R. Proux, and B. D. Gerardot, Nature Communications **8**, 15053 (2017).

A Self-assembled quantum dots with tunable thickness of the wetting layer: Role of vertical confinement on interlevel spacing

Self-assembled quantum dots with tunable thickness of the wetting layer: Role of vertical confinement on interlevel spacing

Lijuan Wang,[1,*] Vlastimil Křápek,[2] Fei Ding,[1,2] Felicity Horton,[1] Andrei Schliwa,[3] Dieter Bimberg,[3] Armando Rastelli,[2,†] and Oliver G. Schmidt[2]

[1]*Max-Planck-Institut für Festkörperforschung, Heisenbergstrasse 1, D-70569 Stuttgart, Germany*

[2]*Institute for Integrative Nanosciences, IFW Dresden, Helmholtzstrasse 20, D-01069 Dresden, Germany*

[3]*Institut für Festkörperphysik, Technische Universität Berlin, Hardenbergstrasse 36, 10623 Berlin, Germany*

(Received 5 May 2009; revised manuscript received 7 July 2009; published 18 August 2009)

Epitaxial self-assembled quantum dots (QDs) are commonly obtained by the Stranski-Krastanow (SK) growth mode, in which QDs form on top of a thin two-dimensional (2D) wetting layer (WL). In SK QDs, the properties of the WL such as thickness and composition are hard to control independently of those of the overlying QDs. We investigate here strain-free GaAs/AlGaAs QDs located under a GaAs quantum well (QW), analogous to the WL in SK QDs. The thickness of such a QW can be arbitrarily controlled, allowing the optical properties of the QDs to be tuned without modifying the QD morphology and/or composition. By means of single-QD photoluminescence spectroscopy, we observe well-resolved excited-state shell structures with intershell spacing increasing monotonically with decreasing QW thickness. This behavior is well reproduced by eight-band $k \cdot p$ calculations combined with the configuration-interaction model taking the realistic QD morphology as input. Furthermore, for the thinnest GaAs layer investigated here, no QW emission is detected, indicating that it is possible to suppress the two-dimensional layer usually connecting QDs. Finally, we find that all recombination involving an electron-hole pair in the ground state, including the positive trion, occurs at the low-energy side of the neutral exciton emission. This behavior, previously observed for GaAs/AlGaAs QWs, is a consequence of the large lateral extent of the QDs, and hence of pronounced self-consistency and correlation effects.

DOI: 10.1103/PhysRevB.80.085309 PACS number(s): 81.07.Ta

I. INTRODUCTION

Semiconductor quantum dots (QDs), also referred to as "artificial atoms," can be conveniently fabricated by self-assembled epitaxial growth. For the realization of QD-based devices, the optical properties of the QDs such as the emission wavelength, the intersublevel spacing energy, the ensemble homogeneity, and even the interactions between nearby QDs should be free for engineering. The most common method to obtain high quality QDs consists in exploiting the Stranski-Krastanow (SK) growth mode during strained heteroepitaxial growth, in which QDs spontaneously form on top of a thin wetting layer (WL). An example is InAs QDs on GaAs(001) substrate. The structural properties of such QDs, such as size, shape, and composition, can be controlled to some extent by varying the growth parameters during InAs deposition. Alternatively, the QD structure can be tuned *in situ* by partial capping and annealing[1,2] or by *ex situ* post-growth rapid thermal annealing.[3–5] Both the transition energies and the intersublevel spacing energies can be adjusted by the above methods either through a reduction in QD height or by promoting In-Ga intermixing, which reduces the QD confinement potential. In both cases, the shape, size, and composition profile of QDs vary during the tuning processes.

In SK QDs, the thickness of the WL can only be controlled in a narrow range, because it is mainly governed by the misfit strain between deposited material and substrate material.[6] On the other hand, unstrained QDs offer the possibility of independent tuning of WL thickness and QD shape/size. Self-assembled unstrained GaAs/AlGaAs QDs can be fabricated by local droplet etching[7] or by modified droplet epitaxy (MDE).[8] With the latter method GaAs QDs on top of a GaAs quantum well (QW) with arbitrary thickness can be obtained. In analogy to SK QDs, we refer to the QW as "WL." The effect of the GaAs WL thickness on the emission of QDs was investigated in Ref. 8 by photoluminescence (PL) spectroscopy. It was shown that a decrease in the WL thickness produces a blueshift in the ground-state (GS) emission and the WL can even be completely suppressed. However, no appreciable effect on the separation between GS and excited-state (ES) emission was observed, possibly because the PL inhomogeneous broadening prevented the observation of well-resolved excited-state "shells."

To eliminate the effect of inhomogeneous broadening we investigate here the light emission of single GaAs/AlGaAs QDs fabricated by "hierarchical self-assembly" (Refs. 9 and 10) as a function of WL thickness. These QDs are defined by filling $Al_{0.45}Ga_{0.55}As$ nanoholes with GaAs with variable thicknesses. Therefore, in contrast to SK and MDE QDs, this growth technique creates inverted GaAs QDs inside $Al_{0.45}Ga_{0.55}As$ holes with a QW (or WL) above the QDs. By depositing small amount of GaAs, the formation of the WL can also be fully suppressed.

Different from commonly investigated SK InAs/GaAs QDs and independent of WL thickness, we find that all optical transitions involving the recombination of a ground-state electron with a ground-state hole, including the positive trion (X^+), are characterized by energies lower than the neutral exciton (X). This behavior is well reproduced by an

eight-band $k \cdot p$ calculation combined with the configuration-interaction model.

Although the shape and lateral extent of the QDs are kept nominally fixed, a reduction in the WL thickness, and hence of the QD height, produces a systematic increase in the GS-ES energy separation. This observation can be seen as a "cross talk" between vertical confinement potential and lateral confinement potential, responsible for the GS-ES splitting. The observed behavior is qualitatively explained with a simple model and quantitatively reproduced by eight-band $k \cdot p$ calculations combined with the configuration-interaction model.

II. EXPERIMENTAL METHODS

The samples studied here were grown by a solid-source molecular-beam epitaxy (MBE) machine equipped with an $AsBr_3$ gas etching unit. A layer of InAs QDs grown on GaAs (001) at a nominal substrate temperature of 500 °C was the starting point for the fabrication of GaAs/AlGaAs QDs. The as-grown InAs QDs were overgrown with 10 nm GaAs and nominal 5-nm-deep $AsBr_3$ etching was applied *in situ*. As a result of the strain-enhanced and material-selective etching rate, bow-tie-shaped nanoholes were created by etching away the buried InAs QDs.[11,12] To create the lower barrier for the QD confinement potential, the obtained GaAs nanoholes were overgrown with 10 nm $Al_{0.45}Ga_{0.55}As$. Due to the low diffusivity of $Al_{0.45}Ga_{0.55}As$ on the GaAs surface, the nanoholes are preserved after the overgrowth. The obtained $Al_{0.45}Ga_{0.55}As$ nanoholes were filled immediately by depositing GaAs of variable thicknesses followed by a one min growth interruption at 500 °C, which allows the diffusion of the GaAs into the nanoholes. This multistep growth leads to the formation of inverted GaAs QDs with tunable QD height and WL thickness.

In order to deduce the morphology and size of the GaAs QDs, the morphology of the $Al_{0.45}Ga_{0.55}As$ nanoholes and uncapped GaAs QDs was studied by atomic force microscopy (AFM) in tapping mode at room temperature. For AFM characterization we employed samples with relatively high surface density of QDs ($\sim 10^9$ cm^{-2}) to collect large statistical information from small area images. For PL characterization of single QDs we used low-density ($\lesssim 10^8$ cm^{-2}) QD samples to avoid using shadow masks. The density was simply tuned by adjusting the amount of deposited InAs. We previously verified that the QD density has negligible effects on the emission energy of the GaAs/AlGaAs QDs, which is a consequence of the fact that we use dome-shaped InAs QDs (Ref. 13) with similar sizes independent of density. We can thus safely use the AFM data to model the optical properties of samples studied by PL spectroscopy.

For PL investigations, the GaAs QDs were buried by 100 nm $Al_{0.35}Ga_{0.65}As$, 20 nm $Al_{0.45}Ga_{0.55}As$, and 10 nm GaAs. The PL spectroscopy of single QDs was performed in a standard micro-PL setup at 6 K by using a laser emission of 532 nm as an excitation source, and a spectrometer with 500 mm focal length equipped with a charge-coupled device for detection.

III. THEORETICAL MODELING

To gain insight into the electronic structure and optical properties of the studied QDs we calculated transition energies of various excitonic complexes confined in QDs. The following two-step process was used: first, we obtained single-particle states using eight-band $k \cdot p$ theory.[14] Second, we performed configuration-interaction (CI) calculations, in which the multiparticle states are expanded into a series of Slater determinants (SDs) constructed from the single-particle states.[15]

The eight-band $k \cdot p$ theory presents an efficient way to obtain the electronic structure with very good accuracy and at acceptable computational expenses. It accounts for the conduction and valence-band mixing, while the effects of strain and piezoelectric field are not considered in this paper due to the negligible lattice mismatch between GaAs and AlGaAs. A numerical implementation consists in the finite difference scheme, which allows for a convenient treatment of arbitrary shape of QDs. The details of the implementation are given elsewhere.[14,16]

In the simulation the QDs are made of pure GaAs, since we expect limited interdiffusion of Al and Ga in the QDs at the low substrate temperature used in the experiment. The bottom surface of the QDs is determined from AFM measurements performed on the unfilled $Al_{0.45}Ga_{0.55}As$ nanoholes. The upper surface of the QDs is assumed to be flat. Although in the experiment a perfectly flat GaAs surface is not recovered after one min annealing (see below), we should point out that the real thickness of the QDs cannot be accessed by AFM measurements and it can only be estimated from the amount of the deposited GaAs d. Due to this uncertainty in the QD height and unavoidable uncertainty in the exact size/shape of the dots investigated by PL spectroscopy, we substitute the realistic profile of the top surface revealed by AFM by a simple plane. Such a treatment is reasonable since a rather flat profile is observed at the center of the filled holes, where the high electron probability occurs. Therefore, a flat top surface is adopted and an adjustable parameter h is introduced in our model, which represents the height of the top plane above the AlGaAs nanohole plane. This parameter roughly corresponds to the nominal WL thickness d. The structure is subsequently discretized for the finite difference calculations. With a grid step of 0.5 nm, a typical grid consists of $120 \times 120 \times 40$ points.

The multiparticle Hamiltonian consists of a sum of single-particle Hamiltonians and Coulomb interaction terms. Approximately, the wave function of a multiparticle complex can be constructed as a SD of single-particle states. However, such a wave function is not the eigenstate of the multiparticle Hamiltonian because the single-particle wave functions are deformed by the mutual Coulomb interaction. This effect is treated within CI by expanding the wave function into a series of SDs. In our calculation we used ten electron and ten hole wave functions, resulting in 100 SDs for the neutral exciton, 450 for the trions, and 2025 for the neutral biexciton.

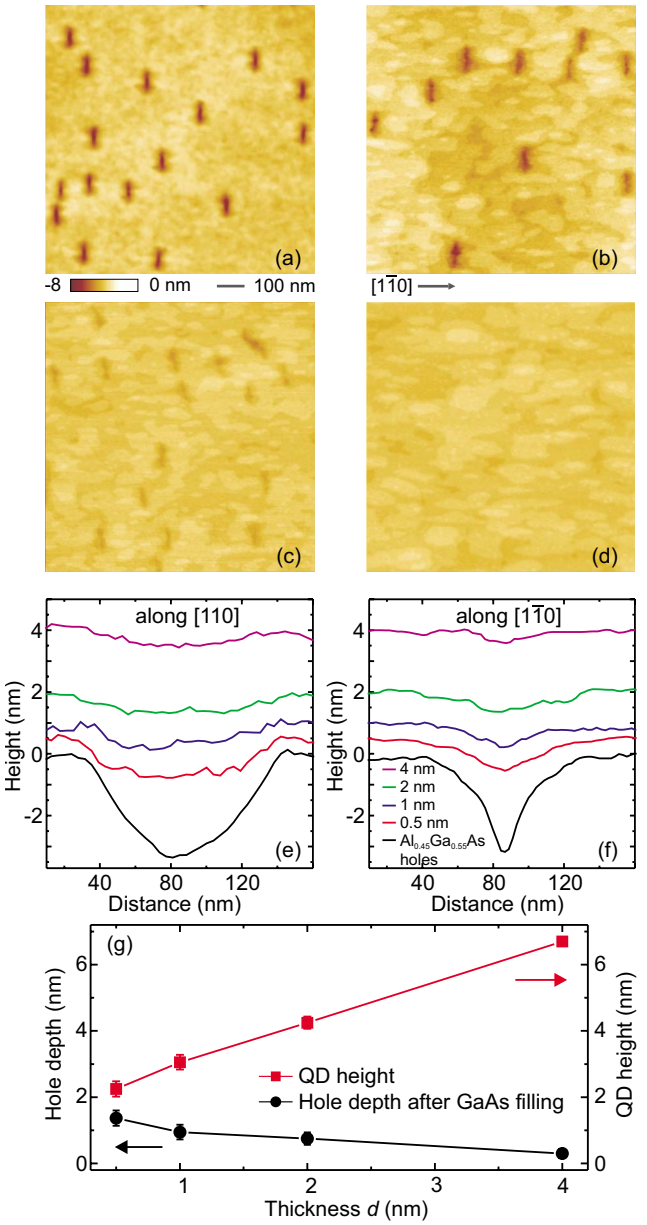

FIG. 1. (Color online) AFM image of $Al_{0.45}Ga_{0.55}As$ nanoholes (a) and of nanoholes filled with GaAs with nominal thickness d of (b) 0.5 nm, (c) 1 nm, and (d) 4 nm followed by one min annealing prior to cooling to room temperature. Linescans of representative nanoholes in the (e) [110] and (f) [1$\bar{1}$0] directions. The lines are offset in vertical direction by an amount equal to d. (g) Depth of the GaAs-filled nanoholes and the deduced height of GaAs QDs for different GaAs fillings. The QD height for each sample is extracted from the difference in depth for the $Al_{0.45}Ga_{0.55}As$ nanoholes and the GaAs-filled nanoholes plus d.

IV. RESULTS AND DISCUSSION

A. Morphology of GaAs/AlGaAs quantum dots

In order to determine the morphology of the GaAs QDs, we imaged by AFM the bottom and the top interfaces with the $Al_{0.45}Ga_{0.55}As$ and $Al_{0.35}Ga_{0.65}As$ barriers, respectively. Figure 1(a) shows an AFM image of $Al_{0.45}Ga_{0.55}As$ nanoholes created by overgrowing the GaAs nanoholes with 10 nm $Al_{0.45}Ga_{0.55}As$. The holes have an average depth of about 3 nm [see Figs. 1(e) and 1(f)] and are elongated in the [110] direction, similar to previous results.[10] The hole depth rapidly decreases as more GaAs is deposited on the AlGaAs surface followed by annealing [Figs. 1(b)–1(d)]. This is due to GaAs diffusion inside the holes driven by the local positive surface curvature. The surface evolution is better seen in Figs. 1(e) and 1(f), where linescans of representative $Al_{0.45}Ga_{0.55}As$ and GaAs-overgrown nanoholes are displayed together along the [110] and [1$\bar{1}$0] crystal directions. Linescans are vertically shifted by an amount d (WL thickness), to illustrate the QD plus WL morphology and size in cross section. From the linescans we see that nanoholes are completely filled with GaAs already for $d=0.5$ nm. On the other hand, the surface above the GaAs QDs is atomically smooth only for $d\sim 4$ nm [see Fig. 1(d)], indicating that the one min annealing step used after GaAs deposition is not sufficient to planarize the structure, especially for small values of d [see Fig. 1(b)].

Figure 1(g) summarizes the values of the depth of the GaAs nanoholes (top interface of GaAs QDs) and estimated QD height as a function of d. The QD height is simply estimated as the difference between the depth of $Al_{0.45}Ga_{0.55}As$ nanoholes and the depth of the subsequently GaAs-filled holes plus d. It is evident that the QD height increases almost linearly as a function of GaAs thickness.

B. Single QD spectroscopy: Evidence of bonding positive trion

The growth protocol used here offers the opportunity to tailor the optical properties, and especially the confinement energy of the QDs, via fine tuning of the growth parameters. Representative PL spectra of the ground-state emission in single QDs with different WL thicknesses are shown in Fig. 2(a). The energy axes are shifted to facilitate the comparison. As expected, the emission energy of the GaAs QDs redshifts when the WL thickness is increased as a result of increased QD height. In spite of different transition energies, the QD emission shows similar spectral features independent of d, i.e., a rather isolated emission line at high energy accompanied by other lines separated by $\gtrsim 2$ meV on the low-energy side. The high-energy peaks dominate at low excitation power and are attributed to neutral exciton recombination (X), as suggested by linear polarization-dependent measurements (see Fig. 3). In all the investigated QDs, an additional line, which dominates the spectrum at relatively high excitation power, appears on the low-energy side of X. Its energy separation from X (which is referred to as its "binding energy" E_B) shows a slight tendency to decrease with increasing GaAs WL thickness d in Fig. 2(a). The E_B values measured for several QDs in samples with different d are presented in Fig. 2(b), which shows broad distributions for each d values. Because of the absence of polarization splitting (see Fig. 3) and the p-background doping in our MBE chamber, we assign the prominent line to a positive trion X^+, as indicated by labels in Figs. 2 and 3. On the other hand, excitation-power-dependent measurements (shown later in Fig. 5) show that such a line appears at higher powers compared to the neutral exciton, letting us conclude that an extra

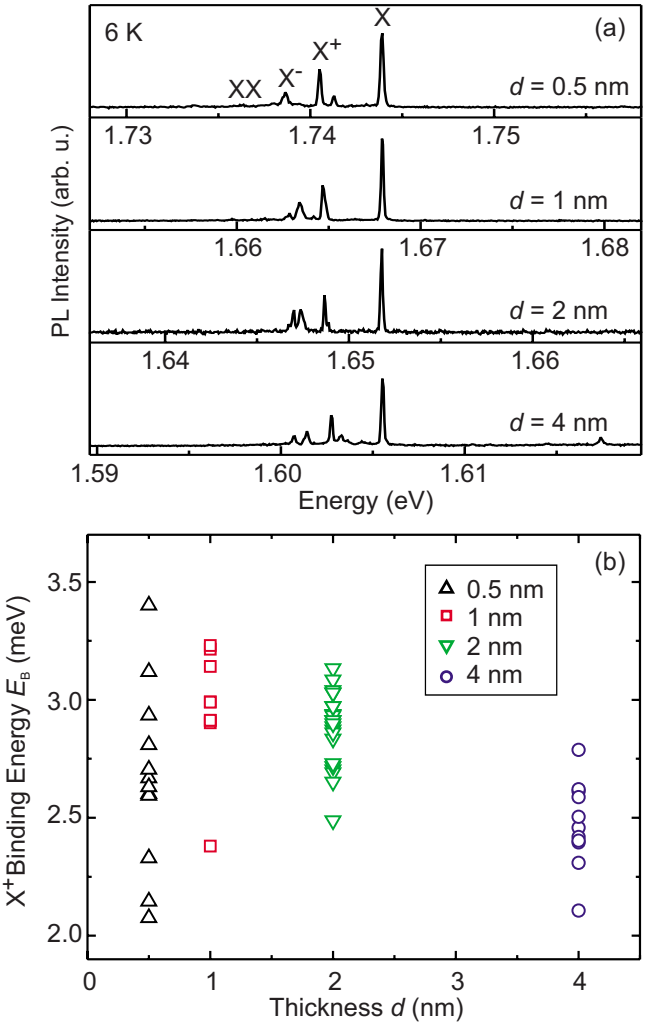

FIG. 2. (Color online) (a) Low-temperature PL spectra of representative QDs for samples of various d. The energy axes are shifted horizontally to facilitate the comparison. (b) Binding energy for the positive trion as a function of d.

carrier (possibly a hole) is not resident in the QD, but is the result of the nonresonant photogeneration process followed by carrier migration and relaxation. While PL alone is thus not sufficient to draw a definite conclusion on the origin of the peak, the calculation results presented later support its assignment to X^+. Furthermore, the positive value of E_B is fully consistent with previous studies on GaAs/AlGaAs QWs.[17]

The small features at lower energies include the negative trion X^- and other multiexcitonic species involving carriers in the QD excited states. The sharp line observed in some QDs at relatively low excitation power is attributed to X^- [see Fig. 2(a)]. As for the X^+, its binding energy tends to decrease with increasing d.

To further support the line assignment and look for signatures of the neutral biexciton (XX), we analyzed the polarization of the PL spectra for several QDs by continuous rotation of an achromatic lambda half wave plate followed by a fixed linear polarizer placed in front of the spectrometer. With the used configuration, only light polarized in the $[1\bar{1}0]$

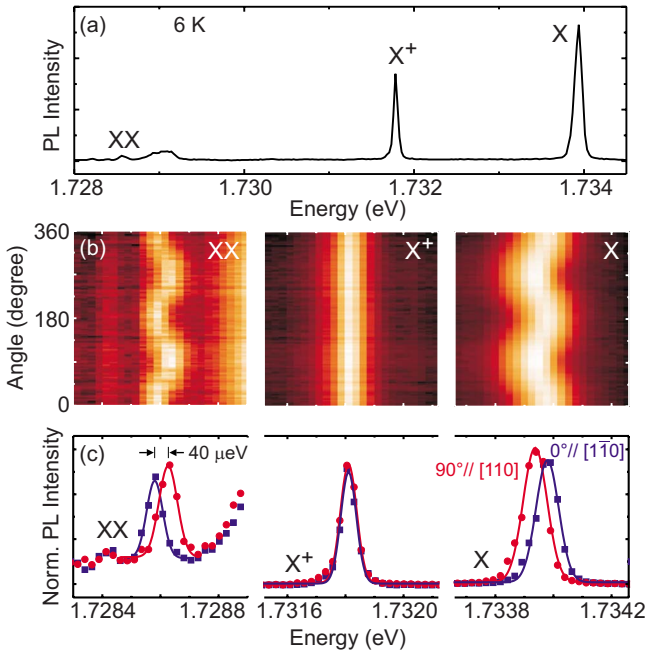

FIG. 3. (Color online) (a) PL spectrum of a QD with d =0.5 nm acquired at a polarization angle of 45°. (b) Polarization-angle-dependent PL intensity (grayscale coded) for the X, X^+, and XX lines. (c) Normalized PL spectra at polarization angle of 0° and 90° for the corresponding peaks.

crystal direction can enter the spectrometer at a polarization angle of 0°, while at 90°, light polarized along the [110] direction is selected. Representative spectra for a GaAs QD in a sample with d=0.5 nm are shown in Fig. 3. Figure 3(a) shows a PL spectrum and Fig. 3(b) the grayscale-coded PL intensity as a function of emission energy and polarization angle for the X, X^+, and XX. The X and XX lines split into two components, which are polarized perpendicular to each other. This behavior is currently ascribed to anisotropic electron-hole exchange interaction, which splits the X level into two lines.[18] Since the X state is the final state of the XX recombination, the XX emission is split by the same amount. In the left and right panels of Fig. 3(b) the X and XX lines show anticorrelated shifts, which confirm the assignment of the peak origin. The X^+ peak energy does not show any polarization angle dependence, confirming that this line originates from a singly charged exciton. Figure 3(c) shows normalized PL spectra for X, X^+, and XX at 0° and 90°. The low-energy component of X is polarized along the elongation direction of the GaAs QD (see Fig. 1), i.e., the [110] direction. The two components of X and XX in Fig. 3(c) are splitted by ~40 μeV. A systematic investigation on the role of shape anisotropy on the X splitting will be presented elsewhere.

Figure 4(a) shows the calculated binding energies of the positive and negative trions and the biexciton as functions of the thickness h [see Sec. III and bottom inset in Fig. 4(a)]. The binding energies are defined as the difference between the transition energy of a certain multiparticle complex and the neutral exciton as indicated in the inset of Fig. 4(a). The binding energy of the biexciton displays only a weak dependence on h; in contrast, the binding energy of the negative

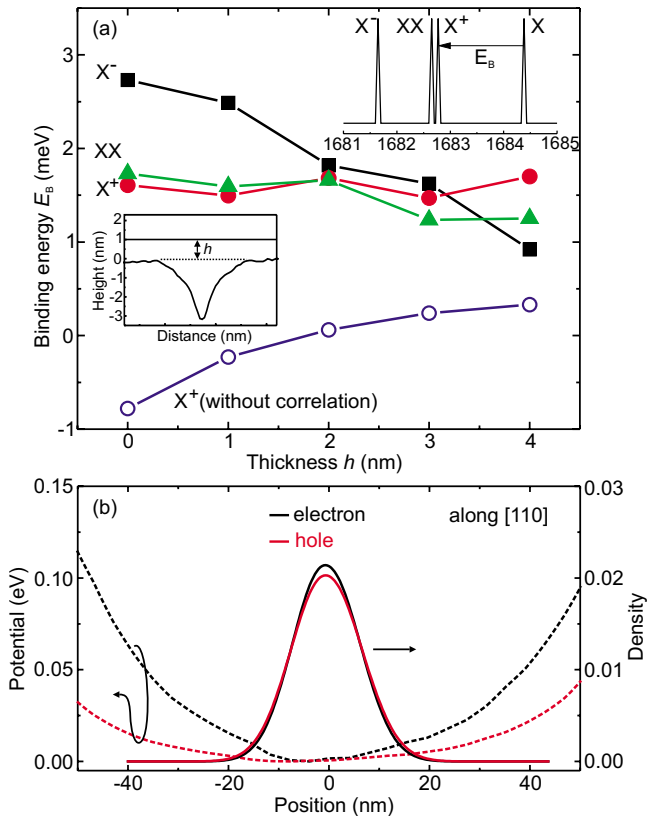

FIG. 4. (Color online) (a) Calculated binding energies of negative trion (squares), positive trion (circles), and biexciton (triangles) as a function of the WL thickness h, which is defined in the left bottom inset. The binding energies of the positive trion without taking into account the correlations (open circles) are also plotted. The top inset shows an example spectrum for $h=0$, where the binding energy for the positive trion is indicated (the energy in the horizontal axis is indicated in meV). (b) Calculated electron and hole densities (solid lines) and the effective potential (see also Fig. 8) felt by the electrons and holes (dashed lines) in the [110] direction.

trion drops substantially as h is increased. The calculated binding energy for the X^+ fluctuates with decreasing h, consistent with the experimental results [see Fig. 2(b)]. Therefore, its attribution to the positive trion emission is supported by theory. The magnitudes of the calculated binding energies, lying between 1.5 and 2 meV, however, are smaller than the observed values (between 2.5 and 3.5 meV for X^+ and around 7 meV for XX). Probably this difference is caused by an underestimation of correlation and self-consistency effects in our calculations. This discrepancy is small for the exciton and increases with the number of particles the complex is composed of. For the biexciton, for instance, Shumway *et al.*[19] observed that only 50% to 65% of the Coulomb corrections are captured by CI for a comparably sized basis set. The quantum Monte Carlo method, however, which was used as benchmark in that work, does not properly work in conjunction with eight-band $k\cdot p$ theory at present. An example of the excitonic absorption spectra, calculated for $h=0$, is shown in the top inset of Fig. 4(a).

We should point out that the binding energy of the X^+ is positive, which is usually not the case for InAs QDs (see, e.g., Ref. 20). This can be easily explained in terms of Coulomb attractions/repulsions among particles with opposite/same charges. In addition to the neutral exciton, the trion energy contains one attractive (electron-hole) and one repulsive (hole-hole) Coulomb term. Because of rather similar spatial distributions of charge densities for both electron and hole in the in-plane direction [see Fig. 4(b)], these terms have similar magnitude. The mutual correlation among particles forming the trion in a large QD slightly favors the attraction, leading to a positive binding energy. To highlight the importance of correlation effects, we present in Fig. 4(a) the binding energy of X^+ by excluding correlation effects. The binding energy is drastically reduced and becomes even negative for small values of h. Table I summarizes the contributions to the X^+ binding energy for different values of h. The binding energy $E_B(X^+)$ is the energy of the constituents (neutral exciton X and a hole) minus the energy of the complex (X^+). Denoting the single-particle energies of electron and hole as E_e and E_h, respectively, the energy of X reads $E(X)=E_e-E_h+C_{eh}+E_C(X)$, where C_{eh} is the Coulomb attraction of electron and hole and $E_C(X)$ is the correlation energy of neutral exciton. The correlation energies are estimated as differences between the CI results obtained on the basis of ten electrons and ten holes versus two electrons and two holes. The energy of X^+ reads $E(X^+)=E_e-2E_h+2C_{eh}+C_{hh}+E_C(X^+)$, where C_{hh} is the Coulomb repulsion of two holes and $E_C(X^+)$ is the correlation energy of positive trion. Finally, the binding energy of positive trion is $E_B(X^+)=-C_{eh}-C_{hh}-E_C(X^+)+E_C(X)$. A positive value of E_B has been previously observed in GaAs QWs (Ref. 17) and in II–VI QDs (see, e.g., Ref. 21), where the exciton radius may be substantially smaller than the QD lateral size.

C. QD shell structure and QDs without wetting layer

To investigate the effect of WL thickness on the shell structures of the GaAs QDs we performed excitation-power-

TABLE I. Calculated components of the binding energy of the positive trion $E_B(X^+)$ as functions of the nominal thickness of the wetting layer h.

h (nm)	C_{eh} (meV)	C_{hh} (meV)	$E_C(X^+)$ (meV)	$E_C(X)$ (meV)	$E_B(X^+)$ (meV)
0	−26.65	27.43	−5.15	−2.76	1.61
1	−23.58	23.81	−3.73	−2.00	1.50
2	−21.26	21.20	−3.36	−1.74	1.68
3	−19.41	19.17	−3.04	−1.80	1.48
4	−17.89	17.56	−3.47	−2.10	1.70

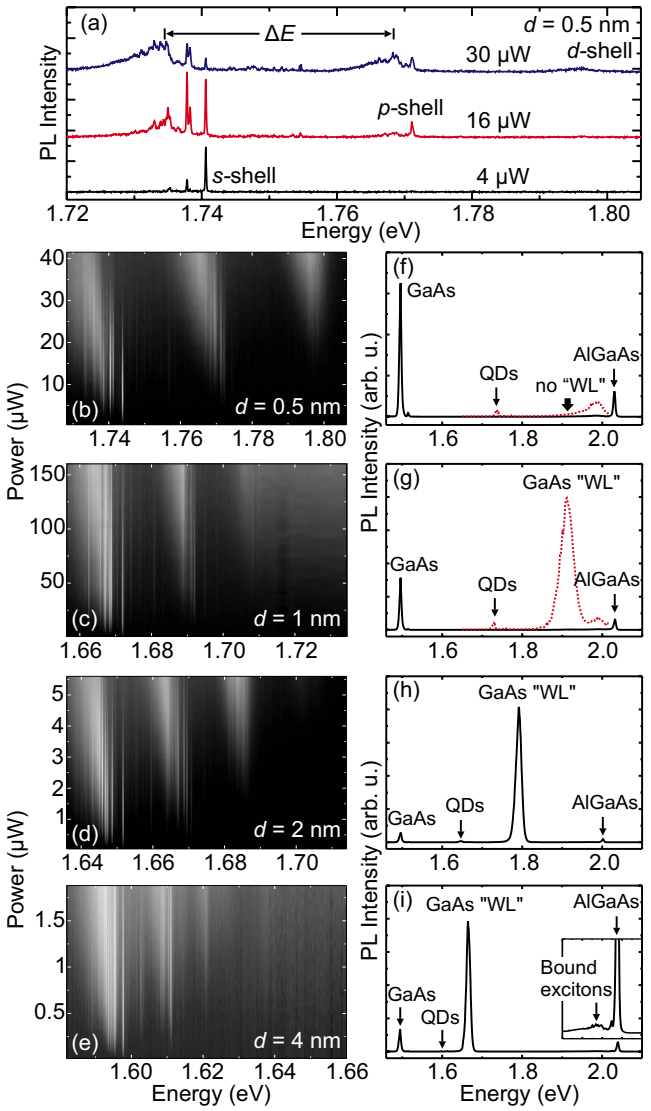

FIG. 5. (Color online) (a) PL spectra at different excitation powers for a QD with $d=0.5$ nm. Grayscale-coded PL intensity measured at 6 K as a function of excitation power and emission energy for single QDs of samples with (b) $d=0.5$ nm, (c) $d=1$ nm, (d) $d=2$ nm, and (e) $d=4$ nm. The right panel shows corresponding PL spectra collected on a wider spectral range, where the emission from bulk GaAs, QDs, GaAs WL, and $Al_{0.35}Ga_{0.65}As$ are indicated. The red dotted lines in (f) and (g) show spectra collected at very high excitation power in the energy range of 1.65–2.02 eV. The inset in (i) shows a high-resolution spectrum between 1.9 and 2.1 eV, where the emission from bound excitons in the $Al_{0.35}Ga_{0.65}As$ barrier is emphasized.

dependent PL measurements on single QDs. Representative PL spectra for a QD in the sample with $d=0.5$ nm are shown in Fig. 5(a) for different excitation powers. The intensities of neutral exciton, positively charged exciton lines, and other species saturate progressively as the excitation power rises. As a result of further increased excitation power, broad bands at the low-energy side of the neutral exciton lines emerge due to emission from multiexcitonic states. To compare the shell structure for QDs in samples with different d, we show the PL intensity as a function of excitation power and emission energy (grayscale coded) in Figs. 5(b)–5(e) for representative QDs in samples with increasing d. For each QD sample with different thicknesses d, the energy spacing between subsequent shells is approximately constant, at least for the first two excited states. The shells can be characterized by a number of nodal planes along the [110] and the $[1\bar{1}0]$ directions. The lowest shell clearly originates from s and the second from $p_{[110]}$ state. The third shell could in principle stem from $p_{[1\bar{1}0]}$ as well as from $d_{[110]}$ states. Our calculations revealed that it originates from the $d_{[110]}$ state (i.e., two nodal planes perpendicular to the [110] direction), while the shell originating from the $p_{[1\bar{1}0]}$ state has even higher energy and is not observed in the measurements. The calculated spacing energy for excitations along the $[1\bar{1}0]$ direction is almost three times higher as that along the [110] direction. Thus, in the following, we will consider only the excitations in the [110] direction.

A comparison between QDs in the four samples shows that the shell-spacing energy decreases as d increases. This observation may appear at first surprising, since the lateral extent of the QDs (which is responsible for the energy spacing between electronic levels in shallow QDs) is nominally the same in all samples. On the other hand a change in the vertical confinement potential affects the effective lateral confinement potential as discussed in more detail below.

Broad range PL spectra of the different samples are shown in Figs. 5(f)–5(i). The emission from the GaAs buffer and substrate, GaAs QDs, and $Al_{0.35}Ga_{0.65}As$ is invariably observed in all samples at a relatively low excitation power. In the sample with $d=1$ nm the emission of the AlGaAs layer is shifted to about 2.0 eV, which is ascribed to a slight deviation in the Al content (0.34 instead of 0.35) from the nominal value. The spectra are dominated by very pronounced emission from the GaAs WL in the case of $d=2$ nm and 4 nm, while only a very weak signal is observed for the sample of $d=1$ nm and no appreciable signal is observed for $d=0.5$ nm GaAs QDs. The amplified spectra at very high excitation power [red dotted spectra in Figs. 5(f) and 5(g)] show that the WL emission becomes evident for GaAs QDs of $d=1$ nm, but is still absent for the QDs of $d=0.5$ nm. In the high power spectrum of Fig. 5(f) only a weak and broad peak near the emission of $Al_{0.35}Ga_{0.65}As$ is observed. This peak is invariably observed in all the samples and is composed of many sharp lines, as shown in the inset of Fig. 5(i) for QDs with $d=4$ nm. We ascribe this emission below the band gap of $Al_{0.35}Ga_{0.65}As$ to the recombination of excitons bound to impurities or confined in alloy fluctuations.[22] Furthermore, by comparing the AFM images shown in Figs. 1(a) and 1(b) we observe that the surface gets smoother after deposition of 0.5 nm GaAs (corresponding to less than two monolayers), indicating that some of the deposited GaAs is consumed partially in planarizing the surface above $Al_{0.45}Ga_{0.55}As$. We can thus conclude that by choosing $d \lesssim 0.5$ nm we can obtain GaAs QDs without a WL connecting them, so that the next "continuum" state is represented by the bulklike top $Al_{0.35}Ga_{0.65}As$ barrier.

Figure 6 summarizes the effect of varying the WL thickness on the emission properties of QDs and WL. The blueshift in QD and WL emission for decreasing d is shown in

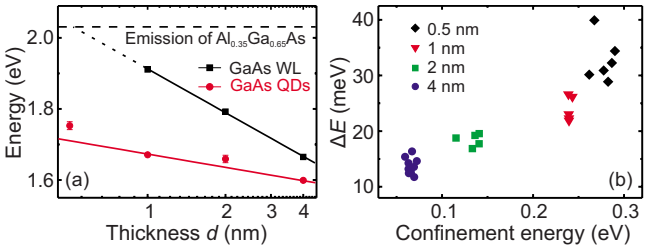

FIG. 6. (Color online) (a) Emission energy of GaAs QDs and WL for samples of various d. Solid lines are linear fits and serve as guide to the eyes. (b) Energy separation between ground state and first excited state for each sample as a function of confinement energy, which is defined by the energy difference between QDs and WL emission for each sample.

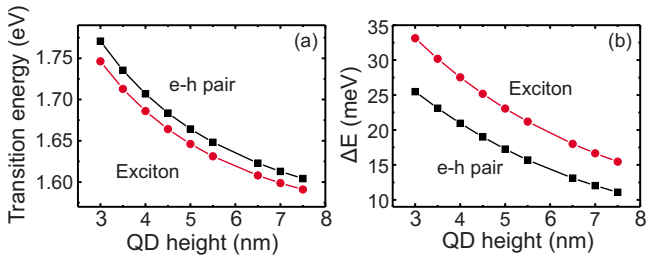

FIG. 7. (Color online) (a) Calculated energy of the lowest transition, excluding (squares) or including (circles) Coulomb interaction, as a function of QD height. (b) Calculated energy spacing between ground state and first excited-state transition, excluding (squares) or including (circles) Coulomb interaction, as a function of QD height.

Fig. 6(a), where the emission energy of the QDs is the average value found for several QDs. This trend is an obvious consequence of the decreased vertical size of QDs and WL, and can be quantitatively reproduced by our calculations (see below).

To quantify the effect of d on the energy spacing between ground state and first excited-state emission ΔE, we fitted the corresponding broad energy shells measured at high excitation power with Gaussian functions and measured the energy separation between their centers. The result of this analysis, performed on several QDs, is shown in Fig. 6(b), where ΔE is plotted as a function of the "confinement energy," defined as the energy difference between the GaAs WL and the ground-state emission of the QDs. For the sample with d $=0.5$ nm, the emission energy of the WL is replaced by that of $Al_{0.35}Ga_{0.65}As$, since no WL emission is observed. The shell energy separation shows a systematic increase from ~ 14 to ~ 32 meV, when the confinement energy is increased, pointing out to a correlation between lateral and vertical confinement potentials. This behavior is different from what is observed with other energy tuning techniques such as rapid thermal annealing.[3–5,23] In that case the blueshift in the QD emission produced by interdiffusion is accompanied by a smaller blueshift in the WL emission, so that the confinement energy decreases and so does the shell separation ΔE.

The calculated lowest transition energy and ΔE are depicted in Figs. 7(a) and 7(b), respectively, as functions of the QD height. As the height increases, all the energies of electrons, holes, and transitions decrease, as well as ΔE. These results are in good agreement with the experimental data shown in Fig. 6. While the decrease in energies is attributed to a reduced confinement energy in the growth direction, the explanation of the decreased spacing energy ΔE is at first not obvious. The spacing is related to the lateral profile of the QDs, which is not influenced by the presence of the WL. The wave functions also do not extend laterally into the WL, although they do vertically. The decrease in ΔE can be thus rationalized in the following way: due to the flat shape of the dots studied here, the lateral confinement can be approximately separated from the vertical potential allowing the separation of variables in the three-dimensional Schrödinger equation. The vertical confinement energy is obtained by solving a one-dimensional Schrödinger equation for the height of the QD at a certain point of the lateral plane. The vertical confinement energy varies laterally as the height varies, forming an effective lateral confinement potential. This reasoning elaborated in more detail can be found in Ref. 24. For smaller values of the height (e.g., when no WL is present), the dependence of the vertical energy on the height is rather steep, resulting in steep lateral potential and distant level spacings (large values of ΔE). On the contrary, for large values of the height (when a thick WL is present), the vertical energy-height dependence is rather shallow, resulting in shallow lateral potential and close level spacings (low values of ΔE). Figure 8(a) shows an example of the effective lateral confinement potential (for electrons) along the [110] direction calculated for different values h of WL thickness {the confinement along $[1\bar{1}0]$ can be approximately decoupled and does not contribute to the observed shell spacing, since all the observed shells originate in the states with nodal planes perpendicular to [110]}. The height profile was taken from an AFM image of the AlGaAs nanohole shown in Fig. 8(b), where the values of h are indicated as horizontal lines.

The effect of the Coulomb interaction on the transition energies is depicted by circles in Fig. 7. Due to the attraction between the electron and the hole forming the exciton, transition energies are reduced. This effect is more pronounced for the ground state than for the first excited state due to its lower spatial extension. The spacing ΔE, therefore, increases if the Coulomb interaction is taken into account.

The comparison of the measured and calculated transition energies and shell spacings is shown in Fig. 9(a). The points

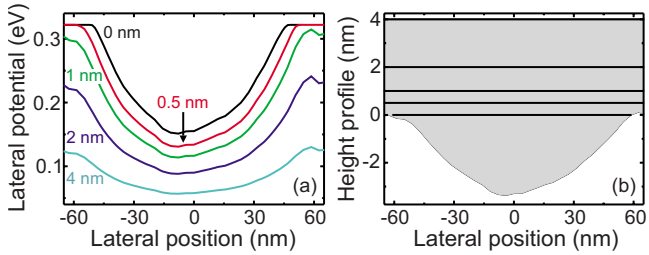

FIG. 8. (Color online) (a) Calculated effective lateral potential (for electrons) along the [110] direction for different thicknesses of WL. (b) AFM linescan of the bottom QD barrier along the [110] direction with indicated filling levels of h used for calculations.

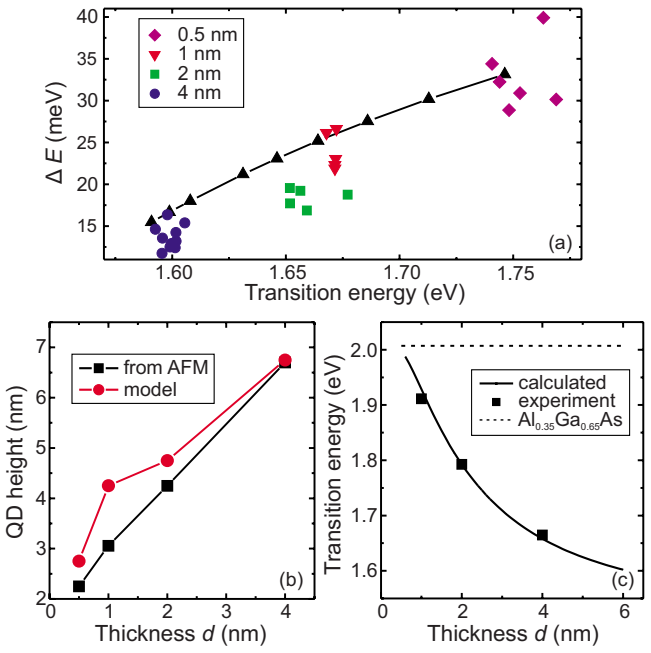

FIG. 9. (Color online) (a) Comparison of measured (symbols) and predicted (line+triangles) transition energies and ground state to excited-state separation. Different symbols correspond to different thicknesses of WL d as indicated. (b) Comparison of QD heights estimated from AFM images [see Fig. 1(g)] (squares) and heights of model structures fitted to the observed energies (circles). (c) Comparison of measured (symbols) and calculated (line) transition energies of GaAs/AlGaAs WL.

corresponding to experimental data lie in close proximity of the model line. The total heights of the QD+WL system estimated from AFM [Fig. 1(g)] are compared with the heights of the model structures as a function of d in Fig. 9(b). For the samples with $d=1$ and 2 nm, the QD height used in the model to reproduce the observed transition energies is slightly larger than the one estimated from AFM, attributed to random size fluctuations. Figure 9(c) shows calculated transition energies for the GaAs WL together with the corresponding experimental data. As pointed out in Fig. 6(a), no emission is observed for $d=0.5$ nm GaAs QDs. The calculation in Fig. 9(c) shows a very good agreement of measured [see Fig. 6(a)] and predicted transition energies for the GaAs WL. This result indicates that the thickness of the WL is not affected by the GaAs diffusion into the nanoholes due to their very low surface density.

V. CONCLUSIONS

We systematically investigated the influence of the confinement potential on the optical properties of unstrained GaAs/AlGaAs QDs with tunable WL thickness and emission energy. For fixed QD shape, a systematic decrease in the energy separation between ground and excited states is observed when the WL thickness is increased. This degree of control, which is not available for commonly studied Stranski-Krastanow QDs, is used to produce QDs without WL. Theoretical calculations of the transition energy of QDs and WL show good agreement with the experimental data and allow us to clarify the impact of the WL thickness on the optical properties of QDs. Finally, different from commonly studied InAs/GaAs QDs, the GaAs/AlGaAs QDs are characterized by a positive trion with emission energy lower than the neutral exciton, which is found to be a consequence of the large lateral extent of the QDs, and hence, of pronounced self-consistency and correlation effects. In particular, the uncommon energetic sequence of XX, X^-, X^+, and X underlines the peculiar nature of our QD system.

ACKNOWLEDGMENTS

The authors thank A. Ulhaq for his contributions to the PL measurements and S. Kiravittaya and M. Benyoucef for fruitful discussions. This work was supported by the BMBF (Grant No. 03N8711), DFG (Grant No. FOR730), and SFB (Grant No. 787). The calculations were performed using the SGI supercomputer at the HLRN Berlin/Hannover.

*lijuan.wang@ifw-dresden.de
†a.rastelli@ifw-dresden.de

[1] J. M. Garcia, T. Mankad, P. O. Holtz, P. J. Wellman, and P. M. Petroff, Appl. Phys. Lett. **72**, 3172 (1998).
[2] L. Wang, A. Rastelli, and O. G. Schmidt, J. Appl. Phys. **100**, 064313 (2006).
[3] S. Fafard and C. N. Allen, Appl. Phys. Lett. **75**, 2374 (1999).
[4] T. M. Hsu, Y. S. Lan, W. H. Chang, N. T. Yeh, and J. I. Chyi, Appl. Phys. Lett. **76**, 691 (2000).
[5] C. N. Allen, P. Finnie, S. Raymond, Z. R. Wasilewski, and S. Fafard, Appl. Phys. Lett. **79**, 2701 (2001).
[6] Y. Tu and J. Tersoff, Phys. Rev. Lett. **93**, 216101 (2004).
[7] Ch. Heyn, A. Stemmann, T. Köppen, Ch. Strelow, T. Kipp, M. Grave, S. Mendach, and W. Hansen, Appl. Phys. Lett. **94**, 183113 (2009).
[8] S. Sanguinetti, K. Watanabe, T. Tateno, M. Gurioli, P. Werner, M. Wakaki, and N. Koguchi, J. Cryst. Growth **253**, 71 (2003).
[9] A. Rastelli, S. Stufler, A. Schliwa, R. Songmuang, C. Manzano, G. Costantini, K. Kern, A. Zrenner, D. Bimberg, and O. G. Schmidt, Phys. Rev. Lett. **92**, 166104 (2004).
[10] A. Rastelli, R. Songmuang, and O. G. Schmidt, Physica E (Amsterdam) **23**, 384 (2004).
[11] S. Kiravittaya, R. Songmuang, N. Y. Jin-Phillipp, S. Panyakeow, and O. G. Schmidt, J. Cryst. Growth **251**, 258 (2003).
[12] R. Songmuang, S. Kiravittaya, and O. G. Schmidt, Appl. Phys. Lett. **82**, 2892 (2003).
[13] G. Costantini, A. Rastelli, C. Manzano, R. Songmuang, O. G. Schmidt, K. Kern, and H. V. Känel, Appl. Phys. Lett. **85**, 5673 (2004).
[14] O. Stier, M. Grundmann, and D. Bimberg, Phys. Rev. B **59**, 5688 (1999).
[15] A. Schliwa, M. Winkelnkemper, and D. Bimberg, Phys. Rev. B

79, 075443 (2009).
[16] V. Mlinar, A. Schliwa, D. Bimberg, and F. M. Peeters, Phys. Rev. B **75**, 205308 (2007).
[17] J. L. Osborne, A. J. Shields, M. Pepper, F. M. Bolton, and D. A. Ritchie, Phys. Rev. B **53**, 13002 (1996).
[18] R. Seguin, A. Schliwa, S. Rodt, K. Pötschke, U. W. Pohl, and D. Bimberg, Phys. Rev. Lett. **95**, 257402 (2005).
[19] J. Shumway, A. Franceschetti, and A. Zunger, Phys. Rev. B **63**, 155316 (2001).
[20] J. J. Finley, M. Sabathil, P. Vogl, G. Abstreiter, R. Oulton, A. I. Tartakovskii, D. J. Mowbray, M. S. Skolnick, S. L. Liew, A. G. Cullis, and M. Hopkinson, Phys. Rev. B **70**, 201308(R) (2004).
[21] H. S. Lee, A. Rastelli, M. Benyoucef, F. Ding, T. W. Kim, H. L. Park, and O. G. Schmidt, Nanotechnology **20**, 075705 (2009).
[22] M. Ramsteiner, R. Hey, R. Klann, U. Jahn, I. Gorbunova, and K. H. Ploog, Phys. Rev. B **55**, 5239 (1997).
[23] J. J. Dubowski, C. N. Allen, and S. Fafard, Appl. Phys. Lett. **77**, 3583 (2000).
[24] A. Hospodková, V. Křápek, K. Kuldová, J. Humlíček, E. Hulicius, J. Oswald, J. Pangrác, and J. Zeman, Physica E (Amsterdam) **36**, 106 (2007).

B Tuning the Exciton Binding Energies in Single Self-Assembled InGaAs/GaAs Quantum Dots by Piezoelectric-Induced Biaxial Stress

Tuning the Exciton Binding Energies in Single Self-Assembled InGaAs/GaAs Quantum Dots by Piezoelectric-Induced Biaxial Stress

F. Ding,[1,2,3,*] R. Singh,[3] J. D. Plumhof,[1] T. Zander,[3] V. Křápek,[1] Y. H. Chen,[2] M. Benyoucef,[1] V. Zwiller,[4] K. Dörr,[5] G. Bester,[3,†] A. Rastelli,[1,‡] and O. G. Schmidt[1]

[1]*Institute for Integrative Nanosciences, IFW Dresden, Helmholtzstrasse 20, D-01069 Dresden, Germany*
[2]*Key Laboratory of Semiconductor Materials Science, Institute of Semiconductors, Chinese Academy of Sciences, Beijing 100083, China*
[3]*Max-Planck-Institut für Festkörperforschung, Heisenbergstrasse 1, D-70569 Stuttgart, Germany*
[4]*Kavli Institute of Nanoscience, Delft University of Technology, P.O. Box 5046, 2600 GA Delft, The Netherlands*
[5]*Institute for Metallic Materials, IFW Dresden, Helmholtzstrasse 20, D-01069 Dresden, Germany*

(Received 3 November 2009; published 12 February 2010)

We study the effect of an external biaxial stress on the light emission of single InGaAs/GaAs(001) quantum dots placed onto piezoelectric actuators. With increasing compression, the emission blueshifts and the binding energies of the positive trion (X^+) and biexciton (XX) relative to the neutral exciton (X) show a monotonic increase. This phenomenon is mainly ascribed to changes in electron and hole localization and it provides a robust method to achieve color coincidence in the emission of X and XX, which is a prerequisite for the possible generation of entangled photon pairs via the recently proposed "time reordering" scheme.

DOI: 10.1103/PhysRevLett.104.067405 PACS numbers: 78.67.Hc, 78.20.hb, 81.05.Ea, 81.40.Tv

Sources of entangled photon pairs *on demand* are a major building block for quantum computation and communication [1]. Recently, the generation of entangled photon pairs from semiconductor quantum dots (QDs) has attracted great interest [2–5]. The polarization-entangled photons are produced in an idealized QD with degenerate intermediate exciton states in the cascade: biexciton (XX) → exciton(X) → ground state (G), where the polarization of a photon pair is determined by the spin of the intermediate exciton state [6]. However, real self-assembled QDs exhibit intermediate exciton ground states split into two states by an energy δ called fine structure splitting (FSS) [7]. This is the consequence of shape and atomistic crystal anisotropy and the electron-hole exchange interactions [8]. The FSS in self-assembled In(Ga)As/GaAs QDs grown along the [001] crystal direction is typically quite large as compared to the radiative linewidth (≈ 1.0 μeV). The nonvanishing FSS encodes the which-path information and destroys the polarization entanglement. The generation of entangled photon pairs by simple preselection of rare dots with δ close to zero [2,4] or by spectral filtering [3] has been demonstrated. Furthermore, a number of postgrowth techniques have been used to reduce δ, such as in-plane magnetic fields [9], lateral electric fields [10,11], uniaxial stress [12], and rapid thermal annealing [13].

An alternative proposal to generate entangled photon pairs from QDs, without any fundamental requirements on the FSS to be smaller than the radiative linewidth, is the so-called time reordering scheme [14]. However, this scheme requires the emission energies of X (E_X) and XX (E_{XX}) to be the same. In this scheme, one entangles the red photons $H1(V2)$ and the blue photons $V1(H2)$ [see the central panel of Fig. 1(a)] across generations in a QD. It is accomplished by performing a unitary operation (time reordering) U on the two-photon state such that $|\langle\phi_H|U_H^\dagger U_V|\phi_V\rangle| > |\langle\phi_H|\phi_V\rangle|$ [14,15], where $|\phi_{H(V)}\rangle$ is the wave packet resulting from the biexciton cascade emis-

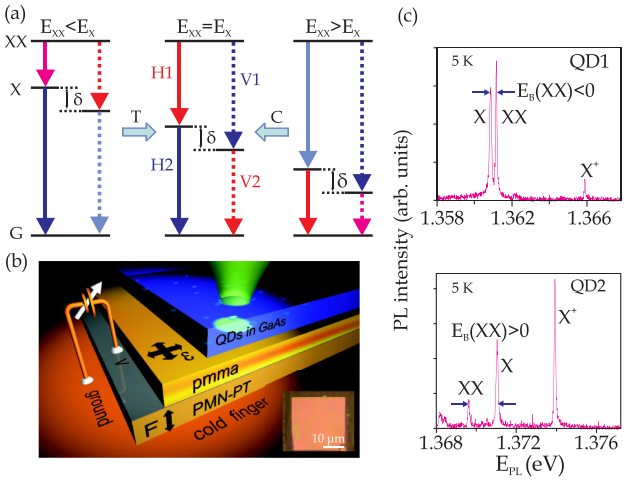

FIG. 1 (color online). (a) Level schemes showing the XX-X cascade. The solid (dashed) line represents the decay channel that yields H (V) polarized photons. Across generation color coincidence of X and XX ($E_X = E_{XX}$) can be achieved by applying tensile (compressive) stress to a QD with positive (negative) $E_B(XX)$. (b) Schematic drawing of the experiment and optical microscopy image of a 200 nm-thick GaAs membrane (inset). (c) Low temperature PL spectra of QDs with negative (QD1) and positive (QD2) XX binding energy.

sion. This novel concept is currently under vivid discussion [15–18]: On one hand the two-photon wave packet may suffer significant dephasing after the time reordering, on the other hand the emission energies E_X and E_{XX} in the as-grown QDs are usually different because of pronounced interactions between charge and spin carriers in a QD.

In this Letter we show that an external biaxial tensile (T) or compressive (C) stress can be used to achieve $E_X \approx E_{XX}$. Stress is provided *in situ* by placing a thin GaAs membrane containing self-assembled InGaAs QDs on top of a piezoelectric actuator, made of $[Pb(Mg_{1/3}Nb_{2/3})O_3]_{0.72}$-$[PbTiO_3]_{0.28}$ (PMN-PT) [see Fig. 1(b)]. With increasing compression, the relative spectral positions of different excitonic species (X, XX, and X^+) show subtle, but systematic changes: The binding energies E_B of both X^+ and XX, defined as $E_B(XX/X^+) = E_X$-E_{XX/X^+} increase in all studied QDs. Based upon million-atom empirical pseudopotential many-body calculations of realistic InGaAs/GaAs QDs, we ascribe this phenomenon to the increase in electron-hole Coulomb interactions due to the increase in confinement of electrons and slight decrease in confinement of holes upon compressive biaxial stress. Finally, different from the behavior observed under in-plane uniaxial stress [12], biaxial strain does not appreciably affect the FSS, a behavior which is also expected from our calculations.

We fabricated 200 nm-thick GaAs membranes with embedded self-assembled InGaAs QDs, and then transferred them onto a 300 μm-thick PMN-PT actuator via PMMA resist [20]. A bias voltage V applied to the PMN-PT results in an out-of-plane electric field F which leads to an in-plane strain $\varepsilon_\parallel$ in the GaAs membrane and the QD structure [see Fig. 1(b)]. The PMN-PT was poled so that $V > 0$ (< 0) corresponds to in-plane compressive (tensile) strain $\varepsilon_\parallel < 0$ (> 0). Figure 1(c) shows low-excitation power photoluminescence (PL) spectra of two QDs with negative $E_B(XX)$ (QD1) and positive $E_B(XX)$ (QD2). The neutral exciton X and the biexciton XX are identified by power- and polarization-dependent PL. (The latter allows us also to determine the FSS of X and XX). An unpolarized line lying at the higher energy side of X and XX is attributed to positive trion X^+ emission. The assignment is supported by the background p-type doping of our structures and by the correlation between $E_B(X^+)$ and $E_B(XX)$ observed in all the studied dots [see Fig. 2(e)].

Figure 2(a) shows the color-coded PL intensity of QD1 as a function of emission energy and voltage V applied to the PMN-PT actuator. V is swept several times between 0 and 1100 V with steps of 20 V, to demonstrate the reversibility of the tuning. For $V > 0$ the QD experiences an in-plane compression (C). The emission energies of different lines show roughly linear blueshifts with V. At the maximum reached bias, E_X shifts by $\sim$1.8 meV, without appreciable deterioration of the emission linewidth and intensity [20]. Similar energy shifts for a given V are observed for different dots in the same device. However,

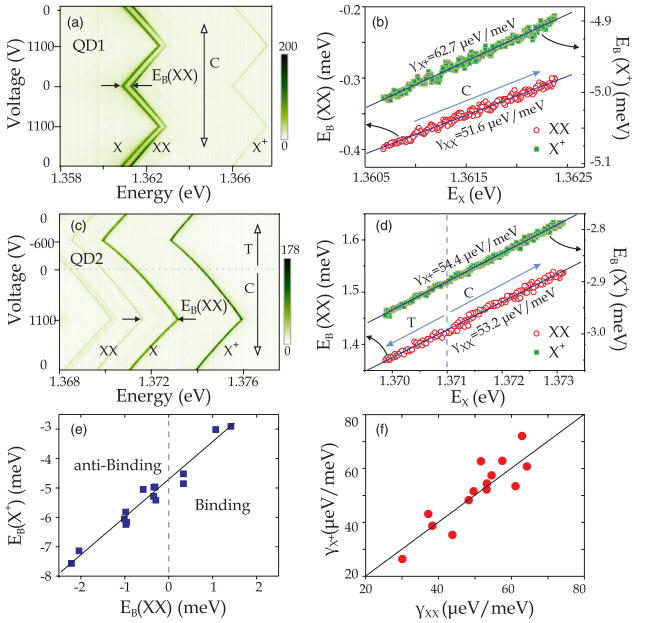

FIG. 2 (color online). Color-coded PL intensity of QD1 (a) and QD2 (c) as a function of emission energy and voltage applied to the actuator. The binding energies of XX and X^+ show a linear increase with E_X for both QDs, as shown in (b) and (d). (e) Binding energies at $V = 0$ and (f) slopes γ_{XX} and γ_{X^+} for 14 different QDs.

different devices show different maximum shifts, which may be due to slight variations in the composition or the mechanical contact of the PMN-PT to the coldfinger. More interestingly, the $E_B(XX)$ and $E_B(X^+)$ show a linear increase with E_X, see Fig. 2(b), with slopes $\gamma_{XX} = 51.6$ and $\gamma_{X^+} = 62.7$ μeV/meV for QD1. The results of a similar experiment performed on QD2 are shown in Figs. 2(c) and 2(d). In this case V is swept to positive and negative values. Under tension ($V < 0$) the QD emission lines redshift and the linear dependence between binding energies and E_X extends also to the tensile (T) strain region.

In order to verify whether these findings are affected by QD structural fluctuations, we have determined the values of γ for 14 different dots. The results are shown in Fig. 2(f). In all the studied dots we observe that both γ_{X^+} and γ_{XX} are *positive* and that for a given dot $\gamma_{X^+} \simeq \gamma_{XX}$. The former observation is interesting as it opens up the possibility to tune $E_B(XX)$ to zero in a controllable way. The latter suggests a common underlying physical mechanism responsible for the changes in binding energy of XX and X^+.

In order to understand the results and estimate the magnitude of the in-plane strain achieved in the experiment, we performed calculations on realistic InGaAs/GaAs QDs containing 3×10^6 atoms using the empirical pseudopotential and the configuration interaction (CI) approaches [21]. The excitonic states are calculated at the correlated CI level, including all configurations generated from 12 electron and 12 hole states (spin included). We model the QD as a lens shaped $In_{0.8}Ga_{0.2}As$ structure with a height of

2.5 nm and elliptical base of major (minor) axis of 10 (7.5) nm along the $[1\bar{1}0]$ ([110]) crystal direction.

Figure 3(a) shows the calculated emission energies of X, XX, and X^+ as a function of biaxial strain $\varepsilon_\parallel = [(a - a_0)/a_0]$, where a (a_0) is the lattice constant of strained (unstrained) GaAs. As in the experiment, all emission lines blueshift for $\varepsilon_\parallel < 0$ and redshift for $\varepsilon_\parallel > 0$. In analogy to the results shown in Figs. 2(b) and 2(d), we plot in Fig. 3(b) the relative binding energies of XX and X^+ as a function of E_X. Although the initial values of E_X and binding energies are somewhat different from those observed in the experiment [Figs. 1(c) and 2(e)], the calculation is able to reproduce the linear increase of $E_B(X^+)$ and $E_B(XX)$ with E_X. For the modeled QD structure the slope of $E_B(XX)$ is $\gamma_{XX} = 114$ μeV/meV, comparable with the experimental values. By repeating similar calculations on a larger QD with a circular base and a height of 3.5 nm with a lower In concentration (60%), we find $\gamma_{XX} = 28.3$ μeV/meV. Although the values of γ's depend on the actual QD structure and size the linear increase of binding energies of XX and X^+ relative to X upon biaxial compression is a rather general phenomenon as we observed in the experiments.

From our empirical pseudopotential calculations, we find that the effect of biaxial strain on the correlation energy is very small. The main changes in the binding energies of XX and X^+ are due to changes in the direct Coulomb interactions between electron and holes and can be approximated by

$$\begin{aligned} \Delta E_B(X^+) &\approx \Delta J_{eh} - \Delta J_{hh}, \\ \Delta E_B(XX) &\approx \Delta E_B(X^+) - [\Delta J_{ee} - \Delta J_{eh}], \end{aligned} \tag{1}$$

where J_{ee}, J_{hh}, and J_{eh} are the Coulomb integrals between lowest electron (e) and hole (h) states. Figure 3(c) shows that ΔJ_{eh} and ΔJ_{ee} increase with compressive strain, with only small deviations from each other. Interestingly, ΔJ_{hh} shows the opposite behavior, but its magnitude is substantially smaller than those of ΔJ_{eh} and ΔJ_{ee}. We thus conclude that the increase in binding energies of XX and X^+ upon compression is mainly a consequence of the increase in the electron-hole attraction term. The fact that $(\Delta J_{ee} - \Delta J_{eh})$ is small, qualitatively explains the similar values of $\Delta E_B(XX)$ and $\Delta E_B(X^+)$, as shown in Fig. 2(f).

To understand the increase in J_{ee}, J_{eh}, and decrease in J_{hh} upon compression, we plot in Fig. 3(d) the strain modified conduction band minimum and the upper two valence bands. For the latter bands we used circles proportional in size to the fraction of heavy-hole character. In the unstrained region, far from the dot, heavy- and light-hole bands are degenerate; close to the dot (inside the dot), the light (heavy)-hole band forms the valence band maximum. Since the QD hole states have up to ~92% heavy-hole character, we define the valence band offset (VBO) as the offset between the heavy-hole bands [Fig. 3(d)]. No such complication arises for the conduction band offset (CBO). In Fig. 3(e) we show a linear increase by ~35 meV for the CBO upon change in biaxial strain from 0.1% to −1%. This represents an increased confinement and localization of wave function: the intuitive picture of a compressed wave function obtained by a compression of the sample, is valid. For the VBO, however, we find a decrease by ~3 meV for the same range of strains. Upon compression, the wave functions tend to become more delocalized. This, rather counterintuitive behavior can be observed directly on the wave functions in Fig. 3(f), where we display the lowest electron state (LUMO) and highest hole state (HOMO) at two different strains. This localization or delocalization gives rise to the increase in J_{ee}, J_{eh}, and decrease in J_{hh} shown in Fig. 3(c). Similar results are obtained also by eight-band kp calculations combined with the CI model [20].

The fact that the biexciton binding energy monotonically increases upon compression provides a controllable strategy to tune $E_B(XX)$ to zero. If XX is initially located at the high (low) energy side of X, a biaxial compression (tension) allows us to tune $E_B(XX)$ so that the color coincidence between XX and X is achievable, depending on the available tuning range, the value of γ_{XX} and the initial value of $E_B(XX)$. Figure 4(a) demonstrates this capability for a QD where $E_B(XX)$ is initially −270 μeV. The total shift of E_X in this device is ~11 meV, which according to the calculations correspond to strain values exceeding ±0.3%. Figure 4(b) shows gray scale coded PL intensity plots of X and XX as a function of linear polarization angle and energy for various values of V. As expected, X and XX

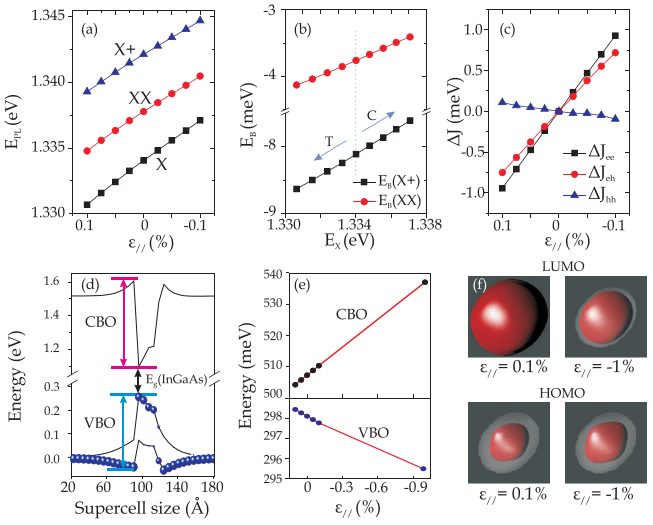

FIG. 3 (color online). (a) Calculated emission energies of X, XX, and X^+ as a function of in-plane biaxial strain $\varepsilon_\parallel$. (b) Relative binding energies of X^+ and XX vs E_X. (c) Changes in Coulomb integrals with biaxial strain. (d) Calculated band offset diagram at $\varepsilon_\parallel = 0$; for the valence band, the size of the circles is proportional to the heavy-hole character of the bands. (e) Changes in CBO (VBO) with strain $\varepsilon_\parallel$. (f) HOMO and LUMO wave functions at $\varepsilon_\parallel = 0.1\%$ and -1%. The red color encloses 75% of the charge density, while light gray color represents the outline of the QD.

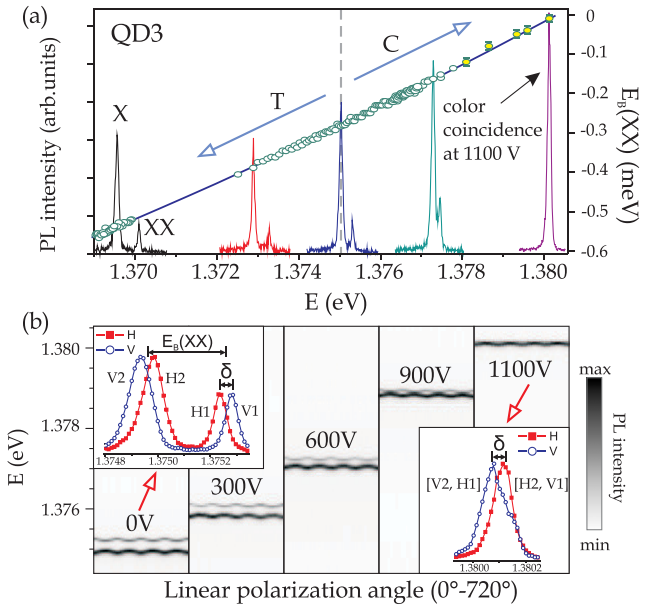

FIG. 4 (color online). (a) Biexciton binding energy of QD3 as a function of E_X. Several spectra are shown, demonstrating the decreasing distance between X and XX with increasing E_X. (b) Polarization-resolved PL map for the X and XX lines at several voltages. At 0 V $E_B(XX)$ is much larger than δ, while $E_B(XX)$ vanishes (limited by the system resolution) and δ dominates at 1100 V.

show anticorrelated shifts as we rotate the analyzer. The FSS for this QD, i.e., the energy separation δ between the H and V components of X or XX is 48 ± 5 μeV. As the voltage increases the magnitude of $E_B(XX)$ decreases, while δ stays constant within the measurement uncertainties. This finding, which is reproduced by our calculations, is not surprising, because the symmetry of the structure is not appreciably changed by biaxial strain. At 1100 V $E_B(XX) \rightarrow 0$ and δ dominates the energy scale in the problem: only two peaks with the splitting of δ can be observed. We have now practically reached the color coincidence of ($V2$, $H1$) and ($H2$, $V1$). For future entanglement measurements, we envision the use of a Michelson interferometer. That will allow the "red" ($V2$, $H1$) and the "blue" ($H2$, $V1$) photons to be directed to the two outputs of the interferometer, and hence spatially separated [22].

In conclusion, we have studied in detail experimentally and theoretically the effect of biaxial strain on the binding energies of different excitonic species confined in single InGaAs/GaAs(001) quantum dots. The most intriguing finding is that biaxial strain is a reliable tool to engineer the QD electronic structure and reach color coincidence between exciton and biexciton emission. While other techniques may be used to reach this goal, such as rapid thermal annealing [13,23] or lateral electric fields [24], strain engineering is advantageous as it can be performed *in situ* and does not produce any appreciable degradation of the emission, which usually occurs at large electric fields [25]. Furthermore, biaxial strain does not alter the excitonic FSS, which should remain sufficiently large for experimental tests on the viability of a newly proposed concept for the generation of entangled photon pairs [14]. Finally, the employed method can be used to study the effect of stress and tune the properties of a broad range of nano- and microstructures, such as optical microcavities [26].

We acknowledge N. Akopian, U. Perinetti, P. Klenovský, C. C. Bof Bufon, R. Hafenbrak, S. Mendach, and P. Michler for fruitful discussions and the financial support of the DFG (FOR730), BMBF (No. 01BM459), NWO (VIDI), CAS-MPG and NSFC China (60625402).

*f.ding@ifw-dresden.de
†g.bester@fkf.mpg.de
‡a.rastelli@ifw-dresden.de

[1] N. Gisin and R. Thew, Nat. Photon. **1**, 165 (2007).
[2] R. J. Young *et al.*, Phys. Rev. Lett. **102**, 030406 (2009).
[3] N. Akopian *et al.*, Phys. Rev. Lett. **96**, 130501 (2006).
[4] R. Hafenbrak *et al.*, New J. Phys. **9**, 315 (2007).
[5] R. Singh and G. Bester, Phys. Rev. Lett. **103**, 063601 (2009).
[6] O. Benson, C. Santori, M. Pelton, and Y. Yamamoto, Phys. Rev. Lett. **84**, 2513 (2000).
[7] D. Gammon *et al.*, Phys. Rev. Lett. **76**, 3005 (1996).
[8] M. Bayer *et al.*, Phys. Rev. B **65**, 195315 (2002).
[9] R. M. Stevenson *et al.*, Phys. Rev. B **73**, 033306 (2006).
[10] B. D. Gerardot *et al.*, Appl. Phys. Lett. **90**, 041101 (2007).
[11] M. M. Vogel *et al.*, Appl. Phys. Lett. **91**, 051904 (2007).
[12] S. Seidl *et al.*, Appl. Phys. Lett. **88**, 203113 (2006).
[13] R. Seguin *et al.*, Appl. Phys. Lett. **89**, 263109 (2006).
[14] J. E. Avron *et al.*, Phys. Rev. Lett. **100**, 120501 (2008).
[15] F. Troiani and C. Tejedor, Phys. Rev. B **78**, 155305 (2008).
[16] G. Pfanner, M. Seliger, and U. Hohenester, Phys. Rev. B **78**, 195410 (2008).
[17] P. K. Pathak and S. Hughes, Phys. Rev. Lett. **103**, 048901 (2009).
[18] J. E. Avron *et al.*, Phys. Rev. Lett. **103**, 048902 (2009).
[19] X. Li *et al.*, Science **301**, 809 (2003).
[20] See supplementary material at http://link.aps.org/supplemental/10.1103/PhysRevLett.104.067405.
[21] G. Bester, J. Phys. Condens. Matter **21**, 023202 (2009).
[22] T. Aichele, G. Reinaudi, and O. Benson, Phys. Rev. B **70**, 235329 (2004).
[23] R. J. Young *et al.*, Phys. Rev. B **72**, 113305 (2005).
[24] M. E. Reimer *et al.*, Phys. Rev. B **78**, 195301 (2008).
[25] M. Korkusinski, M. E. Reimer, R. L. Williams, and P. Hawrylak, Phys. Rev. B **79**, 035309 (2009).
[26] T. Zander *et al.*, Opt. Express **17**, 22 452 (2009).

C Electronic structure of InAs quantum dots with GaAsSb strain reducing layer: Localization of holes and its effect on the optical properties

Electronic structure of InAs quantum dots with GaAsSb strain reducing layer: Localization of holes and its effect on the optical properties

P. Klenovský,[a] V. Křápek, D. Munzar, and J. Humlíček
Department of Condensed Matter Physics, Faculty of Science, Masaryk University, Kotlářská 2, 61137 Brno, Czech Republic

(Received 16 July 2010; accepted 22 October 2010; published online 17 November 2010)

The electronic structure of InAs quantum dots covered with the $GaAs_{1-y}Sb_y$ strain reducing layer has been studied using the $\vec{k}\cdot\vec{p}$ theory. We explain previous experimental observations of the red shift of the photoluminescence emission with increasing y and its blue shift with increasing excitation power. For $y>0.19$, type-II dots are formed with holes localized in the GaAsSb close to the dot base; two segments at the opposite sides of the dot, forming molecular-like states, result from the piezoelectric field. We also propose an experiment that could be used to identify the hole localization using a vertical electric field. © *2010 American Institute of Physics*.
[doi:10.1063/1.3517446]

InAs quantum dots (QDs) covered with the $GaAs_{1-y}Sb_y$ strain reducing layer (SRL) represent an efficient light source at the communication wavelengths of 1.3/1.55 μm.[1,2] The role of the SRL is to reduce the strain inside the QDs and to modify the confinement potential, both effects increasing the otherwise small emission wavelengths of the InAs QDs. Note that the $GaAs_{1-y}Sb_y$ capped QDs differ from the more conventional $In_xGa_{1-x}As$ capped ones[3,4] in several important aspects. The antimony atoms act as surfactant, which helps preserve the shape and the height of the QDs during the overgrowth. The resulting QDs are considerably higher than the $In_xGa_{1-x}As$-capped ones.[5] Moreover, for $y>0.14$, the formation of type-II dots with holes localized in the SRL was reported.[1,2,6] The red shift of the emission energy with y increasing from 0.10 to 0.22 has been found,[2] more pronounced in the type-II confinement regime. A peculiarity of the type-II regime is a large blue shift (up to tens of meV) of the emission energy with the excitation power.[2,6]

We have calculated the electronic structure of QDs capped by the $GaAs_{1-y}Sb_y$ SRL using a two-step approach. First, single particle states were obtained using the Nextnano++ solver [7] based on the eight-band $\vec{k}\cdot\vec{p}$ theory. Second, we calculated the energies of the excitons using the configuration interaction method with the basis set formed from the single particle states.[8] The values of the material constants are given in Ref. 9. Based on the published cross-section scanning tunneling micrographs (XSTM),[5,10] we assume a pyramidal shape of the model QD with the height of 8 nm and the base length of 22 nm. Both the shape and the dimensions were taken from Ref. 5 without any changes. The results of Refs. 5 and 10 also suggest that the QDs are composed of $In_xGa_{1-x}As$ with a trumpet-like composition profile, with $x=0.4$ at the base of the pyramid (low In content) and $x=1.0$ at its top (maximum In content). Here, we adopt this profile. The XSTM cannot very reliably determine the composition profile,[11] thus we studied several other profiles and found only minor differences.[9] The thickness of the SRL has been fixed at 5 nm and y varied between 0.10 and 0.22.

Figure 1 shows the lowest transition energy as a function of y. With y increasing from 0.10 to 0.22, the energy redshifts by 84 meV from 1055 to 971 meV, the origin being illustrated in the inset. This is in very good agreement with the optical data,[2] where the energy shifts by 83 meV from 1050 to 967 meV. We emphasize that the red shift was reproduced without any modification of the shape and dimensions of the model QD. This is consistent with the observations of Ref. 5 that the shape and the size of the QDs are independent of y. Recall that in the $In_xGa_{1-x}As$ capped QDs, a large part of the red shift is caused by the increase of volume.[12] For $y<0.15$ ($y>0.19$), the probability of finding the hole inside the QD is larger than 80% (smaller than 20%), which we call type-I (type-II) confinement in the following. We have found the type I to type II transition not to be abrupt, but rather to be a continuous process starting at low y, accelerated in a certain range of y ($0.15<y<0.19$ for our dot), and finally saturating at high values of y.[9] Note that we found the type-II QDs for larger y than usually reported. The red shift of the type-II confinement is faster because the

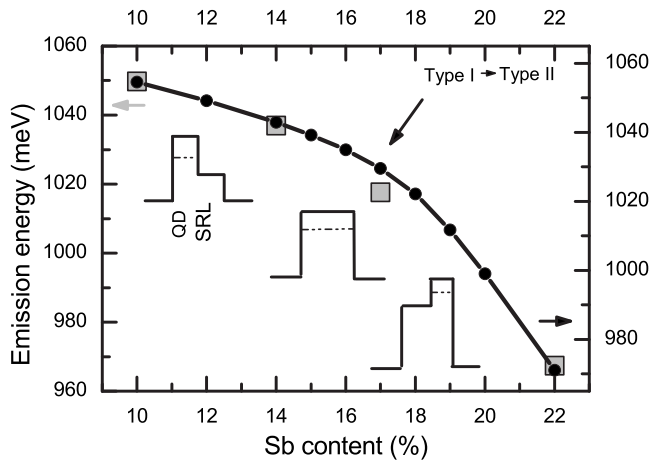

FIG. 1. Calculated values of the emission energy of the model pyramidal QD (circles) compared to the corresponding values obtained from the optical measurements, taken from Ref. 2 (squares). The vertical axis of the experimental values is shifted by 5 meV with respect to that of the model results. The arrow points to the onset of the type-II confinement. A schematic representation of the hole confinement is also shown.

[a]Electronic mail: klenovsky@physics.muni.cz.

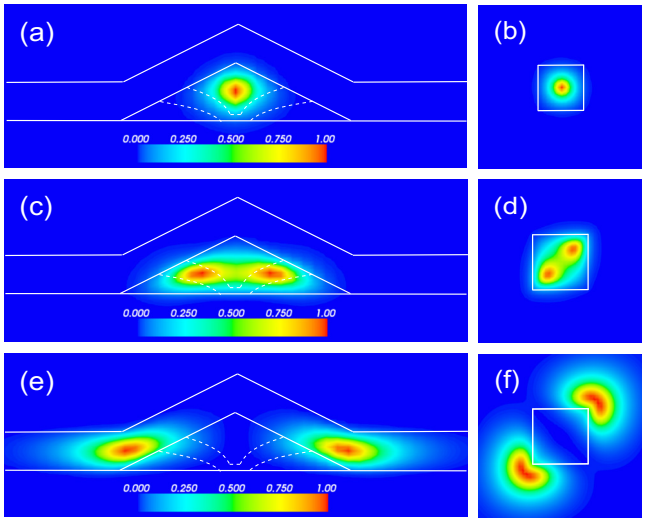

FIG. 2. (Color online) Cross sections of the probability density (arbitrary units) of the lowest electron state for $y=0.10$: (a) $(1\bar{1}0)$ plane, (b) (001) plane; [(c) and (d)] the same for the lowest hole state and $y=0.10$; [(e) and (f)] the same for the lowest hole state and $y=0.22$ (see also Ref. 9). The $(1\bar{1}0)$ planes contain the vertical symmetry axis of the QD and the (001) cross sections are located 3.5 nm (2.5 nm) above the base of the QD for electrons (for holes). The borders of the QD and the SRL are denoted by the solid lines. The dashed lines are the isolines of the In content inside the QD (100% and 60%).

bottom of the potential well shifts and not the barrier as in type I.[1,13,14]

The type I to type II transition is associated with a reduction of the overlap of the electron and hole wave functions and the corresponding decrease of the Coulomb energy of the electron-hole pair from 26 meV at $y=0.10$ to 12 meV at $y=0.22$. The biexciton emission energy calculated using the configuration interaction method[8] with six electrons and eight hole basis states is blue-shifted by 4 meV with respect to the exciton emission energy at $y=0.10$, and blue-shifted by 18 meV at $y=0.22$. While the multiexcitonic ordering in type-I QDs depends on structural properties of the QD,[11] the blue shift of the biexciton with respect to the exciton is a characteristic property of the type-II QDs.[9] We suggest that the blue shift of the emission energy with the pumping intensity reported for type-II QDs[2,6] is caused by the emission from the blue-shifted biexcitons emerging at high pumping powers. This could be verified by intensity-dependent microphotoluminescence measurements. The biexciton energy could be used as the indicator of the type of the confinement.

Next, we address the wave functions. The probability densities of the lowest electron and hole states in the model QD are shown in Fig. 2 ($y=0.10$ for electrons, $y=0.10$ and $y=0.22$ for holes). The electrons are localized in the In-rich region of the QD, the position of the maximum of their probability density being only weakly dependent on y. For $y=0.10$, the holes are localized inside the QD close to the base of the pyramid, in agreement with the previously reported results for the type-I InAs QDs.[15] For $y>0.19$, the holes are located in the SRL. It has been assumed that they reside above the QD.[6,16] We found them, however, to be located close to the base of the dot [see Figs. 2(e) and 2(f)]. This is a consequence of the strain distribution. The shift of the heavy-hole band edge due to the biaxial strain $B=\varepsilon_{zz}-(\varepsilon_{xx}+\varepsilon_{yy})/2$ is given by $\Delta E=-b\cdot B$, where ε_{ij} are the components of the strain tensor and b is the biaxial deformation potential.

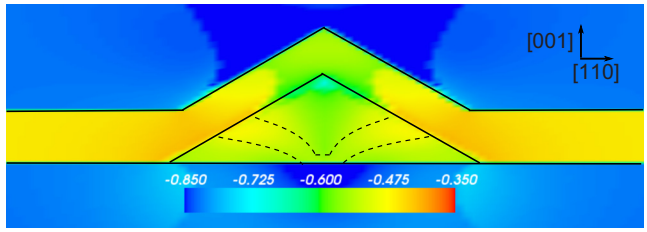

FIG. 3. (Color online) The $(1\bar{1}0)$ cross section of the confinement potential for holes in the type-II QD with $y=0.22$. The scale is in eV. The holes are confined in the two potential minima in the SRL close to the base of the QD.

Since b is negative, the holes prefer the regions with large positive values of B at the dot base, as shown in Fig. 3.

If only the strain is included in the calculations, the maximum of the probability density of the hole ground state forms a ring surrounding the dot base. The piezoelectric field splits it into two segments located along the [110] direction.[9] The wave functions resemble those of quantum dot molecules. Quantum dot molecules (QDMs) are important for the quantum information processing as a potential tool for manipulating the qubits— a quantum gate.[17] Vertical QDMs can be easily manufactured and offer a strong coupling, but they cannot be scaled and suffer from the internal symmetry lowering induced by the strain field.[18] On the other hand, lateral QDMs (LQDMs) reported so far exhibit a weak coupling[19] and their properties cannot be tuned easily. The properties of the "molecules" under consideration are in many aspects superior. Most importantly, the distance between the segments and the tunneling energy can be easily tuned by the size of the QD and the Sb content in the SRL (the value of the tunneling energy corresponding to the QDs under consideration is 0.28 meV). The barrier between the segments is better defined. The clear disadvantage is the confinement of only one type of charge carriers, i.e., holes, ruling out applications in devices involving both electrons and holes. However, there exist promising proposals of devices which require only one type of charge carriers.[17] Our molecules represent an interesting alternative to the LQDMs discussed in this context.

In the following, we propose an experiment that could be used to identify the localization of the holes, based on the Stark shift in the vertical electric field. Figure 4 shows the

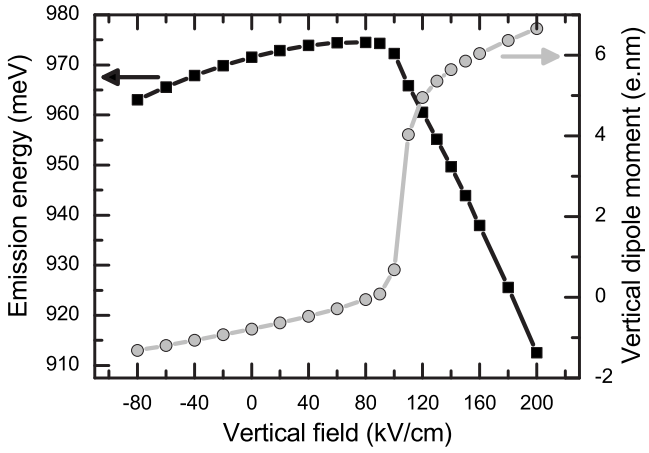

FIG. 4. The emission energy (squares) and the vertical dipole moment (circles) as functions of the vertical electric field in the type-II QD with $y=0.22$.

calculated transition energy and the vertical dipole moment as functions of the applied electric field. According to our calculations, the dipole moment of the exciton in zero field is small and oriented downward (negative direction). The electron and the hole are both rather strongly confined and their vertical polarizability is low. As a consequence, only a weak Stark shift of the emission energy in a vertical electric field is predicted, positive when the field is oriented upward (positive direction). For a sufficiently strong positive field, however, the hole state above the tip of the QD turns to be the ground state,[9] the dipole moment of the exciton increases dramatically and changes its sign, and so does the Stark shift. The transition between the weak negative and large positive dipole moment is fairly steep and should be identifiable. For the hole ground state located above the tip of the QD, a similar transition would occur for a *negative* field. We note that this possibility could occur in real QDs due to, e.g., a higher antimony content in the SRL above the QD.[20]

In conclusion, we have shown that the red shift of the emission energy with increasing Sb content y in the $GaAs_{1-y}Sb_y$ SRL is mainly due to the modified confinement potential in the QD; there is no need to vary the structural parameters of the model dot with changing y to reproduce the optical data. The blue shift of the emission with increasing pumping power is attributed to the increasing proportion of the biexcitons whose emission energy is considerably higher compared to the excitons. We have found that for $y > 0.19$, the holes are localized in the SRL close to the base of the dot, rather than above it. An experiment involving external electric field has been proposed to verify this prediction.

The work was supported by the Institutional Research Program under Grant No. MSM 0021622410 and the GACR under Grant No. GA202/09/0676.

[1]H. Liu, M. Steer, T. Badcock, D. Mowbray, M. Skolnick, F. Suarez, J. Ng, M. Hopkinson, and J. David, J. Appl. Phys. **99**, 046104 (2006).
[2]H. Liu, M. Steer, T. Badcock, D. Mowbray, M. Skolnick, P. Navaretti, K. Groom, M. Hopkinson, and R. Hogg, Appl. Phys. Lett. **86**, 143108 (2005).
[3]V. Mlinar and F. M. Peeters, Appl. Phys. Lett. **91**, 021910 (2007).
[4]J. F. Chen, R. C. C. Chen, C. H. Chiang, Y. F. Chen, Y. H. Wu, and L. Chang, Appl. Phys. Lett. **97**, 092110 (2010).
[5]J. M. Ulloa, I. W. D. Drouzas, P. M. Koenraad, D. J. Mowbray, M. J. Steer, H. Y. Liu, and M. Hopkinson, Appl. Phys. Lett. **90**, 213105 (2007).
[6]C. Y. Jin, H. Y. Liu, S. Y. Zhang, Q. Jiang, S. L. Liew, M. Hopkinson, T. J. Badcock, E. Nabavi, and D. J. Mowbray, Appl. Phys. Lett. **91**, 021102 (2007).
[7]S. Birner, T. Zibold, T. Andlauer, T. Kubis, M. Sabathil, A. Trellakis, and P. Vogl, IEEE Trans. Electron Devices **54**, 2137 (2007).
[8]S. Rodt, A. Schliwa, K. Potschke, F. Guffarth, and D. Bimberg, Phys. Rev. B **71**, 155325 (2005).
[9]See supplementary material at http://dx.doi.org/10.1063/1.3517446 for sections B–F.
[10]P. Offermans, P. Koenraad, J. Wolter, K. Pierz, M. Roy, and P. Maksym, Phys. Rev. B **72**, 165332 (2005).
[11]V. Mlinar, M. Bozkurt, J. M. Ulloa, M. Ediger, G. Bester, A. Badolato, P. M. Koenraad, R. J. Warburton, and A. Zunger, Phys. Rev. B **80**, 165425 (2009).
[12]K. Kuldová, V. Křápek, A. Hospodková, J. Oswald, J. Pangrác, K. Melichar, E. Hulicius, M. Potemski, and J. Humlíček, Phys. Status Solidi C **3**, 3811 (2006).
[13]V. Mlinar, Ph.D. thesis, Universiteit Antwerpen, 2007.
[14]P. Klenovský, V. Křápek, D. Munzar, and J. Humlíček, J. Phys.: Conf. Ser. **245**, 012086 (2010).
[15]O. Stier, M. Grundmann, and D. Bimberg, Phys. Rev. B **59**, 5688 (1999).
[16]A. Hospodková, E. Hulicius, J. Pangrác, J. Oswald, J. Vyskočil, K. Kuldová, T. Šimeček, P. Hazdra, and O. Caha, J. Cryst. Growth **312**, 1383 (2010).
[17]G. Burkard, D. Loss, and D. DiVincenzo, Phys. Rev. B **59**, 2070 (1999).
[18]G. Bester, A. Zunger, and J. Shumway, Phys. Rev. B **71**, 075325 (2005).
[19]G. Beirne, C. Hermannstadter, L. Wang, A. Rastelli, O. Schmidt, and P. Michler, Phys. Rev. Lett. **96**, 137401 (2006).
[20]J. M. Ulloa, R. Gargallo-Caballero, M. Bozkurt, M. del Moral, A. Guzman, P. M. Koenraad, and A. Hierro, Phys. Rev. B **81**, 165305 (2010).

D Modelling of electronic states in InAs/GaAs quantum dots with GaAsSb strain reducing overlayer

Journal of Physics: Conference Series **245** (2010) 012086 doi:10.1088/1742-6596/245/1/012086

Modelling of electronic states in InAs/GaAs quantum dots with GaAsSb strain reducing overlayer

Petr Klenovský[1], Vlastimil Křápek[1], Dominik Munzar[1] and Josef Humlíček[1]

[1]Department of Condensed Matter Physics, Masaryk University, Kotlářská 2, 61137 Brno, Czech Republic

E-mail: klenovsky@physics.muni.cz

Abstract. We present results of our 8-band $\vec{k} \cdot \vec{p}$ calculations of the emission energy of InAs/GaAs quantum dots (QDs) covered with $GaAs_{1-x}Sb_x$ strain reducing overlayer (SRO). In agreement with previous experimental observations we find a strong red shift of the emission with increasing Sb content. We explain this effect by: (1) The lowering of the valence band offset between the QD and the SRO with increasing Sb content resulting in the type-II QDs with holes confined in the SRO for Sb concentration above 14 %. (2) The reduction of compressive strain inside the QDs. The contributions of these mechanisms to the total red shift are estimated and compared. For realistic shape and size of the QD and a realistic value of the SRO thickness the previously measured photoluminescence data are reproduced with fairly good accuracy.

1. Introduction

Self-assembled InAs/GaAs quantum dots (QDs) have been investigated for their interesting physical properties and potential applications; one of the latter is an efficient light emission on the communication wavelengths of $1.3/1.55\,\mu$m. To tune the emission wavelength towards this range, various strategies can be used. One possibility is to use QDs stacked in vertical multilayers [1]. Another option relies on capping QDs with strain reducing overlayers (SRO); here, ternary materials such as $In_xGa_{1-x}As$ [2] and $GaAs_{1-x}Sb_x$ [3] can be used. The resulting red shift with increasing In content in $In_xGa_{1-x}As$ SROs has been explained as an effect of three mechanisms: the reduction of the hydrostatic strain in the InAs QDs, lowering of the barrier height for both electrons and holes at the side of the SRO, and a change in the dot size during the growth process; the latter two were identified as the decisive contributions [2].

We present here a similar analysis for the $GaAs_{1-x}Sb_x$ SROs. The situation is slightly different since the lowering of the valence band offset with increasing Sb content results in a transition to the type-II QDs occurring at the Sb concentration of approximately 14%. Above this value holes are localized in the SRO instead of the QDs. In previous photoluminescence studies, this transition to the type-II QDs has been attributed to be the dominant cause of the observed red shift [4]. However, a detailed theoretical analysis is still missing.

2. Method

QDs capped by $GaAs_{1-x}Sb_x$ SROs were simulated using nextnano++ software [5]. The structure consisted, from bottom to top, of a GaAs substrate, InAs QD, $GaAs_{1-x}Sb_x$ SRO and a GaAs

capping layer. Our calculations started by finding the strain inside the structure, continued by a calculation of the piezoelectric field, and ended with solving the Schrödinger equation using the 8-band $\vec{k} \cdot \vec{p}$ approximation. All these steps were performed using the nextnano++ built-in solvers. The values of the material parameters have been taken from [6], with the exception of the deformation potentials and the InAs/GaAs valence band offset, taken from [7].

To distinguish between the effects of the reduced strain in the QDs and those of the lowered valence band offset, the following calculations were performed: (1) We have calculated the strain field for the $GaAs_{1-x}Sb_x$ SRO and used it subsequently as the input for the piezoelectricity and quantum calculations. Apart from the elastic constants and the lattice parameter, we considered the SRO to correspond to a pure GaAs. In this way we have specified the contribution of the reduced strain within the QDs. (2) We have used the strain field calculated for a pure GaAs overlayer and values of the parameters of the $GaAs_{1-x}Sb_x$ SRO (except for the lattice parameter and the elastic constants) in subsequent calculations to obtain the effect of the modified valence band offset. In this case, also other parameters were changed, such as the conduction band offset and effective masses. However, the most pronounced effect is indeed connected with a modified valence band offset.

3. Results and discussion

In our calculations we have varied the dimensions of the QD and the thickness of the SRO, in order to fit the transition energy and its red shift observed in [3]. We have chosen the semiellipsoidal shape of the QD as it is common for InAs dots large in volume. We have obtained the best agreement for the QD height of 5 nm, the QD diameter of 14 nm and the SRO thickness of 3 nm.

The calculated values of the lowest transition energy are shown in Fig. 1. The experimental data measured at 15 K, taken from [3], are shown for comparison. To facilitate the comparison, the calculated data are blueshifted by 20 meV. The shift could be due, e.g., to the fact that the real QDs consist of InGaAs rather than of pure InAs.

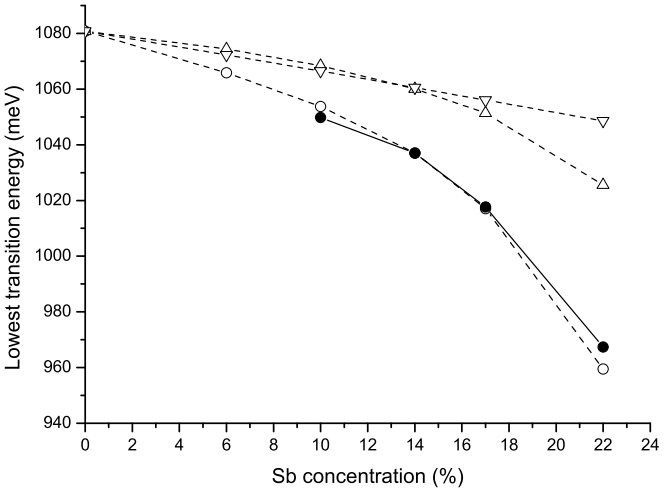

Figure 1. ● Peak emission energy measured at 15 K, taken from [3]; ○ Calculated values of the lowest transition energy; △ The same obtained considering the Sb concentration dependence of the electronic structure parameters only; ▽ The same obtained considering the strain effect only.

The calculated red shift of the lowest transition energy when going from 10 % to 22 % of Sb of 95 meV is in reasonable agreement with the experimental value of 82 meV. We decompose this shift into the contribution of the reduced strain in the QD, and that of the lowered valence band offset between the QD and the SRO. Both contributions are shown separately in Fig. 1. The

modified valence band offset accounts for $\sim 45\,\mathrm{meV}$ of the red shift, while the reduced strain accounts for $\sim 20\,\mathrm{meV}$. The difference of $\sim 30\,\mathrm{meV}$ between the sum of the values and the total red shift is a result of the combination of the effects.

Below the Sb concentration of 14 %, both effects contribute nearly equally to the total shift, with a linear dependence on the Sb concentration. Around 14 %, the transition to the type-II QD occurs and increasing the Sb content further enhances the effect of the lowered valence band offset (which becomes negative). Accordingly, we identify the onset of the type-II QDs as the dominant mechanism causing the red-shift of the emission energy, confirming the assumption of Ref. [4]. However, the influence of the $GaAs_{1-x}Sb_x$ capping layer on the strain in the structure is responsible for a surprisingly large portion of the red shift as compared to the $In_xGa_{1-x}As$ SRO [2].

Fig. 2 shows the hydrostatic component of the strain ($\varepsilon_{xx} + \varepsilon_{yy} + \varepsilon_{zz}$) along the symmetry axis of the dot. The compressive strain inside the dot decreases by 0.3 % when increasing the Sb content from 10 % to 22 %. This corresponds to the red shift of the conduction band edge by $\sim 20\,\mathrm{meV}$, explaining fully the simulated contribution of the reduced strain to the red shift, shown in Fig. 1.

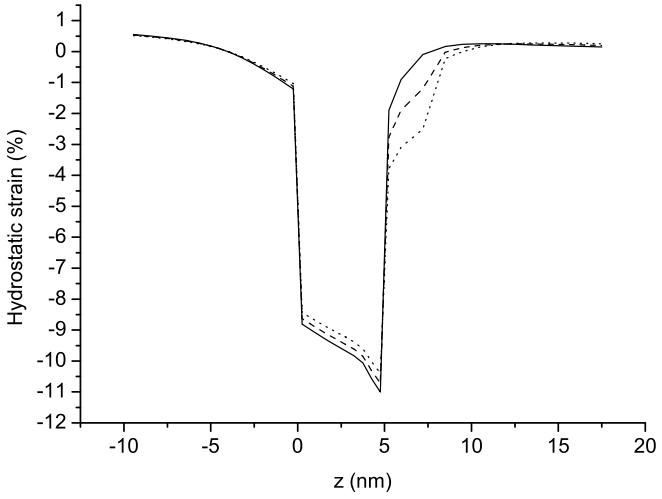

Figure 2. Hydrostatic strain ($\varepsilon_{xx} + \varepsilon_{yy} + \varepsilon_{zz}$) along the symmetry axis of the QD for —— 0 %, - - - - 10 %, ····· 22 % of Sb content in the SRO.

The reduction of the compressive strain inside the QD can be explained as follows. The lattice parameter of $GaAs_{1-x}Sb_x$ is larger than that of GaAs. The presence of the SRO therefore increases the total strain in the structure. However, the contrast in lattice parameters between the QD and the SRO is reduced as compared to the GaAs overlayer, which results in a reduced strain inside the QD. In particular, the material around the sides of the dot has a lower compressive impact. On the contrary, matching the lattice parameter to the GaAs overlayer enhances the compressive strain in the SRO, as seen clearly in Fig. 2.

There is a pronounced difference in the magnitude of the relaxation of the compressive strain inside the QDs with $GaAs_{1-x}Sb_x$ SRO considered here and inside the QDs with $In_xGa_{1-x}As$ SRO studied in Ref. [2]. The lattice parameters of the SROs are nevertheless comparable. The difference likely originates in the different aspect ratios of the QDs in both cases. The $GaAs_{1-x}Sb_x$ covered dots are rather high and the elastic interaction between them and the SRO is more intense than in the flat QDs covered with $In_xGa_{1-x}As$.

4. Conclusion

In conclusion, we have calculated the emission energy of QDs covered with the $GaAs_{1-x}Sb_x$ SRO with various values of the Sb content. We were able to reproduce the observed transition energies, and their red shift with increasing Sb content. In agreement with previous studies, it has been found that the red shift is caused mainly by the transition to the type-II QDs above the Sb concentration of 14 %. Almost one fourth of the red shift is caused by the reduction of the compressive strain inside the QDs; this is much more than in the case of $In_xGa_{1-x}As$ SROs.

Acknowledgments

The work was supported by the Institutional research program MSM0021622410 and the GACR grant GA202/09/0676.

References

[1] Shchukin V A, Ledentsov N N and Bimberg D 2004 *Epitaxy of Nanostructures* (Nanoscience and Nanotechnology) (Berlin: Springer-Verlag)
[2] Kuldová K, Křápek V, Hospodková A, Oswald J, Pangrác J, Melichar K, Hulicius E, Potemski M and Humlíček J 2006 *Phys. Stat. Sol. (c)* **3** 3811
[3] Liu H Y, Steer M J, Badcock T J, Mowbray D J, Skolnick M S, Navaretti P, Groom K M, Hopkins M and Hogg R A 2005 *Appl. Phys. Lett.* **86** 143108
[4] Liu H Y, Steer M J, Badcock T J, Mowbray D J, Skolnick M S, Suarez F, Ng J S, Hopkinson M and David J P R 2006 *J. Appl. Phys.* **99** 046104
[5] Trellakis A, Zibold T, Andlauer T, Birner S, Smith R K, Morschl R, Vogl P 2006 *J. Comp. Elec.* **5** 285
[6] Vurgaftman I, Meyer J R and Ram-Mohan L R 2001 *J. Appl. Phys.* **89** 5815
[7] Wei S and Zunger A 1998 *Appl. Phys. Lett.* **72** 2011

E Experimental investigation and modeling of the fine structure splitting of neutral excitons in strain-free GaAs/AlGaAs quantum dots

PHYSICAL REVIEW B **81**, 121309(R) (2010)

Experimental investigation and modeling of the fine structure splitting of neutral excitons in strain-free GaAs/$Al_xGa_{1-x}As$ quantum dots

J. D. Plumhof,[1] V. Křápek,[1,2] L. Wang,[1,3] A. Schliwa,[4] D. Bimberg,[4] A. Rastelli,[1,*] and O. G. Schmidt[1]
[1]*Institute for Integrative Nanosciences, IFW Dresden, Helmholtzstr. 20, D-01069 Dresden, Germany*
[2]*Institute of Condensed Matter Physics, Masaryk University, Kotlářská 2, 61137 Brno, Czech Republic*
[3]*Max Planck Institute for Solid State Research, Heisenbergstr. 1, D-70569 Stuttgart, Germany*
[4]*Institut für Festkörperphysik, Technische Universität Berlin, Hardenbergstr. 36, D-10623 Berlin, Germany*
(Received 18 January 2010; published 29 March 2010)

We measure, by photoluminescence spectroscopy, the fine structure splitting (FSS) of bright excitons confined in a large number of elongated and unstrained $Al_{0.35}Ga_{0.65}As/GaAs/Al_{0.45}Ga_{0.55}As$ quantum dots (QDs) and quantum-well potential fluctuations (QWPFs). While the FSS values are comparable, the light polarization directions for well-oriented QDs and randomly oriented QWPFs on the same sample are substantially different. We compare the results with model calculations using as input scanning probe microscopy data of QD structures nominally identical to those investigated by photoluminescence. The model reproduces well the polarization orientation for all studied samples and also the magnitude of the FSS, at least for relatively tall dots. We discuss the results and elucidate the role of in-plane elongation on the FSS.

DOI: 10.1103/PhysRevB.81.121309 PACS number(s): 78.67.Hc, 81.07.Ta

Semiconductor quantum dots (QDs) keep attracting much interest due to their potential applications in the field of quantum information processing and communication. As an example, the biexciton-exciton radiative cascade in QDs can be used to generate entangled photon pairs.[1] The neutral exciton consists of two optically dark and two bright states. The energies of the bright states are usually separated by an energy of several tens of micro-electronvolts. This separation, known as fine structure splitting (FSS),[2] is attributed to the anisotropic electron-hole exchange interaction.[3,4] The FSS destroys the polarization entanglement of photons, which can be achieved only on rare QDs with FSS on the order of the homogeneous linewidth[5,6] or by using spectral filtering.[7] For this reason, the FSS of excitons in QDs is currently an active field of research with the aim of better understanding its origin[8–10] and predicting strategies to reduce it.[11]

Despite the efforts, a direct and quantitative comparison of theoretical with experimental results on FSS of QDs remains difficult. This is mostly due to the lack of accurate structural parameters taken into the model, which often results in inconsistencies between theory and experiment. In fact, most of the previous investigations on FSS focused either on strained and intermixed Stranski-Krastanow (SK) QDs (Refs. 12 and 13) where the alloy composition profiles are difficult to access or on potential fluctuations in thin quantum wells (QWs), which have poorly defined shape.[2,14,15] Besides that, the theoretical predictions depend strongly on the employed models,[8] which should be tested on QDs with well-known structural parameters. Therefore, theory and experiments on FSS have remained so far relatively disjointed. Unstrained GaAs/AlGaAs QDs with good structural homogeneity[16–18] are ideally suited to address this problem. Only very recently, Abbarchi *et al.*[19,20] studied the FSS of GaAs QDs but the correlation between FSS and QD morphology was kept at a qualitative level.

In this work, we measure the FSS of "hierarchically self-assembled" GaAs/AlGaAs QDs (Ref. 17) and make a direct comparison with calculations based on eight-band $k\cdot p$ and the configuration-interaction models. We determine the optical properties (FSS and polarization orientation) and the morphology of hundreds of QDs. Due to the lack of lattice mismatch and choice of growth conditions, intermixing, strain, and piezoelectricity are negligible in our QD system. We therefore use the experimentally determined shapes and nominal growth parameters as input for the calculations. We find that the model reproduces well the polarization orientation for all studied samples and also the magnitude of the FSS, at least for relatively tall dots. The agreement on the FSS values is somewhat poorer for flatter dots, where the model predicts values which are generally larger than the observed ones. The comparison between the polarization directions for QDs and for QW potential fluctuations (QWPFs) allows us to highlight the dominant contribution of the shape asymmetry in determining the FSS for the investigated system.

The studied QDs were grown by molecular-beam epitaxy combined with *in situ* selective etching. The latter is used to create nanoholes (NHs) on the GaAs surface starting from SK InAs/GaAs islands.[21] The NHs are overgrown with an $Al_{0.45}Ga_{0.55}As$ layer of thickness D serving as bottom barrier at a nominal substrate temperature of 500 °C. During AlGaAs overgrowth, the shape of the NHs changes slightly, their depth decreases, while their elongation along the [110] axis is maintained.[17] After AlGaAs growth, the NHs are filled by depositing nominal 2 nm of GaAs followed by a 2 min growth interruption, which allows the diffusion of GaAs into the NHs. The deposition of a top $Al_{0.35}Ga_{0.65}As$ barrier yields inverted unstrained GaAs QDs surrounded by a thin GaAs QW. The obtained QDs are characterized by a good size homogeneity resulting in photoluminescence (PL) ensemble linewidths down to ~10 meV, which allows the comparison with theoretical simulations. By terminating the growth right after the deposition of the $Al_{0.45}Ga_{0.55}As$ bottom barrier, we determined the shape of the AlGaAs NHs and hence of the GaAs QDs using scanning tunneling microscopy or atomic force microscopy (STM/AFM). We used AFM to collect data with large statistics and ultrahigh-

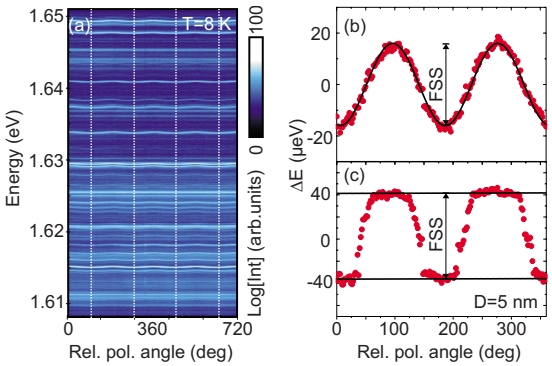

FIG. 1. (Color online) (a) Color-coded PL intensity recorded for varying polarization angle from the sample with $D=5$ nm. The white lines indicate the angles corresponding to emission polarization along the [110] crystal direction. (b) and (c) Results of Lorentzian fits of two split excitonic lines with relatively (b) small and (c) large FSS. The FSS is obtained from the amplitude of a sine fit in (b) or from the energy separation between the top and bottom flat regions in (c). See text for details.

vacuum STM to image the roughness of the AlGaAs layer. Three NH samples with $D=5$, 7, and 10 nm were investigated with AFM and three QD samples produced with the same nominal growth parameters were studied by PL spectroscopy.

The optical investigations were carried out in a standard micro-PL setup at 8 K, with a spectral resolution of ~ 70 μeV. The linear polarization of the QD emission was measured by continuous rotation of a $\lambda/2$ wave plate followed by a linear polarizer in front of the spectrometer. By using samples with relatively high QD density (some 10^9 cm^{-2}), we investigated up to 15 QDs within one measurement cycle, similar to the approach of Ref. 12.

Figure 1(a) shows an example of the PL intensity as the $\lambda/2$ wave plate is rotated by 360° (corresponding to 720° of polarization angle). The laser power was set well below saturation to keep biexciton emission below the detection limit. Each spectrum consists of a number of sharp recombination lines originating from different dots. The wavy patterns are ascribed to the FSS of neutral excitons (both fine structure splitted photons have orthogonal linear polarization). Several lines showing no FSS are attributed to positive trions.[22] All neutral exciton lines appear to "oscillate" in phase in Fig. 1(a), indicating a rather homogeneous orientation of the low- and high-energy components of the doublets.

For the determination of the FSS, we first fit the different excitonic lines with Lorentzian curves as a function of the polarization angle. The results for two representative QDs are shown in Figs. 1(b) and 1(c). Depending on the amplitude of the FSS, the obtained peak positions follow a pattern resembling either a sine wave [for relatively small FSS, where the two components are not spectrally resolved, see Fig. 1(b)] or a square wave [for larger FSS, where the two components are spectrally resolved even without polarization selection, see Fig. 1(c)]. In both cases, we then fit the wavy pattern with a sine function to determine the polarization orientation of the low-energy component of the doublet relative to the [110] crystal direction. In the former case, the sine fit provides also a reliable measure of the FSS [Fig. 1(b)] while in the latter case, we obtain the FSS by fitting the flat regions of the "square wave" with two constant functions and measuring the energy difference [Fig. 1(c)]. The uncertainty of the FSS is estimated to be $\sim(^{+10}_{-5})$ μeV.

Our theoretical simulation of the FSS consists of two steps. First, single-particle states are calculated by eight-band $k\cdot p$ theory by using the structural information obtained by AFM and nominal growth parameters. The shape of the QDs is discretized in steps of 0.5 nm. (A test with 0.25 nm resolution yielded to comparable results.) The resulting wave functions are expressed as

$$\psi_i(\vec{r}) = \sum_{n=1}^{8} \chi_{i,n}(\vec{r}) u_n(\vec{r}),$$

where i is an index of the wave function, $\chi_{i,n}(\vec{r})$ are the so-called envelope functions, and $u_n(\vec{r})$ are Bloch waves in the Γ point. The summation goes over six valence and two conduction bands. Details are given elsewhere.[10,23]

The second step is the configuration-interaction calculation of the exciton states. The exciton wave function $|X\rangle$ is expanded into the basis of configurations $|C(c\alpha,v\beta)\rangle$,

$$|X\rangle = \sum_{\alpha,\beta} |C(c\alpha,v\beta)\rangle, \quad |C(c\alpha,v\beta)\rangle = \hat{a}^{+}_{c\alpha}\hat{a}_{v\beta}|0\rangle.$$

Here α (β) is the index of conduction (valence) single-particle state (the auxiliary labels c and v help to distinguish between conduction and valence electrons), $\hat{a}_i^+$ and $\hat{a}_i$ are the creation and annihilation operators of the ith single-particle state, and $|0\rangle$ is the "vacuum" state (i.e., the valence-electron states are occupied and conduction-electron states are empty).

The exciton Hamiltonian matrix elements are

$$\langle C(c\alpha,v\beta)|\hat{H}|C(c\gamma,v\delta)\rangle = (E_{c\alpha}-E_{v\beta})\delta_{\alpha\gamma}\delta_{\beta\delta} - V_{c\alpha\ v\delta,c\gamma\ v\beta} + V_{c\alpha\ v\delta,v\beta\ c\gamma}$$

with

$$V_{ij,kl} = \int\int d^3\vec{r}_1 d^3\vec{r}_2 \frac{\psi_i^*(\vec{r}_1)\psi_j^*(\vec{r}_2)e^2\psi_k(\vec{r}_1)\psi_l(\vec{r}_2)}{4\pi\varepsilon_0\varepsilon_r|\vec{r}_1-\vec{r}_2|}.$$

Here E_i are single-particle energies, e is the elementary charge, ε_0 is the vacuum permittivity, and ε_r is the dielectric constant. The terms $-V_{c\alpha\ v\delta,c\gamma\ v\beta}$ and $V_{c\alpha\ v\delta,v\beta\ c\gamma}$ represent direct and exchange Coulomb interaction, respectively.

The evaluation of Coulomb matrix elements was carried out following mostly the procedure of Takagahara.[9] The important extension is that we included more terms (zeroth and first order) in the expansion 2.9 of Ref. 9, which were zero in previous works[8,9] because of neglected mixing between conduction and valence bands in single-particle calculations. The energies of the exciton states are found by the Hamiltonian diagonalization and the FSS is retrieved as the energy difference between the two lowest bright exciton states.

The left insets in Fig. 2 show images of NHs on samples with different D obtained by numerical averaging of AFM topographs of around 50 AlGaAs NHs. The average depth of the NHs is 4.8 ± 0.4, 4.1 ± 0.3, and 3.3 ± 0.4 nm for $D=5$, 7, and 10 nm, respectively. While most of the NHs on the same

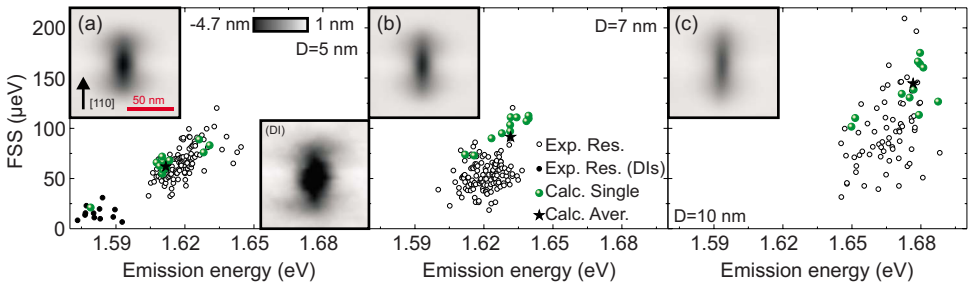

FIG. 2. (Color online) Experimental (black circles) and calculated (dots and stars) FSS as a function of exciton energy for samples with (a) $D=5$, (b) 7, and (c) 10 nm. The filled black circles in (a) correspond to QDs created from DIs. The black stars are the FSS calculated for the averaged depth profiles (insets in the upper left corners of each panel). The inset in the lower right corner in (a) shows the depth profile of a NH created by etching of a DI. The scale of all insets is specified in (a).

sample have rather homogeneous size and orientation, as they are produced by etching of coherent InAs islands with a good size homogeneity, some deeper (about 7 nm) NHs are found in the sample with $D=5$ nm [right inset in Fig. 2(a)]. These nanostructures are likely to originate from relatively large dislocated InAs islands (DIs). Figure 2 shows the relation between FSS and emission energy for QDs in the three different samples. Besides the experimental data (circles), we show the results of the calculations for ten different NHs, which were randomly chosen in the AFM images of each sample (dots) as well as for the averaged shapes (stars). In all plots, we see that the calculation results (dots) corresponding to GaAs dots obtained by etching of coherent InAs islands display "bimodal" distributions in the emission energy (i.e., an apparent gap located, e.g., around 1.62 eV for the sample with $D=5$ nm). This is due to the discretization step size of 0.5 nm used in the calculations.

We first focus on the sample with $D=5$ nm [Fig. 2(a)]. The experimental exciton energy displays a bimodal distribution. QDs emitting at low energy have small FSS (down to ~ 10 μeV) while QDs emitting at higher energy have larger FSS (~ 66 μeV). We ascribe the low-energy emission lines to excitons confined in QDs obtained by etching of DIs. (The fact that these QDs are optically active is interesting, as it indicates that the InAs material and crystal defects are removed during the $AsBr_3$ etching step leaving behind deeper NHs, which can be used as a template to create defect-free GaAs/AlGaAs QDs.) In spite of the spread in FSS values for both families of dots, we also see that the FSS tends to increase with increasing emission energy. The points corresponding to the calculation results for both QD families are well overlapped with the experimental data, indicating that the used model is able to reproduce the emission energies, the magnitude of the FSS, and also the trend of increasing FSS with energy.

If we now compare the images of the NHs in the top insets of Fig. 2, we see that dots tend to become more elongated with increasing D.[17] Qualitatively, we would thus expect an increase in FSS, as also confirmed by the calculations [compare the stars in Figs. 2(a)–2(c)]. The experimental results do not follow however such a clear trend. For the samples with $D=5$, 7, and 10 nm, the average values of the FSS change from 66, to 53 to 96 μeV, with standard deviations increasing with D from 23 to 28 and to 38%, respectively. The broadening of the distributions of the FSS with increasing D can be partly ascribed to the broadening of the distribution of size and shapes of the NHs, which become more irregular as D increases.[17] For the samples with $D=7$ and 10 nm, the calculated and experimental points show some overlap but the predicted FSS values are generally larger and their distribution more homogeneous than the observed ones. Although we cannot definitely track the origin of the poorer agreement compared to the sample with $D=5$ nm, we note that for increasing D, the NH depth decreases so that monolayer-high asperities of the bottom or top AlGaAs interfaces (which are below the resolution used in the calculation) may lead to exciton confinement in a small region of the QD, similar to QW thickness fluctuations. Furthermore, as the dots become flatter, the spilling of the exciton wave function in the alloy barrier increases: alloy disorder (an atomistic effect which is not treated in our model) may contribute to the broadening of the FSS distributions.[24]

To obtain an idea about the contribution of effects other

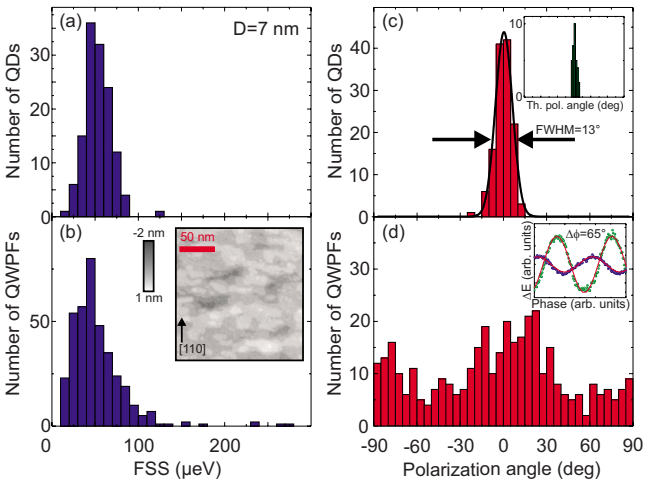

FIG. 3. (Color online) (a) Histogram of the FSS values for QDs and (b) QWPFs measured on the sample with $D=7$ nm. (c) Polarization direction of the low-energy component of the exciton for the QDs and (d) for the QWPFs. A polarization angle of 0° corresponds to the [110] crystal direction. The inset in (b) shows an STM image of the lower barrier of the QW. The inset in (c) shows the calculated polarization distribution for NHs with $D=5$, 7, and 10 nm; the x-axis scale is the same as for the main axis panel. The inset in (d) shows the polarization behavior of two representative QWPF emission lines with relative polarization angle $\Delta\phi$.

than shape anisotropy[24] (e.g., crystal anisotropy, alloy disorder, etc.) to the FSS of our QDs, we studied experimentally the FSS of excitons confined in the potential fluctuations of the rough QW between the QDs. The distribution of the FSS values for the QDs [Fig. 3(a)] in the sample with $D=7$ nm is slightly narrower compared to the distribution for the QWPFs [Fig. 3(b)] of the same sample but the average values are comparable. On the other hand, the polarization direction of light emitted by excitons confined in QDs and QWPFs is remarkably different [Figs. 3(c) and 3(d)]. The low-energy component of the bright excitons in QDs shows a pronounced alignment along the [110] crystal direction [Fig. 3(c)], in all investigated samples. We attribute this finding to the homogeneity in elongation of the AlGaAs NHs. A detailed analysis of around 400 NHs shows in fact that the NHs for all values of D are aligned within $\pm 7°$ with respect to the [110] crystal axis (not shown). This polarization distribution is also reproduced by our simulations on QDs with $D=5$, 7, and 10 nm [inset of Fig. 3(c)] and it appears different from previous studies[3,20] where the high-energy component of the doublets was observed to be parallel to the long QD axis. The reason for this discrepancy is at present unclear. The polarization of light emitted by QWPFs is rather randomly oriented [see Fig. 3(d) and inset], with only a slight preferential alignment along the [110] and $[1\bar{1}0]$ directions. We mainly ascribe this observation to the irregular shape of the confining potentials created by the bottom QW barrier [see STM image in the inset of Fig. 3(b)]. (We expect the top QW interface to be smoother because of the larger diffusivity of Ga compared to Al and the annealing step following GaAs growth.)

Finally, we have also measured the polarization direction for QDs obtained by filling AlGaAs NHs ($D=10$ nm) with only 0.5 nm GaAs. In this case, the emission energies are very close to those of the QWPFs but the polarization of the exciton emission is very similar to that observed for the taller dots discussed here: the low-energy component of the exciton is invariably polarized along directions close to the [110].

In conclusion, we have studied experimentally and theoretically the fine structure splitting of neutral excitons in elongated and unstrained GaAs QDs embedded in AlGaAs barriers. The calculations, which are based on the measured structure and nominal growth parameters, are able to reproduce well the polarization orientation for all studied dots and also the magnitude of the splitting for relatively tall dots. For flatter dots, the predicted values are however slightly larger than the observed ones. Finally, we highlight the impact of shape anisotropy on the FSS by comparing measurements on QDs and on randomly oriented QW potential fluctuations on the same samples.

We acknowledge M. Benyoucef, F. Ding, Ch. Deneke, and S. Baunack for their contribution and C. Manzano, G. Costantini, and K. Kern for providing STM data. This work was supported by the DFG (FOR730 and SFB 787). V.K. was partially supported by the Institutional Research Program MSM0021622410 and GACR under Grant No. GA202/06/0718. V.K. performed the calculations on luna.fzu.cz and wiggum.physik.tu-berlin.de grids.

*a.rastelli@ifw-dresden.de

[1] O. Benson, C. Santori, M. Pelton, and Y. Yamamoto, Phys. Rev. Lett. **84**, 2513 (2000).
[2] D. Gammon, E. S. Snow, B. V. Shanabrook, D. S. Katzer, and D. Park, Phys. Rev. Lett. **76**, 3005 (1996).
[3] L. Besombes, K. Kheng, and D. Martrou, Phys. Rev. Lett. **85**, 425 (2000).
[4] M. Bayer *et al.*, Phys. Rev. B **65**, 195315 (2002).
[5] R. Hafenbrak, S. M. Ulrich, P. Michler, L. Wang, A. Rastelli, and O. G. Schmidt, New J. Phys. **9**, 315 (2007).
[6] R. Stevenson, R. Young, P. Atkinson, K. Cooper, D. Ritchie, and A. Shields, Nature (London) **439**, 179 (2006).
[7] N. Akopian, N. H. Lindner, E. Poem, Y. Berlatzky, J. Avron, D. Gershoni, B. D. Gerardot, and P. M. Petroff, Phys. Rev. Lett. **96**, 130501 (2006).
[8] E. Poem, J. Shemesh, I. Marderfeld, D. Galushko, N. Akopian, D. Gershoni, B. D. Gerardot, A. Badolato, and P. M. Petroff, Phys. Rev. B **76**, 235304 (2007).
[9] T. Takagahara, Phys. Rev. B **62**, 16840 (2000).
[10] O. Stier, M. Grundmann, and D. Bimberg, Phys. Rev. B **59**, 5688 (1999).
[11] R. Singh and G. Bester, Phys. Rev. Lett. **103**, 063601 (2009).
[12] S. Seidl, B. Gerardot, P. Dalgarno, K. Kowalik, A. Holleitner, P. Petroff, K. Karrai, and R. Warburton, Physica E **40**, 2153 (2008).
[13] R. Seguin, A. Schliwa, S. Rodt, K. Pötschke, U. W. Pohl, and D. Bimberg, Phys. Rev. Lett. **95**, 257402 (2005).
[14] C. Ropers *et al.*, Phys. Rev. B **75**, 115317 (2007).
[15] M. Ramsteiner, R. Hey, R. Klann, U. Jahn, I. Gorbunova, and K. H. Ploog, Phys. Rev. B **55**, 5239 (1997).
[16] C. Heyn, A. Stemmann, T. Koppen, C. Strelow, T. Kipp, M. Grave, S. Mendach, and W. Hansen, Appl. Phys. Lett. **94**, 183113 (2009).
[17] A. Rastelli, S. Stufler, A. Schliwa, R. Songmuang, C. Manzano, G. Costantini, K. Kern, A. Zrenner, D. Bimberg, and O. G. Schmidt, Phys. Rev. Lett. **92**, 166104 (2004).
[18] K. Leifer, E. Pelucchi, S. Watanabe, F. Michelini, B. Dwir, and E. Kapon, Appl. Phys. Lett. **91**, 081106 (2007).
[19] M. Abbarchi, T. Kuroda, C. Mastrandrea, A. Vinattieri, S. Sanguinetti, T. Mano, K. Sakoda, and M. Gurioli, Physica E **42**, 881 (2010).
[20] M. Abbarchi, C. A. Mastrandrea, T. Kuroda, T. Mano, K. Sakoda, N. Koguchi, S. Sanguinetti, A. Vinattieri, and M. Gurioli, Phys. Rev. B **78**, 125321 (2008).
[21] R. Songmuang, S. Kiravittaya, and O. G. Schmidt, Appl. Phys. Lett. **82**, 2892 (2003).
[22] L. Wang, V. Křápek, F. Ding, F. Horton, A. Schliwa, D. Bimberg, A. Rastelli, and O. G. Schmidt, Phys. Rev. B **80**, 085309 (2009).
[23] V. Mlinar, A. Schliwa, D. Bimberg, and F. M. Peeters, Phys. Rev. B **75**, 205308 (2007).
[24] V. Mlinar and A. Zunger, Phys. Rev. B **79**, 115416 (2009).

F Strain-induced anticrossing of bright exciton levels in single self-assembled GaAs/ AlGaAs and InGaAs/GaAs quantum dots

PHYSICAL REVIEW B **83**, 121302(R) (2011)

Strain-induced anticrossing of bright exciton levels in single self-assembled GaAs/$Al_xGa_{1-x}As$ and $In_xGa_{1-x}As$/GaAs quantum dots

J. D. Plumhof,[1,*] V. Křápek,[2] F. Ding,[1,3] K. D. Jöns,[4] R. Hafenbrak,[4] P. Klenovský,[2] A. Herklotz,[5] K. Dörr,[5] P. Michler,[4] A. Rastelli,[1,†] and O. G. Schmidt[1]

[1]*Institute for Integrative Nanosciences, IFW Dresden, Helmholtzstrasse 20, D-01069 Dresden, Germany*

[2]*Institute of Condensed Matter Physics, Masaryk University, Kotlářská 2, CZ-61137 Brno, Czech Republic*

[3]*Key Laboratory of Semiconductor Materials Science, Institute of Semiconductors, Chinese Academy of Sciences, Beijing 100083, China*

[4]*Institut für Halbleiteroptik und Funktionelle Grenzflächen, University of Stuttgart, Allmandring 3, D-70569 Stuttgart, Germany*

[5]*Institute for Metallic Materials, IFW Dresden, Helmholtzstrasse 20, D-01069 Dresden, Germany*

(Received 7 February 2011; published 9 March 2011)

We study the effect of elastic anisotropic biaxial strain, induced by a piezoelectric actuator, on the light emitted by neutral excitons confined in different kinds of epitaxial quantum dots. We find that the light polarization rotates by up to ∼80° and the fine structure splitting (FSS) varies nonmonotonically by several tens of μeV as the strain is varied. These findings provide the experimental proof of a recently predicted strain-induced anticrossing of the bright states of neutral excitons in quantum dots. Calculations on model dots qualitatively reproduce the observations and suggest that the minimum reachable FSS critically depends on the orientation of the strain axis relative to the dot elongation.

DOI: 10.1103/PhysRevB.83.121302 PACS number(s): 78.67.Hc, 78.20.hb, 81.07.St, 81.07.Ta

Semiconductor quantum dots (QDs) obtained by epitaxial growth are receiving much attention because of their potential use as building blocks for quantum information processing and communication devices.[1–7] QDs confine the motion of charge carriers in three dimensions and are thus referred to as artificial atoms. Similar to real atoms, external electric and magnetic fields can be used to manipulate the properties of bound states in QDs.[8–13] In addition, the solid-state character of QDs allows for engineering methods which are not available for atoms. Dynamic stress fields[14–17] represent an example, whose wide potential is only recently being recognized.[18,19]

The emission of neutral excitons confined in QDs with symmetry lower than D_{2d} is typically split by several tens of μeV because of the anisotropic electron-hole exchange interaction.[9,20,21] This broken degeneracy of the bright excitonic states, referred to as fine structure splitting (FSS), prevents the use of QDs as sources of entangled photon pairs on demand.[4–7,22] External electric or magnetic fields have been applied to restore the QD symmetry and achieve FSS values comparable to the radiative linewidth.[10,11,13,14] Seidl *et al.*[15] showed that also uniaxial strain can in principle be used to reduce the excitonic FSS. Due to the limited tuning range available, it has, however, remained unclear whether strain is suitable to reach sufficiently low values of FSS[5] and what the mechanisms behind the observed FSS changes are. Based on atomistic model simulations for InGaAs/GaAs QDs, Singh and Bester[19] predicted that uniaxial stress generally leads to an anticrossing of the bright excitonic states. Thereby, the magnitude and phase of the mixing of the bright excitonic states are modified, which results in a change of the FSS and in a rotation of the linear polarization of the emitted photons.[18] Such an anticrossing behavior has been recently observed for QDs under strong vertical electric fields.[13]

Here we present the first experimental proof of the predictions in Ref. 18 for three different kinds of QDs under anisotropic biaxial stress. A continuum model based on eight-band $k \cdot p$ and configuration interaction theory qualitatively reproduces the observations, highlights their physical origin, and shows how the minimum reachable FSS depends on the angle between strain axis and dot orientation.

The measurements are performed on two different samples grown by solid-source molecular beam epitaxy (MBE). The active structures consist of QDs embedded in thin membranes, which are released from the underlying substrate and transferred onto a piezoelectric actuator. The first membrane sample, with total thickness of about 150 nm, contains GaAs/AlGaAs QDs[23] and quantum well (QW) potential fluctuations (QWPFs).[20,23] The latter, which are produced by local thickness or alloy fluctuations in a narrow QW, act as QDs with low confinement potential. The second sample contains standard InGaAs/GaAs QDs embedded in 200-nm-thick membranes.[24]

The external stress is applied using a piezoelectric $[Pb(Mg_{1/3}Nb_{2/3})O_3]_{0.72} - [PbTiO_3]_{0.28}$ (PMN-PT) crystal. By applying a voltage V between the front and the back surface of the crystal [i.e., along the x axis in Fig. 1(b)] the side faces, such as the top x-y plane, expand (or contract) parallel to the direction of the electric field F, for positive (negative) applied voltage. Simultaneously, the side faces contract (or expand) perpendicular to the electric field [i.e., along the y axis in Fig. 1(b)]. We denote the strain parallel to the x and y axes as ε and $\varepsilon_\perp$, respectively. The relation between these strain components is $\varepsilon_\perp \approx -0.7 \times \varepsilon$ (see Ref. 25). By placing membranes with QDs on the side faces of the PMN-PT we can thus apply strongly anisotropic biaxial stress on the QDs. According to previous results,[16,26] we expect values of ε of the order of a few ‰ in the explored range of the electric field F. Photoluminescence (PL) spectroscopy measurements are performed at a temperature of 8 K in a standard micro-PL setup with a spectral resolution of about 70 μeV. The linear polarization of the luminescence is analyzed by combining a rotatable achromatic half-wave plate and a fixed linear polarizer.[24]

Figure 1(a) shows a color-coded PL-intensity map for a neutral exciton (X) confined in a GaAs/AlGaAs QWPF as a function of the emission energy and polarization angle for different values of the electric field F applied to the PMN-PT

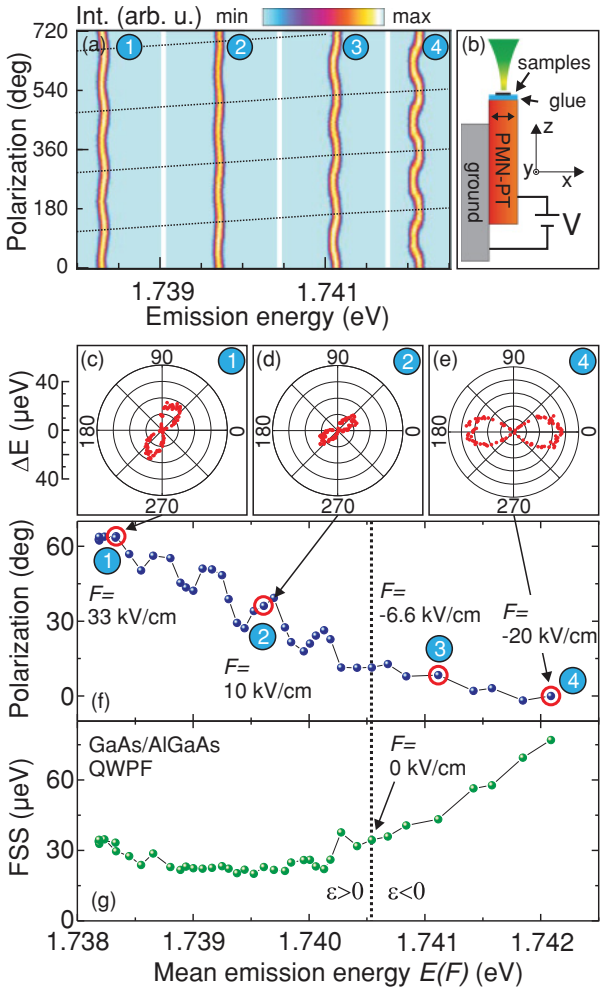

FIG. 1. (Color online) Behavior of a neutral exciton confined in a GaAs/AlGaAs QWPF under anisotropic biaxial stress. (a) Color-coded PL intensity vs polarization angle and energy for different values of electric fields applied to the piezoelectric actuator [the field values for the panels 1–4 are indicated in (f)]. The dashed lines are guides for the eye showing the rotation of the polarization direction. The x direction in (b) corresponds to polarization angles of 0°, 180°, 360°, 540°, and 720° and coincides with the polarization direction of the high-energy component at $F = -20\,\mathrm{kV/cm}$ (panel 4). (b) Sketch of the device consisting of a membrane (sample) glued on a side of a PMN-PT crystal. (c),(d),(e) Polarization dependence in polar coordinates of the relative emission energy for panels 1, 2, and 4, respectively, of (a). The mean emission energy $E(F)$ for each value of F is subtracted. (f) Polarization angle of the high-energy component of X with respect to the direction of the electric field vs $E(F)$. The dots marked by red circles correspond to the data shown in (a). (g) FSS vs average emission energy.

(panels 1–4: $F = 33$, 10, -6.6, and -20 kV/cm). In this membrane the electric field direction forms an angle of about 20° with the $[1\bar{1}0]$ GaAs crystal direction. The periodic energy shift (wavy pattern) observed in PL is ascribed to the excitonic FSS (see, e.g., Ref. 23).

Two striking features clearly emerge from Fig. 1(a): (i) The polarization direction of the excitonic emission, related to the phase of the wavy pattern, rotates by more than 60° when F is changed from 33 to -20 kV/cm (see dotted lines); (ii) the magnitude of the FSS, that is, the amplitude of the oscillations of the wavy patterns, first decreases and then increases with decreasing electric field. To extract quantitative information from the data, we first fit the peak position with a single Lorentzian curve at each polarization angle. The obtained relation of peak position E vs polarization angle ϕ is then fitted by a sine function to estimate both the magnitude of the FSS and the polarization of the X transitions with respect to the field direction [x axis in Fig. 1(b)]. The resolution in the determination of the FSS with this procedure is around 2.5 μeV.[27] For FSS values larger than 10 μeV, the uncertainty in the determination of the polarization direction is less than 10°.

Figures 1(c)–1(e) show polar plots of the relative peak positions $\Delta E = |E(\phi, F) - E(F)|$ extracted from Fig. 1(a) after subtraction of the average emission energy $E(F)$ measured for different values of F. The data, which are averaged over two periods of the polarization-resolved measurements (from 0° to 360° and from 360° to 720°), clearly show the strain-induced changes both in polarization direction and FSS. Figure 1(f) shows the orientation of the linear polarization of the high-energy component of X (with respect to the direction of F) as a function of $E(F)$. Figure 1(g) shows the corresponding behavior of the FSS. When moving from low to high emission energies, that is, from tensile to compressive strain along x, the FSS goes through a broad minimum before increasing again. The maximum observed change of the FSS for this QWPF is about 50 μeV. Concerning the polarization direction we observe that: (i) It shows oscillations (with amplitude larger than the experimental uncertainty) superimposed to a smooth decrease when the FSS is minimum; (ii) It appears to saturate with increasing FSS and, more precisely, it is aligned parallel to F for strong compression (point 4). By performing similar measurements on different QWPFs we consistently observe the same qualitative behavior: The polarization rotation mainly occurs in correspondence to the minimum of the FSS. Interestingly, the minimum value of the FSS varies from one QWPF to another. Examples where the minimum FSS reaches values below about 5 μeV are presented in Fig. 2(d) and in the supplemental information.[24]

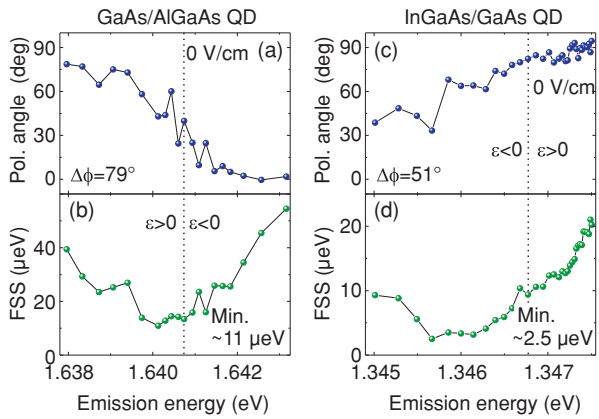

FIG. 2. (Color online) (a),(b) Polarization and FSS behavior of a GaAs/AlGaAs QD and (c),(d) of an InGaAs/GaAs QD. The polarization angle ϕ is defined as the angle of the higher energetic emission line with respect to the x direction in Fig. 1(b). For both QDs shown here the x direction roughly corresponds to the $[1\bar{1}0]$ direction of the GaAs membrane.

In order to test whether these effects occur also for other QD structures, we have performed measurements on GaAs/AlGaAs QDs and InGaAs/GaAs QDs (see Fig. 2).

For compressive strain, the emission energy of the GaAs/AlGaAs QD presented in Figs. 2(a) and 2(b) blueshifts similar to the QWPFs, whereas the emission energy of the presented InGaAs/GaAs QD [Figs. 2(c) and 2(d)] redshifts. The fact that a redshift is observed for the InGaAs QD is in qualitative agreement with the calculations presented in Ref. 19 for In-rich QDs. In spite of the very different structural properties and behavior of the emission energy under anisotropic strain, the excitonic behavior of the two different types of QDs is qualitatively the same as for the GaAs/AlGaAs QWPFs: we observe a clear polarization rotation of the emitted light (by 79° for the GaAs/AlGaAs QD and by 51° for the InGaAs/GaAs QD) [see Figs. 2(a) and 2(c)]. Simultaneously, the FSS is tuned in a range of ∼70 μeV for the GaAs QD and ∼25 μeV for the InGaAs QD [see Figs. 2(b) and 2(d)]. Furthermore, the rotation of the polarization mainly takes place when the FSS reaches its minimum value.

The above findings are consistent with a strain-induced anticrossing of the bright states of a neutral exciton, which was recently predicted by Singh and Bester for InGaAs QDs[19] via atomistic model simulations. In order to gather more insight on the physical origin of the observed phenomena, we calculate the excitonic FSS of model dots by combining the eight-band $k \cdot p$ model and the configuration interaction method following the approach described in Refs. 28, 29, and 23. Strain is introduced via the Pikus-Bir Hamiltonian.[30] In the model we consider a semiellipsoidal GaAs/AlGaAs QD with composition equal to the nominal one used in the experiment. The main axis ε of the anisotropic biaxial strain [x axis in Fig. 1(b)] coincides with the [1$\bar{1}$0] GaAs crystal direction and we assume $\varepsilon_\perp \approx -0.7 \times \varepsilon$ [see insets in Fig. 3(b)]. The main axis of the QD forms an angle α with respect to the [110] direction [see right inset in Fig. 3(a)].[24]

Figures 3(a) and 3(b) show, for different values of α, the calculated polarization angle and the FSS as a function of ε, respectively. We begin with the ideal situation of a QD elongated along the [110] crystal direction ($\alpha = 0$). For zero strain, the QD has a FSS of 33 μeV, which is comparable with typical observed values. When the QD is stretched, both exciton transitions remain linearly polarized and perpendicular to each other (not shown) and the FSS varies in a wide range [see Fig. 3(b)]. For a strain ε of 0.086% the FSS reaches its minimum value below 0.4 μeV. The polarization direction of the high-energy component, shown in Fig. 3(a), is perpendicular to the elongation direction of the QD for strains below 0.086% and abruptly changes by 90° for higher strains.

For increasing α, the polarization direction varies in a wider range of strain values; that is, it rotates smoothly as a function of strain, as shown in Fig. 3(a). Correspondingly, the minimum of the FSS becomes increasingly broad and the reached minimum value increases with increasing α. We also note that at zero strain the polarization angle is determined by the orientation of the dot. As the strain increases, the structural orientation becomes less important and the polarization angle is determined mostly by the magnitude and direction of the strain, yielding similar values for all dot orientations. This behavior is also observed in the experiments: For the largest

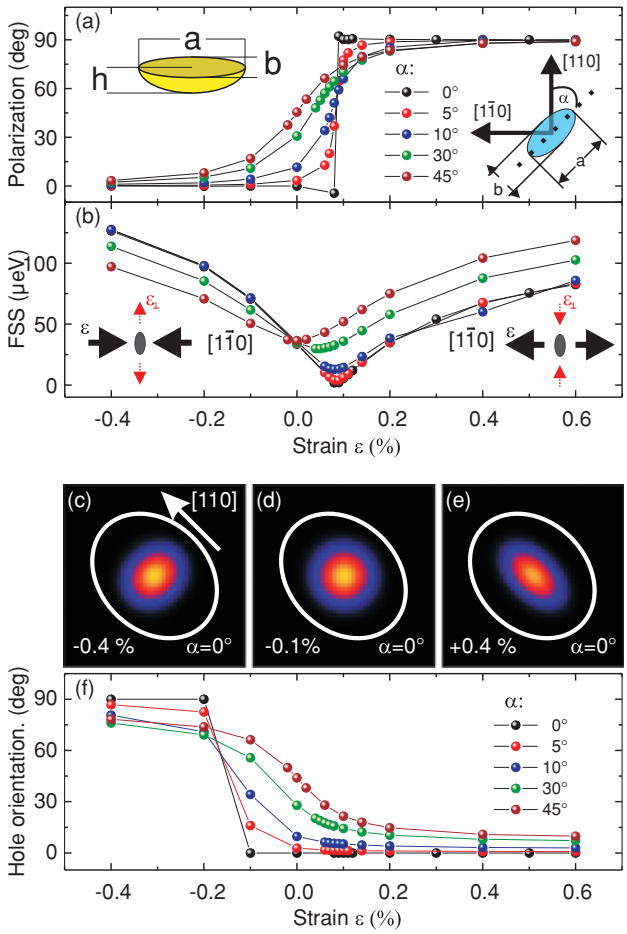

FIG. 3. (Color online) Theoretical study of the influence of anisotropic biaxial strain on the light emitted by a excitons in model GaAs/AlGaAs QDs. The left inset in (a) shows the shape of the artificial structure. (a) Polarization of the high-energy excitonic component with respect to the x direction ([1$\bar{1}$0]) in Fig. 2(b) for different values of α (i.e., angle of the elongation direction with respect to the [110] crystal direction; see right inset). (b) Corresponding values of the FSS, the left (right) inset displays the direction of the applied stress for compressive (tensile) strains ε. (c)–(e) Density map of the ground-state hole wave function for a QD with $\alpha = 0$ for different strain values. The white ellipse indicates the shape of the QD. (f) Orientation of the hole wave function with respect to the [110] direction vs strain. See text for more details.

available strains, and away from the FSS minimum, anisotropic biaxial stress allows us to orient the polarization direction parallel/perpendicular to the strain direction in a predictable way [see Figs. 1(a)–1(e)]. Finally we note that similar results are obtained when the direction of the strain is changed and the QD is kept fixed instead of rotating the QD shape with respect to the crystal direction as discussed here.[24]

By inspecting the single-particle states we found that small strains produce relevant changes on the ground-state hole wave function, while their effect on the electron wave function is much weaker. In particular: (i) The proportion of the light hole band in the hole state is substantially increased (e.g., from 0.6% at $\varepsilon = 0\%$ to 11% at $\varepsilon = 0.2\%$ for $\alpha = 0$); (ii) the hole wave function changes in shape and orientation, as illustrated in Figs. 3(c)–3(e) for $\alpha = 0$. In general, for finite

values of α, the elongation direction of holes rotates by up to 90°, as shown in Fig. 3(f). At the same time the electron wave function rotates by $<7°$ (not shown). These effects are a consequence of the nondiagonal terms in the Pikus-Bir Hamiltonian, which enhance the mixing of the heavy hole band with other bands (in particular, the light hole band) and modify the effective mass causing its pronounced anisotropy along the principal stress axes [110] and $[1\bar{1}0]$. The smooth rotation of the hole wave function observed for finite values of α [see Fig. 3(f)], which is analogous to the behavior observed for the polarization direction [see Fig. 3(a)], is due to the joined influence of the structural anisotropy (elongation of the QD) and the anisotropy of the effective mass, which tends to elongate the wave functions along the [110] or $[1\bar{1}0]$ direction depending on the sign of the applied strain. We note that the effects of the strain-induced band edge shift and the created piezoelectric potential on the FSS are negligible.

In spite of the simplicity of the model QD shape, the presented continuum model is able, for finite values of α, to account for the experimental observations

In conclusion, we have reported on the effects of anisotropic biaxial stress on the emission of neutral excitons confined in single semiconductor QDs. We have shown that relatively small strains are sufficient to produce dramatic changes of the polarization direction and of the energy splitting of the excitonic exchange-split doublet. Qualitatively the same results are obtained from three different kinds of QDs, consistent with a scenario involving a strain-induced anticrossing of the bright excitonic states.[19] Based on a continuum model, which is able to reproduce the main observed features, we ascribe the effects to substantial changes of the hole states. The theoretical investigation also shows that, for a given QD structure, the minimum reachable FSS depends strongly on the direction of the strain.

We acknowledge V. Fomin, S. Kiravittaya, P. Atkinson, T. Zander, R. Trotta, G. Bester, R. Singh, and C. C. Bof Bufon for fruitful discussions and technical support. V.K. and P.K. were supported by Institutional research program MSM 0021622410 and the GACR Grant No. GA202/09/0676. The calculations were partly performed on grid Wiggum (TU-Berlin) using the software package dotkp. This work was supported by the DFG (FOR730 and SFB 787) and the BMBF (QK_QuaHL-Rep, 01BQ1032).

*j.d.plumhof@ifw-dresden.de

†a.rastelli@ifw-dresden.de

[1] S. M. de Vasconcellos, S. Gordon, M. Bichler, T. Meier, and A. Zrenner, Nat. Photon. **4**, 545 (2010).

[2] D. Press, T. D. Ladd, B. Zhang, and Y. Yamamoto, Nature (London) **456**, 218 (2008).

[3] D. Brunner, B. D. Gerardot, P. A. Dalgarno, G. Wüst, K. Karrai, N. G. Stoltz, P. M. Petroff, and R. J. Warburton, Science **325**, 70 (2009).

[4] N. Akopian, N. H. Lindner, E. Poem, Y. Berlatzky, J. Avron, D. Gershoni, B. D. Gerardot, and P. M. Petroff, Phys. Rev. Lett. **96**, 130501 (2006).

[5] A. J. Hudson, R. M. Stevenson, A. J. Bennett, R. J. Young, C. A. Nicoll, P. Atkinson, K. Cooper, D. A. Ritchie, and A. J. Shields, Phys. Rev. Lett. **99**, 266802 (2007).

[6] R. Hafenbrak, S. M. Ulrich, P. Michler, L. Wang, A. Rastelli, and O. G. Schmidt, New J. Phys. **9**, 315 (2007).

[7] A. Dousse, J. Suffczynski, A. Beveratos, O. Krebs, A. Lemaitre, I. Sagnes, J. Bloch, P. Voisin, and P. Senellart, Nature (London) **466**, 217 (2010).

[8] S. Empedocles and M. Bawendi, Science **278**, 2114 (1997).

[9] M. Bayer, G. Ortner, O. Stern, A. Kuther, A. A. Gorbunov, A. Forchel, P. Hawrylak, S. Fafard, K. Hinzer, T. L. Reinecke, S. N. Walck, J. P. Reithmaier, F. Klopf, and F. Schäfer, Phys. Rev. B **65**, 195315 (2002).

[10] B. D. Gerardot, S. Seidl, P. A. Dalgarno, R. J. Warburton, D. Granados, J. M. Garcia, K. Kowalik, O. Krebs, K. Karrai, A. Badolato, and P. M. Petroff, Appl. Phys. Lett. **90**, 041101 (2007).

[11] M. M. Vogel, S. M. Ulrich, R. Hafenbrak, P. Michler, L. Wang, A. Rastelli, and O. G. Schmidt, Appl. Phys. Lett. **91**, 051904 (2007).

[12] R. Stevenson, R. Young, P. Atkinson, K. Cooper, D. Ritchie, and A. Shields, Nature (London) **439**, 179 (2006).

[13] A. J. Bennett, M. A. Pooley, R. M. Stevenson, M. B. Ward, R. B. Patel, A. Boyer de la Giroday, N. Sköld, I. Farrer, C. A. Nicoll, D. A. Ritchie, and A. J. Shields, Nat. Phys. **6**, 947 (2010).

[14] I. E. Itskevich, S. G. Lyapin, I. A. Troyan, P. C. Klipstein, L. Eaves, P. C. Main, and M. Henini, Phys. Rev. B **58**, 4250 (1998).

[15] S. Seidl, M. Kroner, A. Hogele, K. Karrai, R. Warburton, A. Badolato, and P. Petroff, Appl. Phys. Lett. **88**, 203113 (2006).

[16] F. Ding, R. Singh, J. D. Plumhof, T. Zander, V. Křápek, Y. H. Chen, M. Benyoucef, V. Zwiller, K. Dörr, G. Bester, A. Rastelli, and O. G. Schmidt, Phys. Rev. Lett. **104**, 067405 (2010).

[17] M. Metcalfe, S. M. Carr, A. Muller, G. S. Solomon, and J. Lawall, Phys. Rev. Lett. **105**, 037401 (2010).

[18] G. W. Bryant, M. Zieliński, N. Malkova, J. Sims, W. Jaskólski, and J. Aizpurua, Phys. Rev. Lett. **105**, 067404 (2010).

[19] R. Singh and G. Bester, Phys. Rev. Lett. **104**, 196803 (2010).

[20] D. Gammon, E. S. Snow, B. V. Shanabrook, D. S. Katzer, and D. Park, Phys. Rev. Lett. **76**, 3005 (1996).

[21] H. Y. Ramirez, C. H. Lin, C. C. Chao, Y. Hsu, W. T. You, S. Y. Huang, Y. T. Chen, H. C. Tseng, W. H. Chang, S. D. Lin, and S. J. Cheng, Phys. Rev. B **81**, 245324 (2010).

[22] O. Benson, C. Santori, M. Pelton, and Y. Yamamoto, Phys. Rev. Lett. **84**, 2513 (2000).

[23] J. D. Plumhof, V. Křápek, L. Wang, A. Schliwa, D. Bimberg, A. Rastelli, and O. G. Schmidt, Phys. Rev. B **81**, 121309(R) (2010).

[24] See supplemental material at [http://link.aps.org/supplemental/10.1103/PhysRevB.83.121302] for expanded data.

[25] M. D. Biegalski, K. Dörr, D. H. Kim, and H. M. Christen, Appl. Phys. Lett. **96**, 151905 (2010).

[26] T. Zander, A. Herklotz, S. Kiravittaya, M. Benyoucef, F. Ding, P. Atkinson, S. Kumar, J. D. Plumhof, K. Dörr, A. Rastelli, and O. G. Schmidt, Opt. Express **17**, 22452 (2009).

[27] F. Ding, N. Akopian, B. Li, U. Perinetti, A. Govorov, F. M. Peeters, C. C. Bof Bufon, C. Deneke, Y. H. Chen, A. Rastelli, O. G. Schmidt, and V. Zwiller, Phys. Rev. B **82**, 075309 (2010).

[28] O. Stier, M. Grundmann, and D. Bimberg, Phys. Rev. B **59**, 5688 (1999).

[29] T. Takagahara, Phys. Rev. B **62**, 16840 (2000).

[30] G. E. Pikus and G. L. Bir, *Symmetry and Strain Induced Effects in Semiconductors* (Wiley, New York, 1974).

G Tuning of the valence band mixing of excitons confined in GaAs/AlGaAs quantum dots via piezoelectric-induced anisotropic strain

Tuning of the valence band mixing of excitons confined in GaAs/AlGaAs quantum dots via piezoelectric-induced anisotropic strain

J. D. Plumhof,[1,*] R. Trotta,[1,2] V. Křápek,[3] E. Zallo,[1] P. Atkinson,[1,4] S. Kumar,[1] A. Rastelli,[1,2] and O. G. Schmidt[1]

[1]*Institute for Integrative Nanosciences, IFW Dresden, Helmholtzstr. 20, D-01069 Dresden, Germany*

[2]*Institute of Semiconductor and Solid State Physics, Johannes Kepler University Linz, Altenbergerstr. 69 A-4040 Linz, Austria*

[3]*Institute of Condensed Matter Physics, Masaryk University, Kotlářská 2, 61137 Brno, Czech Republic*

[4]*Institut des Nanosciences de Paris, Université Pierre et Marie Curie, Centre National de la Recherche Scientifique, Unité Mixte de Recherche 7588, 4 Place Jussieu, Paris 75005, France*

(Received 20 October 2012; revised manuscript received 5 January 2013; published 13 February 2013)

This work presents an experimental method to tune the degree of heavy-hole (HH) and light-hole (LH) mixing of the ground state of quantum dots (QDs). A ferroelectric crystal is used to apply reversible anisotropic biaxial stress to thin nanomembranes, containing GaAs/AlGaAs QDs. The stress-induced modification of the QD anisotropy leads to a change of the relative intensity of the two emission lines produced by the recombination of neutral bright excitonic states. Such a change is ascribed to a variation of the degree of HH-LH mixing. At the same time the modified anisotropy produces a change of the excitonic fine structure splitting (FSS). Model calculations provide a qualitative insight into the relation between strain, HH-LH mixing, and the FSS in epitaxial GaAs/AlGaAs QDs.

DOI: 10.1103/PhysRevB.87.075311 PACS number(s): 81.07.Ta

The potential use of semiconductor quantum dots (QDs) as hosts for quantum bits renders them appealing building blocks for quantum information and communication.[1,2] The spin of holes, confined in semiconductor QDs, has been proposed as alternative to the spin of electrons for QD-based quantum bits. In fact, the p-orbital-like character of the holes' Bloch waves reduces the interaction between hole spin and the atomic nuclei and hence the hyperfine interaction, which limits the coherence time of the spins.[3,4]

The use of hole-spins as quantum bits requires a minimized mixing of the heavy-hole (HH) and the light-hole (LH) states as mixing can produce dephasing of the hole spin.[5] In turn, this mixing is strictly connected to the symmetry of the QDs. A symmetry lower than D_{2d} allows for: (i) a mixing of HH- and LH bands ($|J=\frac{3}{2},m_J=\pm\frac{3}{2}\rangle \Longleftrightarrow |J=\frac{3}{2},m_J=\pm\frac{1}{2}\rangle$),[6–8] where J is the angular momentum of the hole, and m_J the projection of the hole spin on the z axis, (ii) a mixing of the bright excitonic states ($|+1\rangle \Longleftrightarrow |-1\rangle$), which, together with the exchange interaction, causes the fine structure splitting (FSS).[8,9] The QD anisotropy can have several origins: apart from the QD shape, also intrinsic strain fields or alloy fluctuations can distort the desired symmetry.[6,10–13] It is difficult to find QDs that fulfill these requirements, since technical and physical limits of the growth lead to QDs with emission energies and QD anisotropies differing from the desired characteristics. This makes postgrowth tuning techniques essential. It has been shown that simple tuning techniques such as annealing,[14] electric and magnetic fields (both lateral and vertical),[15–17] optical light fields,[18] as well as external stress fields[19–22] can be used to tune the FSS of neutral excitons, which is related to the QD anisotropy. Very recently it has been shown by our group that the combination of two tuning knobs, namely stress and electric fields, allows the FSS of randomly chosen QDs to be tuned to zero.[23] However, these works have not addressed the influence of the QD anisotropy on the HH-LH mixing.

Recently, Belhadj *et al.*[6] investigated nominally unstrained GaAs/AlGaAs QDs obtained by droplet epitaxy[24–27] and ascribed the occurrence of HH-LH mixing to the shape anisotropy of QDs. A thorough study of the combined effect of strain and shape anisotropy on the excitonic emission of strained InGaAs/GaAs QDs has been presented in Ref. 28.

In Ref. 19 we have investigated the influence of variable anisotropic stress on the FSS and on the polarization orientation for different kinds of QDs. By employing GaAs/AlGaAs QDs with improved optical properties[29,30] we now demonstrate how variable anisotropic stress produced by a piezoelectric actuator can be used to tune the valence band mixing in QDs, as implied by the observed tuning of the relative intensity of the excitonic emission lines. The observed changes in optical properties are in turn attributed to the stress-induced tuning of QD anisotropy.

The sample studied here was grown on a semi-insulating GaAs-(001) substrate by molecular beam epitaxy. The active QD structure was grown by the following procedure:[31] Gallium droplets are first deposited on a 100-nm thick GaAs layer, followed by annealing in an As_4 atmosphere at a substrate temperature of 520°C, which leads to the formation of nano holes. The nano holes are overgrown by a 7 nm thick $Al_{0.44}Ga_{0.56}As$ bottom barrier followed by 3 nm of GaAs, forming the QDs. The QDs are capped with 112 nm of $Al_{0.33}Ga_{0.67}As$ followed by 20 nm of $Al_{0.44}Ga_{0.56}As$ and 19 nm of GaAs. The dots have an irregular shape elongated along the [110] direction.[32] The 261-nm thick active structure containing the QDs was grown on top of an $Al_{0.75}Ga_{0.25}As$ sacrificial layer. This layer is removed via selective wet chemical etching to create thin QD membranes, which are then glued on top of a ferroelectric $[Pb(Mg_{1/3}Nb_{2/3})O_3]_{0.72} - [PbTiO_3]_{0.28}$ (PMN-PT) crystal to apply the stress. A description of the experimental details and of the properties of the PMN-PT can be found in Refs. 19,33–35. By applying an electric field, F, to the PMN-PT in the same geometry as in Ref. 19, a strain $\varepsilon_{\parallel}$ parallel to the electric field and a strain perpendicular

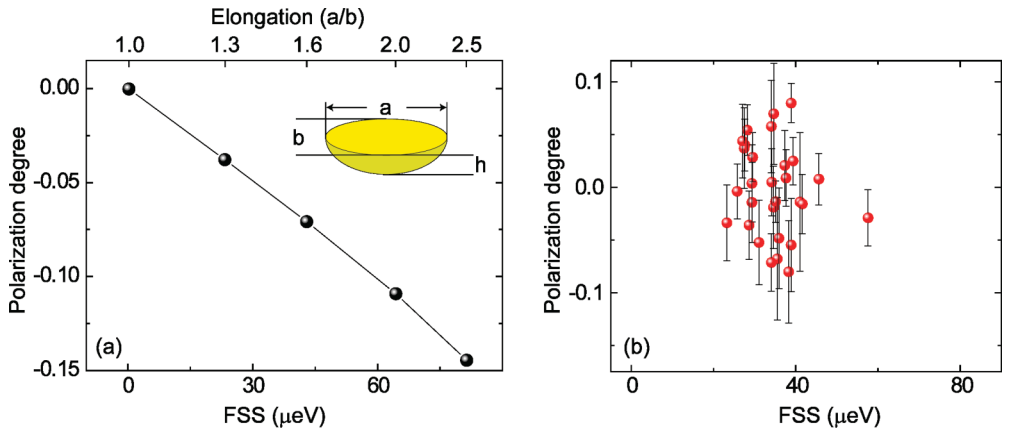

FIG. 1. (Color online) (a) Theoretically expected relation between polarization degree and FSS of unstrained QDs, as the elongation of the QD is varied from 1.0 to 2.5 while the height and the volume are kept constant. The inset shows a sketch of the artificial QD shape, with extensions a, b, and h. The QDs are aligned along the [110] crystal direction. (b) Experimentally obtained polarization degree vs FSS for unstrained QDs measured in the unprocessed sample.

to F, $\varepsilon_\perp$, are created inside the membrane. The ratio of the strains is expected to be $\varepsilon_\perp \approx -0.7 \times \varepsilon_\parallel$. The sign of both strains can be inverted by changing the sign of F. We use polarization-resolved microphotoluminescence (PL) spectroscopy to investigate the QD-emission properties. The experiments were performed in a helium flow cryostat at temperatures of $\sim$6 K. The spectra were recorded by using a spectrometer with a spectral resolution of around 40 μeV. A rotatable $\lambda/2$-wave plate was used in combination with a fixed polarizer to analyze the linear polarization of the emitted light (see also Refs. 10,19). The experimental data are accompanied by calculations relying on the eight-band $k \cdot p$ model in combination with the configuration interaction method, and with strain introduced via the Pikus-Bir Hamiltonian. Details about the theoretical model can be found in Refs. 10,19.

Before discussing the influence of strain on the QD emission, we focus on the unstrained GaAs/AlGaAs QDs. In order to give a measure of the degree of HH-LH mixing, we define the polarization degree, P, based on the intensity I_h (I_l) of the higher (lower) energetic emission line of the fine structure split neutral exciton $P = (I_\mathrm{h} - I_\mathrm{l})/(I_\mathrm{h} + I_\mathrm{l})$.

Figure 1 shows the polarization degree vs the corresponding FSS for model GaAs QDs [Fig. 1(a)] and for the dots studied in the experiment [Fig. 1(b)]. The points in Fig. 1(a) are obtained by calculating the polarization degree and FSS of semiellipsoidally shaped QD structures on top of a 1.5-nm thick wetting layer with a variable lateral elongation (a/b) and a fixed height $h = 4.6$ nm [see inset in Fig. 1(a) for structure]. The volume of the QDs was kept constant to avoid misleading contributions of a different volume to the result (the product of the lateral radii was kept fixed at 1100 nm^2). For FSS other than zero, the polarization degree is negative and follows a clear trend, i.e., the larger the FSS the smaller the polarization degree. This shows that FSS and polarization degree are correlated with each other. The contribution of the LH to the hole ground state increases from 2.6–3.4 % as the elongation increases from 1 to 2.5, the contribution of the other two bands (conduction and split-off) is below 0.2%. Figure 1(b) shows a scatter plot of polarization degree vs FSS obtained by measuring the emission of QDs in an unprocessed sample. The FSS shows a rather narrow distribution with an average value of about 40 μeV. We also note that the polarization direction of the low-energy component of the bright exciton is on average parallel to the [110] crystal direction, which is the elongation direction of the QDs, similar to our previous study.[10] However the polarization degree does not show any clear correlation with the FSS value. We qualitatively ascribe this observation to the fact that, while QDs are invariably elongated along the [110] direction, the shape of the studied dots is rather irregular and varies substantially from dot to dot.[31,32]

To avoid the complications produced by an unknown dot shape, we perform strain-tuning experiments on individual QDs. This allows us to tune the QD anisotropy for a fixed shape. Figure 2 shows the polarization-resolved PL data of a neutral exciton confined in a GaAs/AlGaAs QD embedded in a membrane connected to a PMN-PT actuator, for two different electric fields $F = -10$ kV/cm [Figs. 2(a)–2(c)] and $F = +30$ kV/cm [Figs. 2(d)–2(f)] applied to the PMN-PT. The [1$\bar{1}$0] crystal direction of the membrane is aligned parallel to F ($\varepsilon_\parallel$). Figures 2(a) and 2(d) show a color-coded PL intensity map of the emission of the neutral exciton. In Fig. 2(a), one can resolve the two fine structure split lines, whereas in Fig. 2(d) the two lines have almost the same energy. The FSS is determined in the following way: First the peak position for each polarization angle is obtained by fitting the emission lines with a Lorentzian curve. Then the peak position is plotted vs the polarization angle, as depicted in Figs. 2(b) and 2(e). The relative energy, ΔE, is obtained by subtraction of the average emission energy of the two excitonic emission lines. The magnitude of the FSS is finally obtained by fitting this relation with a sinusoidal curve [indicated by the black line in Figs. 2(b) and 2(e)]. The relative intensities are used as a measure for the HH-LH mixing.[6,8] In Figs. 2(c) and 2(f) the peak intensity of the emission lines is plotted vs the polarization angle. The intensity values are averaged over twelve degrees of polarization angle. The solid (dotted) vertical lines indicate the polarization angles corresponding to the higher (lower) energy emission line. It can be seen that the

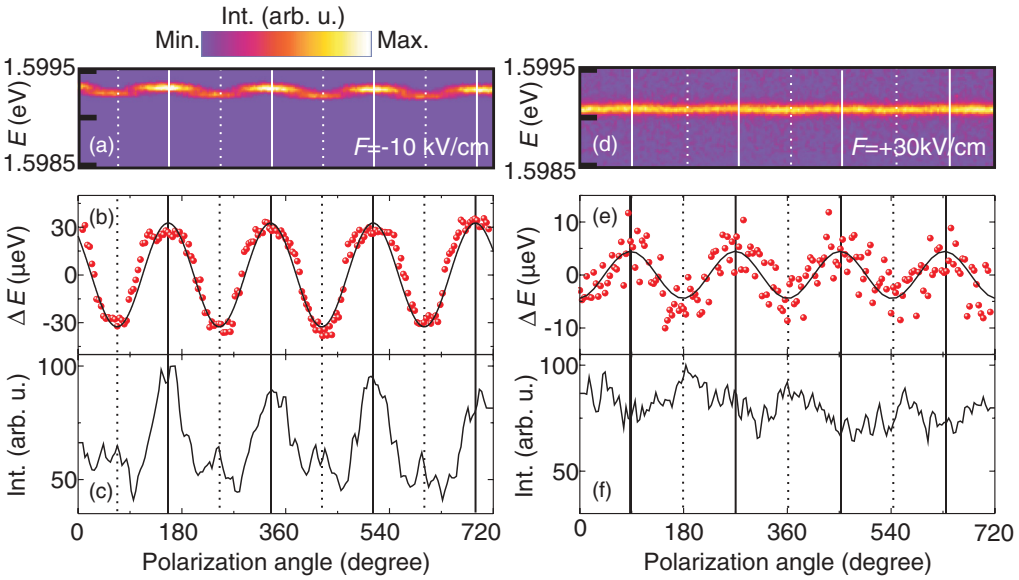

FIG. 2. (Color online) (a) Polarization-resolved color-coded PL signal of the recombination of a neutral exciton confined in a GaAs/AlGaAs QD. (b) Relative emission energy, ΔE, of the two excitonic components as a function of the polarization angle. The red data points display the spectral peak position measured for each single spectrum, the black solid line shows a sinusoidal fit applied to the data points to obtain values for the FSS/orientation of the polarization. (c) Intensity vs polarization angle. The vertical solid lines indicate the angles where the higher energy emission line is selected, while the dotted lines correspond to the lower energy emission line. (a), (b), (c) show a measurement performed at an electric field $F = -10$ kV/cm applied to the PMN-PT, while (d), (e), (f) display the same relations for $F = +30$ kV/cm.

ratio of the intensities for the two different values of F changes significantly.

Figures 3(a)–3(c) show the behavior of the FSS, polarization orientation, and polarization degree, P, when F is varied from $+30$ kV/cm down to -13 kV/cm (i.e., from tensile to compressive strain along the field direction, red data points) and back to $+30$ kV/cm (green data points). Figure 3(a) shows that the FSS decreases as the electric field increases, i.e., as the PMN-PT expands along the field direction. In Fig. 3(b) the angle between the polarization direction of the higher energy emission line and direction of F is plotted vs the electric field. FSS and polarization direction follow the behavior expected for an anticrossing of the bright excitonic states,[16,19] i.e., the polarization rotates mainly when the FSS is close to its minimum value. Similar to our previous results obtained on different types of dots,[19] away from the anticrossing, the high-energy component aligns along the electric field direction ($[1\bar{1}0]$) under compression (negative field values). Figure 3(c) shows how the polarization degree, P, changes with F. The polarization degree can be tuned over a broad range, from negative to positive values by almost 35%. It is worth noting that at $F = 0$ kV/cm, the value of P is slightly higher than the values observed for the QDs shown in Fig. 1(b), which can be explained by prestrain in the QD membrane, which results from the gluing and cooling processes.[29] To see whether the characteristic features of the measured data are stable over longer time, we repeated the same measurement by changing the electric field in the opposite direction (green data points). The green curves reproduce the trend of the red data points, but with a shift in the electric field. This inelastic behavior can be explained by an irreversible behavior of the PMN-PT or of the glue interface.

Figures 3(d)–3(f) show the results of the strain-dependent calculations. To this aim, the strains $\varepsilon_{\parallel}$ and $\varepsilon_{\perp}$ were applied along the $[1\bar{1}0]$ and [110] direction of the GaAs crystal, respectively. The elongation axis of the semiellipsoidal QD is rotated by an arbitrary angle $\alpha = 15^{\circ}$ with respect to the [110] direction. Figures 3(d) and 3(e) show the FSS and the polarization orientation of the higher energy emission line with respect to the $[1\bar{1}0]$ direction as a function of $\varepsilon_{\parallel}$. A typical anticrossing behavior with $\varepsilon_{\parallel}$ is observed, which is in a good agreement with the experimental data (unshadowed area).[16,19] Figure 3(f) illustrates the relation between polarization degree and $\varepsilon_{\parallel}$. For the unstrained QDs the polarization degree is negative and the strain tunes it toward positive values before shifting it to even more negative values for the case of tensile stress.

The unshadowed area in Figs. 3(d)–3(f) allows a direct comparison with the experimental data. A quantitative comparison between theory and experiment is difficult, since the membranes and consequently also the QDs are generally highly prestrained[29] and the modeled shape is much simpler than the experimental shape. The inset in Fig. 3(f) shows the contribution of HH (red data points) and LH (green data points) to the hole ground state. The contribution of the HH decreases from 96% to 74% as the strain is increased from $\varepsilon_{\parallel} = 0\%$ to $\varepsilon_{\parallel} = 0.4\%$. At the same time the LH contribution increases from 4% to 25%, which shows that strain is a powerful tool to control the degree of hole band mixing of excitons confined in QDs. (The sum of the two contributions is generally lower than 1 since also the conduction and spin-orbit split-off bands are included in the calculations.) The pronounced increase of the mixing is attributed to the nondiagonal terms in the Pikus-Bir Hamiltonian. The resulting mixing is present already in the

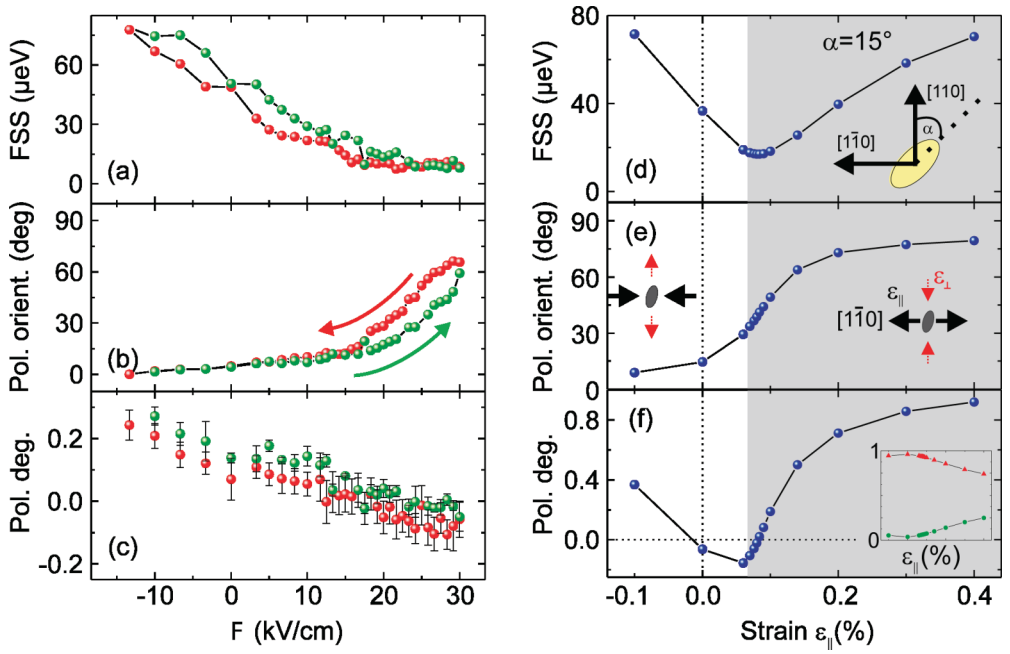

FIG. 3. (Color online) Experimental investigation [(a)–(c)] of the QD shown in Fig. 2 and model results [(d)–(f)]. The electric field F applied to the PMN-PT is varied from $F = +30\,\mathrm{kV/cm}$ to $F = -13\,\mathrm{kV/cm}$ (red data points) and back to $F = +30\,\mathrm{kV/cm}$ (green data points). (a) FSS vs F, (b) F dependence of the polarization angle of the higher energy emission line with respect to the direction of F. (c) Polarization degree vs F. (d)–(f) Model results for a semiellipsoidal QD tilted by 15° with respect to the [1$\bar{1}$0] as strain $\varepsilon_\parallel$ parallel to the [1$\bar{1}$0] direction is varied [see inset in (d)]. (d) Relation of FSS and strain $\varepsilon_\parallel$, (e) polarization direction of the higher energy emission line with respect to the direction of $\varepsilon_\parallel$. The insets in (e) indicate the direction of the strain field applied to the structure. In (f) the relation between polarization degree and $\varepsilon_\parallel$ is plotted. The nonshadowed area in (d)–(f) is a guide to the eye, to allow a link between theory and experiment. The inset in (f) shows the contribution of HH (red data points) and LH (green data points) to the hole ground states. The sum of the two contribution is generally lower than 1 since also the conduction and spin-orbit split-off bands are included in the calculations. The scale of the abscissa is the same as for the main axis.

bulk material and is only moderately/weakly influenced by the confinement. On the other hand, the mixing in the unstrained QDs results only from the lateral confinement. For our flat QDs we expect it to be rather weak.

In conclusion, we demonstrated that anisotropic stress can be used to vary continuously on-chip the QD anisotropy leading to a simultaneous change of the FSS and HH-LH mixing. These findings open up the possibility of using strain to tune the purity of the QD hole state.

We acknowledge F. Ding, K. Dörr, A. Herklotz, V. Fomin, G. Katsaros, J. R. Schröter, Shun-Jen Cheng, and Ch. Deneke for fruitful discussions and technical support. V.K. was supported by the Institutional Research Program MSM 0021622410 and the Czech Science Foundation (GACR), Grant No. GA202/09/0676. This work was supported by the German Research Foundation (FOR730) and Federal Ministry of Education and Research (QuaHL-Rep, Contract No. 01BQ1032).

*j.plumhof@gmx.de

[1] J. Petta, A. Johnson, J. Taylor, E. Laird, A. Yacoby, M. Lukin, C. Marcus, M. Hanson, and A. Gossard, Science **309**, 2180 (2005).
[2] A. Greilich, S. G. Carter, D. Kim, A. S. Bracker, and D. Gammon, Nature Phot. **5**, 703 (2011).
[3] D. Brunner, B. D. Gerardot, P. A. Dalgarno, G. Wuest, K. Karrai, N. G. Stoltz, P. M. Petroff, and R. J. Warburton, Science **325**, 70 (2009).
[4] B. D. Gerardot, D. Brunner, P. A. Dalgarno, P. Ohberg, S. Seidl, M. Kroner, K. Karrai, N. G. Stoltz, P. M. Petroff, and R. J. Warburton, Nature (London) **451**, 441 (2008).
[5] D. V. Bulaev and D. Loss, Phys. Rev. Lett. **95**, 076805 (2005).
[6] T. Belhadj, T. Amand, A. Kunold, C. M. Simon, T. Kuroda, M. Abbarchi, T. Mano, K. Sakoda, S. Kunz, X. Marie *et al.*, Appl. Phys. Lett. **97**, 051111 (2010).
[7] A. V. Koudinov, I. A. Akimov, Y. G. Kusrayev, and F. Henneberger, Phys. Rev. B **70**, 241305 (2004).
[8] C. H. Lin, W. T. You, H. Y. Chou, S. J. Cheng, S. D. Lin, and W. H. Chang, Phys. Rev. B **83**, 075317 (2011).
[9] M. Bayer, G. Ortner, O. Stern, A. Kuther, A. A. Gorbunov, A. Forchel, P. Hawrylak, S. Fafard, K. Hinzer, T. L. Reinecke *et al.*, Phys. Rev. B **65**, 195315 (2002).
[10] J. D. Plumhof, V. Křápek, L. Wang, A. Schliwa, D. Bimberg, A. Rastelli, and O. G. Schmidt, Phys. Rev. B **81**, 121309(R) (2010).

[11]R. Singh and G. Bester, Phys. Rev. Lett. **103**, 063601 (2009).
[12]I. Kegel, T. H. Metzger, A. Lorke, J. Peisl, J. Stangl, G. Bauer, J. M. García, and P. M. Petroff, Phys. Rev. Lett. **85**, 1694 (2000).
[13]R. Seguin, A. Schliwa, S. Rodt, K. Pötschke, U. W. Pohl, and D. Bimberg, Phys. Rev. Lett. **95**, 257402 (2005).
[14]W. Langbein, P. Borri, U. Woggon, V. Stavarache, D. Reuter, and A. D. Wieck, Phys. Rev. B **69**, 161301(R) (2004).
[15]B. D. Gerardot, S. Seidl, P. A. Dalgarno, R. J. Warburton, D. Granados, J. M. Garcia, K. Kowalik, O. Krebs, K. Karrai, A. Badolato *et al*., Appl. Phys. Lett. **90**, 041101 (2007).
[16]A. J. Bennett, M. A. Pooley, R. M. Stevenson, M. B. Ward, R. B. Patel, A. Boyer de la Giroday, N. Skoeld, I. Farrer, C. A. Nicoll, D. A. Ritchie *et al*., Nature Phys. **6**, 947 (2010).
[17]R. M. Stevenson, R. J. Young, P. See, D. G. Gevaux, K. Cooper, P. Atkinson, I. Farrer, D. A. Ritchie, and A. J. Shields, Physica E **32**, 135 (2006).
[18]A. Muller, W. Fang, J. Lawall, and G. S. Solomon, Phys. Rev. Lett. **103**, 217402 (2009).
[19]J. D. Plumhof, V. Křápek, F. Ding, K. D. Joens, R. Hafenbrak, P. Klenovsky, A. Herklotz, K. Dörr, P. Michler, A. Rastelli *et al*., Phys. Rev. B **83**, 121302(R) (2011).
[20]S. Seidl, M. Kroner, A. Hoegele, K. Karrai, R. J. Warburton, A. Badolato, and P. M. Petroff, Appl. Phys. Lett. **88**, 203113 (2006).
[21]D. Xiu-Ming, S. Bao-Quan, W. Bao-Rui, M. Shan-Shan, Z. Rong, H. She-Song, N. Hai-Qiao, and N. Zhi-Chuan, Chin. Phys. Lett. **25**, 1120 (2008).
[22]R. Trotta, P. Atkinson, J. D. Plumhof, E. Zallo, R. O. Rezaev, S. Kumar, S. Baunack, J. R. Schroeter, A. Rastelli, and O. G. Schmidt, Adv. Mater. **24**, 2668 (2012).
[23]R. Trotta, E. Zallo, C. Ortix, P. Atkinson, J. D. Plumhof, J. van den Brink, A. Rastelli, and O. G. Schmidt, Phys. Rev. Lett. **109**, 147401 (2012).
[24]N. Koguchi, S. Takahashi, and T. Chikyow, J. Cryst. Growth **111**, 688 (1991).
[25]S. Sanguinetti, K. Watanabe, T. Tateno, M. Gurioli, P. Werner, M. Wakaki, and N. Koguchi, J. Cryst. Growth **253**, 71 (2003).
[26]M. Abbarchi, C. A. Mastrandrea, T. Kuroda, T. Mano, K. Sakoda, N. Koguchi, S. Sanguinetti, A. Vinattieri, and M. Gurioli, Phys. Rev. B **78**, 125321 (2008).
[27]D. Sonnenberg, A. Graf, V. Paulava, W. Hansen, and C. Heyn, Appl. Phys. Lett. **101**, 143106 (2012).
[28]C. Tonin, R. Hostein, V. Voliotis, R. Grousson, A. Lemaitre, and A. Martinez, Phys. Rev. B **85**, 155303 (2012).
[29]S. Kumar, R. Trotta, E. Zallo, J. D. Plumhof, P. Atkinson, A. Rastelli, and O. G. Schmidt, Appl. Phys. Lett. **99**, 161118 (2011).
[30]In Ref. 19 it was not possible to investigate possible changes in the relative intensity of the two excitonic emission lines (which is related to the degree of HH-LH mixing) because of the lower optical quality of the used QDs, which led to temporal fluctuations of the intensities. Note that the intensities in Fig. 1(a) in Ref. 19 were normalized with respect to the maximum intensity for each value of electric field F applied to the piezoelectric actuator.
[31]P. Atkinson, E. Zallo, and O. G. Schmidt, J. Appl. Phys. **112**, 054303 (2012).
[32]Y. H. Huo, B. J. Witek, S. Kumar, R. Singh, E. Zallo, R. Grifone, D. Kriegner, R. Trotta, N. Akopian, J. Stangl *et al*., arXiv:1208.6554.
[33]T. Zander, A. Herklotz, S. Kiravittaya, M. Benyoucef, F. Ding, P. Atkinson, S. Kumar, J. D. Plumhof, K. Dörr, A. Rastelli *et al*., Opt. Express **17**, 22452 (2009).
[34]M. D. Biegalski, K. Dörr, D. H. Kim, and H. M. Christen, Appl. Phys. Lett. **96**, 151905 (2010).
[35]A. Herklotz, J. D. Plumhof, A. Rastelli, O. G. Schmidt, L. Schultz, and K. Dörr, J. Appl. Phys. **108**, 094101 (2010).

H Volume dependence of excitonic fine structure splitting in geometrically similar quantum dots

PHYSICAL REVIEW B **90**, 041304(R) (2014)

Volume dependence of excitonic fine structure splitting in geometrically similar quantum dots

Y. H. Huo,[1,*] V. Křápek,[2] A. Rastelli,[1,3] and O. G. Schmidt[1,4]

[1]*Institute for Integrative Nanosciences, IFW Dresden, Helmholtzstrasse 20, D-01069 Dresden, Germany*

[2]*Central European Institute of Technology, Brno University of Technology, Technická 10, 61600 Brno, Czech Republic*

[3]*Institute of Semiconductor and Solid State Physics, Johannes Kepler University Linz, Altenbergerstrasse 69, A-4040 Linz, Austria*

[4]*Center for Advancing Electronics Dresden (CfAED), Dresden University of Technology, 01067 Dresden, Germany*

(Received 5 May 2014; revised manuscript received 7 July 2014; published 30 July 2014)

We investigate the fine structure splitting (FSS) of excitons confined in strain-free, highly symmetric GaAs/AlGaAs quantum dots (QDs) as a function of size. QDs with similar geometry are created by filling nanoholes on an AlGaAs surface with different amounts of GaAs. In turn, nanoholes of regular reversed-cone shape are obtained by Al-droplet etching of an AlGaAs layer. The resulting QDs have high optical quality, as witnessed by emission linewidths smaller than 20 μeV under nonresonant excitation. The average FSS decreases from 12.5 $\pm$ 6.4 to 3.6 $\pm$ 1.7 μeV as the QD height increases from 5.4 $\pm$ 0.3 to 8.0 $\pm$ 0.2 nm, following the expected 1/volume dependence. Theoretical calculations using atomic force microscopy data of QD structures as input show that the geometrical similarity of QDs is reflected in invariant aspect ratio and lateral elongation of the wave functions and reproduce the experimental FSS energies.

DOI: 10.1103/PhysRevB.90.041304 PACS number(s): 81.07.Ta, 78.67.Hc, 71.35.Lk, 71.70.Gm

Single quantum dots (QDs) have been recognized as promising candidates for all-solid-state single photon [1] and entangled photon pair [2–5] sources to be used in quantum communication and computation [6–8]. To generate polarization entangled photons using the biexciton-exciton cascade, the involved exciton states should be degenerate, i.e., the so called fine structure splitting (FSS) of the optically bright doublet should be smaller than the natural linewidth of the exciton recombination. In the past decade different factors have been identified to be responsible for the FSS [9–17], such as shape elongation, piezoelectricity, etc. In addition, several methods have been demonstrated to reduce the FSS to values suitable for entanglement photon generation [4,18–31].

However, even if the sources of FSS have been theoretically analyzed, systematic experimental demonstrations of the correlation between FSS and specific QD structural parameters have largely lagged behind because of lack of suitable samples. Difficulties mainly fall into uncontrollable details of the QD growth processes. In the widely used Stranski-Krastanow QDs, like In(Ga)As/GaAs QDs, anisotropic migration of adatoms, indium segregation, and atom interdiffusion introduce shape elongation, composition, and strain inhomogeneity [14–17,32]. Because these effects occur together, it is difficult to separate their contributions. For example, the FSS should decrease when the QD size increases because the electron-hole exchange interaction decreases with increasing spatial extension of the electron and hole wave functions [13,33,34]. However, larger QDs tend to display larger FSS values [15,35,36], as shape asymmetry and piezoelectricity also increase when the QD size increases. In this respect, GaAs/AlGaAs QDs are a simpler system because of the negligible lattice mismatch between QD and barrier material. Surface segregation and interdiffusion are also much reduced compared with indium-containing QDs. Different methods have been used to grow GaAs/AlGaAs QDs such as monolayer fluctuations in thin quantum wells [37], "hierarchical self-assembly" using $AsBr_3$-etched nanoholes (NHs) [38–40], droplet epitaxy (DE) [41,42], overgrowth on patterned recesses [43,44], or local-droplet-etched (LDE) NHs [45–48]. In the first method, QD sizes and shapes are poorly defined. In the second method, QDs have a strongly elongated shape and the only study on the FSS dependence as a function of QD size considered QDs with different shapes [39]. In the DE method, shape asymmetry is also observed for large QDs [36]. In the other two approaches, the QD shape is defined by the NH shape since subsequent filling with GaAs does not change the NH shape appreciably. However, no clear dependence of the FSS on QD size has been reported so far [49]. Here we address experimentally and theoretically this point focusing on highly symmetric GaAs/AlGaAs QDs grown on GaAs(001) substrates and having different volumes but consistent shape.

The samples were grown using molecular beam epitaxy (MBE). We first grew a layer of $Al_{0.4}Ga_{0.6}As$ on a GaAs(001) buffer at a substrate temperature of 600 °C. We then deposited 0.5 monolayers (ML) Al in arsenic debt environment at an AlAs-equivalent rate of 0.5 ML/s to form droplets, followed by 5 min annealing under arsenic flux. During this step the droplets react with the underlying $Al_{0.4}Ga_{0.6}As$ forming NHs surrounded by a circular rim of recrystallized material. Figure 1(a) shows an atomic force microscopy (AFM) image of a droplet-etched $Al_{0.4}Ga_{0.6}As$ surface displaying NHs with a surface density of less than 1 μm^{-2}. The NH shape can be approximated by a reversed cone, as sketched in Fig. 1(b). Figure 1(c) shows a scatter plot of the NH aspect ratio, i.e., the ratio between hole depth h and base diameter D, versus the hole depth. (The depth is measured as the vertical distance between the rim and the NH deepest point.) To obtain QDs with different sizes, we overgrew the surface with NHs with different amounts of GaAs at 0.1 ML/s followed by 2 min annealing. The resulting QDs were capped with another $Al_{0.4}Ga_{0.6}As$ layer acting as a top barrier.

To measure the QD morphology, we etched NHs on the surface of the top $Al_{0.4}Ga_{0.6}As$ layer and filled them with the

*y.huo@ifw-dresden.de

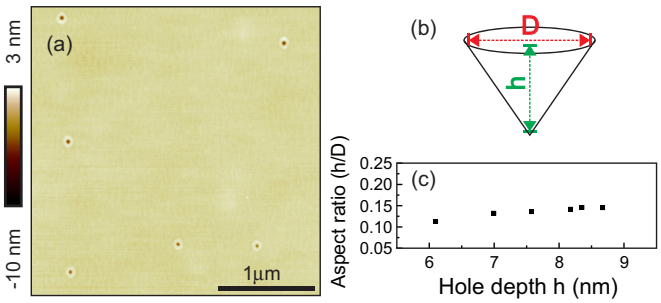

FIG. 1. (Color online) (a) A 3 μm × 3 μm AFM image of Al-droplet-etched NHs on an $Al_{0.4}Ga_{0.6}As$ surface. (b) Sketch of the hole shape, which is close to a reversed cone. (c) NH depth and aspect ratio [between hole depth (h) and base diameter (D)].

same amount of GaAs as for the buried QDs using the same growth parameters. Figures 2(a)–2(f) are representative AFM images and line scans of NHs before and after 1.5 and 2.5 nm GaAs overgrowth, see Supplemental Material [50] for more images. The surface progressively flattens with increasing filling because GaAs migrates preferentially into the NHs, as the negative surface curvature produces a minimum in the chemical potential [51]. By subtracting the average depths after GaAs filling from the original NH depth, we estimate the QD heights. We measured 7–9 QDs for each sample using 2 × 2 μm^2 AFM images with resolution of 512 × 512 pixels. The mean QD heights after filling with 1.5 and 2.5 nm GaAs are 6.4 ± 0.3 and 8.0 ± 0.2 nm, respectively. We note that the real NH depth can deviate slightly from the quoted value because of AFM tip convolution, surface oxidation, or possible fluctuations during growth. Since intermixing between GaAs and AlGaAs is negligible, QDs are expected to have the same shape as the holes.

Polarization-resolved microphotoluminescence (μ-PL) measurements were carried out at ∼5 K to measure the FSS values of neutral excitons confined in QDs [52,53]. A laser beam with 532 nm wavelength was focused on the sample surface with a 50× microscope objective. PL was collected with the same objective, passed through a rotatable $\lambda/2$ achromatic retarder, a linear polarizer, and dispersed by a spectrometer

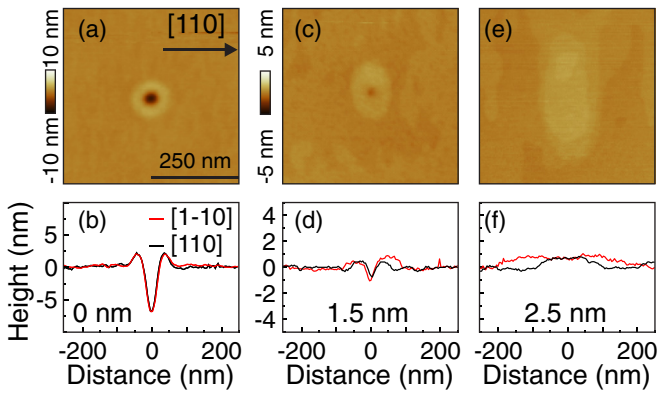

FIG. 2. (Color online) AFM images (top) and line scans (bottom) of representative NHs before [(a), (b)] and after filling with 1.5 [(c), (d)] and 2.5 [(e), (f)] nm GaAs. Line scans are taken along [110] and [1−10] crystal directions.

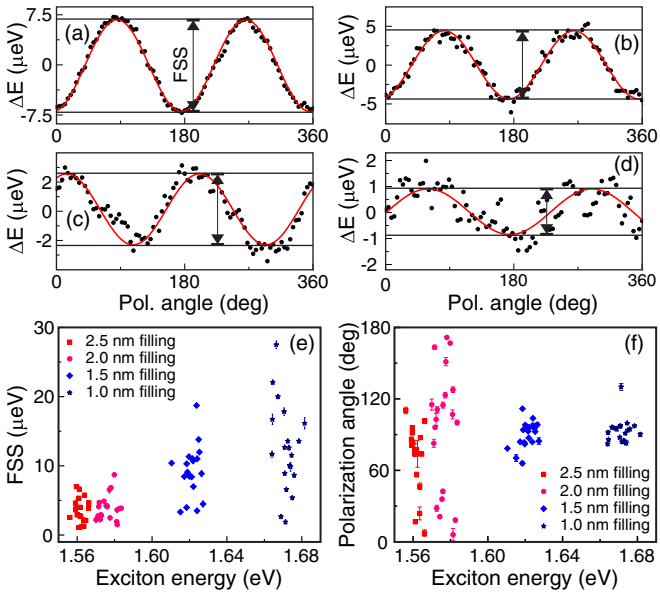

FIG. 3. (Color online) (a)–(d) Relative emission energies obtained by fitting polarization-resolved μ-PL spectra of representative QDs as a function of polarization angle using a Lorentzian line shape. The QDs are formed by filling the NHs with 1.0, 1.5, 2.0, and 2.5 nm GaAs, respectively. 0 deg corresponds to the [110] crystal direction. FSS values are obtained from a sine fit (solid line) of the peak energies. (e) and (f) FSS and polarization angle of QD emissions as a function of exciton energy. Twenty QDs were chosen randomly in each sample. The angles in (f) represent the polarization direction of the high energy component of the bright doublets with respect to the [110] crystal direction.

with spectral resolution of ∼20 μeV. Figures 3(a)–3(d) show the relative peak positions extracted from Lorentzian fits of the polarization-resolved μ-PL spectra of representative QDs, formed by filling 1.0, 1.5, 2.0, and 2.5 nm GaAs in NHs, as a function of polarization angle. (See Supplemental Material [50] for the corresponding PL spectra.) The amplitude of the oscillations corresponds to the FSS, which clearly decreases as the QD size increases. The resulting values of FSS are 13.8, 8.8, 4.8, and 1.6 μeV for QDs with fillings of 1.0, 1.5, 2.0, and 2.5 nm, respectively. The corresponding full width at half maximum (FWHM) of single excitonic lines is resolution limited (∼20 μeV), indicating good optical quality of the QDs. To draw more general conclusions on the dependence of FSS on QD size, we have performed statistical investigations by measuring the FSS of 20 randomly selected QDs in each sample. Figure 3(e) shows the measured values of FSS as a function of exciton energy for different fillings. When the filling amount (and hence the QD size) increases, the excitonic energy and FSS both decrease. For fillings of 1.0, 1.5, 2.0, and 2.5 nm, the average FSS values are 12.5 ± 6.4, 9.2 ± 3.7, 3.9 ± 1.8, and 3.6 ± 1.7 μeV. From Fig. 3(f), which shows the polarization angles of the high energy component of the bright doublets, we see that the increase in FSS and broadening of FSS distribution with decreasing QD size is accompanied by a narrowing of the distribution of polarization angles.

To understand the experimental results, we calculated the single particle wave functions and excitonic FSS by combining eight-band $k \cdot p$ theory and configuration interaction following

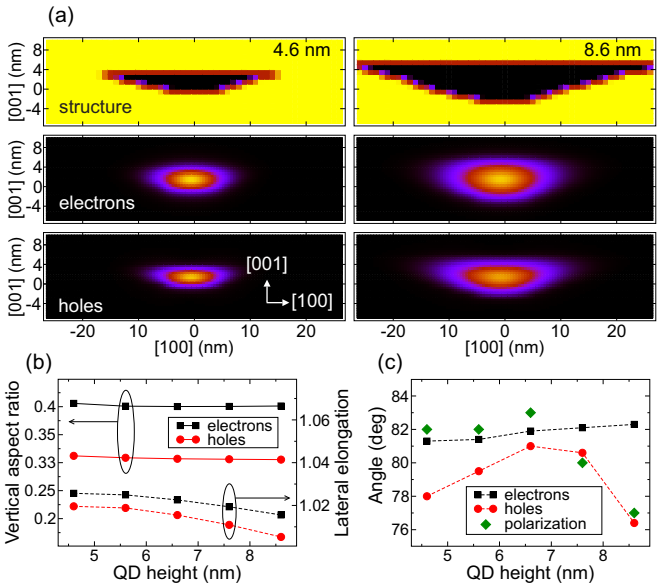

FIG. 4. (Color online) (a) QD structures with heights of 4.6 and 8.6 nm, respectively, used for the model calculations and corresponding probability densities of the lowest electron and hole states. (b) Calculated vertical aspect ratio (solid lines) and lateral aspect ratio (dashed lines) of the spatial extension of electron and hole probability densities. Electrons are represented by black squares, holes by red circles. (c) The angle between the long axis of the probability density distribution and [1−10] crystallographic axis for electrons (black squares) and holes (red circles) and the polarization angle of the lower component of the bright doublet (diamond symbols).

the approach described in Refs. [11,54]. In the calculation we used the AFM image of a NH to define the lower boundary of the model dot, while a flat top boundary was set in accord with the measured QD heights. Figure 4(a) shows the QD structures with heights 4.6 and 8.6 nm and corresponding electron and hole wave functions. From the analysis of the wave function we observe that: (1) Electron and hole wave functions are rather similar, sharing the barycenter located in the midheight of the QD. The vertical separation of both charge carriers is below 0.1 nm resulting in a negligible electric dipole moment. This is in contrast with InAs/GaAs QDs where the carriers are separated due to the inhomogeneous biaxial strain and the inhomogeneous InGaAs composition profile. The similarity of the lateral extensions, despite different effective masses, was discussed in Ref. [40]. (2) The extensions of the wave functions scale with the height of the QD. The extension parameters are obtained by fitting a three-dimensional Gaussian distribution to the probability density and are used to define the vertical aspect ratio (vertical-to-mean-lateral extension) and the lateral elongation (ratio of the lateral extensions). These parameters, shown in Fig. 4(b), exhibit only minor variations as a function of QD height, reflecting the geometrical similarity of the QD structures. Only for the largest filling, when the NH becomes overfilled and a continuous quantum well is formed, the aspect ratio of the hole wave function is somewhat reduced. This fact does not influence our conclusions as there is only a minor impact on FSS as the lateral elongation is preserved and such height is out of our experimentally studied range.

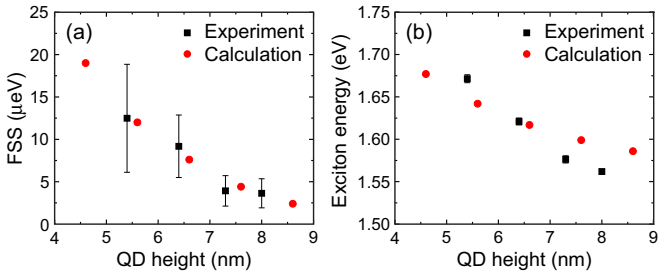

FIG. 5. (Color online) Fine structure splitting (a) and exciton energy (b) as a function of QD size. Black squares are the experiment data, red circles are theoretical calculations.

From Fig. 5(a), which shows the average FSS values vs QD height, we see that the FSS decreases with increasing QD height. Figure 5(b) shows that also the exciton energy decreases, consistent with quantum confinement effects. The calculated FSS and exciton energies, also shown in Fig. 5, are in good agreement with experimental data. The small discrepancies may originate from the simplified QD morphology with a flat top and from atomistic contributions such as alloy fluctuations in the barrier, which are not included in the model calculation of FSS.

To further understand the above results we consider the origins of FSS. Since our QDs are formed in an almost lattice-matched heterostructure and are characterized by a rather uniform shape distribution and negligible intermixing, factors like shape irregularity, strain, and piezoelectricity play no important roles. Based on the calculations we can fully attribute the observed magnitude of FSS to the minor structural elongation of the QDs. However, the prediction of similar polarization angles for all heights [Fig. 4(c)] is in contrast with the observed broad polarization distribution for large heights [Fig. 3(f)]. We infer that the FSS is affected by weak (several μeV) randomizing effects such as the Al-rich and irregularly shaped rim of NHs or alloy fluctuations in the barrier. Such effects are negligible for small QDs (with large FSS due to pronounced electron-hole overlap), but are responsible for the broadening of the polarization angle distribution when the dominant contribution of structural elongation becomes low (i.e., for large heights).

In conclusion, we have obtained highly symmetric strain-free GaAs/AlGaAs QDs by filling Al-droplet-etched NHs in AlGaAs with GaAs. By changing the GaAs filling amount we obtain QDs of different sizes but similar shape, which offer an ideal platform to study QD size effects on FSS. Through statistical investigation of QD size and excitonic FSS, we find that the FSS does depend on QD size and that it decreases when the QD size increases. Calculations using eight-band $k \cdot p$ theory and configuration interaction reproduce well the experimental results.

This work was financially supported by the BMBF project QuaHL-Rep (Contracts No. 01BQ1032 and No. 01BQ1034) and the European Union Seventh Framework Programme (FP7/2007-2013) under Grant Agreement No. 601126 (HANAS). V.K. was supported by the European Regional Development Fund, project No. CZ. 1.07/2.3.00/30.0005. We thank E. Zallo and R. Engelhard for MBE assistance, and S. Kumar and R. Trotta for assistance with the optical measurements.

[1] P. Michler, A. Kiraz, C. Becher, W. V. Schoenfeld, P. M. Petroff, L. D. Zhang, E. Hu, and A. Imamoglu, Science **290**, 2282 (2000).
[2] O. Benson, C. Santori, M. Pelton, and Y. Yamamoto, Phys. Rev. Lett. **84**, 2513 (2000).
[3] N. Akopian, N. H. Lindner, E. Poem, Y. Berlatzky, J. Avron, D. Gershoni, B. D. Gerardot, and P. M. Petroff, Phys. Rev. Lett. **96**, 130501 (2006).
[4] R. M. Stevenson, R. J. Young, P. Atkinson, K. Cooper, D. A. Ritchie, and A. J. Shields, Nature (London) **439**, 179 (2006).
[5] J. W. Pan, Z. B. Chen, C. Y. Lu, H. Weinfurter, A. Zeilinger, and M. Zukowski, Rev. Mod. Phys. **84**, 777 (2012).
[6] T. Jennewein, G. Weihs, J. W. Pan, and A. Zeilinger, Phys. Rev. Lett. **88**, 017903 (2001).
[7] N. Gisin, G. Ribordy, W. Tittel, and H. Zbinden, Rev. Mod. Phys. **74**, 145 (2002).
[8] P. Kok, W. J. Munro, K. Nemoto, T. C. Ralph, J. P. Dowling, and G. J. Milburn, Rev. Mod. Phys. **79**, 135 (2007).
[9] R. Singh and G. Bester, Phys. Rev. Lett. **103**, 063601 (2009).
[10] A. Schliwa, M. Winkelnkemper, A. Lochmann, E. Stock, and D. Bimberg, Phys. Rev. B **80**, 161307(R) (2009).
[11] T. Takagahara, Phys. Rev. B **62**, 16840 (2000).
[12] M. Bayer, G. Ortner, O. Stern, A. Kuther, A. A. Gorbunov, A. Forchel, P. Hawrylak, S. Fafard, K. Hinzer, T. L. Reinecke, S. N. Walck, J. P. Reithmaier, F. Klopf, and F. Schäfer, Phys. Rev. B **65**, 195315 (2002).
[13] M. Gong, B. Hofer, E. Zallo, R. Trotta, J.-W. Luo, O. G. Schmidt, and C. Zhang, Phys. Rev. B **89**, 205312 (2014).
[14] I. Kegel, T. H. Metzger, A. Lorke, J. Peisl, J. Stangl, G. Bauer, K. Nordlund, W. V. Schoenfeld, and P. M. Petroff, Phys. Rev. B **63**, 035318 (2001).
[15] R. Seguin, A. Schliwa, S. Rodt, K. Pötschke, U. W. Pohl, and D. Bimberg, Phys. Rev. Lett. **95**, 257402 (2005).
[16] G. Bester, S. Nair, and A. Zunger, Phys. Rev. B **67**, 161306(R) (2003).
[17] J. W. Luo, R. Singh, A. Zunger, and G. Bester, Phys. Rev. B **86**, 161302(R) (2012).
[18] J. D. Plumhof, R. Trotta, A. Rastelli, and O. G. Schmidt, Nano Res. Lett. **7**, 336 (2012)
[19] E. Stock, T. Warming, I. Ostapenko, S. Rodt, A. Schliwa, J. A. Töfflinger, A. Lochmann, A. I. Toropov, S. A. Moshchenko, D. V. Dmitriev, V. A. Haisler, and D. Bimberg, Appl. Phys. Lett. **96**, 093112 (2010).
[20] T. Mano, M. Abbarchi, T. Kuroda, B. McSkimming, A. Ohtake, K. Mitsuishi, and K. Sakoda, Appl. Phys. Express **3**, 065203 (2010).
[21] G. Juska, V. Dimastrodonato, L. O. Mereni, A. Gocalinska, and E. Pelucchi, Nature Photon. **7**, 527 (2013).
[22] J. Treu, C. Schneider, A. Huggenberger, T. Braun, S. Reitzenstein, S. Höfling, and M. Kamp, Appl. Phys. Lett. **101**, 022102 (2012).
[23] W. Langbein, P. Borri, U. Woggon, V. Stavarache, D. Reuter, and A. D. Wieck, Phys. Rev. B **69**, 161301(R) (2004).
[24] A. I. Tartakovskii, M. N. Makhonin, I. R. Sellers, J. Cahill, A. D. Andreev, D. M. Whittaker, J-P. R. Wells, A. M. Fox, D. J. Mowbray, M. S. Skolnick, K. M. Groom, M. J. Steer, H. Y. Liu, and M. Hopkinson, Phys. Rev. B **70**, 193303 (2004).
[25] R. J. Young, R. M. Stevenson, A. J. Shields, P. Atkinson, K. Cooper, D. A. Ritchie, K. M. Groom, A. I. Tartakovskii, and M. S. Skolnick, Phys. Rev. B **72**, 113305 (2005).
[26] J. D. Mar, X. L. Xu, J. S. Sandhu, A. C. Irvine, M. Hopkinson, and D. A. Williams, Appl. Phys. Lett. **97**, 221108 (2010).
[27] A. J. Bennett, M. A. Pooley, R. M. Stevenson, M. B. Ward, R. B. Patel, A. B. de la Giroday, N. Sköld, I. Farrer, C. A. Nicoll, D. A. Ritchie, and A. J. Shields, Nat. Phys. **6**, 947 (2010).
[28] K. Kowalik, O. Krebs, A. Lemaître, S. Laurent, P. Senellart, P. Voisin, and J. A. Gaj, Appl. Phys. Lett. **86**, 041907 (2005).
[29] S. Seidl, M. Kroner, A. Hoegele, K. Karrai, R. J. Warburton, A. Badolato, and P. M. Petroff, Appl. Phys. Lett. **88**, 203113 (2006).
[30] J. D. Plumhof, V. Křápek, F. Ding, K. D. Jöns, R. Hafenbrak, P. Klenovský, A. Herklotz, K. Dörr, P. Michler, A. Rastelli, and O. G. Schmidt, Phys. Rev. B **83**, 121302(R) (2011).
[31] R. Trotta, E. Zallo, C. Ortix, P. Atkinson, J. D. Plumhof, J. van den Brink, A. Rastelli, and O. G. Schmidt, Phys. Rev. Lett. **109**, 147401 (2012).
[32] T. Walther, A. G. Cullis, D. J. Norris, and M. Hopkinson, Phys. Rev. Lett. **86**, 2381 (2001).
[33] M. Nirmal, D. J. Norris, M. Kuno, M. G. Bawendi, A. L. Efros, and M. Rosen, Phys. Rev. Lett. **75**, 3728 (1995).
[34] D. J. Norris, A. L. Efros, M. Rosen, and M. G. Bawendi, Phys. Rev. B **53**, 16347 (1996).
[35] H. Y. Ramirez, C. H. Lin, C. C. Chao, Y. Hsu, W. T. You, S. Y. Huang, Y. T. Chen, H. C. Tseng, W. H. Chang, S. D. Lin, and S. J. Cheng, Phys. Rev. B **81**, 245324 (2010).
[36] M. Abbarchi, C. A. Mastrandrea, T. Kuroda, T. Mano, K. Sakoda, N. Koguchi, S. Sanguinetti, A. Vinattieri, and M. Gurioli, Phys. Rev. B **78**, 125321 (2008).
[37] D. Gammon, E. S. Snow, B. V. Shanabrook, D. S. Katzer, and D. Park, Phys. Rev. Lett. **76**, 3005 (1996).
[38] A. Rastelli, S. Stufler, A. Schliwa, R. Songmuang, C. Manzano, G. Costantini, K. Kern, A. Zrenner, D. Bimberg, and O. G. Schmidt, Phys. Rev. Lett. **92**, 166104 (2004).
[39] J. D. Plumhof, V. Křápek, L. Wang, A. Schliwa, D. Bimberg, A. Rastelli, and O. G. Schmidt, Phys. Rev. B **81**, 121309(R) (2010).
[40] L. Wang, V. Křápek, F. Ding, F. Horton, A. Schliwa, D. Bimberg, A. Rastelli, and O. G. Schmidt, Phys. Rev. B **80**, 085309 (2009).
[41] N. Koguchi, S. Takahashi, and T. Chikyow, J. Cryst. Growth **111**, 688 (1991).
[42] N. Koguchi and K. Ishige, Jpn. J. Appl. Phys. **32**, 2052 (1993).
[43] Q. Zhu, J. D. Ganière, Z. B. He, K. F. Karlsson, M. Byszewski, E. Pelucchi, A. Rudra, and E. Kapon, Phys. Rev. B **82**, 165315 (2010).
[44] L. O. Mereni, V. Dimastrodonato, R. J. Young, and E. Pelucchi, Appl. Phys. Lett. **94**, 223121 (2009)
[45] Zh. M. Wang, B. L. Liang, K. A. Sablon, and G. J. Salamo, Appl. Phys. Lett. **90**, 113120 (2007).
[46] Ch. Heyn, A. Stemmann, T. Köppen, Ch. Strelow, T. Kipp, M. Grave, S. Mendach, and W. Hansen, Appl. Phys. Lett. **94**, 183113 (2009).
[47] E. Zallo, P. Atkinson, A. Rastelli, and O. G. Schmidt, J. Cryst. Growth **338**, 232 (2012).
[48] P. Atkinson, E. Zallo, and O. G. Schmidt, J. Appl. Phys. **112**, 054303 (2012).
[49] Ch. Heyn, M. Klingbeil, Ch. Strelow, A. Stemmann, S. Mendach, and W. Hansen, Nanoscale Res. Lett. **5**, 1633 (2010).

[50] See Supplemental Material at http://link.aps.org/supplemental/10.1103/PhysRevB.90.041304 for more AFM images and color-coded polarization-resolved μ-PL spectra.

[51] B. Yang, F. Liu, and M. G. Lagally, Phys. Rev. Lett. **92**, 025502 (2004).

[52] Y. H. Huo, A. Rastelli, and O. G. Schmidt, Appl. Phys. Lett. **102**, 152105 (2013).

[53] Y. H. Huo, B. J. Witek, S. Kumar, J. R. Cardenas, J. X. Zhang, N. Akopian, R. Singh, E. Zallo, R. Grifone, D. Kriegner, R. Trotta, F. Ding, J. Stangl, V. Zwiller, G. Bester, A. Rastelli, and O. G. Schmidt, Nat. Phys. **10**, 46 (2014).

[54] O. Stier, M. Grundmann, and D. Bimberg, Phys. Rev. B **59**, 5688 (1999).

I Excitonic fine structure splitting in type-II quantum dots

Excitonic fine structure splitting in type-II quantum dots

V. Křápek*
Central European Institute of Technology, Brno University of Technology, Technická 10, 616 00 Brno, Czech Republic

P. Klenovský
Institute of Condensed Matter Physics, Masaryk University, Kotlářská 2, 611 37 Brno, Czech Republic
and Central European Institute of Technology, Masaryk University, Kamenice 753, 625 00 Brno, Czech Republic

T. Šikola
Central European Institute of Technology, Brno University of Technology, Technická 10, 616 00 Brno, Czech Republic
and Institute of Physical Engineering, Brno University of Technology, Technická 2, 616 69 Brno, Czech Republic
(Received 30 April 2015; revised manuscript received 9 September 2015; published 25 November 2015)

Excitonic fine structure splitting in quantum dots is closely related to the lateral shape of the wave functions. We have studied theoretically the fine structure splitting in InAs quantum dots with a type-II confinement imposed by a GaAsSb capping layer. We show that very small values of the fine structure splitting comparable with the natural linewidth of the excitonic transitions are achievable for realistic quantum dots despite the structural elongation and the piezoelectric field. For example, varying the capping layer thickness allows for a fine tuning of the splitting energy. The effect is explained by a strong sensitivity of the hole wave function to the quantum dot structure and a mutual compensation of the electron and hole anisotropies. The oscillator strength of the excitonic transitions in the studied quantum dots is comparable to those with a type-I confinement which makes the dots attractive for quantum communication technology as emitters of polarization-entangled photon pairs.

DOI: 10.1103/PhysRevB.92.195430 PACS number(s): 71.35.−y, 73.21.La, 81.05.Ea

I. INTRODUCTION

Excitonic fine structure splitting (FSS) is a tiny energy splitting of two bright exciton states confined in quantum dot (QD) heterostructures with a typical magnitude ranging from units to hundreds μeV. It is manifested in a doublet structure of the exciton recombination band. It was observed for the first time in GaAs/AlGaAs quantum wells with fluctuating thickness [1] and then in various QD systems [2–5]. Soon after its discovery it was attributed to the electron-hole exchange interaction [6] and its finite value was related to the reduced symmetry, which needs to be lower than D_{2d} [2].

The interest in FSS is triggered by both fundamental and application points of view. FSS helps to distinguish the spectral features originating in the recombination of exciton (doublet), biexciton (doublet with opposite polarization-energy dependence), and trion (singlet) [2,7,8]. It plays an important role in the spin initialization, e.g., in electron spin memories [9] or in exciton dynamics and dephasing [10–13]. It provides some insight into the size and shape of QDs [14,15]. Benson's proposal of the source of entangled photon pairs relying on zero FSS [16] has called for the preparation of QD systems with low FSS. Using (111) substrates for the growth of InAs QDs reduced both structural asymmetry and piezoelectric contribution [17]. Another attempt involved strain-free GaAs/AlGaAs QDs with zero piezoelectric field, which, however, still exhibited a finite FSS due to structural elongation [5,18]. Postgrowth annealing of InAs QDs allowed one to decrease FSS from 96 μeV to a mere 6 μeV [19] or even to invert the bright exciton levels with the minimum FSS value of 4 μeV [20] (which might be underestimated, though, as the rotation of the polarization upon the levels anticrossing was disregarded). Another class of approaches is based on in-operation tuning, where the originally large value of FSS is reduced by applying the external field: electric [21,22], magnetic [2,23], or strain. The external strain field allowed one to reach FSS below experimental resolution in GaAs/AlGaAs QDs [24,25]; the simultaneous application of electric field allowed for a more powerful symmetry restoration and rather universal recovery of low FSS [26]. The experimental generation of polarization-entangled photon pairs in low-FSS QDs has been reported [27–31]. FSS has also been studied in QDs emitting at infrared telecommunication wavelengths [32–36].

Various effects contributing to the FSS can be divided into two classes based on the involved length scale: atomic and macroscopic. Atomic-scale effects are connected with the irregularities of the crystal lattice such as the interfaces, particular elements distribution in alloys [37], charged defects [38], etc. The magnitude of these effects is still the subject of investigation; the atomistic simulations based on the tight-binding method [39] predict considerably larger values than those relying on the empirical pseudopotential method [40]. In general, atomic-scale effects are weak compared to those on macroscale. For example, the magnitudes of about 1 μeV are reported for a specific alloy distribution in the AlGaAs barrier [37] of GaAs QDs. The effect is more pronounced when the dot material is an alloy, which should therefore be avoided when aiming at low FSS. A lower bound of several μeV was predicted for strain-tuned FSS in ternary $In_{0.6}Ga_{0.4}As$ QDs [41]. By macroscopic scale we mean for the purpose of the foregoing discussion that the characteristic length of the effect is comparable with the dimensions of a QD and the underlying crystal lattice is perceived as a homogeneous environment. Thus, the crystal symmetry is no longer relevant and the finite

*vlastimil.krapek@ceitec.vutbr.cz

values of FSS are now related to the symmetry lower than C_4, i.e., to the lateral elongation of the wave functions (e.g., envelope functions of the $\mathbf{k}\cdot\mathbf{p}$ theory). Principal contributions to the FSS on macroscopic scale arise from the asymmetric (elongated) shape of a QD and piezoelectric field. Further, it is possible to use the external strain field to induce the anisotropic effective mass tensor and modify the elongation of the hole wave functions and the related value of FSS [24].

Further information is contained in the polarization properties of the exciton doublet. Simple considerations assuming a purely heavy-hole exciton in an elliptic-disk-shaped QD [6] predicted a linear polarization of both transitions with the low-energy component polarized parallel with the long QD axis and the high-energy component having the orthogonal polarization. Typically, both structural-elongation and piezoelectric axes are parallel with the crystal axes [110] and $[1\bar{1}0]$, and so are the polarizations of both components. However, in some structures with shallow irregular confinement potential, such as quantum well thickness fluctuations, stochastic polarization directions were observed [5]. Further, when the light-hole contribution to the exciton ground state becomes important, the polarization orthogonality of both components is lost [24,42]. Thus, the definition of FSS as the difference between the exciton emission energies at [110] and $[1\bar{1}0]$ is not always correct, although it is widely used [14,20].

We focus here on QDs with type-II confinement, in which one type of charge carrier is confined in QD volume and the other in the barrier close to the QD vicinity. Possible inner/outer material combinations leading to the type-II confinement include InAs/GaAsSb and InP/GaInP with electrons bound in the inner material, and InP/GaP, GaSb/GaAs, or Ge/Si with holes bound in the inner material. In II-VI core/shell nanocrystals, electrons are confined in the core for CdTe/CdSe and holes for ZnSe/CdTe material combination [43]. The characteristic properties of type-II QDs are often discussed in the context of future applications. The radiative lifetime of excitations is tunable and can reach values considerably larger than in type I [44,45], which is exploited in QD flash memories [46,47]. In solar cells, QDs are used to enhance the infrared spectral response; the type-II QDs allow for an easier charge extraction due to their larger electron-hole separation [48,49].

The energies of excitons and excitonic complexes in type-II QDs have been frequently studied experimentally [50–54] and theoretically [55–63]. Those works focused on the energy scale above several meV (such as transition or binding energies). The excitonic FSS in type-II QDs has not been addressed so far.

The particular system of interest is InAs QDs with a thin $GaAs_{1-y}Sb_y$ overlayer embedded in GaAs [64–81]. One reason for selecting this material system is the possibility to induce a smooth crossover between type-I and type-II confinement regimes simply by changing y; the crossover values between 0.14 and 0.18 have been reported [65–67]. The other is that it belongs to systems with *holes* bound outside. Owing to their large effective mass the holes are more susceptible to the local potential profile or external perturbations, offering a larger potential for tuning their wave functions and the related FSS. The photoluminescence of $GaAs_{1-y}Sb_y$ capped QDs is rather intense [68,69] despite the type-II confinement with the radiative lifetimes as low as 10 ns [70,71]. The strain-reducing effect of the $GaAs_{1-y}Sb_y$ layer together with the surfacting effect of antimony allow one to increase the emission wavelengths of standard InAs QDs and reach the telecommunication wavelengths of 1.3 and 1.55 μm [72–74]. Various shapes of $GaAs_{1-y}Sb_y$ QDs have been reported, including a lens [75,76,82] or a pyramid with a graded In concentration [77]. Notably, the hole wave function is expected to be composed of two segments localized in the minima of the piezoelectric potential [66].

In this work we present a theoretical study of excitonic fine structure splitting of InAs QDs with $GaAs_{1-y}Sb_y$ overlayer. We propose a method to tune the FSS by setting the thickness of the $GaAs_{1-y}Sb_y$ layer. The values comparable with the natural linewidth can be achieved. The paper is organized as follows: In Sec. II a theory of FSS is described. To gain a qualitative understanding of the relations between the wave functions and FSS we discuss in Sec. III a simplified single-band model with Gaussian wave functions. The full calculations are presented in Sec. IV. We summarize and conclude in Sec. V.

II. THEORY

The single-particle states were calculated within the eight-band $\mathbf{k}\cdot\mathbf{p}$ theory [83,84], in which the wave functions are expanded into products of periodic parts of Bloch functions u_b in the Γ point and corresponding envelope functions χ_b,

$$\psi(\mathbf{r}) = \sum_{b\in\{x,y,z,s\}\otimes\{\uparrow,\downarrow\}} u_b(\mathbf{r})\chi_b(\mathbf{r}). \tag{1}$$

In this equation b is the band index, the bands x, y, z correspond to the valence band Bloch waves which are antisymmetric with respect to the corresponding mirror plane, and s corresponds to the conduction band Bloch wave. Following usual conventions, z denotes the growth direction. The calculations include the effects of the elastic strain via the Pikus-Bir Hamiltonian [85] and the piezoelectric field. The numeric simulations were performed with Nextnano 3D [86], which employs the finite difference method. The simulation space was discretized with a step of 1 nm. Material parameters were taken from the Nextnano database and they are also listed in the Supplementary material of Ref. [66].

Once the single-particle states are calculated, it is convenient to use them as a basis for the exciton state $|X\rangle$. First the Slater determinants $|X(ci,vj)\rangle = c^\dagger_{ci}c_{vj}|0\rangle$ are formed, where $|0\rangle$ is Fermi vacuum state (empty quantum dot), $c^\dagger_{ci}$ creates an electron in the ith conduction state, and c_{vj} annihilates an electron in the jth valence state; the corresponding single-particle wave functions are denoted ψ_{ci} and ψ_{vj}, respectively. For the calculations of FSS we used four Slater determinants formed from the ground hole and electron states. Following Ref. [6] [Eq. (2.3)] the exciton Hamiltonian matrix elements read

$$\begin{aligned}&\langle X(ci,vj)|\hat{H}|X(ck,vl)\rangle\\ &\quad = (E_i - E_j)\delta_{ik}\delta_{jl} + C(ci,vj,ck,vl) + EX(ci,vj,ck,vl),\end{aligned}$$

where E_i is the energy of the ith single-particle state, C represents the direct Coulomb interaction, and EX represents the exchange interaction.

Defining

$$S_{c,v}(\mathbf{r}) = \sum_{b\in\{s,x,y,z\}\otimes\{\uparrow,\downarrow\}} \chi^*_{c,b}(\mathbf{r})\chi_{v,b}(\mathbf{r})$$

and vector $\mathbf{T}$ with the components

$$T^x_{c,v}(\mathbf{r}) = \frac{P}{E_g}\sum_{\sigma\in\uparrow,\downarrow}[\chi^*_{c,s\sigma}(\mathbf{r})\chi_{v,x\sigma}(\mathbf{r}) + \chi^*_{c,x\sigma}(\mathbf{r})\chi_{v,s\sigma}(\mathbf{r})]$$

and T^y, T^z defined analogously (E_g is the fundamental band gap and P is one of the Kane's parameters related to the nonvanishing coordinate matrix elements $\langle x|x|s\rangle = P/E_g$), we can write

$$C(c1,v1;c2,v2) = -\frac{e^2}{4\pi\varepsilon}\int d\mathbf{r}_1\int d\mathbf{r}_2\frac{1}{|\mathbf{r}_1-\mathbf{r}_2|} \times S_{c1,c2}(\mathbf{r}_1)S_{v2,v1}(\mathbf{r}_2)$$

(e denotes the elementary charge and ε the dielectric function). The exchange Coulomb interaction term EX can be expressed as a sum of the following three terms:

$$EX_0(c1,v1;c2,v2) = \frac{e^2}{4\pi\varepsilon}\int d\mathbf{r}_1\int d\mathbf{r}_2\frac{1}{|\mathbf{r}_{12}|}S_{c1,v1}(\mathbf{r}_1)S_{v2,c2}(\mathbf{r}_2), \quad (2)$$

$$EX_1(c1,v1;c2,v2) = \frac{e^2}{4\pi\varepsilon}\int d\mathbf{r}_1\int d\mathbf{r}_2\frac{1}{|\mathbf{r}_{12}|^3}\mathbf{r}_{12}\cdot[S_{v2,c2}(\mathbf{r}_2)\mathbf{T}_{c1,v1}(\mathbf{r}_1) - S_{c1,v1}(\mathbf{r}_1)\mathbf{T}_{v2,c2}(\mathbf{r}_2)], \quad (3)$$

and

$$EX_2(c1,v1;c2,v2) = \frac{e^2}{4\pi\varepsilon}\int d\mathbf{r}_1\int d\mathbf{r}_2\frac{1}{|\mathbf{r}_{12}|^5}\sum_{\alpha,\beta\in x,y,z}\sum T^{(\alpha)}_{c1,v1}(\mathbf{r}_1)T^{(\beta)}_{v2,c2}(\mathbf{r}_2) \times\left[\delta_{\alpha\beta}|\mathbf{r}_{12}|^2 - 3r^\alpha_{12}r^\beta_{12}\right], \quad (4)$$

where $\mathbf{r}_{12} = \mathbf{r}_1 - \mathbf{r}_2$ and $\delta_{\alpha\beta}$ is the Kronecker delta. We note that S is nonzero only when the mixing of valence and conduction bands is taken into account. Thus, only the third term of the multipole expansion, Eq. (4), contributes to the FSS when this mixing is neglected, e.g., when single-band or six-band [87] $\mathbf{k}\cdot\mathbf{p}$ theory is used to obtain the wave function of individual particles. However, as the scaling of the terms with the linear extension of the wave function L goes as $EX_0 \sim 1/L$, $EX_1 \sim 1/L^2$, $EX_2 \sim 1/L^3$, the low-order terms are important, in particular, in larger QDs.

III. MODEL OF GAUSSIAN WAVE FUNCTIONS

Before treating realistic quantum dots with the full-complexity model, it is worth providing an intuitive understanding of the relation between the shape of the excitonic wave function and the value of FSS. To this end we employed a simplified model with the exciton composed of a single Slater determinant, no band mixing, and the electron and hole densities having the form of three-dimensional Gaussian functions. The electron and hole envelope functions read

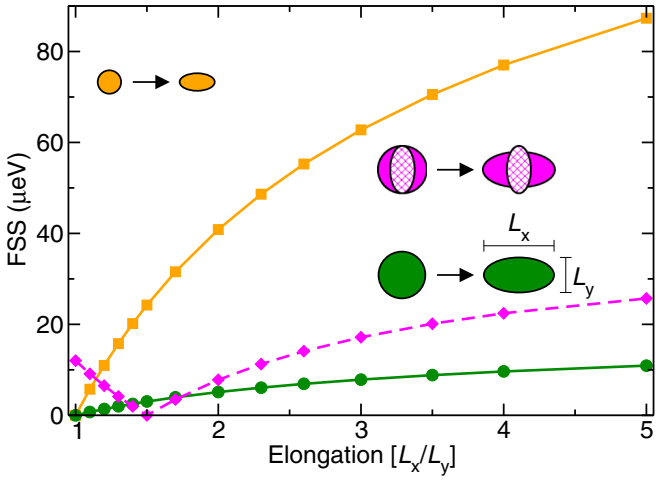

FIG. 1. (Color online) FSS as a function of the lateral elongation of the wave functions, defined as $E_w = L_x/L_y$. Orange line: A smaller dot with the extension parameters $L_x \times L_y = 25$ nm^2, $L_z = 2$ nm. The lateral extensions are varied preserving the value of their product (and thus the volume and vertical aspect ratio of a QD). Electron and hole wave functions have the same extensions and are elongated equally. Green line: A larger dot with the extensions twice larger than for the smaller dot, i.e., $L_x \times L_y = 100$ nm^2, $L_z = 4$ nm. Magenta line: A smaller dot, $L_x \times L_y = 25$ nm^2, $L_z = 2$ nm, with opposite electron and hole elongation. For electrons, E_w has a constant value of 2/3. For holes, E_w is varied and FSS is displayed as a function of the hole elongation. Insets: The insets schematically depict the wave functions. Hatched magenta ellipses correspond to the electron wave functions.

(normalization constant omitted for simplicity)

$$\chi_{e,h}(\mathbf{r}) \propto \sqrt{\exp\left[-\frac{(x-x_0)^2}{L_x^2} - \frac{(y-y_0)^2}{L_y^2} - \frac{(z-z_0)^2}{L_z^2}\right]},$$

where $L_{x,y,z}$ determine the spatial extensions of a particle and x_0, y_0, z_0 are the coordinates of its center. As the band mixing is neglected in the model, only the dipole-dipole exchange term [Eq. (4)] contributes to the FSS.

A crucial parameter for FSS is the lateral elongation of the envelope functions defined as $E_w = L_x/L_y$. It follows directly from Eq. (4) that for nonelongated envelope functions ($L_x = L_y$) FSS acquires a zero value. The dependence of the FSS on the elongation is shown in Fig. 1. In order to isolate the effect of the elongation and avoid unintentional variation of other parameters, we preserved the volume and the effective vertical aspect ratio of the model dots, i.e, values of L_z and the product $L_x \times L_y$ were kept constant. First, we assumed the same envelope function for both electrons and holes (orange and green lines). Such case corresponds, e.g., to strain-free GaAs/AlGaAs dots [88]. FSS exhibits a monotonically increasing concave dependence on the lateral elongation E_w. To demonstrate the effect of the QD volume, we show FSS for a smaller dot (extension parameters $L_x \times L_y = 25$ nm^2, $L_z = 2$ nm) and a larger dot with two-times larger dimensions (e.g., eight-times larger volume). The values of FSS for a larger QD are exactly eight times smaller. The inverse proportionality of FSS to the QD volume or to the third power of a characteristic linear dimension L can be directly inferred from Eq. (4).

With the band mixing taken into account, additional terms proportional to $1/L$ and $1/L^2$ emerge. However, the $1/L^3$ or $1/V$ scaling law (V representing a volume of the QD) has been recently demonstrated experimentally in realistic strain-free GaAs/AlGaAs QDs [15]. FSS values exceed the natural linewidth of the exciton recombination lines (up to units of μeV) even for a modest elongation. For example, for $E_w = 1.2$ we predict FSS of 11 μeV (1.4 μeV) in the smaller (larger) QD. We note that for the QDs studied in Ref. [15] we found the values of $L_x \times L_y$ between 11 and 36 nm^2 and L_z between 1 and 2 nm. The smaller dot case thus corresponds well to realistic GaAs/AlGaAs QDs.

Next, we introduce an important concept of the compensated elongation. For a suitable exciton wave function shape, FSS can attain a zero value even in the system that lacks the required symmetry C_{4v}. We consider the electron envelope function to be elongated in the direction perpendicular to the elongation of the hole envelope function, $E_{we} = 2/3$ (the subscripts e and h are used, when required, to distinguish the parameters of electrons and holes, respectively). The extension parameters correspond to the smaller dot: $L_x \times L_y = 25$ nm^2, $L_z = 2$ nm. FSS is plotted as a function of the hole elongation $E_{wh} \geqslant 1$ in Fig. 1 (magenta line). The prominent feature of the dependence is the zero-value minimum at $E_{wh} = 3/2$ (i.e., the inverse of the electron elongation. Intuitively, this can be described as the mutual compensation of both electron and hole elongations. The integral in Eq. (4) attains a zero value, which is, however, not related to the symmetry. In realistic QDs, the condition of the inverse elongation does not hold (due to band mixing or different volume of the envelope function of electrons and holes) but the effect is preserved. The minimum value of FSS can be larger than zero in case of QDs with the irregular shape. The effect of the compensated elongation has already been demonstrated experimentally utilizing the anisotropic external strain to vary the elongation of the hole envelope function [24]. In the following we will demonstrate that the elongation of the hole envelope function can be efficiently varied in type-II InAs QDs with GaAsSb capping layer.

The transition between type-I and type-II confinement in $GaAs_{1-y}Sb_y$ capped QDs is accompanied by the splitting of the hole wave function into two segments [66], evenly spread along the central electron wave function in QDs with a sufficient symmetry [Figs. 6(b) and 6(c)]. The behavior of FSS under such transition is shown in Fig. 2. When the segments are shifted from the central position along their long axis (orange line), small shifts effectively enhance the hole elongation and consequently the FSS. For larger shifts the wave function disintegrates; now the effect of increased distance of electron and hole prevails resulting into a decrease of FSS. The same behavior is predicted for nonelongated wave functions (green line), where the FSS dependence starts at a zero value, increases as the holes become effectively elongated, and decreases when the separation effects prevail. When the segments are shifted along their short axis, the effective elongation of the holes decreases as the segments are separated, and so happens with FSS. Depending on the magnitude of the original elongation, two possibilities exist: (1) The hole eventually becomes elongated in opposite direction (magenta line; note the magenta insets of Fig. 2 schematically depicting the change in the elongation direction). FSS goes through a zero value and starts to increase again. Finally, the separation effects prevail and FSS decreases. (2) When the original elongation is large, the hole disintegrates before the elongation direction is changed (maroon line). In such case a monotonously decreasing dependence of FSS on the segment distance is observed, governed first by the decrease of the effective elongation and then by the separation effects.

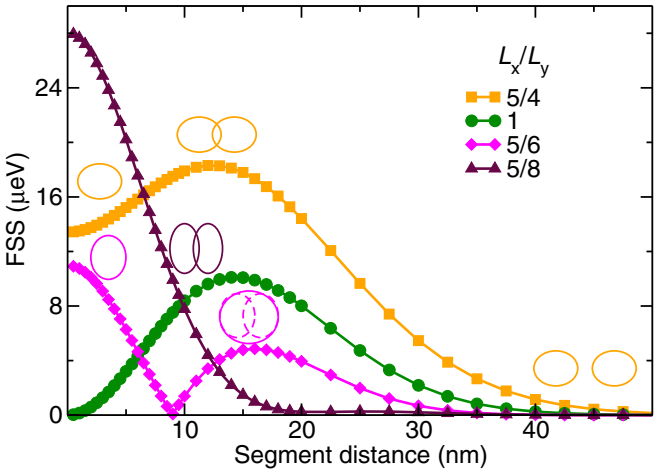

FIG. 2. (Color online) FSS for a hole wave function composed of two segments. The extensions of both electron and hole wave functions fulfill $L_x \times L_y = 25$ nm^2, $L_z = 2$ nm, with the lateral elongation $E_w = L_x/L_y$ of 5/4 (orange line, squares), 1 (green line, circles), 5/6 (magenta line, diamonds), and 5/8 (maroon line, triangles). The electron wave function is composed of a single Gaussian ($x_0 = 0$) while the hole wave function is split along x into two identical Gaussian segments evenly positioned around the central electron wave function ($x_0 = \pm d/2$, d being the segment distance). FSS is plotted as a function of the distance between the centers of the segments. Insets schematically depict the position and shape of the segments.

In strongly asymmetric QDs the minima in confinement potential corresponding to both segments can differ considerably and a single-segment hole wave function displaced from the central electron wave function can be formed. In such case there is no effective change in the elongation and the separation effect leads to a monotonous decrease of FSS (not shown).

IV. REALISTIC QUANTUM DOTS

We will now focus on realistic InAs QDs with a $GaAs_{1-y}Sb_y$ capping layer. We will show that FSS in such structures can be tuned by the thickness of the $GaAs_{1-y}Sb_y$ layer. Three QD geometries will be considered here, denoted as pyramidal, symmetric lens shaped, and elongated lens shaped. The *pyramidal* QD is adopted from Ref. [77] and has the shape of a pyramid with the base length of 22 nm, height of 8 nm, and the trumpet indium composition profile within the pyramid (see Ref. [77] for details). For the other structures we assume QDs composed of pure InAs. The *symmetric lens-shaped* QD motivated by Refs. [75,82] is modeled as a top of a sphere with the base radius of 8 nm and the height of 4 nm. A prominent form of the lateral asymmetry of QDs is their structural elongation. So far no elongation was reported for InAs QDs

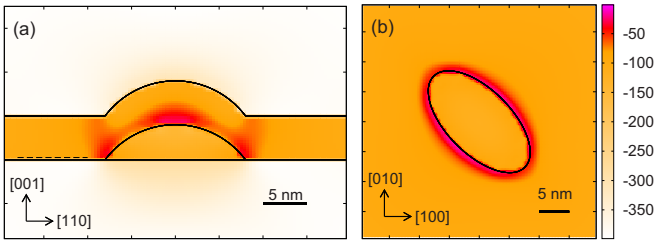

FIG. 3. (Color online) *Effective* confinement potential (color bar scale in meV) without the contribution of the piezoelectric field for holes in the *lens-shaped* QD. (a) $E_s = 1$, plane $(1\bar{1}0)$ through the QD center; (b) $E_s = 2$, plane (001) just above the QD base [the vertical position is shown in panel (a) by a dashed line]. Boundaries between different materials are schematically depicted. The potential is given from the electron view; the holes are confined near the largest values represented by the red/orange spots.

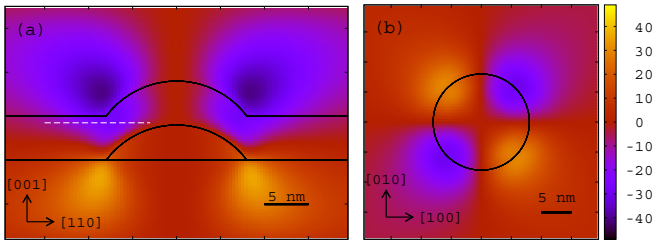

FIG. 4. (Color online) Piezoelectric potential (color bar scale in meV) for the *symmetric lens-shaped* QD. (a) plane $(1\bar{1}0)$ through the QD center; (b) plane (001) just above the top of the QD [i.e., above the horizontal nodal plane; the vertical position is shown in panel (a) by a white dashed line].

with $GaAs_{1-y}Sb_y$ overlayer, which is in striking contrast with InAs QDs capped by pure GaAs [89,90]. This can be attributed to the surfacting effect of antimony but it is also possible that the elongation has been overlooked as the methods involved in experimental studies were insensitive to it. Therefore, we consider in our study also the possibility that QDs are elongated. In accordance with GaAs capped InAs QDs [90,91] we select the direction $[1\bar{1}0]$ as the main elongation axis and quantify the elongation by the ratio of characteristic lateral dimensions along $[1\bar{1}0]$ and [110], denoted as E_s in the following (the subscript s is used to differentiate the structural elongation from the wave-function elongation used in the previous section). The *elongated lens-shaped* QDs are formed from the lens-shaped dot by its stretching along $[1\bar{1}0]$ and compressing along [110] by the same factor so that the QD volume and height are preserved; the radii for $E_s = 2$ read 11.3 and 5.65 nm, etc. All QDs are capped with the $GaAs_{0.8}Sb_{0.2}$ layer of a certain thickness and further embedded in GaAs. Our choice of the Sb content is similar to the values reported in experiments [71,77,78] and was motivated by its proximity to the crossover between the type-I and type-II confinement which allows one to adjust the type of confinement by selecting a proper thickness of the $GaAs_{1-y}Sb_y$ layer.

The shape of the wave functions is closely connected with the confinement potential, which is contributed by the band-edge offsets, strain field, and piezoelectric potential. Here, we visualize the confinement by the *effective* potential constructed from the eigenvalues of the pointwise diagonalized Hamiltonian (terms containing the spatial derivatives are discarded and the Hamiltonian is then diagonalized at each point of the simulation grid). In contrast with the standard confinement potential entering the Schrödinger equation, the *effective* potential involves the strain-induced band mixing.

The hole *effective* potentials in all type-II QDs discussed further in the paper exhibit qualitatively similar features. We will present them for the *lens-shaped* QD with the GaAsSb layer thickness of 5 nm and with the elongation E_s of either 1 or 2. Figure 3 shows the potential profile without the piezoelectric contribution. The potential is given from the electron view; the largest values correspond to the minima of the hole confinement. Zero energy is set to the valence band edge of bulk unstrained InAs. Two local minima of the hole confinement potential are formed in the GaAsSb layer along the sides of the QD and above its top [Fig. 3(a)]. The top minimum is of the light-hole character and therefore penalized by the quantum confinement. The ground hole state will be localized in the side minimum which forms a ring around the QD [Fig. 3(b)], in which weak variations of the potential are present with two rather shallow absolute minima along the long QD side (i.e., in [110] direction from the QD center). Depending on the magnitude of these variations, the wave function might form a ring or be split into two segments.

The piezoelectric field has an octopole shape, shown in Fig. 4. Its contribution is rather important as its magnitude of about 50 meV is comparable to the variations of the rest of the confinement potential inside the $GaAs_{1-y}Sb_y$ layer. The horizontal nodal plane of the piezoelectric octopole lies close to the side minimum of the confinement potential. The piezoelectric potential therefore tends to split the wave function of the holes in the side minimum into two segments situated along [110] below the nodal plane or along $[1\bar{1}0]$ above the nodal plane.

The total *effective* confinement potential is shown in Fig. 5. The following shapes of the hole wave function are possible: (i) inside a QD (type I), (ii) a ringlike shape along the QD when the piezoelectric field is too weak to localize the holes in its minima, (iii) two segments at the dot base situated along [110] [Figs. 5(a) and 5(c)], and (iv) two segments at the QD sides above the piezoelectric nodal plane situated along $[1\bar{1}0]$ due to the piezoelectric field [Fig. 5(b)] or along [110] when the structural elongation along $[1\bar{1}0]$ prevails [Fig. 5(d) is close to that case]. In pyramidal QDs with the trumpet In composition profile, both the side minimum of the confinement potential and the piezoelectric octopole are shifted up towards the region of large In content. In short, there is a rich variety of the hole wave-function shapes. Variation of the parameters such as the thickness or the composition of the GaAsSb layer are supposed to induce transitions between those shapes. For example, switching between the deep narrow minima below the nodal plane [Figs. 5(a) and 5(c)] and shallow broad minima above the nodal plane [Figs. 5(b) and 5(d)] shall be achievable. Considering the effect of the compensated elongation, this results in nontrivial dependences of FSS on structural parameters and opens an interesting prospect for the tuning of FSS.

Figure 6(d) shows the dependence of FSS on the thickness of the $GaAs_{1-y}Sb_y$ layer in two *lens-shaped* QDs: *symmetric*

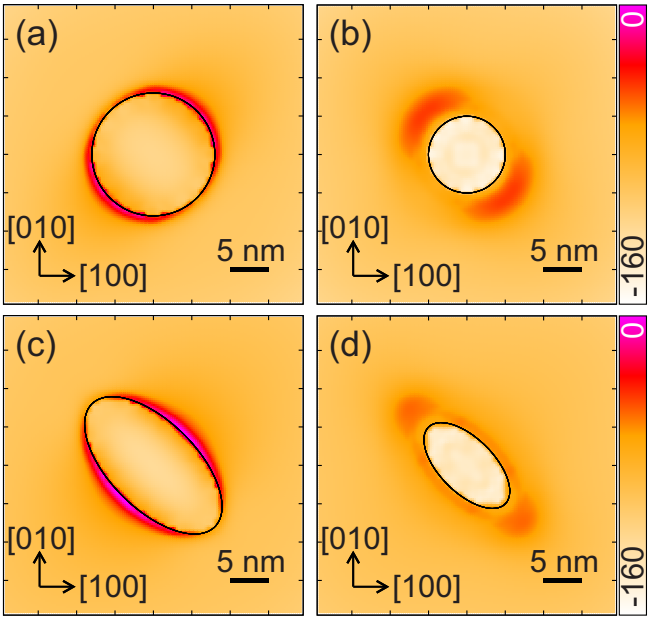

FIG. 5. (Color online) Total *effective* confinement potential (color bar scale in meV) including the contribution of the piezoelectric field for holes in the *lens-shaped* QD. (a), (c) Plane (001) below the nodal plane of the piezoelectric potential (just above the QD base), $E_s = 1$ (a) and 2 (c). (b), (d) Plane (001) above the nodal plane of the piezoelectric potential (3 nm above the QD base), $E_s = 1$ (b) and 2 (d). Black circles and ellipses display the QD boundary at respective heights. The potential is given from the electron view; the holes are confined near the largest values represented by the red/orange spots.

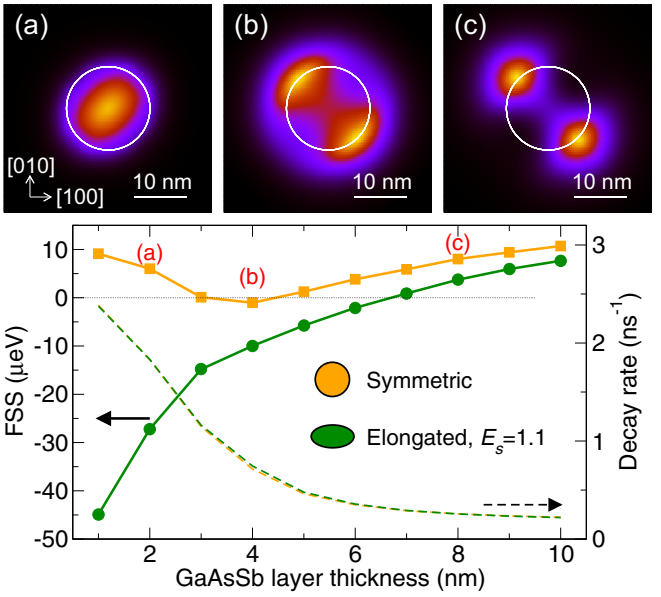

FIG. 6. (Color online) (a)–(c) Planar probability density of the hole ground state in the *symmetric lens-shaped* QD (height 4 nm, radius 8 nm), plane (001) (integrated over [001]) for the $GaAs_{0.8}Sb_{0.2}$ layer thickness of (a) 2 nm, (b) 4 nm, and (c) 8 cm. The QD boundary at the base height is displayed with the white line. (d) FSS (thick solid lines with symbols, left) and exciton radiative decay rate (thin dashed lines) between the ground electron and hole state in the *symmetric lens-shaped* QD (orange) and the *elongated lens-shaped* QD with $E_s = 1.1$ (green) as functions of the GaAsSb layer thickness. The polarization of the lower exciton component is encoded into the sign of FSS: positive/negative sign corresponds to the polarization along $[110]/[1\bar{1}0]$, respectively. The red labels denote the points corresponding to the maps of the probability density.

and weakly elongated ($E_s = 1.1$). We exploit the fact that the excitons in our model exhibit only two well-defined polarizations and encode the polarization of the lower exciton component into the sign of the FSS. In this way, the level crossing is better visible. We will first discuss the case of the symmetric QD. The electron wave function is weakly elongated in the $[1\bar{1}0]$ direction and as it resides within the QD, its variation with the thickness of the $GaAs_{1-y}Sb_y$ layer is negligible. For a thin $GaAs_{1-y}Sb_y$ layer (up to 3 nm) the ground hole wave function resides inside the QD, too. It experiences the bottom part of the piezoelectric octopole and is thus elongated in [110], as shown in Fig. 6(a). The polarization of the lower exciton component is [110]. With increasing thickness a hole ground state gradually shifts into the $GaAs_{1-y}Sb_y$ layer and also slightly upwards (for about 1.3 nm for the full range of thicknesses). Consequently, it becomes split by the upper part of the piezoelectric octopole into two segments along $[1\bar{1}0]$. For the thickness interval between 3 and 5 nm, the segmented wave function behaves as effectively elongated in $[1\bar{1}0]$ [Fig. 6(b)] and the lower exciton component is also polarized along $[1\bar{1}0]$. For the thickness values above 5 nm, the segments are well separated and the elongation of each segment in [110] determines the character of the wave function. The lower exciton component is again polarized along [110]. Thus, we distinguish three regions of different exciton polarization. At each of the two transitions between those regions, exciton levels cross and FSS is reduced to zero. We note that minimum values obtained in our calculations are nonzero due to the finite step in the thickness dependence and read 0.1 and 1 μeV for the first and second transition, respectively. The observed behavior of FSS corresponds well to the qualitative prediction of the model of Gaussian function for $L_x/L_y = 5/6$ (cf. Fig. 2, magenta line).

Similar behavior is observed in a lens-shaped QD weakly elongated in $[1\bar{1}0]$ [Fig. 6(d), green lines]. The first region is now missing, as the elongation of the hole wave function within the QD volume (for a thin $GaAs_{1-y}Sb_y$ layer) is now $[1\bar{1}0]$ because the structural elongation dominates over the piezoelectric contribution. The zero FSS is reached for a $GaAs_{1-y}Sb_y$ layer thickness of 7 nm. Figure 7 shows the FSS dependence on the thickness of the $GaAs_{1-y}Sb_y$ layer in a *pyramidal* QD with the trumpet profile (height of 8 nm and base size of 22 nm). As in the case of the lens-shaped QDs, the hole wave function changes its effective elongation during the crossover between the type-I and type-II confinement and in turn, exciton levels cross and FSS is reduced towards zero. Thus, variations of the $GaAs_{1-y}Sb_y$ layer thickness present a universal approach to tune and reduce FSS. For a typical lifetime of InAs QDs of 1 ns, the natural linewidth of the exciton recombination is 4 μeV; experimentally predicted spectral linewidth approaches 100 μeV [92]. Both values are larger than the minimum accessible values predicted here for the $GaAs_{1-y}Sb_y$ capped QDs.

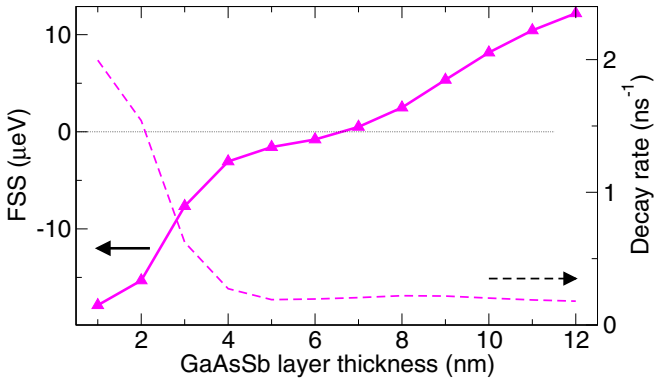

FIG. 7. (Color online) FSS (thick solid line with symbols, left) and exciton radiative decay rate (thin dashed line) between the ground electron and hole state in the pyramid-shaped QD as functions of the GaAsSb layer thickness. The polarization of the lower exciton component is encoded into the sign of FSS: positive/negative sign corresponds to the polarization along [110]/[1$\bar{1}$0], respectively.

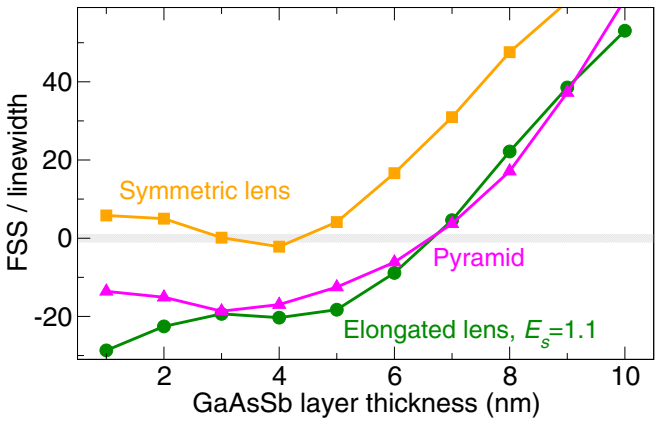

FIG. 8. (Color online) FSS divided by the natural spectral linewidth of exciton transitions between the ground electron and hole state in the *symmetric lens-shaped* QD (orange), the *elongated lens-shaped* QD with $E_s = 1.1$ (green), and the *pyramid-shaped* QD (magenta) as functions of the GaAsSb layer thickness. The polarization of the lower exciton component is encoded into the sign of FSS: positive/negative sign corresponds to the polarization along [110]/[1$\bar{1}$0], respectively.

We note that due to the idealized QD shapes considered in the study the exciton levels exhibit crossing, i.e., FSS goes through zero and the polarizations of the transitions are changed abruptly. In realistic QDs, which are always somewhat irregular, exciton levels undergo anticrossing with a nonzero minimum FSS and smooth polarization variations. We do not address this issue here as no experimental data related to the irregularities is available. The interested reader is referred to a detailed discussion [93] and studies of different QD systems [24,37].

Finally we argue that $GaAs_{1-y}Sb_y$ capped InAs QDs can be good emitters even in the type-II confinement regime. There is experimental evidence of intense photoluminescence from the $GaAs_{1-y}Sb_y$ capped InAs QDs [70], about four times weaker than for the reference type-I sample and about three times stronger after rapid thermal annealing. Roughly 15-times higher exciton lifetime has been reported (0.7 ns in type I compared to 11.2 ns in type II) [70]. We support these observations with the calculations of the exciton radiative decay rate γ_R shown in Figs. 6(d) and 7. The radiative exciton lifetime $\tau_R = \gamma_R^{-1}$ reads [94]

$$\tau_R^{-1} = \frac{e^2 n_r E_X}{\pi m_0^2 \varepsilon_0 \hbar^2 c^3} \sum_{\mathbf{e}} |\langle 0|\mathbf{e}\cdot\hat{\mathbf{p}}|X\rangle|^2,$$

where e is the elementary charge, n_r is the refractive index (a square root of the relative permittivity given in Ref. [66]), E_X is the exciton energy, m_0 is the free electron mass, $\hbar$ is the Planck constant, c is the speed of light, $|X\rangle$ and $|0\rangle$ denote the exciton and vacuum wave function, respectively, $\hat{\mathbf{p}}$ is the momentum operator, $\mathbf{e}$ is the polarization vector, and the summation goes over three independent polarizations. Typical calculated lifetimes for type-I QDs are in the range 0.4–0.5 ns. The values corresponding to the minima of FSS are 0.9 and 2.2 ns for the *symmetric lens-shaped* QD, 3.4 ns for the *elongated lens-shaped* QD, and 4.8 ns for the *pyramidal* QD. The comparison with the experimental values suggests that the theoretical values might be somewhat underestimated but the trends shall be reproduced. Thus, roughly twice to ten-times higher exciton lifetime as compared to type-I QDs is expected. For this reason we are convinced that the extraction of individual photons from individual $GaAs_{1-y}Sb_y$ capped QDs will be experimentally feasible.

The natural linewidth of the exciton transitions is $\hbar/\tau_R$. The increase of the lifetime in type-II structures therefore results in narrower transitions. For the generation of entangled photon pairs the FSS needs to be compared with the spectral linewidth. The FSS divided by the spectral linewidth for all previously considered QDs is shown in Fig. 8. The gray-shaded rectangle highlights the area of quasidegenerate exciton transitions (with the FSS lower than the spectral width), in which the generation of the entangled photon pairs is possible. As the area is rather narrow, a postgrowth selection of QDs or further tuning might be required to produce the polarization-entangled photon pairs.

V. CONCLUSIONS

In $GaAs_{1-y}Sb_y$ capped InAs QDs, lateral symmetry of the hole wave functions can be to a large extent influenced by the thickness of the $GaAs_{1-y}Sb_y$ layer. In particular, during the crossover between type-I and type-II confinement regimes, the hole wave function is shifted upwards across the nodal plane of the piezoelectric octopole, which is accompanied by the change of the direction of lateral elongation. Due to the mechanism of compensated elongation, a crossing of the bright exciton levels and a reduction of FSS to zero is predicted for certain thicknesses of the $GaAs_{1-y}Sb_y$ layer. Low natural FSS and efficient photoluminescence make the $GaAs_{1-y}Sb_y$ capped InAs QDs attractive as a possible source of entangled photon pairs.

ACKNOWLEDGMENTS

This work was supported by European Social Fund (Grant No. CZ.1.07/2.3.00/30.0005), European Regional Development Fund (Project No. CZ.1.05/1.1.00/02.0068),

Czech Science Foundation (Grant No. 15-21581S), Technology Agency of the Czech Republic (Grant No. TE01020233), and EU 7th Framework Programme (Contracts No. 286154—SYLICA and No. 280566—UnivSEM). P.K. was supported by the internal project MUNI/A/1496/2014.

[1] D. Gammon, E. S. Snow, B. V. Shanabrook, D. S. Katzer, and D. Park, Phys. Rev. Lett. **76**, 3005 (1996).
[2] M. Bayer, G. Ortner, O. Stern, A. Kuther, A. A. Gorbunov, A. Forchel, P. Hawrylak, S. Fafard, K. Hinzer, T. L. Reinecke *et al.*, Phys. Rev. B **65**, 195315 (2002).
[3] D. Kovalev, H. Heckler, G. Polisski, and F. Koch, Phys. Status Solidi B **215**, 871 (1999).
[4] V. D. Kulakovskii, G. Bacher, R. Weigand, T. Kümmell, A. Forchel, E. Borovitskaya, K. Leonardi, and D. Hommel, Phys. Rev. Lett. **82**, 1780 (1999).
[5] J. D. Plumhof, V. Křápek, L. Wang, A. Schliwa, D. Bimberg, A. Rastelli, and O. G. Schmidt, Phys. Rev. B **81**, 121309 (2010).
[6] T. Takagahara, Phys. Rev. B **62**, 16840 (2000).
[7] N. I. Cade, H. Gotoh, H. Kamada, H. Nakano, and H. Okamoto, Phys. Rev. B **73**, 115322 (2006).
[8] M. E. Ware, E. A. Stinaff, D. Gammon, M. F. Doty, A. S. Bracker, D. Gershoni, V. L. Korenev, S. C. Bădescu, Y. Lyanda-Geller, and T. L. Reinecke, Phys. Rev. Lett. **95**, 177403 (2005).
[9] M. Kroutvar, Y. Ducommun, D. Heiss, M. Bichler, D. Schuh, G. Abstreiter, and J. J. Finley, Nature (London) **432**, 81 (2004).
[10] T. Takagahara, Phys. Rev. B **60**, 2638 (1999).
[11] W. Langbein, R. Zimmermann, E. Runge, and J. Hvam, Phys. Status Solidi B **221**, 349 (2000).
[12] N. Accanto, F. Masia, I. Moreels, Z. Hens, W. Langbein, and P. Borri, ACS Nano **6**, 5227 (2012).
[13] F. Masia, N. Accanto, W. Langbein, and P. Borri, Phys. Rev. Lett. **108**, 087401 (2012).
[14] R. Seguin, A. Schliwa, S. Rodt, K. Pötschke, U. W. Pohl, and D. Bimberg, Phys. Rev. Lett. **95**, 257402 (2005).
[15] Y. H. Huo, V. Křápek, A. Rastelli, and O. G. Schmidt, Phys. Rev. B **90**, 041304 (2014).
[16] O. Benson, C. Santori, M. Pelton, and Y. Yamamoto, Phys. Rev. Lett. **84**, 2513 (2000).
[17] A. Schliwa, M. Winkelnkemper, A. Lochmann, E. Stock, and D. Bimberg, Phys. Rev. B **80**, 161307 (2009).
[18] M. Abbarchi, C. A. Mastrandrea, T. Kuroda, T. Mano, K. Sakoda, N. Koguchi, S. Sanguinetti, A. Vinattieri, and M. Gurioli, Phys. Rev. B **78**, 125321 (2008).
[19] W. Langbein, P. Borri, U. Woggon, V. Stavarache, D. Reuter, and A. D. Wieck, Phys. Rev. B **69**, 161301 (2004).
[20] R. J. Young, R. M. Stevenson, A. J. Shields, P. Atkinson, K. Cooper, D. A. Ritchie, K. M. Groom, A. I. Tartakovskii, and M. S. Skolnick, Phys. Rev. B **72**, 113305 (2005).
[21] B. D. Gerardot, S. Seidl, P. A. Dalgarno, R. J. Warburton, D. Granados, J. M. García, K. Kowalik, O. Krebs, K. Karrai, A. Badolato *et al.*, Appl. Phys. Lett. **90**, 041101 (2007).
[22] M. M. Vogel, S. M. Ulrich, R. Hafenbrak, P. Michler, L. Wang, A. Rastelli, and O. G. Schmidt, Appl. Phys. Lett. **91**, 051904 (2007).
[23] R. M. Stevenson, R. J. Young, P. See, D. G. Gevaux, K. Cooper, P. Atkinson, I. Farrer, D. A. Ritchie, and A. J. Shields, Phys. Rev. B **73**, 033306 (2006).
[24] J. D. Plumhof, V. Křápek, F. Ding, K. D. Jöns, R. Hafenbrak, P. Klenovský, A. Herklotz, K. Dörr, P. Michler, A. Rastelli *et al.*, Phys. Rev. B **83**, 121302 (2011).
[25] A. Rastelli, F. Ding, J. D. Plumhof, S. Kumar, R. Trotta, C. Deneke, A. Malachias, P. Atkinson, E. Zallo, T. Zander *et al.*, Phys. Status Solidi B **249**, 687 (2012).
[26] R. Trotta, E. Zallo, C. Ortix, P. Atkinson, J. D. Plumhof, J. van den Brink, A. Rastelli, and O. G. Schmidt, Phys. Rev. Lett. **109**, 147401 (2012).
[27] N. Akopian, N. H. Lindner, E. Poem, Y. Berlatzky, J. Avron, D. Gershoni, B. D. Gerardot, and P. M. Petroff, Phys. Rev. Lett. **96**, 130501 (2006).
[28] M. Ghali, K. Ohtani, Y. Ohno, and H. Ohno, Nat. Commun. **3**, 661 (2012).
[29] M. A. M. Versteegh, M. E. Reimer, K. D. Jöns, D. Dalacu, P. J. Poole, A. Gulinatti, A. Giudice, and V. Zwiller, Nat. Commun. **5**, 5298 (2014).
[30] T. Huber, A. Predojević, M. Khoshnegar, D. Dalacu, P. J. Poole, H. Majedi, and G. Weihs, Nano Lett. **14**, 7107 (2014).
[31] R. Trotta, J. S. Wildmann, E. Zallo, O. G. Schmidt, and A. Rastelli, Nano Lett. **14**, 3439 (2014).
[32] L. Sapienza, R. N. E. Malein, C. E. Kuklewicz, P. E. Kremer, K. Srinivasan, A. Griffiths, E. Clarke, M. Gong, R. J. Warburton, and B. D. Gerardot, Phys. Rev. B **88**, 155330 (2013).
[33] X. Liu, N. Ha, H. Nakajima, T. Mano, T. Kuroda, B. Urbaszek, H. Kumano, I. Suemune, Y. Sakuma, and K. Sakoda, Phys. Rev. B **90**, 081301 (2014).
[34] E. Goldmann, S. Barthel, M. Florian, K. Schuh, and F. Jahnke, Appl. Phys. Lett. **103**, 242102 (2013).
[35] A. I. Tartakovskii, M. N. Makhonin, I. R. Sellers, J. Cahill, A. D. Andreev, D. M. Whittaker, J.-P. R. Wells, A. M. Fox, D. J. Mowbray, M. S. Skolnick *et al.*, Phys. Rev. B **70**, 193303 (2004).
[36] A. I. Tartakovskii, R. S. Kolodka, H. Y. Liu, M. A. Migliorato, M. Hopkinson, M. N. Makhonin, D. J. Mowbray, and M. S. Skolnick, Appl. Phys. Lett. **88**, 131115 (2006).
[37] J.-W. Luo, R. Singh, A. Zunger, and G. Bester, Phys. Rev. B **86**, 161302 (2012).
[38] R. Singh and G. Bester, Phys. Rev. B **85**, 205405 (2012).
[39] M. Zieliński, Phys. Rev. B **88**, 155319 (2013).
[40] R. Singh and G. Bester, Phys. Rev. B **84**, 241402 (2011).
[41] R. Singh and G. Bester, Phys. Rev. Lett. **104**, 196803 (2010).
[42] J. D. Plumhof, R. Trotta, V. Křápek, E. Zallo, P. Atkinson, S. Kumar, A. Rastelli, and O. G. Schmidt, Phys. Rev. B **87**, 075311 (2013).
[43] S. Kim, B. Fisher, H.-J. Eisler, and M. Bawendi, J. Am. Chem. Soc. **125**, 11466 (2003).
[44] Y. Jang, T. Badcock, D. Mowbray, M. Skolnick, J. Park, D. Lee, H. Liu, M. Steer, and M. Hopkinson, Appl. Phys. Lett. **92**, 251905 (2008).
[45] L. P. Balet, S. A. Ivanov, A. Piryatinski, M. Achermann, and V. I. Klimov, Nano Lett. **4**, 1485 (2004).

[46] A. Marent, M. Geller, A. Schliwa, D. Feise, K. Pötschke, D. Bimberg, N. Akçay, and N. Öncan, Appl. Phys. Lett. **91**, 242109 (2007).

[47] M. Geller, A. Marent, T. Nowozin, D. Bimberg, N. Akçay, and N. Öncan, Appl. Phys. Lett. **92**, 092108 (2008).

[48] R. Laghumavarapu, A. Moscho, A. Khoshakhlagh, M. El-Emawy, L. Lester, and D. Huffaker, Appl. Phys. Lett. **90**, 173125 (2007).

[49] S. Itzhakov, H. Shen, S. Buhbut, H. Lin, and D. Oron, J. Phys. Chem. C **117**, 22203 (2013).

[50] K. Matsuda, S. V. Nair, H. E. Ruda, Y. Sugimoto, T. Saiki, and K. Yamaguchi, Appl. Phys. Lett. **90**, 013101 (2007).

[51] M. Nakaema, F. Iikawa, M. Brasil, E. Ribeiro, G. Medeiros-Ribeiro, W. Carvalho, Jr., M. Maialle, and M. Degani, Appl. Phys. Lett. **81**, 2743 (2002).

[52] M. Hayne, J. Maes, S. Bersier, V. V. Moshchalkov, A. Schliwa, L. Müller-Kirsch, C. Kapteyn, R. Heitz, and D. Bimberg, Appl. Phys. Lett. **82**, 4355 (2003).

[53] F. Iikawa, M. P. F. Godoy, M. K. K. Nakaema, M. J. S. P. Brasil, M. Z. Maialle, M. A. Degani, E. Ribeiro, G. Medeiros-Ribeiro, W. Carvalho, Jr., and J. A. Brum, Braz. J. Phys. **34**, 555 (2004).

[54] P. Klenovský, M. Brehm, V. Křápek, E. Lausecker, D. Munzar, F. Hackl, H. Steiner, T. Fromherz, G. Bauer, and J. Humlíček, Phys. Rev. B **86**, 115305 (2012).

[55] J. M. Rorison, Phys. Rev. B **48**, 4643 (1993).

[56] P. Lelong, K. Suzuki, G. Bastard, H. Sakaki, and Y. Arakawa, Physica E **7**, 393 (2000).

[57] K. L. Janssens, B. Partoens, and F. M. Peeters, Phys. Rev. B **66**, 075314 (2002).

[58] K. L. Janssens, B. Partoens, and F. M. Peeters, Phys. Rev. B **67**, 235325 (2003).

[59] M. P. F. de Godoy, P. F. Gomes, M. K. K. Nakaema, F. Iikawa, M. J. S. P. Brasil, R. A. Caetano, J. R. Madureira, J. R. R. Bortoleto, M. A. Cotta, E. Ribeiro *et al.*, Phys. Rev. B **73**, 033309 (2006).

[60] V. Mlinar, M. Tadić, and F. M. Peeters, Phys. Rev. B **73**, 235336 (2006).

[61] J. R. Madureira, M. P. de Godoy, M. Brasil, and F. Iikawa, Appl. Phys. Lett. **90**, 212105 (2007).

[62] A. Piryatinski, S. A. Ivanov, S. Tretiak, and V. I. Klimov, Nano Lett. **7**, 108 (2007).

[63] J. M. Miloszewski, S. Tomić, and D. Binks, J. Phys.: Conf. Ser. **526**, 012005 (2014).

[64] K. Akahane, N. Yamamoto, and N. Ohtani, Physica E **21**, 295 (2004).

[65] H. Y. Liu, M. J. Steer, T. J. Badcock, D. J. Mowbray, M. S. Skolnick, F. Suarez, J. S. Ng, M. Hopkinson, and J. P. R. David, J. Appl. Phys. **99**, 046104 (2006).

[66] P. Klenovský, V. Křápek, D. Munzar, and J. Humlíček, Appl. Phys. Lett. **97**, 203107 (2010).

[67] P. Klenovský, V. Křápek, D. Munzar, and J. Humlíček, J. Phys.: Conf. Ser. **245**, 012086 (2010).

[68] K. Akahane, N. Yamamoto, S. Gozu, and N. Ohtani, Physica E **26**, 395 (2005).

[69] H. Y. Liu, M. J. Steer, T. J. Badcock, D. J. Mowbray, M. S. Skolnick, P. Navaretti, K. M. Groom, M. Hopkinson, and R. A. Hogg, Appl. Phys. Lett. **86**, 143108 (2005).

[70] J. M. Ulloa, J. M. Llorens, B. Alén, D. F. Reyes, D. L. Sales, D. González, and A. Hierro, Appl. Phys. Lett. **101**, 253112 (2012).

[71] W.-S. Liu, H.-L. Tseng, and P.-C. Kuo, Opt. Express **22**, 18860 (2014).

[72] J. M. Ripalda, D. Granados, Y. González, A. M. Sánchez, S. I. Molina, and J. M. García, Appl. Phys. Lett. **87**, 202108 (2005).

[73] A. Hospodková, E. Hulicius, J. Pangrác, J. Oswald, J. Vyskočil, K. Kuldová, T. Šimeček, P. Hazdra, and O. Caha, J. Cryst. Growth **312**, 1383 (2010).

[74] M. Zíková, A. Hospodková, J. Pangrác, J. Oswald, P. Krčil, E. Hulicius, P. Komninou, and J. Kioseoglou, J. Cryst. Growth **414**, 167 (2015).

[75] W.-T. Hsu, Y.-A. Liao, F.-C. Hsu, P.-C. Chiu, J.-I. Chyi, and W.-H. Chang, Appl. Phys. Lett. **99**, 073108 (2011).

[76] A. Hospodková, J. Pangrác, J. Vyskočil, M. Zíková, J. Oswald, P. Komninou, and E. Hulicius, J. Cryst. Growth **414**, 156 (2015).

[77] J. M. Ulloa, I. W. D. Drouzas, P. M. Koenraad, D. J. Mowbray, M. J. Steer, H. Y. Liu, and M. Hopkinson, Appl. Phys. Lett. **90**, 213105 (2007).

[78] C. Y. Jin, H. Y. Liu, S. Y. Zhang, Q. Jiang, S. L. Liew, M. Hopkinson, T. J. Badcock, E. Nabavi, and D. J. Mowbray, Appl. Phys. Lett. **91**, 021102 (2007).

[79] J. M. Ulloa, R. Gargallo-Caballero, M. Bozkurt, M. del Moral, A. Guzmán, P. M. Koenraad, and A. Hierro, Phys. Rev. B **81**, 165305 (2010).

[80] K. Gradkowski, T. J. Ochalski, N. Pavarelli, H. Y. Liu, J. Tatebayashi, D. P. Williams, D. J. Mowbray, G. Huyet, and D. L. Huffaker, Phys. Rev. B **85**, 035432 (2012).

[81] A. Hospodková, M. Zíková, J. Pangrác, J. Oswald, K. Kuldová, J. Vyskočil, and E. Hulicius, J. Cryst. Growth **370**, 303 (2013).

[82] A. Hospodková, M. Zíková, J. Pangrác, J. Oswald, J. Kubištová, K. Kuldová, P. Hazdra, and E. Hulicius, J. Phys. D: Appl. Phys. **46**, 095103 (2013).

[83] G. Bastard, Phys. Rev. B **24**, 5693 (1981).

[84] O. Stier, M. Grundmann, and D. Bimberg, Phys. Rev. B **59**, 5688 (1999).

[85] G. E. Pikus and G. L. Bir, Sov. Phys. Solid State **1**, 1502 (1960).

[86] S. Birner, T. Zibold, T. Andlauer, T. Kubis, M. Sabathil, A. Trellakis, and P. Vogl, IEEE Trans. Electron Dev. **54**, 2137 (2007).

[87] J. M. Luttinger and W. Kohn, Phys. Rev. **97**, 869 (1955).

[88] L. Wang, V. Křápek, F. Ding, F. Horton, A. Schliwa, D. Bimberg, A. Rastelli, and O. G. Schmidt, Phys. Rev. B **80**, 085309 (2009).

[89] V. Křápek, K. Kuldová, J. Oswald, A. Hospodková, E. Hulicius, and J. Humlíček, Appl. Phys. Lett. **89**, 153108 (2006).

[90] K. Kuldová, V. Křápek, A. Hospodková, O. B. Zrzavecká, J. Oswald, E. Hulicius, and J. Humlíček, Mater. Sci. Eng. C **26**, 983 (2006).

[91] R. Songmuang, S. Kiravittaya, and O. Schmidt, J. Cryst. Growth **249**, 416 (2003).

[92] J. Skiba-Szymanska, A. Jamil, I. Farrer, M. B. Ward, C. A. Nicoll, D. J. P. Ellis, J. P. Griffiths, D. Anderson, G. A. C. Jones, D. A. Ritchie *et al.*, Nanotechnology **22**, 065302 (2011).

[93] J. D. Plumhof, R. Trotta, A. Rastelli, and O. G. Schmidt, Nanoscale Res. Lett. **7**, 336 (2012).

[94] M. Sugawara, Phys. Rev. B **51**, 10743 (1995).

J Type-I and Type-II Confinement in Quantum Dots: Excitonic Fine Structure

Proceedings the 44th International School and Conference on the Physics of Semiconductors "Jaszowiec 2015", Wisła 2015

Type-I and Type-II Confinement in Quantum Dots: Excitonic Fine Structure

V. Křápek[a,*], P. Klenovský[b], T. Šikola[a,c]

[a]Central European Institute of Technology, Brno University of Technology, Technická 10, 616 00 Brno, Czech Republic

[b]Central European Institute of Technology, Masaryk University, Kamenice 753, 625 00 Brno, Czech Republic

[c]Institute of Physical Engineering, Brno University of Technology, Technická 2, 616 69 Brno, Czech Republic

We have theoretically studied type-I and type-II confinement in InAs quantum dots with $GaAs_{1-y}Sb_y$ capping layer. The character of the confinement can be adjusted by the Sb content. We have found that upon the transition from type-I to type-II confinement the hole wave functions change the topology from a compact shape to a two-segment shape, resulting in the complex changes in the exciton fine structure splitting with zero values at particular compositions. Additionally, a high exciton radiative recombination probability is preserved even in type-II. This allows to design strongly luminescent quantum dots with naturally low fine structure splitting, which could serve as sources of entangled photon pairs for quantum communication.

DOI: 10.12693/APhysPolA.129.A-66

PACS: 71.35.–y, 73.21.La, 81.05.Ea

1. Introduction

The ability of the quantum dots to isolate and manipulate individual charge carriers and their integrability into more complex devices make them a candidate for various applications in field of quantum information processing. The source of entangled photon pairs, a crucial element of distinct quantum communication protocols, has been proposed [1] and later realized [2] using the biexciton-exciton radiative cascade. For this it is important that the splitting of the bright exciton doublet (so called fine structure splitting, FSS) is lower than the transition linewidth. FSS was attributed to the anisotropic electron-hole exchange interaction [3] which emerges when the symmetry is lower than D_{2d} [4]. FSS of as-grown structures is usually by far too large and elaborate methods are employed in order to reduce it. The usual lateral asymmetry is suppressed by the growth of symmetric strain-free quantum dots [5] or by the growth on [111] substrates [6]. Post-growth tuning of FSS is possible by means of the external electric [7], magnetic [4], or strain field [8, 9].

Type-II QDs confine one type of charge carriers in the QD volume while the other type resides in a barrier and is only loosely bound by local variations of the confinement potential or the Coulomb coupling to the carrier inside the QD. Here we focus on InAs QDs with $GaAs_{1-y}Sb_y$ capping layer (CL), in which holes are localized in the barrier close to the vicinity of the QD. The type of confinement can be set by the Sb content y; the transition values between 0.14 and 0.18 have been reported [10, 11]. The photoluminescence of the QDs is rather strong even in type-II regime up to $y = 0.28$ [12].

In this work we study theoretically the properties of InAs QDs with the $GaAs_{1-y}Sb_y$ CL in type-I and type-II confinement regimes. We have demonstrated that with increasing Sb content the smooth crossover between type-I and type-II regimes is induced, accompanied by the red shift of the transition energy, the segmentation of the hole wave function, and non-trivial changes in the FSS magnitude and polarization of the bright exciton transitions. We predict the possibility to prepare QDs with naturally low FSS and efficient photoluminescence by setting a proper Sb content.

2. Theory

The single particle states were calculated within the eight-band $\boldsymbol{k}\cdot\boldsymbol{p}$ theory [13] using the Nextnano 3D software package [14]. Realistic strain and piezoelectric fields were included. Next, the exciton states were calculated using the configuration interaction method [15] in which the wave functions are expanded into a basis of Slater determinants formed from the single particle states. The matrix elements of the Coulomb Hamiltonian were calculated following the approach of Refs. [3, 16].

3. Results

We consider here a lens-shaped InAs QD with the height of 4 nm and the radius of 8 nm on GaAs substrate, capped with a $GaAs_{1-y}Sb_y$ layer with the thickness of 6 nm. The axis of the lens is parallel with the [001] crystal axis, the related coordinate is denoted z. To induce the crossover between the type-I and type-II confinement regimes, we have varied the antimony content y between

*corresponding author; e-mail: vlastimil.krapek@ceitec.vutbr.cz

0.1 and 0.22. The bulk valence band edges of InAs and $GaAs_{1-y}Sb_y$ cross for $y_{CO} \approx 0.15$ with the InAs valence band being higher in energy (i.e., confining the holes) for $y < y_{CO}$.

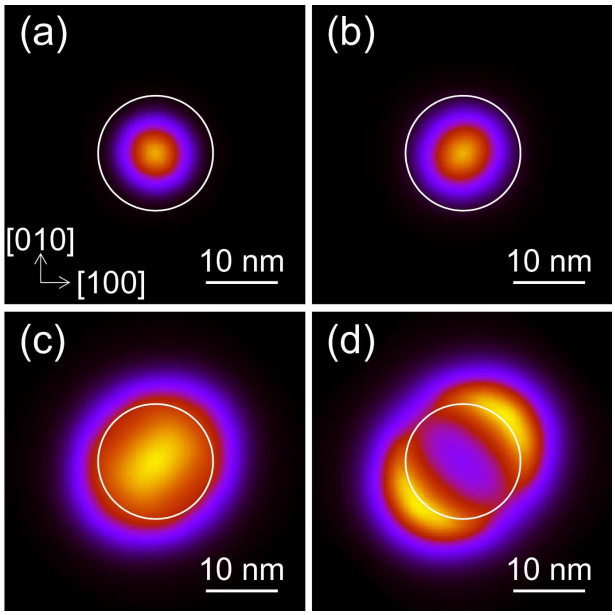

Fig. 1. In-plane probability density (integrated over z) of the ground state of (a) electron, $y = 0.10$, (b) hole, $y = 0.10$, (c) hole, $y = 0.20$, (d) hole, $y = 0.22$. White circles denote the QD boundary at the height of the base.

We will first inspect the wave functions. In-plane probability densities (quadrate moduli of the wave functions integrated over direction z parallel with the lens axis) are shown in Fig. 1. The electrons (Fig. 1a) are localized inside the QD volume, slightly elongated along $[1\bar{1}0]$ due to the piezoelectric field, and remain practically invariant under the change of Sb content y. Holes are for lower antimony content also localized within the QD volume (Fig. 1b) and slightly elongated along [110]. As y increases, the hole wave function extends laterally more into barrier (Fig. 1c). Finally, holes are expelled from the QD volume and become confined in the $GaAs_{1-y}Sb_y$ layer (Fig. 1d), where their wave function forms two segments [11] located along the [110] direction, each elongated along $[1\bar{1}0]$. The vertical position and extension of the holes undergo negligible variations during the transition between type-I and type-II regimes.

To describe the type-I–type-II crossover quantitatively, we introduce the probability of finding a particle inside the QD volume (i.e., within InAs). It is shown in Fig. 2a for electrons and holes. While the electron probability displays only negligible variations of less than 1%, the hole probability gradually decreases from 85% at $y = 0.10$ to 19% at $y = 0.22$, reaching 50% for $y = 0.17$ which can be thus considered as the crossover value of the Sb content for the particular nanostructure. Nevertheless, the transition between type-I and type-II regimes

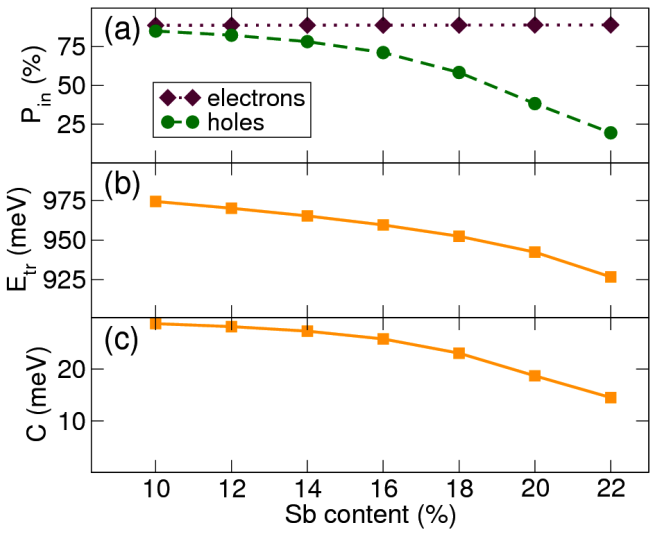

Fig. 2. (a) Probability of finding a particle inside the QD volume, (b) transition energy of the ground exciton state, (c) Coulomb energy between the electron and hole ground states.

is smooth and no abrupt changes are observed. The transition energy redshifts as the y increases (Fig. 2b) due to the decreased potential barrier in type-I and the shift of the confinement potential edge in type-II and some other effects. The red shift has been already observed [17] and theoretically explained [11]. An important consequence of the electron–hole separation in type-II is the reduced electron–hole Coulomb coupling. The direct coupling energy, which is equal to the binding energy of exciton and contributes the binding energy of excitonic complexes, is shown in Fig. 2c; it gradually decreases from 29 to 15 meV. The decrease is first subtle, caused by the increased extension of the hole wave function that is still localized inside the QD, and becomes steeper when charge carriers are separated and two-segmented hole wave function outside the QD is formed. A dependence of FSS on Sb content is shown in Fig. 3. The FSS evolution is dominated by the variations of the lateral symmetry of the wave functions and further contributed by a reduction of the exchange Coulomb coupling due to the separation of electron and hole wave function with increasing y (the latter is responsible for a kink at $y = 0.18$). The polarization properties of the exciton transitions are encoded into the sign of FSS: positive (negative) sign corresponds to the linear polarization of the lower-energy exciton transition along [110] ($[1\bar{1}0]$), respectively. Due to the symmetry of the crystal lattice and the structure, only these two polarizations are observed. The higher-energy transition is linearly polarized in perpendicular direction to the lower-energy transition. In terms of the wave function properties the polarization direction of the lower-energy transition corresponds to the long axis of the elongated wave function. In symmetric lens-shaped QDs, holes and electrons are elongated in perpendicular

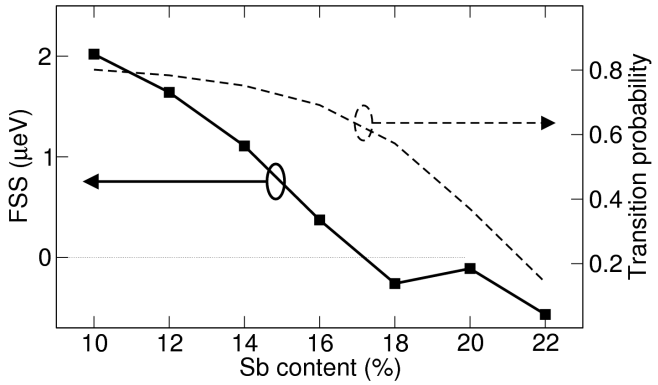

Fig. 3. FSS (thick solid line with symbols, left) and transition probability (thin dashed line, right) between the ground electron and hole state in the lens-shaped QD as functions of the GaAsSb layer composition.

directions, partly compensating the overall anisotropy. For y below 0.16, hole elongation along [110] dominates, resulting in positive FSS. Above 0.18, electron elongation along $[1\bar{1}0]$ becomes stronger, changing the sign of FSS. Finally, after the formation of the segmented hole function, the hole segments are also elongated along $[1\bar{1}0]$, increasing the magnitude of FSS. Noteworthy, FSS acquires a zero value at $y \approx 0.17$, which is an essential ingredient for the realization of the polarization-entangled photon pairs [1]. In addition, $GaAs_{1-y}Sb_y$ capped InAs QDs are good emitters even in type-II regime. The calculated values of transition probability for the ground exciton recombination, shown in Fig. 3, exhibit only a moderate decrease with increasing Sb content with a reduction towards 25% of the type-I value for $y = 0.22$. The observations of a strong photoluminescence in type-II regime [12] corroborate our prediction.

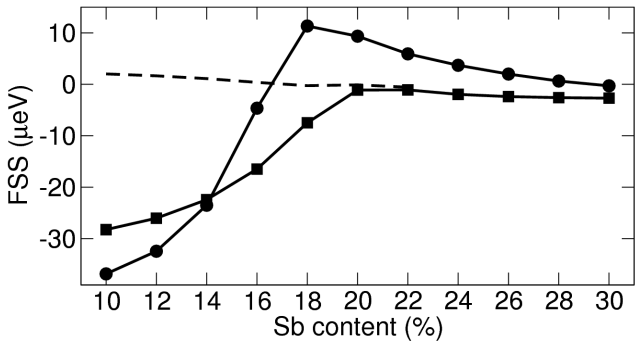

Fig. 4. FSS in the elongated lens-shaped QD as a function of the GaAsSb layer antimony content. The thickness of CL is 4 nm (squares) or 7 nm (circles). For comparison, FSS in symmetric lens-shaped QD with the CL height of 6 nm is shown (dashed line).

A reduction of FSS towards zero can be achieved also in more realistic non-symmetric QDs. In Fig. 4 we show FSS in lens-shaped QDs elongated along $[1\bar{1}0]$ with the ratio of the lateral dimensions of 1.1 for two thicknesses of the CL (4 and 7 nm). The shape elongation causes the large negative FSS in type-I regime. Although FSS in type-I regime is large compared to a natural exciton linewidth (about 4 μeV for a typical life time of 1 ns [12]), for both CL thicknesses it is reduced below the linewidth during the crossover to the type-II regime. Thus, by setting a proper composition of the $GaAs_{1-y}Sb_y$ overlayer, QDs with a low value of FSS can be produced.

4. Conclusions

The character of confinement in InAs quantum dots capped with a $GaAs_{1-y}Sb_y$ overlayer depends on the composition of the overlayer, with the holes coupled inside the QD for low Sb content and outside the QD for high Sb content. During the crossover between type-I and type-II confinement, the lateral profile of the hole wave functions is modified, resulting in the strong variations of the FSS. By setting a proper Sb content it shall be possible to prepare QDs with naturally low FSS and efficient photoluminescence, which are important for quantum communication as the source of polarization-entangled photon pairs.

Acknowledgments

This work was supported by European Social Fund (grant No. CZ.1.07/2.3.00/30.0005), European Regional Development Fund (project No. CZ.1.05/1.1.00/02.0068), the Grant Agency of the Czech Republic (grant No. 15-21581S), Technology Agency of the Czech Republic (grant No. TE01020233), and EU 7th Framework Programme (Contracts No. 286154 — SYLICA and 280566 — UnivSEM). P.K. was supported by the internal project MUNI/A/1496/2014.

References

[1] O. Benson, C. Santori, M. Pelton, Y. Yamamoto, *Phys. Rev. Lett.* **84**, 2513 (2000).

[2] N. Akopian, N.H. Lindner, E. Poem, Y. Berlatzky, J. Avron, D. Gershoni, B.D. Gerardot, P.M. Petroff, *Phys. Rev. Lett.* **96**, 130501 (2006).

[3] T. Takagahara, *Phys. Rev. B* **62**, 16840 (2000).

[4] M. Bayer, G. Ortner, O. Stern, A. Kuther, A.A. Gorbunov, A. Forchel, P. Hawrylak, S. Fafard, K. Hinzer, T.L. Reinecke, S.N. Walck, J.P. Reithmaier, F. Klopf, F. Schäfer, *Phys. Rev. B* **65**, 195315 (2002).

[5] Y.H. Huo, V. Křápek, A. Rastelli, O.G. Schmidt, *Phys. Rev. B* **90**, 041304 (2014).

[6] A. Schliwa, M. Winkelnkemper, A. Lochmann, E. Stock, D. Bimberg, *Phys. Rev. B* **80**, 161307 (2009).

[7] R. Trotta, E. Zallo, C. Ortix, P. Atkinson, J.D. Plumhof, J. van den Brink, A. Rastelli, O.G. Schmidt, *Phys. Rev. Lett.* **109**, 147401 (2012).

[8] J.D. Plumhof, V. Křápek, F. Ding, K.D. Jöns, R. Hafenbrak, P. Klenovský, A. Herklotz, K. Dörr, P. Michler, A. Rastelli, O.G. Schmidt, *Phys. Rev. B* **83**, 121302 (2011).

[9] J.D. Plumhof, R. Trotta, V. Křápek, E. Zallo, P. Atkinson, S. Kumar, A. Rastelli, O.G. Schmidt, *Phys. Rev. B* **87**, 075311 (2013).

[10] H.Y. Liu, M.J. Steer, T.J. Badcock, D.J. Mowbray, M.S. Skolnick, F. Suarez, J.S. Ng, M. Hopkinson, J.P.R. David, *J. Appl. Phys.* **99**, 046104 (2006).

[11] P. Klenovský, V. Křápek, D. Munzar, J. Humlíček, *Appl. Phys. Lett.* **97**, 203107 (2010).

[12] J.M. Ulloa, J.M. Llorens, B. Alén, D.F. Reyes, D.L. Sales, D. González, A. Hierro, *Appl. Phys. Lett.* **101**, 253112 (2012).

[13] O. Stier, M. Grundmann, D. Bimberg, *Phys. Rev. B* **59**, 5688 (1999).

[14] S. Birner, T. Zibold, T. Andlauer, T. Kubis, M. Sabathil, A. Trellakis, P. Vogl, *IEEE Trans. Electron Dev.* **54**, 2137 (2007).

[15] R. Seguin, A. Schliwa, S. Rodt, K. Pötschke, U.W. Pohl, D. Bimberg, *Phys. Rev. Lett.* **95**, 257402 (2005).

[16] V. Křápek, P. Klenovský, T. Šikola, *Phys. Rev. B* **92**, 195430 (2015).

[17] A. Hospodková, M. Zíková, J. Pangrác, J. Oswald, J. Kubištová, K. Kuldová, P. Hazdra, E. Hulicius, *J. Phys. D Appl. Phys.* **46**, 095103 (2013).

K Spontaneous brightening of dark excitons in GaAs/AlGaAs quantum dots near a cleaved facet

Spontaneous brightening of dark excitons in GaAs/AlGaAs quantum dots near a cleaved facet

Y. H. Huo,[1,2,3,*] V. Křápek,[4,†] O. G. Schmidt,[5] and A. Rastelli[1]

[1]*Institute of Semiconductor and Solid State Physics, Johannes Kepler University Linz, Linz Institute of Technology, Altenbergerstrasse 69, A-4040 Linz, Austria*

[2]*Hefei National Laboratory for Physical Sciences at Microscale, University of Science and Technology of China, Hefei, Anhui 230026, China*

[3]*CAS-Alibaba Quantum Computing Laboratory, USTC Shanghai branch, Shanghai 201315, China*

[4]*Central European Institute of Technology, Brno University of Technology, Purkyňova 123, 61200 Brno, Czech Republic*

[5]*Institute for Integrative Nanosciences, IFW Dresden, Helmholtzstrasse 20, D-01069 Dresden, Germany*

(Received 18 October 2016; revised manuscript received 13 March 2017; published 27 April 2017)

Dark excitons (DEs) confined in epitaxial quantum dots (QDs) are interesting because of their long lifetime compared to bright excitons (BEs). For the same reason they are usually difficult to access in optical experiments. Here we report on the observation of vertically polarized light emission from DEs confined in high-quality epitaxial GaAs/AlGaAs QDs located in proximity of a cleaved facet of the QD specimen. Calculations based on the eight-band **k·p** method and configuration interaction allow us to attribute the brightening of the DE to the anisotropic strain present at the sample edge, which breaks the symmetry of the system and enhances valence-band mixing. The mechanism of DE brightening is discussed in detail by inspecting both the Bloch and envelope wave functions of the involved hole states. In addition, by investigating experimentally and theoretically QDs with different sizes, we find that the energy separation between DE and BEs tends to decrease with increasing QD height. Finally, the presence of a cleaved facet is found also to enhance the BE fine structure splitting. This work provides a simple method to optically probe dark excitonic states in QDs and shows that the properties of QDs can be significantly affected by the presence of nearby edges.

DOI: 10.1103/PhysRevB.95.165304

I. INTRODUCTION

The simplest low-temperature excitation in a quantum dot (QD) is a neutral exciton consisting of an electron in the lowest confined conduction-band state and a hole in the uppermost valence-band state. Most of the semiconductor QDs obtained by epitaxial growth of zincblende semiconductors, such as GaAs, are characterized by an uppermost valence-band state of heavy-hole (HH) character. The confined hole, with a total angular momentum quantum number $J = 3/2$ and projection $J_z = \pm 3/2$ along the growth direction z, interacts with the confined electron, with spin projection quantum number $S_z = \pm 1/2$, through the Coulomb and exchange interaction, leading to four possible excitonic configurations. Two of them, with total angular momentum of ± 1, are dipole allowed and are thus referred to as "bright excitons" (BEs). The corresponding transition electric-dipole moments are parallel to the growth plane [(001) GaAs for the dots considered here]. The remaining two, with total angular momentum of ± 2, are dipole forbidden and are therefore called "dark excitons" (DEs). Because of their negligible oscillator strength, DEs have been largely neglected compared to BEs. However, because of their much longer lifetime, DEs are interesting for spin storage for quantum information processing [1–3].

To access the optically inactive DEs, different methods and conditions have been used. Examples include the electrical [2] or optical [3] injection of a single electron or hole into afore-prepared DE states, spin-flip interaction with a magnetic impurity [4], two-photon pumping [5], mixing of carrier spins by an in-plane magnetic field [6–11], and mixing hole states induced by built-in strain or shape asymmetries [12–14].

In this paper we report on the observation of DE emission in GaAs/AlGaAs QDs, which are obtained by local Al-droplet etching of AlGaAs. In absence of perturbations, the studied dots are practically unstrained and are characterized by a round shape [15–17], leading to weak hole mixing [17] and strongly suppressed DE emission. In order to access the DEs, we investigate the light emission of QDs located in proximity of a cleaved facet of the sample, using polarization-resolved microphotoluminescence (μ-PL) spectroscopy. The cleaved edge reduces the symmetry of the QD environment and leads to a spontaneous brightening of the DE emission. By using the eight-band $\mathbf{k} \cdot \mathbf{p}$ method and the realistic structure as input, we show that the enhanced optical activity of DEs in QDs stems from anisotropic strain induced by the cleaved edge in its neighborhood and consequent HH–light-hole (LH) mixing. By studying QDs with different sizes, we find that DEs are optically accessible only when the QD size is sufficiently large and disappear for the smallest QDs. We also find that the energy splitting between DE and BE tends to decrease when the QD size increases. These observations are consistent with the results of our calculations. On one hand, this work shows that nearby edges can significantly influence the optical properties of QDs, which is important in view of their integration in nanophotonic structures [18]. On the other hand, it provides a simple method to achieve spontaneous brightening of DEs in QDs, opening up the possibility to have similar dots with and without the DE emission in the same sample.

The paper is organized into eight sections. Section II presents experimental and theoretical methods involved in the study and Sec. III presents the photoluminescence data. In Sec. IV we discuss symmetry factors related to the cleaved

*yongheng@ustc.edu.cn

†krapek@monoceros.physics.muni.cz

edge and conclude that it is a weak strain field with in-plane anisotropy in the vicinity of the edge that makes the dark excitons optically accessible. In Sec. V we discuss the components of the hole wave function in presence of mixing. Section VI is dedicated to the effects of QD size and in Sec. VII we discuss the fine structure splitting and its variation in the presence of the cleaved edge. Section VIII concludes the paper.

II. EXPERIMENTAL AND THEORETICAL METHODS

The experiments were performed on three different QD samples grown on 350-μm-thick intrinsic GaAs(001) substrates using molecular beam epitaxy. The QD heterostructure, grown on a 25-nm-thick AlAs layer, consists of a 200-nm-thick $Al_{0.4}Ga_{0.6}As$ layer with a layer of GaAs QDs in its center. The QDs were obtained as described in Refs. [15,16]: first round-shaped nanoholes were produced on an $Al_{0.4}Ga_{0.6}As$ surface by Al droplets; then the nanoholes were filled by depositing 1, 1.5, and 2 nm of GaAs for the three different samples. Because of capillarity effects, the corresponding QD heights are about 4, 6, and 7.5 nm.

To access the DE signal, which is expected to be polarized along the growth direction [13], we performed polarization-resolved μ-PL measurements by collecting the PL signal from an edge of the samples, cleaved along the [110] crystal direction, using the configuration sketched in Fig. 1(b). Linear polarization analysis was performed using a rotatable achromatic half-wave plate and a fixed Glan-Thompson polarizer. In all the measurements, the temperature was kept at about 9 K.

The interpretation of the experimental data is supported by theoretical calculations. Exciton energies and optical selection rules are calculated using the configuration interaction (CI) approach on top of single-particle calculations based on eight-band **k·p** theory applied to QDs with realistic shape and composition.

The eight-band **k·p** theory is a state-of-the-art method for the calculation of single-particle properties of QDs [19]. Based on the original formulation of **k·p** theory for bulk crystals [20], it was adapted for quantum heterostructures [21]. For direct band gap semiconductors such as GaAs, the wave function is expanded into a series of zone-center Bloch waves $u_n(\mathbf{r})$ with the space-dependent expansion coefficients $\chi_n(\mathbf{r})$ denoted as envelope functions:

$$\psi(\mathbf{r}) = \sum_{n=1}^{8} \chi_n(\mathbf{r}) u_n(\mathbf{r}). \quad (1)$$

Here the summation goes over two conduction bands and six valence bands—heavy-hole band, light-hole band, and spin-orbit split-off band (each doubly degenerate due to spin). When relevant, the effects of strain are incorporated via Pikus-Bir Hamiltonian [22] and piezoelectric potential is calculated and added to the total Hamiltonian. We note that this applies only to the cleaved-edge related strain as the built-in strain due to lattice mismatch in our GaAs/AlGaAs QDs is negligibly small. A numerical implementation consists in a finite difference scheme with a grid step of 1 nm and a typical grid size of 78 × 78 × 30 (i.e., 1.8×10^5) voxels.

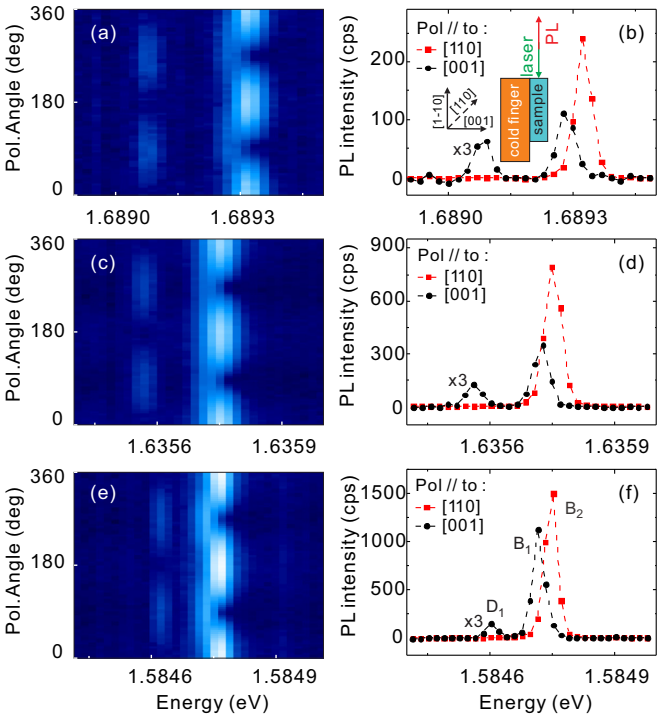

FIG. 1. (a), (c), and (e) Color-coded linear-polarization-resolved spectra collected from a cleaved facet of QD samples with GaAs QDs obtained by filling AlGaAs nanoholes with 1, 1.5, and 2 nm GaAs, respectively. 0° corresponds to the [110] crystal direction, while 90° corresponds to the [001] direction (growth direction). Logarithmic color scale is used for the spectrum intensity. (b), (d), and (f) Spectra extracted from (a), (c), and (e), respectively, at polarization angles of 0° (red squares) and 90° (black circles). D_1 labels the DE component, B_1/B_2 labels the lower/higher components of the BE doublet. The intensity of D_1 and B_1 is magnified by a factor of 3. The insets in (b) show the experimental configuration for the measurements and the sketched crystal directions (the excitation laser and collection path are parallel to the [1–10] crystal direction).

The eigenenergies of the Hamiltonian are found using an optimized Davidson algorithm [23].

The single-particle states were subsequently employed to calculate the exciton structure following the procedure outlined in Refs. [24,25]. Here the exciton wave function is expanded into Slater determinants constructed from the single-particle states. We restricted our basis to the ground electron and hole states and employed optimized evaluation of exchange interaction matrix elements [26].

In the calculations we implemented the nanohole shape measured by AFM to define the lower boundary and a flat plane for the top boundary of the model QD. Such approach was justified in our previous studies [16,27]. The selected height range of the model structures covers the range of the experimentally studied samples.

III. PHOTOLUMINESCENCE SPECTRA FROM A CLEAVED FACET

Figures 1(a), 1(c), and 1(e) show color-coded polarization-resolved spectra obtained from one representative QD contained in each of the three samples discussed above, collected

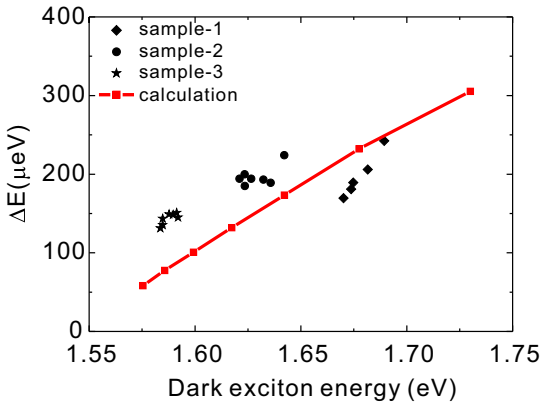

FIG. 2. Experimental and calculated energy separation between DE (D_1) and BE (B_2) as a function of dark exciton energy. The scattered symbols are experimental data. The line plus symbols show the calculated results of QDs with height from 2.6 to 8.6 nm with a step of 1 nm.

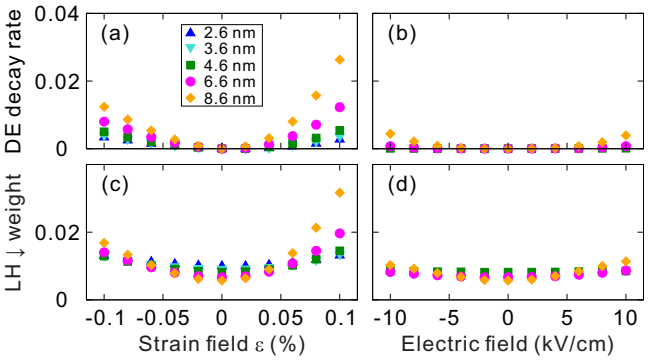

FIG. 3. Relative DE decay rate (divided by the BE decay rate) and $|LH\downarrow\rangle$ weight (in the spin-up hole ground state $\psi_H^{\uparrow}$, which is dominated by $|HH\uparrow\rangle$) as functions of local strain field (a) and (c) and electric field (b) and (d) for several QDs with different sizes. The $|LH\uparrow\rangle$ component is not included because it does not contribute to the optical response (see text). The strain along [1–10] and the electric field along the [1–10] crystal direction are taken as the independent variables.

along the [1–10] direction. Figures 1(b), 1(d), and 1(f) show the corresponding spectra polarized along the [110] and [001] directions. Hereafter we use D_1 to label the DE line, and B_1/B_2 to label the lower/higher energy component of the BE doublet. D_1 appears below B_1/B_2 and is polarized along the [001] direction (i.e., the growth direction, which coincides with the main confinement direction of the QD). Similar observations were reported for CdTe/ZnTe QDs, which are—different from the present case—strongly strained [12]. B_2 appears to be polarized along the [110] direction. B_1 is expected to be polarized along the [1–10] direction. Due to total internal reflection at the interface between the (001) sample surface and air, B_1 can be partially collected along [1–10] as explained in Ref. [17]. Here we point out that in even smaller QDs, obtained by filling the nanoholes with less than 1 nm GaAs, we were not able to detect DE emission.

From Fig. 1 we see that the energy splitting between dark and bright excitonic lines increases with decreasing QD size. The scatter plots in Fig. 2 confirm that the energy splitting ΔE_{DB} between D_1 and B_2 lines measured on different dots in the three different samples tends to increase with increasing exciton energy, i.e., with decreasing QD size.

IV. SYMMETRY-BREAKING FACTORS RELATED TO A CLEAVED FACET

The first question we want to address is: why is the DE visible at all? In the following we will show that the DE brightening stems from the anisotropic strain related to the cleaved edge, which results in enhanced mixing of LHs into dominantly HH-like ground state. Different from the aforementioned works [2–15], our QDs are characterized by very small strain and a regular shape, so that HH-LH mixing in QDs located far away from edges is expected to be small and to have negligible impact on the observability of dark excitons. This statement, which is also supported by atomistic pseudopotential calculations presented in Ref. [17], will be further justified in Sec. V. Because the used materials in our samples are nonmagnetic and the QD has regular shape, the only symmetry-breaking factor is the presence of the cleaved edge. This may introduce (i) an anisotropic strain field with major axis parallel to the [1–10] direction (due to the oxidation of the AlAs layer present below the QD structure, surface reconstruction and oxidation of the cleaved facet, and slight strain relaxation of the Al(Ga)As structure [28]), and/or (ii) a local electric field (from oxidation and surface depletion [29–32]).

To explore the effects of strain and electric field on the visibility of the DE, we used a theoretical model based on eight-band **k·p** theory [19]. The introduced local strain is assumed to have a major component ε along [1–10] (with magnitude up to 0.1%) and a minor component along [001]. The strain along [110] is assumed to be 0 because the layer is fixed to the macroscopic substrate and cannot relax parallel to the cleaved edge [28]. The homogeneous electric field is assumed to be parallel to the [1–10] direction (i.e., perpendicular to the sample edge) with a magnitude up to 10 kV/cm [33].

The results of the calculations are summarized in Fig. 3(a), which shows the values of the DE decay rates relative to the BE decay rates. These values, which are obtained in the dipole approximation [23], roughly correspond to the relative ratio of D_1 and B_2 intensities. The decay rate of the DE is negligibly small if no symmetry-breaking field is present. With increasing strain field the brightness of the DE increases. In addition, the effect is more pronounced for larger QDs, while for smaller QDs the DE decay rate remains small. For the strain $\varepsilon = 0.1\%$, the relative DE decay rates read 0.005, 0.012, and 0.026 for QD heights 4.6, 6.6, and 8.6, respectively. These values have the same order of magnitude as in the experimental data [27]. A direct quantitative comparison is however not possible, since in the experiment we do not know the exact distance of each QD from the cleaved edge, the precise QD shapes, and the values of local strain. By inspecting the wave functions of confined holes as a function of strain we find that the increase of the DE decay rate is accompanied by an enhanced weight of the LHs in the ground hole state (in particular, spin-down LHs

TABLE I. Exciton quadruplet in a QD with the height of 6.6 nm. E is the energy of each exciton component relative to the lowest one. $P_{[110],[1-10],z}$ are the transition probabilities for the emission/absorption with linear polarizations in the respective direction (neglecting a weak elliptical part). The first and second lines correspond to the dark pair, the third and fourth lines correspond to the bright pair.

E (μeV)	$P_{[110]}$	$P_{[1-10]}$	P_z
0	0	0	0
0.9	0	0	0
128.6	0.015	0.863	0
136.1	0.853	0.015	0

for spin-up hole state), as shown in Fig. 3(c). On the contrary, we find that realistic values of electric fields are not sufficient to strengthen the decay rate of DEs to a level comparable to experiments (the weight of the LHs remains negligible), see Figs. 3(b) and 3(d).

The calculated exciton structure in a particular QD (height of 6.6 nm) is detailed in Tables I and II for the case without strain and with strain ($\varepsilon = 0.1\%$), respectively. Without strain, the ground exciton quadruplet is composed of two almost degenerate DEs at low energy and two BEs at higher energy. The DEs are fully optically inactive. The BEs exhibit optical transitions with the linear polarizations close to [110] (high energy) and [1–10] (low energy). The splitting between the BEs (fine structure splitting, FSS) resulting from the slight structural asymmetry of the QD was studied in detail elsewhere [15,16]. The strain produces a brightening of one of the DEs with the polarization along [001], which is more than 50-times weaker than the BE (see Table II). At the same time anisotropic strain also induces an in-plane polarization anisotropy of the bright pair and increases the FSS.

V. MECHANISM OF DARK EXCITON BRIGHTENING

To explain the mechanism of the dark exciton brightening we have to first understand the role of the LH components in the hole state. As stated by Eq. (1), the wave function is represented by an eight-component Luttinger spinor [34]. The zone-center Bloch basis can be conveniently represented in angular momentum representation as $|J, J_z\rangle$ where J and J_z represent quantum numbers of total angular momentum and its z projection. Alternatively, it can be given in Cartesian representation, in which $|S\rangle$ represents the zone-center Bloch wave for conduction band electrons (derived from atomic s orbitals) and $|X\rangle$, $|Y\rangle$, $|Z\rangle$ represent the components of the electron Bloch waves in the valence band (derived from atomic p_x, p_y, p_z orbitals), which transform as the respective coordinates under the crystal point group symmetry operations. The basis states u_n in Eq. (1) read

$$|EL\uparrow\rangle = \left|S, +\frac{1}{2}\right\rangle = |S\uparrow\rangle,$$

$$|HH\uparrow\rangle = \left|\frac{3}{2}, +\frac{3}{2}\right\rangle = \frac{1}{\sqrt{2}}(|X\uparrow\rangle + i|Y\uparrow\rangle),$$

$$|LH\uparrow\rangle = \left|\frac{3}{2}, +\frac{1}{2}\right\rangle = \frac{1}{\sqrt{6}}(|X\downarrow\rangle + i|Y\downarrow\rangle - 2|Z\uparrow\rangle),$$

$$|SO\uparrow\rangle = \left|\frac{1}{2}, +\frac{1}{2}\right\rangle = \frac{1}{\sqrt{3}}(|X\downarrow\rangle + i|Y\downarrow\rangle + |Z\uparrow\rangle),$$

$$|EL\downarrow\rangle = \left|S, -\frac{1}{2}\right\rangle = |S\downarrow\rangle,$$

$$|HH\downarrow\rangle = \left|\frac{3}{2}, -\frac{3}{2}\right\rangle = -\frac{1}{\sqrt{2}}(|X\downarrow\rangle - i|Y\downarrow\rangle),$$

$$|LH\downarrow\rangle = \left|\frac{3}{2}, -\frac{1}{2}\right\rangle = -\frac{1}{\sqrt{6}}(|X\uparrow\rangle - i|Y\uparrow\rangle + 2|Z\downarrow\rangle),$$

$$|SO\downarrow\rangle = \left|\frac{1}{2}, -\frac{1}{2}\right\rangle = \frac{1}{\sqrt{3}}(|X\uparrow\rangle - i|Y\uparrow\rangle - |Z\downarrow\rangle).$$

Here EL, HH, LH, and SO correspond to electrons in the conduction, heavy-hole, light-hole, and spin-orbit split-off bands, respectively. The only nonzero optical matrix element is of the spin-conserving type $\langle S\uparrow|\, p_x|X\uparrow\rangle$ with the polarization direction corresponding to the valence band symmetry (x polarization for $|X\rangle$, etc.). Thus, a heavy-hole corresponding to a missing spin-up electron ($|HH\uparrow\rangle$) can be combined with a spin-up electron $|EL\uparrow\rangle$ to form a bright exciton ($\langle S\uparrow|\, p_x|X\uparrow\rangle$ is nonzero and $\Delta J_z = 1$). In contrast, the same state forms a dark exciton when combined with a spin-down electron $|EL\downarrow\rangle$ ($\langle S\downarrow|p_x|X\uparrow\rangle$ is zero and $\Delta J_z = 2$—such an angular momentum cannot be carried by a single photon).

The ground hole state forms a Kramers doublet and is dominated by a heavy-hole component with a weight of above 90% according to our calculations. [From Eq. (1), the weight of one of the basis bands u_n in the valence-band state ψ_H can be defined as $\langle \chi_n \mid \chi_n \rangle$.] Both states of the Kramers doublet can be combined so their major-spin heavy-hole components are maximized and the minor-spin heavy-hole components are virtually zero. In the following, we refer to these two states as $\psi_H^{\uparrow}$ and $\psi_H^{\downarrow}$ and focus on the $\psi_H^{\uparrow}$ state, which is dominated by the $|HH\uparrow\rangle$ component. As it was explained, a hole in this state forms a BE with the spin-up electron $|EL\uparrow\rangle$ and a DE with the spin-down electron $|EL\downarrow\rangle$. When the light hole corresponding to a missing spin-up electron $|LH\uparrow\rangle$ is mixed to this state, the presence of a $|Z\uparrow\rangle$ component adds an out-of-plane polarized transition to the BE (with $|EL\uparrow\rangle$) and two bright (but weak for moderate HH-LH mixing) in-plane

TABLE II. Exciton quadruplet as in Table I (QD height 6.6 nm) in presence of strain field (tensile strain $\varepsilon = 0.1\%$ along [1–10] with a proper relaxation along [001]).

E (μeV)	$P_{[110]}$	$P_{[1-10]}$	P_z
0	0	0	0.010
2.4	0	0	0
114.5	0.001	0.720	0
149.3	0.975	0	0

polarized transitions to the DE (with $|EL\downarrow\rangle$). The presence of a $|LH\downarrow\rangle$ component in the $\psi_H^{\uparrow}$ may lead instead to a polarization anisotropy of the BE transitions and adds a bright out-of-plane polarized transition to the DE. Our experiment reveals an out-of-plane polarization for DE transitions, which corresponds to the $|LH\downarrow\rangle$ component mixed into the $\psi_H^{\uparrow}$ hole state (and $|LH\uparrow\rangle$ component mixed into $\psi_H^{\downarrow}$ state).

In as-grown QDs without additional strain or electric fields, the LHs are coupled to the dominant HH primarily by the quantum confinement. (Additional effects, such as interface disorder, which are not modified by strain, are discussed in Ref. [35].) In the case considered in Table I (QD height 6.6 nm, no strain) the $|LH\uparrow\rangle$ and $|LH\downarrow\rangle$ weights in the spin-up hole state $\psi_H^{\uparrow}$ are 4.1% and 0.7%, respectively. Despite a small but significant weight of LHs (about 5% in total), mixing does not affect appreciably the optical properties, which are very close to those of a purely HH exciton, i.e., there is no emission with out-of-plane polarization. We note that the dominant LH contribution to the $\psi_H^{\uparrow}$ state is given by $|LH\uparrow\rangle$. According to the form of the Bloch waves (see discussion above), this LH state would induce in-plane polarized emission for the DE and out-of-plane polarized emission for the BEs, in contrast to the experimental data. The reason can be understood by inspecting the envelope functions of the hole wave functions and their overlap with the electron wave function. Figures 4(a) and 4(b) display the probability density distribution corresponding to the conduction-band envelope function for an electron confined in a QD with structure displayed in Figs. 4(c) and 4(d). The probability density distributions of the $|HH\uparrow\rangle$, $|LH\uparrow\rangle$, and $|LH\downarrow\rangle$ components of the ground hole state $\psi_H^{\uparrow}$ [i.e., $|\langle u_n \,|\, \psi_H^{\uparrow}\rangle|^2 = |\chi_n(\boldsymbol{r})|^2$, see Eq. (1)] are shown in Figs. 4(e) and 4(f), Figs. 4(i) and 4(j), and Figs. 4(m) and 4(n), respectively. Note that the color scales are normalized to be able to observe features of the weak LH components. While the electron wave function and $|HH\uparrow\rangle$ envelope function strongly overlap, the donut-shaped $|LH\uparrow\rangle$ envelope function has only a weak overlap with them. Additionally, due to its in-plane quasiantisymmetry (not shown) its contribution to the optical matrix elements is close to zero. The same considerations apply to the $|LH\downarrow\rangle$ component.

In presence of strain with $\varepsilon = 0.1\%$ (Table II), the weight of the LHs is increased to 5.0% ($|LH\uparrow\rangle$) and 2.0% ($|LH\downarrow\rangle$). Strain modifies the probability density distributions of the $|HH\uparrow\rangle$, $|LH\uparrow\rangle$, and $|LH\downarrow\rangle$ components of the state $\psi_H^{\uparrow}$, which are displayed in Figs. 4(g) and 4(h), Figs. 4(k) and 4(l), and Figs. 4(o) and 4(p), respectively. (The electron wave function is only negligibly modified by the strain and is not shown.) While the $|LH\uparrow\rangle$, which is mostly induced by the quantum confinement (as discussed above), still has negligible overlap with the electron wave function [Figs. 4(k) and 4(l)], the strain-enhanced $|LH\downarrow\rangle$ [Figs 4(o) and 4(p)] has a sizable overlap with the electron and exhibits in-plane quasisymmetry. Therefore, it contributes to the optical transitions and leads to the DE brightening. The corresponding transition dipole is oriented along the growth direction, as observed experimentally. To avoid confusion, we also note that the exciton is still mostly heavy-hole-like with a small contribution of light holes and differs considerably from the purely light-hole exciton studied in Ref. [17].

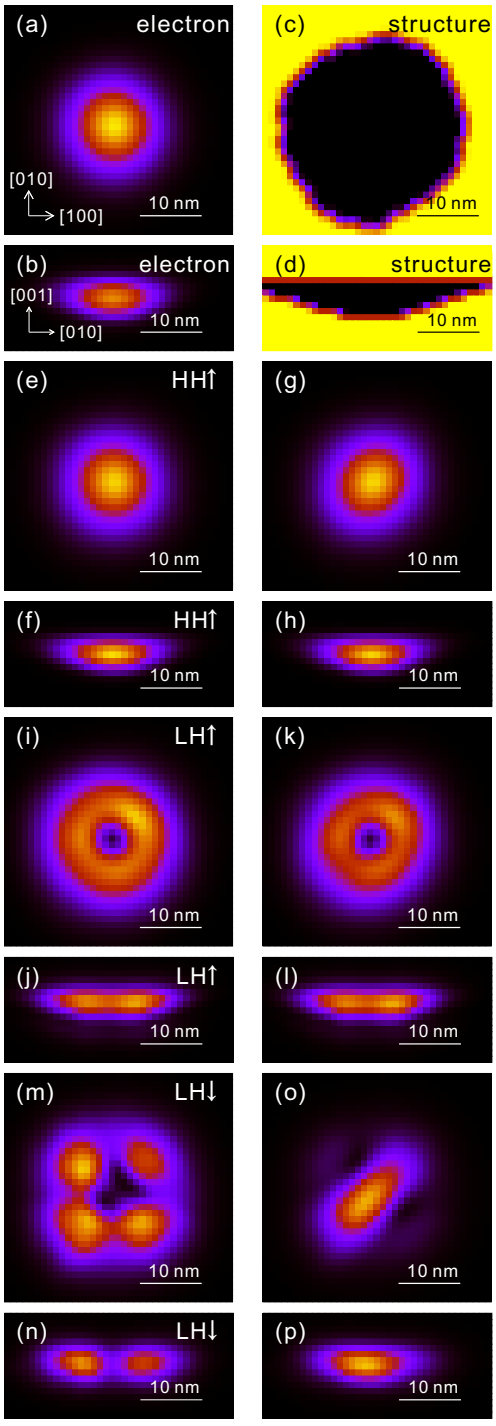

FIG. 4. Significant envelope functions (represented by probability density distributions) of the ground spin-up electron and hole states in a GaAs QD with a height of 6.6 nm. (a) and (b) electron, $|S\uparrow\rangle$ component. (c) and (d) QD planar cross sections on the (001) plane through the midheight and on the (1-10) plane through the center, respectively (black: GaAs, yellow: $Al_{0.4}Ga_{0.6}As$). (e)–(p) Components of the spin-up hole ground state $\psi_H^{\uparrow}$: $|HH\uparrow\rangle$ with no strain (e) and (f) and with an additional uniaxial strain ($\varepsilon = 0.1\,\%$) along the [1–10] direction (g) and (h); $|LH\uparrow\rangle$ with no strain (i) and (j) and with strain (k) and (l); $|LH\downarrow\rangle$ with no strain (m) and (n) and with strain (o) and (p). The two-dimensional graphs are constructed by integrating the density over the third (nondisplayed) coordinate. The color scale is normalized to the respective maxima.

It is instructive to discuss the envelope functions of different components of the ground hole state from the point view of symmetry. We introduce the total angular momentum $F = J + l^{\chi}$ of a particle as a sum of its zone-center Bloch wave total angular momentum J and the envelope function angular momentum l^{χ}. For a cylindric symmetry of the confinement potential (or as long as the deviation is small, which is the case of zero strain), the z projection of the total angular momentum F_z is a good quantum number and every component of the Luttinger spinor carries the same value of F_z. The dominant component of the valence-band spin-up ground-state $\psi_H^{\uparrow}$ is $|HH\uparrow\rangle$ with $J_z = +\frac{3}{2}$. The corresponding envelope function has $l_z^{\chi} = 0$, resulting in $F_z = +\frac{3}{2}$. Consequently, the envelope functions for $|LH\uparrow\rangle$ and $|LH\downarrow\rangle$ components (with $J_z = +\frac{1}{2}$ and $-\frac{1}{2}$) must have angular momentum l_z^{χ} of $+1$ and $+2$, respectively. The value of 1 for l_z^{χ} of the $|LH\uparrow\rangle$ is responsible for the node in the center of the density distribution (a donut shape of the envelope function) in Figs. 4(i) and 4(j). On the other hand, when external stress is applied, the symmetry is reduced and F_z is no longer a good quantum number. For that reason, the envelope function for the $|LH\downarrow\rangle$ component in Figs. 4(o) and 4(p) has $l_z^{\chi} = 0$ character. It has therefore nonzero spatial integral with the electron and renders the DE optically active.

The above discussion, which is based on noninteracting single electrons and mixed holes in our QDs, allows us to understand the origin of the observed brightening of DEs. However, the Coulomb, exchange, and correlation interactions must be taken into account to achieve a quantitative and complete description of the excitonic spectrum of QDs, i.e., the transition energies and decay rates. As an example, the above arguments are not sufficient to explain why only one of the two originally dark excitons is brightened (see Tables I and II).

VI. EFFECTS OF QD SIZE ON DARK EXCITON INTENSITY AND EMISSION ENERGY

The size of the QD affects the optical activity of the DE (in small QDs, the DEs remain dark, for larger QDs they become bright although no quantitative trend was experimentally observed) and the dark-to-bright exciton energy separation (which decreases with increasing QD size as shown in Fig. 2).

The fact that the strain brightens the DE more effectively in large QDs can be explained as follows. While the HHs and LHs are degenerate in the bulk, quantum confinement introduces an energy splitting between confined HH and LH levels. The larger the QD, the smaller is the splitting. For a particular value of anisotropic in-plane strain (and thus for the same magnitude of the mixing term in the Hamiltonian) the HH-LH mixing is more effective for small HH-LH splitting, i.e., in large QDs. This naturally results into a stronger optical activity of the DE. This conclusion is supported also by the simulations, as shown in Figs. 3(a) and 3(c).

Next, we discuss the dependence of ΔE_{DB} on the QD size. In Fig. 2 we show both experimental and theoretical values of ΔE_{DB} as functions of the exciton transition energy, which is used to represent the QD size (lower transition energy corresponds to taller QD and vice versa). We see that our calculations reproduce well both the magnitude of ΔE_{DB} and its increase with decreasing QD height. Note that strain has minor effects on ΔE_{DB}, as mentioned above. The increase of ΔE_{DB} with decreasing size (increasing emission energy) is attributed to the stronger Coulomb (and exchange) interaction in smaller QDs, which are characterized by more compact wave functions. The spread of the experimental data collected on small QDs may be due to the strong sensitivity to the specific shape of the nanoholes.

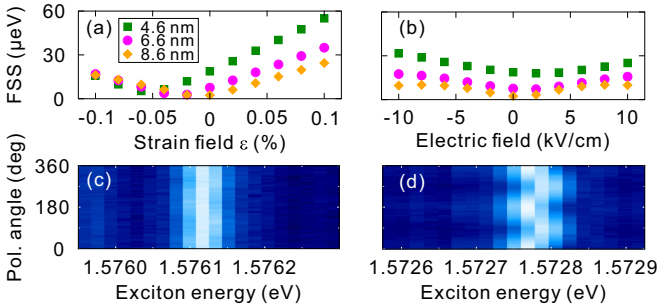

FIG. 5. (a) and (b) Calculated fine structure splitting (FSS) of the bright in-plane-polarized excitons as a function of strain (a) and electric field (b) for QDs with different sizes. (c) and (d) Representative color-coded polarization-resolved spectra (collected along the growth direction) of QDs, obtained by 2 nm GaAs filling, in the center and near the cleaved edge of a sample.

VII. EFFECTS OF CLEAVED FACET ON THE BRIGHT EXCITON FINE STRUCTURE SPLITTING

To further corroborate our conclusion that anisotropic strain is responsible for the brightening of DEs, we test here one prediction of our model, i.e., that the strain-induced symmetry reduction at cleaved facets leads to a sizable increase of the FSS of the bright doublets. Figures 5(a) and 5(b) show the calculated FSS as a function of strain field and electric field, respectively. The strain field results into an increase of FSS while the effect of an in-plane electric field is much smaller. Figures 5(c) and 5(d) show representative polarization-resolved spectra of QDs in the center and close to the edge (within 1 μm) of a 3 mm $\times$ 3 mm sample, respectively. In this case, μ-PL spectra were acquired with excitation and collection along the growth direction. Already from the raw data we see an increased FSS for QDs close to the sample edge, as expected. This observation is confirmed by measuring the FSS of several QDs [28]. The agreement between experiments and calculations supports our conclusions on the effects of strain and our explanation of the brightening of DE in the GaAs QDs.

VIII. CONCLUSION

In conclusion, we have reported on the observation of dark excitons confined in GaAs QDs close to a cleaved facet. The DEs are clearly visible in large dots and their energy separation from the dominant BEs tends to decrease with increasing QD size. We attribute the spontaneous brightening

of DEs to the symmetry breaking provided by anisotropic strain fields present at cleaved edges. Theoretical calculations using eight-band **k·p** theory reproduce well the experimental results and show that, while modest heavy-/light-hole mixing is already present in our QDs due to the quantum confinement, only anisotropic strain can lead to a significant brightening of the DEs. This work presents a straightforward method to access DEs in symmetric QDs, which may be used as long-lived states for spin storage in quantum technologies. At the same time it shows that both the hole mixing in QDs and the FSS of bright excitons are significantly affected by nearby edges. This means that even a cleaved edge suffices to make a dark exciton optically active, which has to be taken into account when a long lifetime of dark excitons is desirable or when integrating QDs in nanophotonic structures. On the other hand, we propose the possibility to have both optically active and inactive dark excitons on a single sample, where the patterning of the sample would allow their positions to be controlled. Finally, by relying on the progress in dynamic manipulation of strain in QDs [36,37], we envision the possibility of dynamically switching on/off a DE via application of anisotropic stress pulses.

ACKNOWLEDGMENTS

This work was financially supported by the FWF (project P29603), BMBF project QuaHL-Rep (Contracts No. 01BQ1032 and No. 01BQ1034), the European Union Seventh Framework Programme (FP7/2007-2013) under Grant Agreement No. 601126 (HANAS), and the Natural Science Foundation of Shanghai (Contract No. 17ZR1443900). Huo thanks the support of CAS 100 Talents Programme, V.K. was supported by the Ministry of Education of the Czech Republic, Project No. LQ1601 (CEITEC 2020). We thank E. Zallo and R. Engelhard for MBE assistance, A. Halilovic for SEM assistance, and J. X. Zhang, S. Kumar, and R. Trotta for discussions on the optical measurements.

[1] S. Lüker, T. Kuhn, and D. E. Reiter, Phys. Rev. B **92**, 201305(R) (2015).
[2] J. McFarlane, P. A. Dalgarno, B. D. Gerardot, R. H. Hadfield, R. J. Warburton, K. Karrai, A. Badolato, and P. M. Petroff, Appl. Phys. Lett. **94**, 093113 (2009).
[3] E. Poem, Y. Kodriano, C. Tradonsky, N. H. Lindner, B. D. Gerardot, P. M. Petroff, and D. Gershoni, Nat. Phys. **6**, 993 (2010).
[4] M. Goryca, P. Plochocka, T. Kazimierczuk, P. Wojnar, G. Karczewski, J. A. Gaj, M. Potemski, and P. Kossacki, Phys. Rev. B **82**, 165323 (2010).
[5] C. Gautham, D. W. Snoke, A. Rastelli, and O. G. Schmidt, Appl. Phys. Lett. **104**, 143114 (2014).
[6] M. Nirmal, D. J. Norris, M. G. Bawendi, A. L. Efros, and M. Rosen, Phys. Rev. Lett. **75**, 3728 (1995).
[7] M. Bayer, A. Kuther, A. Forchel, A. Gorbunov, V. B. Timofeev, F. Schäfer, J. P. Reithmaier, T. L. Reinecke, and S. N. Walck, Phys. Rev. Lett. **82**, 1748 (1999).
[8] M. Bayer, O. Stern, A. Kuther, and A. Forchel, Phys. Rev. B **61**, 7273 (2000).
[9] D. Gammon, Al. L. Efros, T. A. Kennedy, M. Rosen, D. S. Katzer, D. Park, S. W. Brown, V. L. Korenev, and I. A. Merkulov, Phys. Rev. Lett. **86**, 5176 (2001).
[10] M. Bayer, G. Ortner, O. Stern, A. Kuther, A. A. Gorbunov, A. Forchel, P. Hawrylak, S. Fafard, K. Hinzer, T. L. Reinecke, S. N. Walck, J. P. Reithmaier, F. Klopf, and F. Schäfer, Phys. Rev. B **65**, 195315 (2002).
[11] K. Kowalik, O. Krebs, A. Golnik, J. Suffczyński, P. Wojnar, J. Kossut, J. A. Gaj, and P. Voisin, Phys. Rev. B **75**, 195340 (2007).
[12] T. Smoleński, T. Kazimierczuk, M. Goryca, T. Jakubczyk, Ł. Kłopotowski, Ł. Cywiński, P. Wojnar, A. Golnik, and P. Kossacki, Phys. Rev. B **86**, 241305(R) (2012).
[13] M. Korkusinski and P. Hawrylak, Phys. Rev. B **87**, 115310 (2013).
[14] S. Kumar, E. Zallo, Y. H. Liao, P. Y. Lin, R. Trotta, P. Atkinson, J. D. Plumhof, F. Ding, B. D. Gerardot, S. J. Cheng, A. Rastelli, and O. G. Schmidt, Phys. Rev. B **89**, 115309 (2014).
[15] Y. H. Huo, A. Rastelli, and O. G. Schmidt, Appl. Phys. Lett. **102**, 152105 (2013).
[16] Y. H. Huo, V. Křápek, A. Rastelli, and O. G. Schmidt, Phys. Rev. B **90**, 041304(R) (2014).
[17] Y. H. Huo, B. J. Witek, S. Kumar, J. R. Cardenas, J. X. Zhang, N. Akopian, R. Singh, E. Zallo, R. Grifone, D. Kriegner, R. Trotta, F. Ding, J. Stangl, V. Zwiller, G. Bester, A. Rastelli, and O. G. Schmidt, Nat. Phys. **10**, 46 (2014).
[18] P. Lodahl, S. Mahmoodian, and S. Stobbe, Rev. Mod. Phys. **87**, 347 (2015).
[19] O. Stier, M. Grundmann, and D. Bimberg, Phys. Rev. B **59**, 5688 (1999).
[20] J. M. Luttinger and W. Kohn, Phys. Rev. **97**, 869 (1955).
[21] G. Bastard, Phys. Rev. B **24**, 5693 (1981).
[22] G. E. Pikus and G. L. Bir, Fiz. Tverd. Tela (Leningrad) **1**, 1642 (1959) [Sov. Phys. Solid State **1**, 1502 (1960)].
[23] O. Stier, Electronic and optical properties of quantum dots and wires, Ph.D. thesis, Technische Universitat Berlin, Berlin, 2001.
[24] T. Takagahara, Phys. Rev. B **62**, 16840 (2000).
[25] J. D. Plumhof, V. Křápek, L. Wang, A. Schliwa, D. Bimberg, A. Rastelli, and O. G. Schmidt, Phys. Rev. B **81**, 121309 (2010).
[26] V. Křápek, P. Klenovský, and T. Šikola, Phys. Rev. B **92**, 195430 (2015).
[27] L. Wang, V. Křápek, F. Ding, F. Horton, A. Schliwa, D. Bimberg, A. Rastelli, and O. G. Schmidt, Phys. Rev. B **80**, 085309 (2009).
[28] See Supplemental Material at http://link.aps.org/supplemental/10.1103/PhysRevB.95.165304 for details of the cleaved edge, intensity and polarization of the excitonic emissions, and excitonic fine structure splitting.
[29] G. P. Srivastava, Rep. Prog. Phys. **60**, 561 (1997).
[30] J. M. Dallesasse, N. Holonyak Jr., A. R. Sugg, T. A. Richard, and N. El-Zein, Appl. Phys. Lett. **57**, 2844 (1990).
[31] J. H. Luscombe and C. L. Frenzen, Solid-State Electron. **46**, 885 (2002).
[32] T. A. Germer, K. W. Kołasinski, J. C. Stephenson, and L. J. Richter, Phys. Rev. B **55**, 10694 (1997).
[33] As all our samples have no intentional doping, the depletion field from background doping is in fact rather small (∼3 kV/cm). Depletion length $W = [2\varepsilon\Phi/(e2N_d)]^{1/2}$, ε is dielectric

constant, Φ is surface potential energy barrier ($\sim$0.68 eV), e is charge of electron, and N_d is background doping density ($\sim 2.5 \times 10^{14}\,\mathrm{cm}^{-3}$).

[34] J. I. Climente, M. Korkusinski, G. Goldoni, and P. Hawrylak, Phys. Rev. B **78**, 115323 (2008).

[35] J.-W. Luo, G. Bester, and A. Zunger, Phys. Rev. B **92**, 165301 (2015).

[36] J. Martín-Sánchez, R. Trotta, G. Piredda, C. Schimpf, G. Trevisi, L. Seravalli, P. Frigeri, S. Stroj, T. Lettner, M. Reindl, J. S. Wildmann, J. Edlinger, and A. Rastelli, Adv. Opt. Mater. **4**, 682 (2016).

[37] F. J. R. Schülein, E. Zallo, P. Atkinson, O. G. Schmidt, R. Trotta, A. Rastelli, A. Wixforth, and H. J. Krenner, Nat. Nanotechnol. **10**, 512 (2015).

L Quantum entanglement in lateral GaAs/AlGaAs quantum dot molecules

Journal of Physics: Conference Series **245** (2010) 012027 doi:10.1088/1742-6596/245/1/012027

Quantum entanglement in lateral GaAs/AlGaAs quantum dot molecules

V Křápek[1,2], P Klenovský[1], A Rastelli[2], O G Schmidt[2] and D Munzar[1]

[1]Department of Condensed Matter Physics, Masaryk University, Kotlářská 2, 61137 Brno, Czech Republic

[2]Institute for Integrative Nanosciences, IFW-Dresden, Helmholtzstr. 20, D01187 Dresden, Germany

E-mail: krapek@physics.muni.cz

Abstract. We calculate the excitonic structure of pairs of GaAs/AlGaAs quantum dots forming lateral molecules and obtain the entanglement of exciton states. The following advantages of the lateral geometry over the vertical one are found: (1) The energy structures of the dots forming a molecule can be in principle identical. (2) Comparable tunneling of electrons and holes ensures a high entanglement of antisymmetric excitons. A drawback of existing structures are very low tunneling energies, which make the entanglement vulnerable against differences in the sizes and shapes of both dots.

1. Introduction

Peculiar properties of the quantum computing allow to design algorithms superior to classic ones. A prominent example is Shor's algorithm factoring large numbers with a polynomial time complexity. Quantum algorithms rely on two-state quantum systems – qubits, and devices coherently manipulating qubits – quantum gates. They might be realized in various physical systems, among which semiconductor quantum dots (QDs) offer several advantages such as easy integration with existing electronic devices. The representation of the qubit by a charge confined in a vertical quantum dot molecule (QDM), with the position in the lower/upper dot representing the 0/1 state, has been proposed [1]. The proposal has been later criticized as based on non-realistic assumptions [2]. In particular, inevitable differences between the electronic structures of the individual dots lower the entanglement significantly. Another drawback is the difference between the tunneling energies for electrons and holes, which further reduces the entanglement of optically dark excitons.

Recent progress in the growth technology makes it possible to prepare *lateral* QDMs. The interaction between the laterally closely spaced dots has been reported for the InAs/GaAs system [3]. There are also GaAs/AlGaAs quantum dot pairs in which a mutual interaction is expected [4]. The main advantage of the lateral topology is that there is no *a-priori* obstruction in making both dots identical from the point of view of their electronic structure. In contrast, in the vertical arrangement the strain field in the lower dot and in the upper dot differs. By manipulating the dot sizes, we can put into resonance either the electron levels or the hole levels, but not both at the same time. No such restriction applies to the lateral topology. Lateral QDMs also have the advantage of comparable tunneling energies of electrons and holes [5].

In this paper we present calculations of the excitonic structure of lateral QDMs consisting of two overlapping cones and of the related entanglement. We briefly discuss the characteristic energies of QDMs and their impact on the entanglement: Coulomb attraction, tunneling, and detuning. Realistic calculations follow, which combine the eight-band $\vec{k} \cdot \vec{p}$ method for single particle states with the configuration interaction method; the typical shape and dimensions of the dots are taken from Refs. [4, 6].

2. Entanglement: Effect of characteristic energies

A quantum system consisting of two particles A and B in states $|\phi_A\rangle$ and $|\phi_B\rangle$ is described by the product state $|\phi_{AB}\rangle = |\phi_A\rangle|\phi_B\rangle$, e.g., $|0_A 0_B\rangle$. Applying the principle of superposition to the product states we can construct also states which cannot be expressed as products of individual particle states, a prominent example being $|0_A 0_B\rangle + |1_A 1_B\rangle$. These are so called *entangled* states. If the system is in an entangled state, the properties of the components are correlated. Here the composed system is an exciton and the components are an electron and a hole.

The entanglement of an exciton in a QDM can be explained in terms of an interplay of three characteristic mechanisms: Coulomb attraction, tunneling, and detuning. To study this effect we employ a simple tight binding (TB) model of a QDM [1, 2]. Let $|e_0\rangle$, $|e_1\rangle$ denote the states of electrons in individual dots labelled as 0 and 1 (representing the 0 and 1 of a qubit), $|h_0\rangle$, $|h_1\rangle$ denote the corresponding hole states. In the basis $|e_0 h_0\rangle$, $|e_0 h_1\rangle$, $|e_1 h_0\rangle$, $|e_1 h_1\rangle$, the Hamiltonian reads

$$\begin{bmatrix} E_0 - H_0 - U_{00} & -t_H & -t_E & 0 \\ -t_H & E_0 - H_1 - U_{01} & 0 & -t_E \\ -t_E & 0 & E_1 - H_0 - U_{10} & -t_H \\ 0 & -t_E & -t_H & E_1 - H_1 - U_{11} \end{bmatrix}$$

Here E_i and H_i are energies of electrons and holes in dot i, t_E and t_H are the tunneling matrix elements and $-U_{ij}$ are the Coulomb energies.

The number of parameters can be further reduced by the following assumptions. We introduce the *detuning* energy Δ due to the difference in the dot dimensions: $E_0 = E_1 + \Delta/2$, $H_0 = H_1 - \Delta/2$. We assume that $U_{00} = U_{11} = U_D$, $U_{01} = U_{10} = U_I$; $U = U_D - U_I$ is the *Coulomb* energy favoring the direct configurations over the indirect. Denoting $E_g = E_1 - H_1 - U_I$ we rewrite the Hamiltonian as

$$\begin{bmatrix} E_g + \Delta - U & -t_H & -t_E & 0 \\ -t_H & E_g + \Delta/2 & 0 & -t_E \\ -t_E & 0 & E_g + \Delta/2 & -t_H \\ 0 & -t_E & -t_H & E_g - U \end{bmatrix}$$

Following [1, 2], we classify the eigenstates according to the following fully entangled states: $|a\rangle = (|e_0 h_0\rangle + |e_1 h_1\rangle)/\sqrt{2}$ (direct, symmetric), $|b\rangle = (|e_0 h_1\rangle + |e_1 h_0\rangle)/\sqrt{2}$ (indirect, symmetric), $|c\rangle = (|e_0 h_1\rangle - |e_1 h_0\rangle)/\sqrt{2}$ (indirect, antisymmetric), $|d\rangle = (|e_0 h_0\rangle - |e_1 h_1\rangle)/\sqrt{2}$ (direct, antisymmetric). The degree of entanglement can be quantified via the entropy of entanglement $S = -\mathrm{Tr}\rho_A \log_2 \rho_A$ with $\rho_A = \mathrm{Tr}_\mathrm{B}\rho$, where ρ is the density matrix of the exciton, ρ_A is the reduced density matrix of one component (e.g., electron), Tr_B is the partial trace over the other component (e.g., hole). The maximal value of the entropy of entanglement for the considered system is 1.

Figure 1 shows the entanglement of the two lowest excitonic states $|\alpha\rangle$ (with the dominant component $|a\rangle$) and $|\delta\rangle$ (with the dominant component $|d\rangle$) calculated for $U = 10$ meV, $\Delta = 1$ meV and variable t_E and t_H. We consider either $t_E = t_H$ (the ideal case) or $t_E = 3t_H$ (the largest difference found in our realistic model of lateral QDMs, see Fig. 2). For $|\alpha\rangle$ there exists an optimal tunneling for which the entanglement is the largest. For lower tunneling, the

detuning prevents the formation of symmetric and antisymmetric orbitals and only one direct configuration dominates the state. For higher tunneling, the Coulomb term looses its importance and the contribution of indirect terms increases. The state $|\delta\rangle$ exhibits similar behavior with a slightly enhanced entanglement if t_E and t_H differ. However, if $t_E = t_H$, then entanglement of this state increases as tunneling increases and is fairly large.

The strategies to obtain a large degree of entanglement have to aim at $\Delta \ll t \ll U$. Exploiting of $|\delta\rangle$ is recommendable because of the larger entanglement as compared to $|\alpha\rangle$.

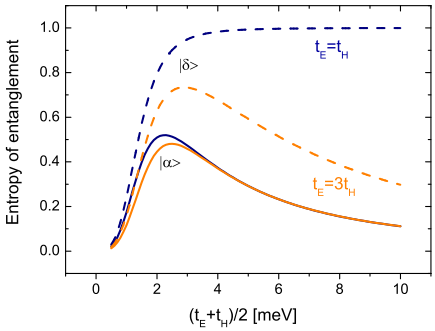

Figure 1. The entropy of entanglement of two lowest excitonic states: $|\alpha\rangle$ (full lines) and $|\delta\rangle$ (dashed lines) from a TB model. The values of the input parameters are $U = 10$ meV, $\Delta = 1$ meV. The values of t_E and t_H are either the same (blue lines) or $t_E = 3t_H$ (orange lines).

3. Realistic lateral molecules

The realistic calculations consist of two steps. First, we employ the eight band $\vec{k} \cdot \vec{p}$ method to obtain the single particle states. Second, these states are used as basis states for the configuration interaction method yielding the excitons. The values of the material parameters are taken from [7].

The model dots studied here correspond to two realistic systems which use GaAs as the dot material and AlGaAs as the host material: "molecules" [4] and "single dots" [6]. As described in Refs. [4, 6], the dots consist of pure GaAs, the bottom barrier consists of $Al_{0.45}Ga_{0.55}As$ and the top barrier of $Al_{0.35}Ga_{0.65}As$. The shape and dimensions of the structures are obtained with a rather good accuracy from atomic force micrographs. The dots forming the molecule are not completely separate (see Fig. 18 of Ref. [4] and inset of Fig. 2). "Molecules" are modeled as two reverted cones with the characteristic height h of 4 nm, the characteristic radius r of 30 nm, and the distance between the centers of the cones d of 32 nm. For "single dots" structure the values of the parameters are $h = 4$ nm, $r = 14$ nm, $d = 20$ nm; further, the tips of both cones are connected with a mound, which turns the hypothetic molecule into a single dot. However, there is still a lateral narrowing between the tips. In our study we adopted the shape of two reverted cones (we do not consider the connecting mound in "single dots"). We also allow d to vary in order to explore possibilities of improving the existing structures.

For very low values of d the QDM behaves as a single QD. Since the proposal of the qubit under consideration requires that the position of individual particles in one of the dots is well defined, we set the following criterion: The system of two cones forms a molecule if the probability density of the ground state in the area separating the cones is below 25 % of its maximum value. This criterion is fulfilled if $d > 14$ nm for $r = 14$ nm and $d > 21$ nm for $r = 30$ nm. To validate that such structures are molecules, we have calculated the effect of an electric field on them (not shown here). In a molecule it is possible to localize the charge carrier in one of the dots by adding a proper detuning (represented by the electric field), different from single dots. The molecular behavior of our structures was confirmed. Modifying the above mentioned criterion to 1 % leads to $d > 20$ nm for $r = 14$ nm and $d > 29$ nm for $r = 30$ nm, resulting in an extremely weak coupling between the dots. Therefore we have to accept a large probability density in the separation area as a drawback of considered lateral QDMs. The reason for this undesirable behavior is the shallow barrier between the dots, realized as the narrowing of the dot material only. This point should be considered in improving the growth technology.

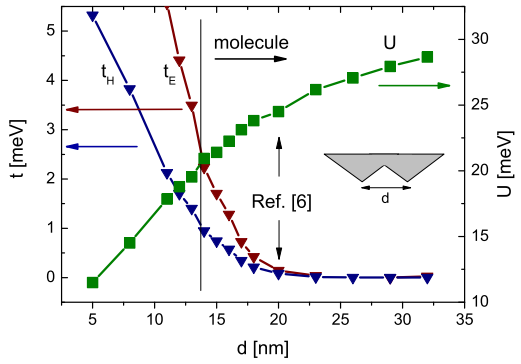

Figure 2. Tunneling energies t_E (brown) and t_H (blue) and the Coulomb energy U (green) as functions of d for a model QDM with $h = 4$ nm and $r = 14$ nm. The molecular limit (probability density in the separation area equal to 25 % of its maximum) is displayed as the vertical black line, the realistic d is denoted with the black arrows. The inset shows a schema of the model structure.

Figure 2 shows t_E, t_H and U as functions of d for $h = 4$ nm and $r = 14$ nm (the results for $r = 30$ nm are not shown). The electron tunneling for d corresponding to existing structures (32 and 20 nm for r of 30 and 14 nm, respectively) is below 0.15 meV, yielding a negligible entanglement for a realistic detuning. At the molecular limit, however, it increases towards 2.2 meV ($r = 14$ nm) and 1.5 meV ($r = 30$ nm). The t_E/t_H ratio varies between 2 and 3. This is a considerable improvement compared to vertical QDMs, where values above 10 are predicted [2]. The Coulomb energy U is around 20 meV for the distances d yielding a reasonable tunneling. Using the TB model and assuming a detuning $\Delta = 1$ meV, we obtain the maximum entanglement for t_E around 3 meV, a slightly larger value than that we obtained for simulated QDMs. We also calculated the expected detuning by varying the radius of a model dot. The distribution of r with a standard deviation of 0.25 nm (1 nm) yielded a detuning up to 1 meV (5 meV). For the molecule with $h = 4$ nm, $r_1 = 13.9$ nm, $r_2 = 14.1$ nm, $d = 14$ nm we obtained the entropy of entanglement $S = 0.17$ for $|\alpha\rangle$ and $S = 0.20$ for $|\delta\rangle$, while for zero detuning it was $S = 0.94$ for $|\alpha\rangle$ and $S = 0.99$ for $|\delta\rangle$. The minimization of the detuning is therefore essential.

4. Conclusion

In conclusion, existing lateral QDMs presented in Ref. [4] suffer from low tunneling energies (below 0.15 meV). Nevertheless, sufficiently large values (up to 2 meV) can be obtained for the dots brought closer to each other. The ratio t_E/t_H is considerably smaller than in vertical QDMs. The strategy to enhance the entanglement should consist of the following steps: (1) Reducing the distance between QDs in a QDM. (2) Reducing the lateral dimension of QDs and improving the barrier properties, resulting in a full separation of the QDs. (3) Minimization of the detuning by improving the homogeneity of QDs.

Acknowledgments

The work was supported by the Institutional research program MSM 0021622410, the GACR grant GA202/09/0676, and the DFG (FOR730).

References

[1] Bayer M, Hawrylak P, Hinzer K, Fafard S, Korkusinski M, Wasilewski Z, Stern O and Forchel A 2001 *Science* **291** 451
[2] Bester G, Zunger A and Shumway J 2005 *Phys. Rev. B* **71** 075325
[3] Beirne G, Hermannstadter C, Wang L, Rastelli A, Schmidt O and Michler P 2006 *Phys. Rev. Lett.* **96** 137401
[4] Wang L, Rastelli A, Kiravittaya S, Benyoucef M and Schmidt O G 2009 *Adv. Mater.* **21** 2601
[5] Wang L, Křápek V, Ding F, Horton F, Schliwa A, Bimberg D, Rastelli A and Schmidt O G 2009 *Phys. Rev. B* **80** 085309
[6] Rastelli A, Stufler S, Schliwa A, Songmuang R, Manzano C, Costantini G, Kern K, Zrenner A, Bimberg D and Schmidt O 2004 *Phys. Rev. Lett.* **92** 166104
[7] Vurgaftman I, Meyer J and Ram-Mohan L 2001 *J. Appl. Phys.* **89** 5815

M Strain-induced active tuning of the coherent tunneling in quantum dot molecules

PHYSICAL REVIEW B **89**, 241303(R) (2014)

Strain-induced active tuning of the coherent tunneling in quantum dot molecules

E. Zallo,[1,*] R. Trotta,[1,2] V. Křápek,[3] Y. H. Huo,[1] P. Atkinson,[4] F. Ding,[1] T. Šikola,[3] A. Rastelli,[1,2] and O. G. Schmidt[1,5,6]

[1]*Institute for Integrative Nanosciences, IFW Dresden, Helmholtzstrasse 20, D-01069 Dresden, Germany*

[2]*Institute of Semiconductor and Solid State Physics, Johannes Kepler University Linz, Altenbergerstrasse 69, A-4040 Linz, Austria*

[3]*Central European Institute of Technology, Brno University of Technology, Technická 10, CZ-61600 Brno, Czech Republic*

[4]*Sorbonne Universités, UPMC Université Paris 06, CNRS, UMR 7588, INSP, 4 place Jussieu, F-75005 Paris, France*

[5]*Material Systems for Nanoelectronics, Technische Universität Chemnitz, Reichenhainerstrasse 70, D-09107 Chemnitz, Germany*

[6]*Center for Advancing Electronics Dresden, Technische Universität Dresden, Georg-Schumannstrasse 11, D-01187 Dresden, Germany*

(Received 13 November 2013; revised manuscript received 12 May 2014; published 19 June 2014)

We demonstrate experimentally the possibility to manipulate the coupling strength in an asymmetric pair of electronically coupled InGaAs quantum dots by using externally induced strain fields. The coupling strength of holes confined in the dots increases linearly with increasing tensile strain. A model based on $\boldsymbol{k}\cdot\boldsymbol{p}$ theory explains the effect in terms of modified weight of the light hole component mediating the coupling in the barrier. Our results are relevant to the creation and control of entangled states in optically active quantum dots.

DOI: 10.1103/PhysRevB.89.241303 PACS number(s): 78.67.Hc, 78.20.hb, 78.55.Cr, 85.35.Be

A quantum dot molecule (QDM)—two semiconductor QDs separated by a thin barrier—represents a striking example of the analogy between artificial and natural atomic combinations. Similar to the energy levels in a hydrogen molecule, bonding and antibonding states are formed via coherent tunneling [1] of charges in a QDM, giving rise to anticrossing (AC) patterns in the electric-field dependent photoluminescence (PL) spectra [2–5]. This artificial quantum system has a potential application as a quantum gate in quantum information processing [6–8], mainly due to the possibility to initialize and control entanglement between solid-state qubits [9–13]. Although the fine structure of the optical spectra and the spin properties of QDMs made of two vertically stacked InGaAs QDs in a GaAs matrix are now well understood [11,14–16], active control of the coupling strength between the two QDs—the key parameter determining the operation rate of quantum gates [9,10]—still needs to be demonstrated. In particular, the probability of a Landau-Zener transition [17] (the transition from one AC branch to the other), important in qubit manipulation [10], increases exponentially as the coupling strength is decreased. Some qubit proposals [1] also require comparable electron and hole tunneling rates [13]. Contrary to (optically inactive) electrostatically defined QDMs [18,19], the spacer thickness in vertical QDMs is frozen and there is no growth protocol [20] allowing an active control over the spin qubit. A postgrowth tuning of the coherent tunneling would overcome this shortcoming. Longitudinal or transverse magnetic fields were predicted to affect the coupling strength in vertical QDMs [21–24], but more recent experiments and refined theoretical treatments have shown no significant changes for fields up to 6 T [25]. Therefore, it remains unclear if and how the tunneling rate of carriers in a vertical QDM can be tuned.

In this Rapid Communication, we demonstrate active tuning of the coupling strength of holes confined in individual InGaAs/GaAs QDMs by externally induced strains. Eight-band $\boldsymbol{k}\cdot\boldsymbol{p}$ calculations reveal that the origin of the observed effect is a strain-induced modification of the heavy hole (HH) and light hole (LH) effective confinement potentials, which in turn change the probability density for the hole states and thus the coupling strength between the dots.

The device design employed in this work [26,27] allows large stress and electric fields to be applied to single QDMs. The QDMs consist of two vertically stacked InGaAs QDs [28] embedded in the intrinsic region of n-i-p nanomembranes integrated onto piezoelectric actuators made of lead magnesium niobate–lead titanate (PMN-PT); see Fig. 1(a). The QDs are grown on a semi-insulating GaAs (001) substrate by molecular beam epitaxy at the center of a 10 nm thick $GaAs/Al_{0.4}Ga_{0.6}As$ quantum well, in order to reduce carrier escape at high electric fields (F_d) across the diode [29]. The QD height, which has a major influence on the confinement energy, was controlled by means of the *indium flush* method [30]. The different confined energy levels in the two dots are tuned into resonance by applying a voltage (V_d) across the nanomembranes. Simultaneously, in-plane (compressive or tensile) biaxial stress is transferred to the QD layers [31] by applying a voltage (V_p) across the PMN-PT. While piezoelectric-induced strains have been used previously to control several properties of semiconductor structures [32–36], their potential in the field of QDMs still needs to be explored. The micro-PL (μPL) measurements were performed at 6 K in a helium flow cryostat with a 50× microscope objective (numerical aperture = 0.42). The device was excited with a 532 nm continuous-wave laser and the signal was collected by the same microscope objective used for the excitation and analyzed by a single (double) spectrometer featuring ~30 μeV (~15 μeV) spectral resolution. The degree of linear polarization of the PL signal was analyzed by combining a rotatable achromatic half-wave plate and a fixed linear polarizer. For more details see the Supplemental Material [37].

Figure 1(b) shows the simultaneous effect of electric and strain fields on a representative InGaAs QDM. By sweeping the electric field across the diode (F_d in $[-14.4,-6.5]$ kV/cm), the X-shaped pattern of the positively charged exciton (X^+) [4] can be clearly observed. The magnitude of AC energy gaps (ΔE_{AC}) [20], defined as the minimum energy splitting between bonding and antibonding states, and polarized cross-correlation measurements between X^+ and X^0 [38] confirm

*e.zallo@ifw-dresden.de

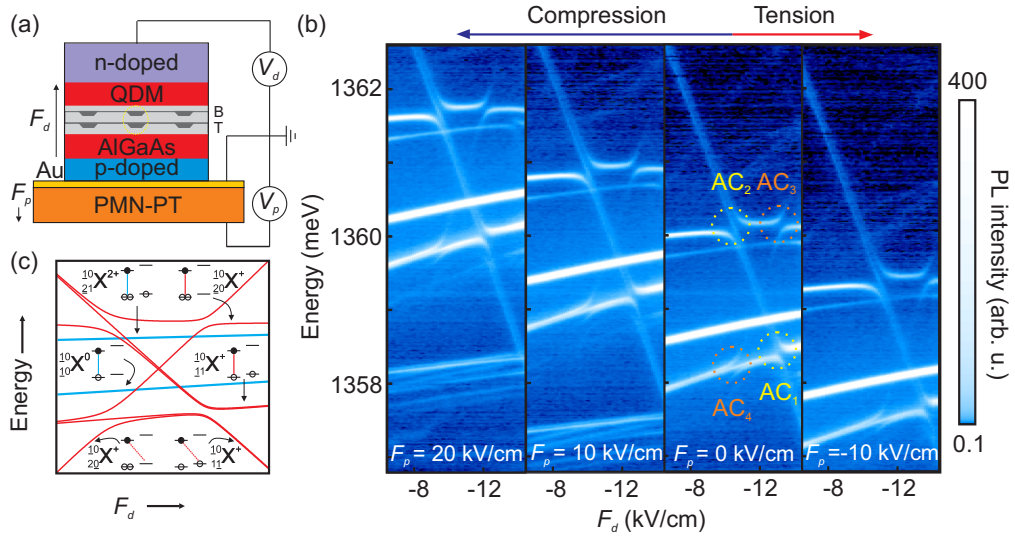

FIG. 1. (Color online) (a) Sketch of the device. Vertically stacked, disk-shaped InGaAs QDs (bottom-B/top-T QD with a nominal height of 2.9/3.3 nm and a spacer thickness of 5.4 nm) are embedded in n-i-p nanomembranes integrated on top of a piezoelectric actuator (PMN-PT) allowing in situ application of biaxial stresses by tuning the voltage (electric field) V_p (F_p). Independently, a voltage V_d applied to the nanomembranes allows the electric field (F_d) across the QDs to be controlled. (b) Color-coded microphotoluminescence (μPL) maps of a representative QDM as a function of F_p and F_d (PL intensity in logarithmic scale). The typical anticrossings observed (AC_{1-4}) are associated with hole tunneling and are marked on the map at $F_p = 0$ kV/cm. (c) Sketch of the transition energies of the positively charged (X^+) and neutral (X^0) excitons in a QDM (the X^+ pattern is obtained by the formula reported in the Supplemental Material [37]). By sweeping F_d, different transitions are defined: two direct (${}^{10}_{20}X^+$ and ${}^{10}_{11}X^+$) and two indirect (${}^{10}_{11}X^+$ and ${}^{10}_{20}X^+$) with a larger Stark shift. The two additional lines are direct recombinations arising from the neutral exciton (${}^{10}_{10}X^0$) and the doubly positively charged exciton (${}^{10}_{21}X^{2+}$).

this identification. The typical behavior of the excitonic energy levels as a function of the electric field is sketched in Fig. 1(c). As in Ref. [4], we consider transitions between the initial (X^+) and the final (single hole) states. Two indirect transitions, ${}^{10}_{11}X^+$ and ${}^{10}_{20}X^+$, where electrons and holes recombine in different dots, anticross two direct transitions, ${}^{10}_{20}X^+$ and ${}^{10}_{11}X^+$, where the recombination takes place in the same dot [39]. The ACs have a magnitude ranging between 0.2 and 0.4 meV, reflecting the overlap of the charge carrier wave functions in the interdot region [1], and appear at different F_d because of different Coulomb interaction values. The AC_1 and AC_2 (see the map at the strain field $F_p = 0$ kV/cm) represent the anticrossing of ${}^{10}_{11}X^+$ and ${}^{10}_{20}X^+$, respectively, with ${}^{10}_{11}X^+$. The AC_3 and AC_4 are obtained by the anticrossing of the direct trion recombinations with the weak transition ${}^{10}_{20}X^+$, theoretically forbidden because of no holes in the final state but partially tunnel induced in the experiment. The lines going through AC_2 and AC_4 have previously been assigned to the spin triplet configuration of the two holes in X^+ due to Pauli blocking [15,40], because tunneling conserves spin and the anticrossing lines represent singlet spin states. Indirect transitions show more pronounced Stark shifts (the change in energy with electric field) than direct excitons due to their larger static electric dipole. From the slope of the energy of the indirect transitions with respect to F_d we infer an electron-hole (e-h) average distance of ∼7 nm, in reasonable agreement with the nominal center-to-center dot separation ($d = 8.5$ nm). Two additional direct recombination lines are observed in the spectra: The brightest line stems from the neutral exciton, ${}^{10}_{10}X^0$, and the weak line from the doubly positively charged exciton, ${}^{10}_{21}X^{2+}$. From the slope of the direct transition we obtain a permanent exciton dipole ∼0.48 e nm, where the positive sign means that the electron wave function is shifted towards the dot apex, possibly due to local In enrichment [41].

In the following we focus on the strain effects on the coupling signature of the X^+. When biaxial stress is applied to the nanomembrane, the spectrum changes significantly. The PL emission lines blueshift (redshift) for positive (negative) F_p, due to compressive (tensile) strain [35,36]. At the same time the values of F_d at which ACs occur increase (decrease) under compressive (tensile) strain, as predicted in Ref. [42]. By comparison with previous work [27], we estimate that in-plane strain transferred to the GaAs nanomembrane varies by about 0.06%, when F_p is swept through the whole tuning range ($\Delta F_p = 30$ kV/cm), and the corresponding energy shift of the neutral exciton (ΔE_p) is about 2.4 meV.

The most important result of this work is revealed by the higher resolution μPL spectra of the same QDM, shown in Fig. 2. In Figs. 2(a) and 2(b) we compare the region of AC_1 at the highest and lowest F_p (20 and −10 kV/cm), corresponding respectively to the highest value of compressive and tensile strains achieved in our device. We observe that application of compressive (tensile) stress leads to a reduction (increase) of the tunnel coupling. In particular, we measure a linear increase of ΔE_{AC_1} by 27 μeV for $\Delta E_p = 2.4$ meV [see Fig. 2(f)], where ΔE_{AC_1} was obtained by fitting the energy splitting between bonding and antibonding states (ΔE) as a function of F_d [see Fig. 2(e)]. For details about the fitting procedure, see Ref. [37]. A more pronounced effect was measured for AC_2 with a tuning range of 48 μeV in the same interval of fields, as shown in Figs. 2(c), 2(d), and 2(f). Therefore, our data clearly demonstrate that the combination of strain and

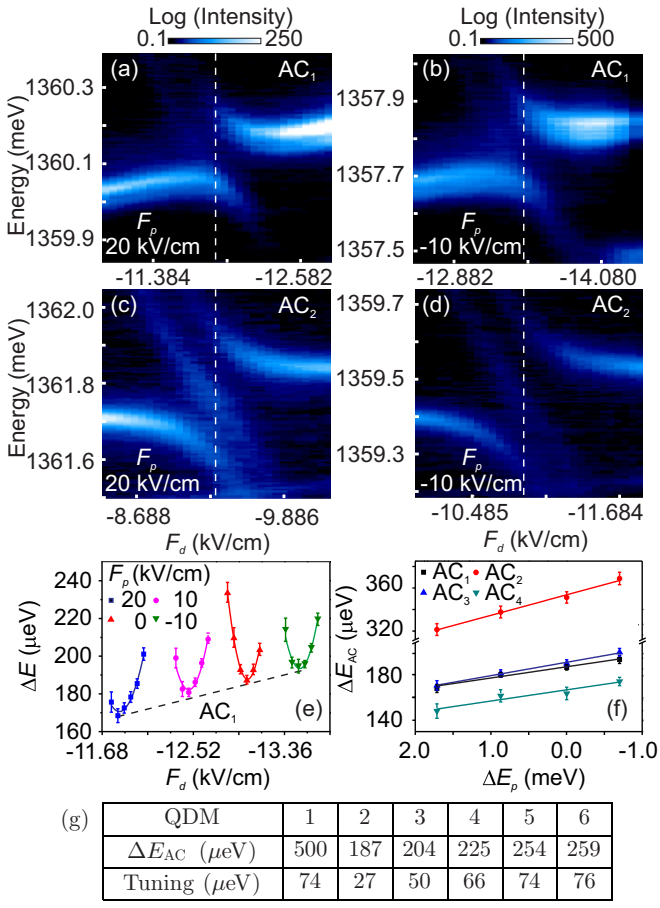

(g)

QDM	1	2	3	4	5	6
ΔE_{AC} (μeV)	500	187	204	225	254	259
Tuning (μeV)	74	27	50	66	74	76

FIG. 2. (Color online) Color-coded μPL maps of the (a), (b) AC_1 and (c), (d) AC_2 regions as a function of F_d at $F_p = 20$ kV/cm (compressive strain, -0.04%) and $F_p = -10$ kV/cm (tensile strain, 0.02%), respectively. The dashed line marks the AC position. (e) Parabolic behavior of the energy splitting (ΔE) between the bonding and antibonding molecular states around AC_1 as a function of F_d at $F_p = 20$, 10, 0, -10 kV/cm. (f) Behavior of ΔE_{AC} at AC_{1-4} as a function of the neutral exciton PL energy shift (ΔE_p), when F_p is varied through the whole tuning range ($\Delta F_p = 30$ kV/cm). (g) ΔE_{AC} and the tuning range of the coupling strength in the range $F_p = 20$ to -10 kV/cm for six QDMs.

electric fields allows the coupling strength of the QDM to be actively manipulated.

Very similar results were obtained in six other QDMs chosen randomly in our device; see Fig. 2(g). Specifically, we find that ΔE_{AC} fluctuates between different QDMs with an average value of (270 ± 120) μeV. This is due to fluctuations over the size, shape, and composition among the different QDs and it is related to the lack of control over the QD growth processes. On the other hand, the effect of the induced strain is quite similar for all the investigated QDMs, with an average value of (61 ± 19) μeV. We argue that by increasing the strain induced in the membrane up to 0.4%, as obtained in Ref. [27], we would be able to obtain the same predefined coupling strength for any QDM in our sample (see Ref. [37] for details).

From the linear fit of the ΔE_{AC} as a function of ΔE_p we obtain a slope ratio $\alpha(AC_2)/\alpha(AC_1) = 1.9$. This result is consistent with the coupling dynamics obtained by the formula $\Delta E_{AC_2} = \sqrt{2}\Delta E_{AC_1}\sqrt{1 + 2J_{eh}^2/\Delta E_{AC_1}^2}$ as reported in Ref. [15], where J_{eh} is the e-h exchange energy [16] and the factor $\sqrt{2}$ considers the tunneling of two holes between the two dots. The unpaired hole spin of $^{10}_{11}X^+$ results in the doublet structure of intense lines in Figs. 2(a) and 2(b) with the splitting increasing with tensile strain. Moreover, the line that passes almost unaffected through AC_2 at the resonance point is no longer in the center and its energy separation from the antibonding branch (higher energy component) is slightly increased, as shown in Figs. 2(c) and 2(d). This reflects a different influence of strain on the triplet and singlet states. A similar strain effect on the coupling strength is measured on all the other anticrossings [see Fig. 2(f) and Ref. [37] for details].

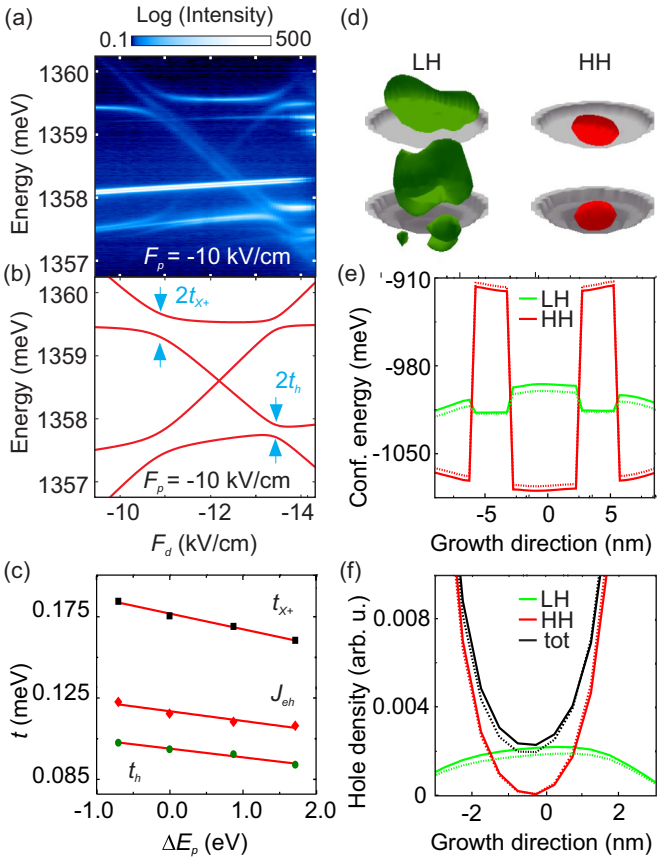

FIG. 3. (Color online) (a) Color-coded μPL map of a representative QDM as a function of F_d at $F_p = -10$ kV/cm. (b) Transition energies of X^+ in the QDM (AC lines) resulting from a fit to the experimental spectrum of (a). All the parameters used to fit the data are listed in Table S1 [37]. (c) Tunneling energies of single hole (t_h) and X^+ (t_{X^+}) and electron-hole exchange interaction (J_{eh}) as a function of ΔE_p, when F_p is varied in the whole range. (d) Three-dimensional hole probability density of light hole (LH, green) and heavy hole (HH, red) in the QDM (gray). The center-to-center dot separation is 8.5 nm. (e) Confinement potentials of LH (green) and HH (red) for the structure without (solid) and with induced compressive strain of $\epsilon_{xx} = \epsilon_{yy} = -0.1\%$ (dotted). Energy is displayed in the electron view. (f) Hole probability density in the barrier region of LH (green), HH (red), and total (black) for the unstrained (solid) and strained (dotted) case.

In order to extract the relevant parameters of the QDM and their evolution upon application of stress, we describe the system with a modified Hamiltonian from the model reported in Ref. [4], by taking into account the Stark shifts of the direct transitions. We consider the transitions between the initial state with one electron and two holes ($\hat{H}_{X^+}$) and the final state with a single hole ($\hat{H}_h$) focusing on the four lines that anticross each other and neglecting the spin-exchange interaction; see Ref. [37]. The pattern is obtained by diagonalizing the two matrices,

$$\hat{H}^{(2\times2)}_{X^+} = \begin{pmatrix} \Gamma^{(-)} & -t_{X^+} \\ -t_{X^+} & -F'_d d^*_{X^+} \end{pmatrix}, \quad \hat{H}_h = \begin{pmatrix} \epsilon_h & -t_h \\ -t_h & \epsilon_h - F'_d d^*_h \end{pmatrix},$$

where $\hat{H}^{(2\times2)}_{X^+}$ is the reduced Hamiltonian of the singlet states, $\Gamma^{(-)}$ is the energy distance between $^{10}_{20}X^+$ and $^{10}_{11}X^+$, $t = \Delta E_{\mathrm{AC}}/2$ is the tunneling energy, F'_d is the electric field ($F'_d = 0$ at AC_1), d^* is the effective interdot distance, and ϵ_h is the ground state energy of the hole. Finally, the energy differences $E_{1,2}[\hat{H}^{(2\times2)}_{X^+}] - E_{1,2}[\hat{H}_h]$ provide the pattern plotted in Fig. 3(b) at $F_p = -10$ kV/cm, which fits the experimental data reported in Fig. 3(a). The fitting parameters are $\Gamma^{(-)}$, d^*_h, $d^*_{X^+}$, $\Delta E_{\mathrm{AC}_1} = 2t_h$, and $\Delta E_{\mathrm{AC}_2} = 2t_{X^+}$. Under compression both t_h and t_{X^+} decrease linearly as a function of ΔE_p; see Fig. 3(c). Using the same formula reported above linking t_h and t_{X^+}, we found that $J_{eh} \sim 115$ μeV at $F_p = 0$ kV/cm, consistent with singlet-triplet splittings measured in similar structures [16], and it decreases with compressive strain. Additional information is obtained by looking at the screening, that is, the difference $d - d^*$, as a function of ΔE_p; see Ref. [37]. This difference at $F_p = 0$ kV/cm for the initial state (X^+) is $\sim$11% larger with respect to the final state (single hole) because of the extra *e*-*h* pair.

In order to understand the physical origin of the observed changes in ΔE_{AC}, we calculated the electronic structure and the optical properties of the studied QDMs using the eight-band $\boldsymbol{k}\cdot\boldsymbol{p}$ calculations including realistic strain distribution and piezoelectric field; see Ref. [37] (see also Refs. [3,4] therein). For the system under study with $F_p = 0$ kV/cm, we obtain a transition energy $\sim$1.37 eV for the neutral exciton, an energy difference between the symmetric and antisymmetric states ΔE_{AC_1} of 284 μeV, and a decrease of 46 μeV in the tunnel coupling while sweeping the externally induced strain from tensile 0.02% to compressive -0.04%, in agreement with the experimental results [43]. Inspection of the wave functions reveals that the hole probability density in the barrier region is dominated by the LH component, as shown in Figs. 3(d) and 3(f), Refs. [13] and [44]. This is because the band edge of LHs in the GaAs barrier is about 80 meV below the HH band edge, due to the local tensile strain induced by the QDs. The HHs penetrate the barrier region only by exponentially decaying tails at the QD boundaries, leaving negligible probability density in the barrier center. The compressive strain increases the energy of LHs with respect to the HHs [see Fig. 3(e)], leading to a reduction of the LH component in the barrier and therefore the tunnel coupling. We note that reducing the center-to-center dot separation below 8 nm will promote the HHs in the barrier region eventually leading to the opposite dependence of ΔE_{AC_1} on strain, i.e., increase of tunnel coupling upon lateral compression.

In conclusion, we have demonstrated that externally induced strains can be employed to tune the coupling strength in single InGaAs/GaAs QDMs. The strain changes the effective confinement potential of the HH and LH in the barrier and dot region, resulting in the reduction of the hole tunneling for compressive strain. By applying electric and strain fields, ΔE_{AC_1} is varied up to 27 μeV and ΔE_{AC_2} up to 48 μeV. This achievement may pave the way to a precise and flexible control of the entanglement between solid-state spin qubits in optically active QDMs. We envision using the strain field to tune the coupling strength of different QDMs to predetermined reference values combined with fast electric pulses across the device [45] to both initialize and readout the desired delocalized QDM states. Faster control may be achieved by strain modulations of the coupling strength provided by surface acoustic waves [46–48].

We thank C. Ortix, D. Gammon, S. Kumar, G. Bester, and J. Zhang for fruitful discussions, B. Eichler, D. J. Thurmer, R. Engelhardt, and D. Grimm for technical support, and K. Dörr and A. Herklotz for help with the piezoelectric actuators. The work was financially supported by the BMBF project QuaHL-Rep (Contracts No. 01BQ1032 and No. 01BQ1034), the DFG (FOR 730, contract RA1634/1-1), and the European Union Seventh Framework Programme 209 (FP7/2007-2013) under Grant Agreement No. 601126 210 (HANAS). V.K. was supported by European Social Fund, Grant No. CZ.1.07/2.3.00/30.0005. T.Š. was supported by European Regional Development Fund, Project No. CZ.1.05/1.1.00/02.0068.

[1] M. Bayer, P. Hawrylak, K. Hinzer, S. Fafard, M. Korkusinski, Z. R. Wasilewski, O. Stern, and A. Forchel, Science **291**, 451 (2001).

[2] H. J. Krenner, M. Sabathil, E. C. Clark, A. Kress, D. Schuh, M. Bichler, G. Abstreiter, and J. J. Finley, Phys. Rev. Lett. **94**, 057402 (2005).

[3] G. Ortner, M. Bayer, Y. Lyanda-Geller, T. L. Reinecke, A. Kress, J. P. Reithmaier, and A. Forchel, Phys. Rev. Lett. **94**, 157401 (2005).

[4] E. A. Stinaff, M. Scheibner, A. S. Bracker, I. V. Ponomarev, V. L. Korenev, M. E. Ware, M. F. Doty, T. L. Reinecke, and D. Gammon, Science **311**, 636 (2006).

[5] A. Boyer de la Giroday, N. Sköld, I. Farrer, D. A. Ritchie, and A. J. Shields, J. Appl. Phys. **110**, 083511 (2011).

[6] D. Loss and D. P. DiVincenzo, Phys. Rev. A **57**, 120 (1998).

[7] J. R. Petta, A. C. Johnson, J. M. Taylor, E. A. Laird, A. Yacoby, M. D. Lukin, C. M. Marcus, M. P. Hanson, and A. C. Gossard, Science **309**, 2180 (2005).

[8] L. Robledo, J. Elzerman, G. Jundt, M. Atatüre, A. Högele, S. Fält, and A. Imamoğlu, Science **320**, 772 (2008).
[9] D. Kim, S. G. Carter, A. Greilich, A. S. Bracker, and D. Gammon, Nat. Phys. **7**, 223 (2011).
[10] G. Cao, H.-O. Li, T. Tu, L. Wang, C. Zhou, M. Xiao, G.-C. Guo, H.-W. Jiang, and G.-P. Guo, Nat. Commun. **4**, 1401 (2013).
[11] K. M. Weiss, J. M. Elzerman, Y. L. Delley, J. Miguel-Sanchez, and A. Imamoğlu, Phys. Rev. Lett. **109**, 107401 (2012).
[12] A. Greilich, S. G. Carter, D. Kim, A. S. Bracker, and D. Gammon, Nat. Photonics **5**, 702 (2011).
[13] G. Bester, A. Zunger, and J. Shumway, Phys. Rev. B **71**, 075325 (2005).
[14] M. F. Doty, J. I. Climente, M. Korkusinski, M. Scheibner, A. S. Bracker, P. Hawrylak, and D. Gammon, Phys. Rev. Lett. **102**, 047401 (2009).
[15] M. Scheibner, M. F. Doty, I. V. Ponomarev, A. S. Bracker, E. A. Stinaff, V. L. Korenev, T. L. Reinecke, and D. Gammon, Phys. Rev. B **75**, 245318 (2007).
[16] A. Greilich, Ş. C. Bădescu, D. Kim, A. S. Bracker, and D. Gammon, Phys. Rev. Lett. **110**, 117402 (2013).
[17] C. Zener, Proc. R. Soc. London, Ser. A **137**, 696 (1932).
[18] A. K. Hüttel, S. Ludwig, H. Lorenz, K. Eberl, and J. P. Kotthaus, Phys. Rev. B **72**, 081310(R) (2005).
[19] Y. Hu, H. O. H. Churchill, D. J. Reilly, J. Xiang, C. M. Lieber, and C. M. Marcus, Nat. Nanotechnol. **2**, 622 (2007).
[20] A. S. Bracker, M. Scheibner, M. F. Doty, E. A. Stinaff, I. V. Ponomarev, J. C. Kim, L. J. Whitman, T. L. Reinecke, and D. Gammon, Appl. Phys. Lett. **89**, 233110 (2006).
[21] G. Burkard, G. Seelig, and D. Loss, Phys. Rev. B **62**, 2581 (2000).
[22] M. Korkusiński and P. Hawrylak, Phys. Rev. B **63**, 195311 (2001).
[23] L. G. G. V. Dias da Silva, J. M. Villas-Bôas, and S. E. Ulloa, Phys. Rev. B **76**, 155306 (2007).
[24] J. J. Climente, Appl. Phys. Lett. **93**, 223109 (2008).
[25] J. Planelles, J. I. Climente, F. Rajadell, M. F. Doty, A. S. Bracker, and D. Gammon, Phys. Rev. B **82**, 155307 (2010).
[26] R. Trotta, E. Zallo, C. Ortix, P. Atkinson, J. D. Plumhof, J. van den Brink, A. Rastelli, and O. G. Schmidt, Phys. Rev. Lett. **109**, 147401 (2012).
[27] R. Trotta, P. Atkinson, J. D. Plumhof, E. Zallo, R. O. Rezaev, S. Kumar, S. Baunack, J. R. Schröter, A. Rastelli, and O. G. Schmidt, Adv. Mater. **24**, 2668 (2012).
[28] Q. Xie, A. Madhukar, P. Chen, and N. P. Kobayashi, Phys. Rev. Lett. **75**, 2542 (1995).
[29] A. J. Bennett *et al.*, Nat. Phys. **6**, 947 (2010).
[30] Z. R. Wasilewski, S. Fafard, and J. P. McCaffrey, J. Cryst. Growth **201-202**, 1131 (1999).
[31] S. Kumar, R. Trotta, E. Zallo, J. D. Plumhof, P. Atkinson, A. Rastelli, and O. G. Schmidt, Appl. Phys. Lett. **99**, 161118 (2011).
[32] C. Y. Hung, T. E. Schlesinger, and M. L. Reed, Appl. Phys. Lett. **59**, 3598 (1991).
[33] M. Shayegan, K. Karrai, Y. P. Shkolnikov, K. Vakili, E. P. De Poortere, and S. Manus, Appl. Phys. Lett. **83**, 5235 (2003).
[34] T. Gokmen, M. Padmanabhan, and M. Shayegan, Nat. Phys. **6**, 621 (2010).
[35] S. Seidl, M. Kroner, A. Högele, K. Karrai, R. J. Warburton, A. Badolato, and P. M. Petroff, Appl. Phys. Lett. **88**, 203113 (2006).
[36] F. Ding *et al.*, Phys. Rev. Lett. **104**, 067405 (2010).
[37] See Supplemental Material at http://link.aps.org/supplemental/10.1103/PhysRevB.89.241303 for experimental and theoretical details.
[38] M. H. Baier, A. Malko, E. Pelucchi, D. Y. Oberli, and E. Kapon, Phys. Rev. B **73**, 205321 (2006).
[39] The upper (lower) numbers in the notation of the quantum states are the numbers of electrons (holes) in the bottom and top dot, respectively, and the underlines represent where the recombination takes place.
[40] F. H. L. Koppens, J. A. Folk, J. M. Elzerman, R. Hanson, L. H. Willems van Beveren, I. T. Vink, H. P. Tranitz, W. Wegscheider, L. P. Kouwenhoven, and L. M. K. Vandersypen, Science **309**, 1346 (2005).
[41] P. W. Fry *et al.*, Phys. Rev. Lett. **84**, 733 (2000).
[42] J. Wang, D. Shang, H. Mao, J. Yu, Q. Zhao, P. Yang, and H. Xing, Physica B **408**, 98 (2013).
[43] The small difference between the experimental and theoretical values for the emission energy and $\Delta E_{\mathrm{AC_1}}$ are explained by the strong dependence on structural parameters, in particular, the thickness of the spacing layer.
[44] W. Sheng and J.-P. Leburton, Appl. Phys. Lett. **81**, 4449 (2002).
[45] J. Zhang, F. Ding, E. Zallo, R. Trotta, B. Höfer, L. Han, S. Kumar, Y. H. Huo, A. Rastelli, and O. G. Schmidt, Nano Lett. **13**, 5808 (2013).
[46] J. R. Gell, M. B. Ward, R. J. Young, R. M. Stevenson, P. Atkinson, D. Anderson, G. A. C. Jones, D. A. Ritchie, and A. J. Shields, Appl. Phys. Lett. **93**, 081115 (2008).
[47] M. Metcalfe, S. M. Carr, A. Muller, G. S. Solomon, and J. Lawall, Phys. Rev. Lett. **105**, 037401 (2010).
[48] S. Völk, F. J. R. Schülein, F. Knall, D. Reuter, A. D. Wieck, T. A. Truong, H. Kim, P. M. Petroff, A. Wixforth, and H. J. Krenner, Nano Lett. **10**, 3399 (2010).

N Spatially resolved electron energy loss spectroscopy of crescent-shaped plasmonic antennas

Spatially resolved electron energy loss spectroscopy of crescent-shaped plasmonic antennas

V. Křápek,[1,*] A. L. Koh,[2] L. Břínek,[1,3] M. Hrtoň,[1,3] O. Tomanec,[3,4] R. Kalousek,[1,3] S. A. Maier,[5] and T. Šikola[1,3]

[1]*Central European Institute of Technology, Brno University of Technology, Technická 10, 616 00 Brno, Czech Republic*
[2]*Stanford Nano Shared Facilities, Stanford University, Stanford, California 94305, USA*
[3]*Institute of Physical Engineering, Brno University of Technology, Technická 2, 616 69 Brno, Czech Republic*
[4]*also at Faculty of Science, Palacký University, Šlechtitelů 11, 78371 Olomouc, Czech Republic*
[5]*The Blackett Laboratory, Department of Physics, Imperial College London, London SW7 2AZ, United Kingdom*
**vlastimil.krapek@ceitec.vutbr.cz*

Abstract: We present a study of the optical properties of gold crescent-shaped antennas by means of electron energy loss spectroscopy. These structures exhibit particularly large field enhancement near their sharp features, support two non-degenerate dipolar (i.e., optically active) localised surface plasmon resonances, and are widely tunable by a choice of their shape and dimensions. Depending on the volume and shape, we resolved up to four plasmon resonances in metallic structures under study in the energy range of 0.8 – 2.4 eV: two dipolar and quadrupolar mode and a multimodal assembly. The boundary-element-method calculations reproduced the observed spectra and helped to identify the character of the resonances. The two lowest modes are of particular importance owing to their dipolar nature. Remarkably, they are both concentrated near the tips of the crescent, spectrally well resolved and their energies can be tuned between 0.8 – 1.5 eV and 1.2 – 2.0 eV, respectively. As the lower spectral range covers the telecommunication wavelengths 1.30 and 1.55 μm, we envisage the possible use of such nanostructures in infrared communication technology.

OCIS codes: (160.4236) Nanomaterials; (240.6680) Surface plasmons; (250.5403) Plasmonics; (310.6628) Subwavelength structures, nanostructures.

References and links

1. M. Specht, J. D. Pedarnig, W. M. Heckl, and T. W. Hänsch, "Scanning plasmon near-field microscope," Phys. Rev. Lett. **68**, 476–479 (1992).
2. A. G. Brolo, R. Gordon, B. Leathem, and K. L. Kavanagh, "Surface plasmon sensor based on the enhanced light transmission through arrays of nanoholes in gold films," Langmuir **20**, 4813–4815 (2004).
3. M. A. Noginov, G. Zhu, A. M. Belgrave, R. Bakker, V. M. Shalaev, E. E. Narimanov, S. Stout, E. Herz, T. Suteewong, and U. Wiesner, "Demonstration of a spaser-based nanolaser," Nature **460**, 1110–1112 (2009).
4. M. S. Anderson, "Locally enhanced raman spectroscopy with an atomic force microscope," Appl. Phys. Lett. **76**, 3130–3132 (2000).
5. P. Anger, P. Bharadwaj, and L. Novotny, "Enhancement and quenching of single-molecule fluorescence," Phys. Rev. Lett. **96**, 113002 (2006).

#235070 - $15.00 USD Received 23 Feb 2015; revised 7 Apr 2015; accepted 9 Apr 2015; published 27 Apr 2015

6. H. A. Atwater and A. Polman, "Plasmonics for improved photovoltaic devices," Nat. Mater. **9**, 205 (2010).
7. J. N. Farahani, D. W. Pohl, H.-J. Eisler, and B. Hecht, "Single quantum dot coupled to a scanning optical antenna: A tunable superemitter," Phys. Rev. Lett. **95**, 017402 (2005).
8. M. Pfeiffer, K. Lindfors, C. Wolpert, P. Atkinson, M. Benyoucef, A. Rastelli, O. G. Schmidt, H. Giessen, and M. Lippitz, "Enhancing the optical excitation efficiency of a single self-assembled quantum dot with a plasmonic nanoantenna," Nano Lett. **10**, 4555–4558 (2010).
9. N. Liu, M. L. Tang, M. Hentschel, H. Giessen, and A. P. Alivisatos, "Nanoantenna-enhanced gas sensing in a single tailored nanofocus," Nat. Mater. **10**, 631–636 (2011).
10. J. F. Hainfeld, "Site-specific cluster labels," Ultramicroscopy **46**, 135–144 (1992).
11. K. Li, L. Clime, B. Cui, and T. Veres, "Surface enhanced raman scattering on long-range ordered noble-metal nanocrescent arrays," Nanotechnology **19**, 145305 (2008).
12. R. Bukasov, T. A. Ali, P. Nordlander, and J. S. Shumaker-Parry, "Probing the plasmonic near-field of gold nanocrescent antennas," ACS Nano **4**, 6639–6650 (2010).
13. M. Retsch, M. Tamm, N. Bocchio, N. Horn, R. Förch, U. Jonas, and M. Kreiter, "Parallel preparation of densely packed arrays of 150-nm gold-nanocrescent resonators in three dimensions," Small **5**, 2105–2110 (2009).
14. A. Aubry, D. Y. Lei, S. A. Maier, and J. B. Pendry, "Broadband plasmonic device concentrating the energy at the nanoscale: The crescent-shaped cylinder," Phys. Rev. B **82**, 125430 (2010).
15. A. I. Fernández-Domínguez, Y. Luo, A. Wiener, J. B. Pendry, and S. A. Maier, "Theory of three-dimensional nanocrescent light harvesters," Nano Lett. **12**, 5946–5953 (2012).
16. D. Boyer, P. Tamarat, A. Maali, B. Lounis, and M. Orrit, "Photothermal imaging of nanometer-sized metal particles among scatterers," Science **297**, 1160–1163 (2002).
17. K. Lindfors, T. Kalkbrenner, P. Stoller, and V. Sandoghdar, "Detection and spectroscopy of gold nanoparticles using supercontinuum white light confocal microscopy," Phys. Rev. Lett. **93**, 037401 (2004).
18. C. Sönnichsen, S. Geier, N. E. Hecker, G. von Plessen, J. Feldmann, H. Ditlbacher, B. Lamprecht, J. R. Krenn, F. R. Aussenegg, V. Z.-H. Chan, J. P. Spatz, and M. Möller, "Spectroscopy of single metallic nanoparticles using total internal reflection microscopy," Appl. Phys. Lett. **77**, 2949–2951 (2000).
19. C. Sönnichsen, T. Franzl, T. Wilk, G. von Plessen, J. Feldmann, O. Wilson, and P. Mulvaney, "Drastic reduction of plasmon damping in gold nanorods," Phys. Rev. Lett. **88**, 077402 (2002).
20. J. J. Mock, M. Barbic, D. R. Smith, D. A. Schultz, and S. Schultz, "Shape effects in plasmon resonance of individual colloidal silver nanoparticles," J. Chem. Phys. **116**, 6755–6759 (2002).
21. M. Hu, C. Novo, A. Funston, H. Wang, H. Staleva, S. Zou, P. Mulvaney, Y. Xia, and G. V. Hartland, "Dark-field microscopy studies of single metal nanoparticles: understanding the factors that influence the linewidth of the localized surface plasmon resonance," J. Mater. Chem. **18**, 1949–1960 (2008).
22. M. Scharte, R. Porath, T. Ohms, M. Aeschlimann, B. Lamprecht, H. Ditlbacher, and F. R. Aussenegg, "Lifetime and dephasing of plasmons in ag nanoparticles," Proc. SPIE **4456**, 14–21 (2001).
23. A. Lewis, H. Taha, A. Strinkovski, A. Manevitch, A. Khatchatouriants, R. Dekhter, and E. Ammann, "Near-field optics: from subwavelength illumination to nanometric shadowing," Nat. Biotechnol. **21**, 1377–1386 (2003).
24. P. Dvořák, T. Neuman, L. Břínek, T. Šamořil, R. Kalousek, P. Dub, P. Varga, and T. Šikola, "Control and near-field detection of surface plasmon interference patterns," Nano Lett. **13**, 2558–2563 (2013).
25. F. J. García de Abajo and M. Kociak, "Probing the photonic local density of states with electron energy loss spectroscopy," Phys. Rev. Lett. **100**, 106804 (2008).
26. U. Hohenester, H. Ditlbacher, and J. R. Krenn, "Electron-energy-loss spectra of plasmonic nanoparticles," Phys. Rev. Lett. **103**, 106801 (2009).
27. N. Zabala and A. Rivacoba, "Electron energy loss near supported particles," Phys. Rev. B **48**, 14534–14542 (1993).
28. P. E. Batson, "Surface plasmon coupling in clusters of small spheres," Phys. Rev. Lett. **49**, 936–940 (1982).
29. M. Bosman, V. J. Keast, M. Watanabe, A. I. Maaroof, and M. B. Cortie, "Mapping surface plasmons at the nanometre scale with an electron beam," Nanotechnology **18**, 165505 (2007).
30. A. L. Koh, A. I. Fernández-Domínguez, D. W. McComb, S. A. Maier, and J. K. W. Yang, "High-resolution mapping of electron-beam-excited plasmon modes in lithographically defined gold nanostructures," Nano Lett. **11**, 1323–1330 (2011).
31. G. Boudarham, N. Feth, V. Myroshnychenko, S. Linden, J. García de Abajo, M. Wegener, and M. Kociak, "Spectral imaging of individual split-ring resonators," Phys. Rev. Lett. **105**, 255501 (2010).
32. B. Goris, G. Guzzinati, C. Fernández-López, J. Pérez-Juste, L. M. Liz-Marzán, A. Trügler, U. Hohenester, J. Verbeeck, S. Bals, and G. Van Tendeloo, "Plasmon mapping in au@ag nanocube assemblies," J. Phys. Chem. C **118**, 15356–15362 (2014).
33. A. L. Koh, K. Bao, I. Khan, W. E. Smith, G. Kothleitner, P. Nordlander, S. A. Maier, and D. W. McComb, "Electron energy-loss spectroscopy (eels) of surface plasmons in single silver nanoparticles and dimers: Influence of beam damage and mapping of dark modes," ACS Nano **3**, 3015–3022 (2009).
34. S. Mazzucco, N. Geuquet, J. Ye, O. Stéphan, W. Van Roy, P. Van Dorpe, L. Henrard, and M. Kociak, "Ultralocal modification of surface plasmons properties in silver nanocubes," Nano Lett. **12**, 1288–1294 (2012).
35. F.-P. Schmidt, H. Ditlbacher, U. Hohenester, A. Hohenau, F. Hofer, and J. R. Krenn, "Universal dispersion of

#235070 - $15.00 USD Received 23 Feb 2015; revised 7 Apr 2015; accepted 9 Apr 2015; published 27 Apr 2015

surface plasmons in flat nanostructures," Nat. Commun. **5**, 3604 (2014).
36. G. Boudarham and M. Kociak, "Modal decompositions of the local electromagnetic density of states and spatially resolved electron energy loss probability in terms of geometric modes," Phys. Rev. B **85**, 245447 (2012).
37. S. M. Collins and P. A. Midgley, "Surface plasmon excitations in metal spheres: Direct comparison of light scattering and electron energy-loss spectroscopy by modal decomposition," Phys. Rev. B **87**, 235432 (2013).
38. G. Mie, "Beiträge zur Optik trüber Medien, speziell kolloidaler Metallösungen," Ann. Phys. **330**, 377–445 (1908).
39. R. Kalousek, P. Dub, L. Břínek, and T. Šikola, "Response of plasmonic resonant nanorods: an analytical approach to optical antennas," Opt. Express **20**, 17916–17927 (2012).
40. F. J. García de Abajo and A. Howie, "Relativistic electron energy loss and electron-induced photon emission in inhomogeneous dielectrics," Phys. Rev. Lett. **80**, 5180–5183 (1998).
41. F. J. García de Abajo and A. Howie, "Retarded field calculation of electron energy loss in inhomogeneous dielectrics," Phys. Rev. B **65**, 115418 (2002).
42. U. Hohenester and A. Trügler, "MNPBEM - A Matlab toolbox for the simulation of plasmonic nanoparticles," Comput. Phys. Commun. **183**, 370–381 (2012).
43. E. D. Palik, *Handbook of Optical Constants of Solids* (Academic Press, Burlington, 2002).
44. H. R. Philipp, "Optical properties of silicon nitride," J. Electrochem. Soc. **120**, 295–300 (1973).
45. R. Olmon, B. Slovick, T. Johnson, D. Shelton, S.-H. Oh, G. Boreman, and M. Raschke, "Optical dielectric function of gold," Phys. Rev. B **86**, 235147 (2012).
46. A. Kinkhabwala, Z. Yu, S. Fan, Y. Avlasevich, K. Mullen, and W. E. Moerner, "Large single-molecule fluorescence enhancements produced by a bowtie nanoantenna," Nat. Photonics **3**, 654–657 (2009).
47. A. C. Atre, A. García-Etxarri, H. Alaeian, and J. A. Dionne, "Toward high-efficiency solar upconversion with plasmonic nanostructures," J. Opt. **14**, 024008 (2012).
48. F. P. Schmidt, H. Ditlbacher, F. Hofer, J. R. Krenn, and U. Hohenester, "Morphing a plasmonic nanodisk into a nanotriangle," Nano Lett. **14**, 4810–4815 (2014).

1. Introduction

Localised surface plasmons (LSP) are collective oscillations of free electrons in metal nano- and microstructures of specific shapes and dimensions (antennas) coupled to the electromagnetic field. Their characteristic feature is the subwavelength confinement of the electromagnetic field, utilized in near field imaging [1,2] and ultracompact nanolasers [3]. Further, a strong modification of the field magnitude with respect to the vacuum state, reflected in the photonic local density of states, can be used to control the rate of optical processes, which is exploited e.g. in tip enhanced Raman spectroscopy [4], single molecule fluorescence [5], improving the efficiency of solar cells [6], or enhancing the photoluminescence of quantum dots [7,8]. Another applications, such as sensing [9] or labeling [10], are found in biology, environmental sciences, or human medicine. Antennas of a crescent shape possess several advantageous properties. They can be prepared by electron beam lithography (EBL) [11], but also conveniently manufactured using nanosphere template lithography, whereby a thin gold layer is deposited at an oblique angle on polymer nanospheres [12,13], opening thus the way to the cheap mass production. Close to their sharp tips hot spots of enhanced electric field and electromagnetic local density of states are formed, allowing to enhance the optical processes [14]. In addition, similar to split-ring resonators, crescent geometry supports circular-current plasmon modes, which interact with the magnetic component of the field and are a prerequisite for metamaterials with a negative refraction index [13]. Having only one lateral mirror plane, the crescent antennas allow for a directional response. Recently, they were also used to enhance the performance of the solar cells [14,15].

Properties of LSP are extensively studied by numerous experimental methods. Far-field spectroscopic methods such as absorption spectroscopy [16,17], dark-field microscopy [18–21], or time-resolved two-photon photoemission [22] provide the energy and lifetime [21,22] of LSP. Several imaging techniques exist to reveal the spatial distribution of plasmon near fields. Scanning near field optical microscopy enables the optical mapping of near fields of LSP [23] and surface plasmon polaritons [24], but the spatial resolution is limited to about 50 nm. Scanning transmission electron microscopy (STEM) applied simultaneously with electron energy-loss

#235070 - $15.00 USD Received 23 Feb 2015; revised 7 Apr 2015; accepted 9 Apr 2015; published 27 Apr 2015

spectroscopy (EELS) facilitates the excitation and detection of particular plasmonic modes in antennas [25–27]. The electron beam induces the oscillations of free electrons inside antennas. Importantly, the electromagnetic field induced by these oscillations acts back on the impinging electrons, changing both their energy and momentum. By analysing the spectral dependence of the energy loss suffered by electrons, one can deduce the characteristic energies of the various plasmonic modes of antennas. Furthermore, by extracting the energy loss spectral maps, one can observe the spatial distribution of the excitation efficiency of the plasmonic modes. EELS has been successfully applied to map LSP modes in nanospheres [28], nanorods [29], bow-tie antennas [30], split-ring resonators [31], and complex plasmonic assemblies [32], to study the hybridization of plasmons in nanoparticle dimers [33] or the symmetry breaking induced by the substrate [34], to reveal universal dispersion relations [35], *etc*.

The interpretation of the EELS maps of LSP modes is not straightforward. Despite original attempts to relate EELS to the photonic local density of states (LDOS) [25], pronounced differences between both plasmonic mode characteristics were demonstrated [26]; in particular, EELS was shown to be rather insensitive to the hot spots [26] between the particle dimers. Only since very recently, complex methodologies mutually relating EELS and photonic LDOS, that are based on the modal decomposition of involved quantities, have been developed [36,37]. Thus, it is preferable to accompany EELS measurements by the theory-based interpretation. The simplistic antenna geometries allow for the analytic solution [38,39], but for more complex ones numerical methods specially developed for this purpose should be used [40,41].

2. Methods

2.1. Gold antennas preparation

Gold crescent antennas of height 20 nm and various lateral dimensions were prepared using focused-ion-beam lithography. The silicon nitride membranes with areas of $500 \times 500\ \mu\text{m}^2$ and thickness of 40 nm were used as the substrate. First, a 20nm-thick Au layer was deposited by ion beam sputtering on the substrate. After that, the antennas were fabricated by focused 30 keV Ga^+ ion beam (FIB) milling of the gold film in a dual beam system Tescan Lyra. Each antenna was located in the middle of a $1 \times 1\,\mu\text{m}^2$ metal-free square. To verify that plasmonic structures do not significantly interact with the surrounding metallic frames, spectra of equivalent plasmonic antennas embedded in the metal-free squares of different sizes were compared first. Annular dark-field (ADF) STEM images of the samples are shown in Fig. 1. Here, a micro-grain structure of the antennas is clearly visible.

2.2. Electron energy loss spectroscopy

EELS measurements were carried out using a FEI Titan 80-300 environmental (scanning) transmission electron microscope operated at 300 kV in scanning, monochromated mode. The instrument was equipped with a Gatan Tridiem 866 spectrometer. A 50 μm C3 aperture, camera length of 38 mm, and a spectrometer entrance aperture of 2.5 mm and 0.01 eV per channel dispersion were used for the data acquisition. This corresponds to a convergence semi-angle of 9.2 mrad and a collection semi-angle of 20.7 mrad. The spatial and energy resolution (defined by the full-width-half-maximum of the zero-loss peak), are 0.3 nm and 0.2 eV, respectively. The structure dimensions considered in the calculations were extracted from ADF-STEM images of the samples. The plasmon excitation maps were obtained by extracting the spectrum image in energy slices with 0.1 eV intervals.

#235070 - $15.00 USD Received 23 Feb 2015; revised 7 Apr 2015; accepted 9 Apr 2015; published 27 Apr 2015

2.3. Simulations

To obtain insight into the physical origin of the observed peaks, the EELS response was simulated using the boundary element method (BEM) following Refs [40,41]. To this end we used a free software MNPBEM toolbox [42] together with an in-house developed extension for EELS. The model structure was formed by two discs: from the basic disc of the radius r_B another disc of the radius r_S, displaced by a distance c from the first one, was subtracted. The edges were subsequently rounded with a radius of 5 nm. The height of both discs was set to the value $h = 20$ nm following the value set for the lithographic process. The other parameters of the antenna geometry were chosen in the way so that the model structures comply with the ADF-STEM images (Fig. 1). For example, the structure A1, the spectra of which are presented in Fig. 2(a), was modelled using $r_B = 56$ nm, $r_S = 55$ nm, $c = 36$ nm. A triangular mesh approximating the surface of the resulting structure was created by a Delaunay triangulation algorithm using COMSOL Multiphysics software. A typical mesh consisted of about 3000 boundary elements and provided accuracy in peak positions of about 10 meV (determined by a comparison with a mesh with about 10000 elements). In most calculations the substrate was not included, as it increases the number of boundary elements considerably and has only a quantitative influence on the results (red shift of the peaks by about 0.2 – 0.3 eV). The substrate (modeled as a finite-size particle attached to the bottom of the gold antenna) was included in some calculations for the accurate determination of the plasmon resonance energies. The dielectric function of gold was taken from Ref. [43], for silicon nitride an infrared value at 1 eV of $3.9 + 0\,j$ was used [44] neglecting the dispersion. Apart from neglecting the substrate, the calculation accuracy is limited by the uncertainties and irregularities of the antenna shape. Remarkably, the variation of the antenna height by 1 nm (5 %) shifts the resonant peak energy by up to 20 meV. Further, sputtered gold forming the antennas is porous and composed of grains. Hence, its dielectric function can deviate from the bulk case used in the simulations [45], which contributes to the simulation error. In total, we estimate the accuracy of the calculated peak positions of 0.1 – 0.15 eV.

3. Plasmon mode mapping

Table 1. Lateral dimensions of six antennas involved in the study determined using ADF-STEM images: length L (longitudinal tip – tip distance), thickness T (transverse outer-edge – inner-edge distance, and width W (transverse outer-edge – tip distance). The energies of their plasmon modes D_L (longitudinal dipolar), D_T (transverse dipolar), Q (quadrupolar), and MA (multimodal) as obtained from the EEL spectra.

Sample	L (nm)	T (nm)	W (nm)	D_L (eV)	D_T (eV)	Q (eV)	MA (eV)
A1	120	60	86	1.3	1.7		2.4
A2	93	45	60	1.5	2.0		2.5
A3	275	120	230	0.8	1.2		2.0
A4	248	86	187	0.85	1.25	1.8	2.1
A5	250	120	218	0.75	1.25	1.8	1.95
A6	230	116	194	0.9	1.3	1.8	2.0

In total six gold crescent-like antennas of various sizes manifesting qualitatively similar plasmonic properties were studied. Annular dark-field (ADF) STEM images of the samples are shown in Fig. 1. The lateral dimensions of the antennas, schematically depicted in Fig. 1, are

#235070 - $15.00 USD Received 23 Feb 2015; revised 7 Apr 2015; accepted 9 Apr 2015; published 27 Apr 2015

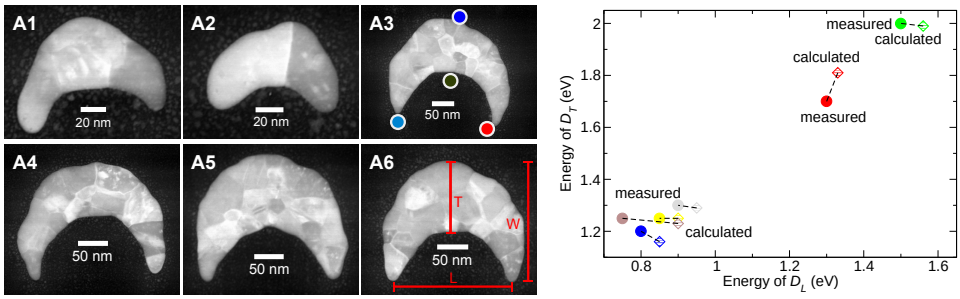

Fig. 1. Left: ADF-STEM images of six gold plasmonic antennas involved in this study. The inset in panel A3 displays characteristic spots of electron beam impingement (tips, inner edge, and outer edge of the antenna). The inset in panel A6 shows the lateral antenna dimensions used in the text (length L, width W, and thickness T). Right: The points represent the energies of two dipolar plasmon resonances – D_L mode (horizontal axis) and D_T mode (vertical axis). Experimental (full circles) and numerical (hatched diamonds) values are compared. Different colors correspond to particular structures (red: A1, green: A2, blue: A3, yellow: A4, brown: A5, gray: A6), the dashed lines connect the experimental and numerical results for a particular structure to guide the eye. The theoretical values of the mode energies already reflect the influence of the substrate.

summarized in Table 3, the height was kept at 20 nm. The antennas can be divided into two subgroups according to their dimensions. In the following, first the *smaller* antennas (A1, A2) will be discussed thoroughly, and then the distinct features of the *larger* antennas (A3, A4, A5, A6) briefly described.

Broad range EEL spectra were acquired for the electron beam focused to specific spots close to the antennas (see Fig. 2) as follows: the tips of the crescent (T1, T2), the center of the inner edge (IE), and the center of the outer edge (OE). The distance between the beam and the antenna boundary was set to several nm to assure a strong response while avoiding the penetration of the electron beam into the metal and thus related losses. The electron trajectories are schematically depicted in the inset of Fig. 2(a). With the corresponding colors, the energy loss spectra for a particular *smaller* structure (A1) are shown in Fig. 2(a). The characteristic EEL spectrum of *smaller* antennas is composed of three peaks, denoted as D_L, D_T, and *MA* with increasing energy. It will be shown that the D_L peak corresponds to a longitudinal dipolar mode (the electron oscillations between the tips T1 and T2 along the axial antenna direction. The D_T peak corresponds to a transverse dipolar mode related to electron oscillations between the inner edge of the antenna and its tips forming a dipole moment perpendicular to the longitudinal one, while the *MA* peak corresponds to several high-order plasmonic modes and its position is related to the onset of interband absorption in gold rather than the geometry of the nanostructure. The D_L peak dominates the spectrum obtained for the excitation spots T1,2 (further T1,2 spectrum), while it is missing or weak in IE and OE spectra. This is not surprising, the odd symmetry of the mode with respect to the mirror plane of the crescent prevents its coupling to the electron beam with the trajectory involved in the mirror plane. The weak non-zero signal is attributed to a non-ideal shape of the crescent and/or to the electron beam positioned slightly out of the mirror plane. The D_T peak is most pronounced in the OE spectrum. It is also present in the T1,2 spectrum as a shoulder of the stronger D_L mode. It is weak in the IE spectrum which can be explained by a similar argument as for the D_L mode in the IE and OE spectra. Although there is no longitudinal mirror plane, the IE spot is close to the center of mass of the structure and the electric field of the D_T mode is rather uniformly distributed along the longitudinal plane

#235070 - $15.00 USD Received 23 Feb 2015; revised 7 Apr 2015; accepted 9 Apr 2015; published 27 Apr 2015

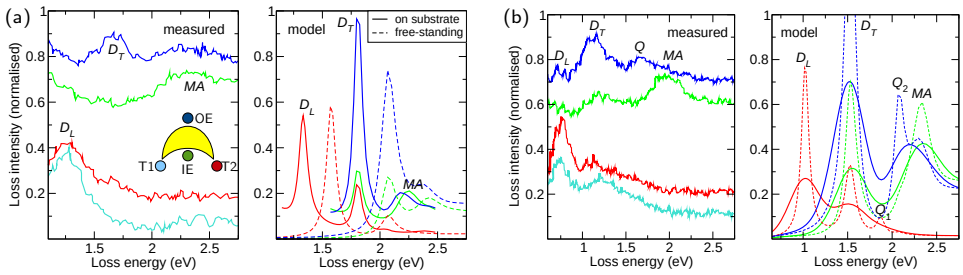

Fig. 2. (a) Left: Measured energy-dependent loss spectra for the structure A1 ($L = 120$ nm, $T = 60$ nm, $W = 86$ nm) and the electron beam impinging close to the tips (spots T1 and T2, light blue and red line), outer edge (spot OE, dark blue line), and inner edge (spot IE, green line) of the antenna. The inset schematically shows the electron beam positions (the same colors as in the main graph). Right: Energy loss spectra calculated with MNPBEM (colors correspond to the same spots as in the left panel). Solid and dashed lines are related to the antenna on substrate and the free-standing antenna, respectively. (b) Left: Measured EEL spectra for the *larger* structure A4 ($L = 248$ nm, $T = 86$ nm, $W = 187$ nm) and the electron beam impinging close to the tips (spots T1 and T2; red and light blue line), outer edge (spot OE; dark blue line) and inner edge (spot IE; green line) of the antenna. Right: Energy loss spectra calculated with MNPBEM for a free-standing antenna (dashed lines) and subsequently modified using convolution with a Gaussian function of 0.15 eV FWHM (solid lines). Colors correspond to the same spots as in the left panel.

containing the spot IE. Thus, the coupling of the mode whose field has the quasi-odd symmetry with respect to that plane to the electron beam the field of which possesses the even symmetry is weak. The *MA* peak is present in all spectra. The IE spectrum is most suitable for studying its properties due to the absence of the D_L and D_T peaks.

The calculated EEL spectra for the structure A1 and the relevant electron beam spots are shown in the right panel of Fig. 2(a) (both for the antenna on the substrate and free-standing antenna). As in the experiment, we identify three peaks in the spectra. Their energies of 1.3(3), 1.8(1) and 2.3 eV (or 1.5(8), 2.0(8), and 2.4 eV neglecting the substrate) are in a reasonable agreement with the experimental values of 1.3, 1.7, and 2.4 eV, respectively. Similarly, the relative intensities of the modes for each electron beam spot correspond rather well to the experiment. The D_L peak is pronounced at the T1,2 spots and is also weakly excited when moving the beam slightly off the mirror plane (not shown in Fig. 2). The D_T peak is the strongest at the OE spot. In the theoretical IE spectrum it is rather weak, yet stronger than in the experimental IE spectrum – a signature that the model structure does not fully reflect the quasi-odd longitudinal symmetry discussed in the previous paragraph. The *MA* peak is visible at both the IE and OE spots. Both the D_T and *MA* peaks are visible or at least perceived in the theoretical T1,2 spectra. The FWHM of the peaks is generally lower than in the experiment, which is attributed to the finite energy spread of the electron beam and the resolution of the spectrometer. Right panel of Fig. 1 compares the experimental and calculated energies of the lowest two plasmon resonances (D_L, D_T) for all six studied antennas. The calculation of the theoretical values of the antenna mode energies took into account the influence of the substrate. Based on the noise of the measured spectra and the spectral width of the peaks we estimate the experimental uncertainty of the peak energies of about 0.1 eV. Considering the theoretical error of peak energies of about 0.15 eV, the agreement of the theory and the experiment is satisfying. The calculated values are systematically overestimated by about 0.1 eV, which can be attributed e.g. to the difference between the actual dielectric function of gold and the bulk dielectric function used

#235070 - $15.00 USD Received 23 Feb 2015; revised 7 Apr 2015; accepted 9 Apr 2015; published 27 Apr 2015

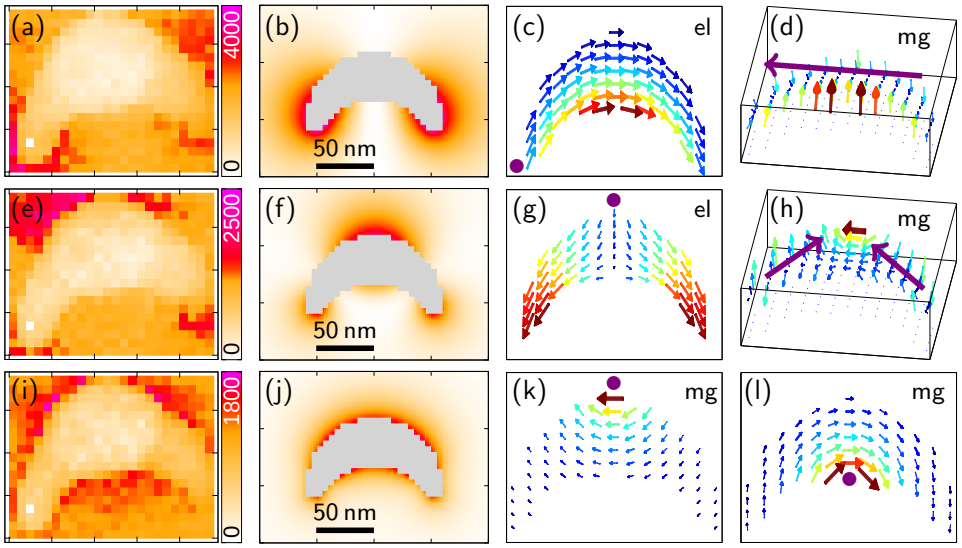

Fig. 3. Top: D_L mode of the A1 antenna (a–d). Measured (a) and calculated (b) spatial distribution of the loss intensity. Electric (c) and magnetic (d) field induced in the antenna by the electron beam passing nearby the left tip [violet spot in (c)]. The violet arrow in (d) shows the direction of the induced current. Middle: D_T mode of the A1 antenna (e–h). Measured (e) and calculated (f) spatial distribution of the loss intensity. Electric (g) and magnetic (h) field induced in the antenna by the electron beam passing nearby the outer edge [violet spot in (g)]. The violet arrow in (h) show the direction of the induced current. Bottom: *MA* mode of the A1 antenna (i–l). Measured (i) and calculated (j) spatial distribution of the loss intensity. Magnetic field induced in the antenna by the electron beam passing nearby the outer edge (k, violet spot) and inner edge (l, violet spot). The white spot in left bottom corner of the experimental EEL maps (a,e,i) corresponds to a missing data due to a failed measurement. The color scale unit of panels (a,e,i) is count.

in the simulations.

In order to obtain insight into the nature of the modes, the spatial distribution of the loss intensity was studied. Figure 3 displays measured and calculated maps of the loss intensity over the antenna A1 at the loss energy corresponding to the D_L, D_T, and *MA* peaks. The calculated values are shown only for the electron beam spots in the antenna surroundings. Further, the calculated spatial distribution of the electric and magnetic fields inside the antenna (in its mid-height) is shown. For them, we chose a specific electron beam spot at which the selected peaks dominate (the T1,2 spots for the longitudinal dipolar mode D_L, the OE spot for the transverse dipolar mode D_T, and the IE and OE spots for the multimodal peak *MA*). We note that both fields are complex quantities. As their real and imaginary parts exhibit a similar spatial distribution, we show for clarity only the dominant components, i.e., the imaginary part of the electric field intensity and the real part of the magnetic field.

The loss intensity related to the D_L mode exhibits two maxima located around the tips of the antenna and a minimum along the transverse central plane of the crescent (i.e., a nodal plane coinciding with the transverse mirror plane in the model crescent). The electric and magnetic field distributions associated with the D_L mode result from a charge separation and a current flowing in the longitudinal direction [violet arrow in Fig. 3(d)], confirming our assignment of this spectral feature to the longitudinal dipolar mode. Note that the field distribution nearly

#235070 - $15.00 USD Received 23 Feb 2015; revised 7 Apr 2015; accepted 9 Apr 2015; published 27 Apr 2015

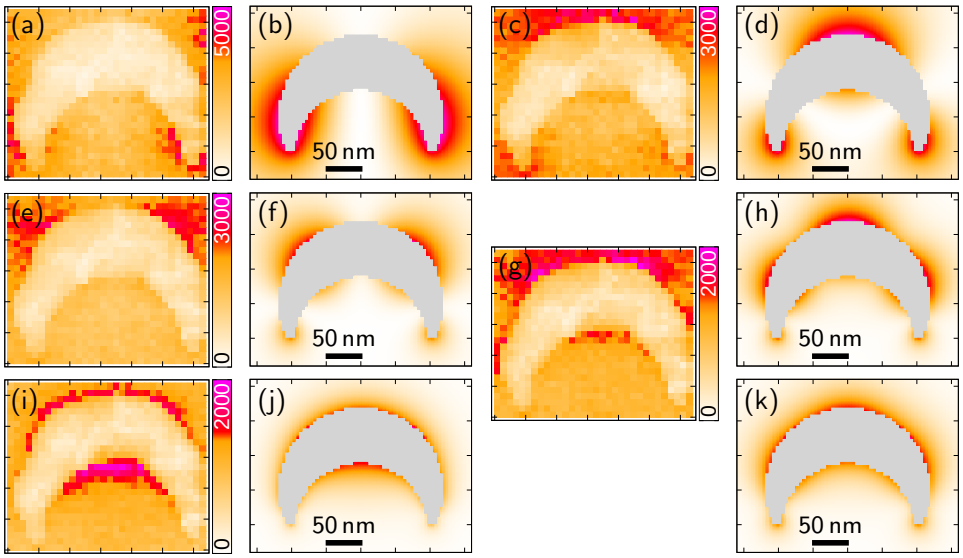

Fig. 4. D_L mode of the A4 antenna: Measured (a) and calculated (b) spatial distribution of the loss intensity. D_T mode of the A4 antenna: Measured (c) and calculated (d) spatial distribution of the loss intensity. Q_1 mode of the A4 antenna: Measured (e) and calculated (f) spatial distribution of the loss intensity. Q_2 mode of the A4 antenna: Measured (g) and calculated (h) spatial distribution of the loss intensity. *MA* mode of the A4 antenna: Measured (g) and calculated (h) spatial distribution of the loss intensity. (k) A sum of calculated loss intensities of modes Q_1, Q_2, and *MA* with relative weights of 0.2, 1, and 0.5, respectively.

possesses a mirror plane symmetry, although the excitation is highly non-symmetric. This symmetric field distribution is preserved as the electron beam scans the antenna surrounding. This is a rather strong evidence that only a single plasmon mode dominates the response at the corresponding energy. Similar features are found in the loss intensity and electromagnetic field distribution associated with the D_T peak, but the dipole is oriented along the transverse axis and the loss intensity distribution possesses three maxima [Figs. 3(e) and 3(f)]. Remarkably different behavior is observed in the case of the *MA* peak [Figs. 3(i)–3(l)]. The loss intensity shows only weak spatial selectivity and is almost homogeneously distributed along the circumference of the crescent. The electromagnetic field distribution is strongly sensitive to the position of the electron beam. To demonstrate this sensitivity, the response of the crescent for the electron beam impinging nearby its inner and outer edge was compared. The magnetic field distribution, shown in Figs. 3(k) and 3(l), corresponds to the excitation current of the electron beam rather than to the current generated by specific plasmonic oscillations. On account of these findings, we conclude that the *MA* peak is formed by several overlapping plasmon modes. Indeed, at the energies above 2.4 eV the interband transitions contribute substantially to the dielectric function, leading to the broadening of the individual plasmon modes. Further, the energy separation between the modes usually decreases with the increasing order of the modes, as was recently demonstrated in silver nanodisks [35] and also qualitatively follows from the concave (down-bending) character of the surface-plasmon-polariton dispersion curve. It is thus plausible to assume that at higher energies the plasmon modes become unresolvable.

Figure 2(b) shows the measured and calculated EEL spectra for one of the larger antennas (A4). In comparison with the small antenna A1 [Fig. 2(a)], the D_L and D_T peaks are red-shifted

#235070 - $15.00 USD Received 23 Feb 2015; revised 7 Apr 2015; accepted 9 Apr 2015; published 27 Apr 2015

and a new peak emerges between the D_T and *MA* peaks. This new feature is denoted as Q to reflect its prevailing quadrupolar character (note that due to low symmetry of antennas the mode is not purely quadrupolar, but has also dipolar and higher-order components). The calculated spectra again reasonably reproduce the measured ones as long as the substrate is considered (not shown). As the calculated peaks are sharper, the additional Q peak splits into a weak Q_1 peak and a stronger Q_2 peak. It is reasonable to assume that the broadening of spectral peaks arises from the finite resolution of the monochromator and spectrometer. To include this broadening in the calculated data they were convoluted with a Gaussian function. The best agreement with the experiment was obtained for a FWHM of 0.15 eV [shown by solid lines in the right panel of Fig. 2(b)], which is a plausible value for our experimental setup. The measured and calculated maps of the loss intensity are shown in Fig. 4. The D_L, D_T, and *MA* peaks are similar to those in A1 antenna. The calculated maps of the loss intensity display 4 and 5 maxima for the Q_1 and Q_2 peaks, respectively. The experimental maps are in reasonable agreement with the calculations. In measurements, the Q_2 peak is not fully resolved from its adjacent peaks Q_1 and *MA*. In particular, a strong loss intensity at the IE spot in Fig. 4(g), not present in the calculated data in Fig. 4(h), belongs to the *MA* peak. Similarly, a bulky maximum at the OE spot is observed in Fig. 4(g) instead of three separate predicted in Fig. 4(h) because of the contribution of the Q_1 peak. We therefore show in Fig. 4(k) a linear combination of calculated maps of loss intensity of the three peaks (Q_1, Q_2, and *MA* with relative weights of 0.2, 1, and 0.5, respectively), which agrees well with the measured map of loss intensity of Q_2 peak.

4. Characteristic properties of plasmonic resonances in crescents

So far the plasmonic modes supported by crescent-shaped antennas have been identified and understood. Next the plasmonic properties which are *characteristic* for this specific shape and make it attractive for applications will be discussed. In particular, it will be shown that the crescent antennas (i) support two non-degenerate dipolar plasmon resonances (ii) which are both concentrated at the sharp antenna tips where a large field enhancement is possible, (iii) are independently tunable in a wide range of energies by selecting a proper crescent dimensions, and (iv) are compatible with the infrared telecommunication technologies.

One of the prominent features of low-symmetry antennas, including crescents, is that they support two dipolar plasmon resonances at different energies, while for high-symmetry antennas (e.g. discs) the modes are degenerate. Several applications indeed profit from the possibility to use plasmonic antennas for a simultaneous control of optical processes in two different spectral regions. For example, in the plasmon fluorescence enhancement the high energy resonance can be tuned to the energy of the exciting light to enhance the absorption while the low energy resonance is tuned to the energy of the emitter and enhances its radiative decay rate [5,46]. A similar setup was proposed to enhance the efficiency of solar cells by capturing the transmitted subbandgap photons, upconverting them and reflecting back to the active region of the solar cell [47]. In the following the properties of the dipolar resonances will be studied theoretically. In particular we address the evolution of two dipolar modes as the antenna geometry transforms from a disc to a crescent and the possibility to adjust the energies of the plasmon resonances by setting an antenna geometry.

For the transition from the disc to crescent antenna geometry, the antenna was again modelled by mutual subtraction of two displaced discs. From the basic disc ($r_B = 55$ nm), the intersection with the detracting disc ($r_S = 50$ nm) was removed. The center-to-center distance between the discs was varied from 105 nm to 25nm so that the full basic disc is smoothly converted to a thin crescent of a thickness of 30 nm. The evolution of the EEL spectra with the changing crescent geometry is shown in Fig. 5 for the relevant electron beam spots (T1,2, IE, OE), at a distance of 5 nm from an antenna boundary. Even as small perturbation as removing a wedge of a thickness

#235070 - $15.00 USD Received 23 Feb 2015; revised 7 Apr 2015; accepted 9 Apr 2015; published 27 Apr 2015

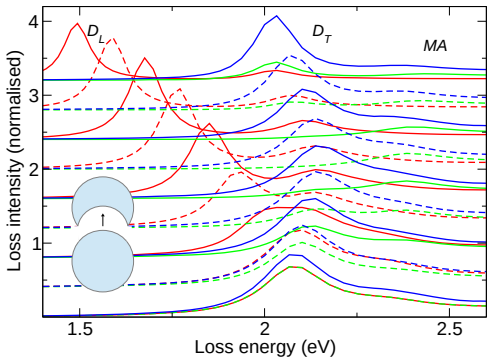

Fig. 5. The simulated energy loss spectra for crescents of various thicknesses T (inner-edge to outer-edge transverse dimension). The bottom spectrum corresponds to a full disc with a radius $r_B = 55$ nm (degenerate modes) and for each other spectrum the thickness is consecutively reduced by 10 nm down to 30 nm for the topmost spectrum. The peaks corresponding to the longitudinal and transverse dipolar modes are denoted D_L and D_T, respectively. Different line colors correspond to the electron beam spots T1,2 (red), OE (blue), and IE (green). The solid and dashed lines are alternated only to improve the clarity of the figure.

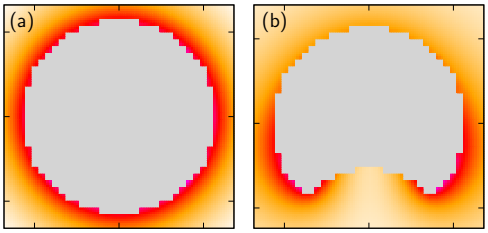

Fig. 6. The map of the simulated energy loss intensity for (a) a disc-shaped antenna ($c = 105$ nm, $T = 110$ nm) for a peak energy of the dipolar mode (2.07 eV) and (b) a crescent antenna rather close to the disc shape ($c = 75$ nm, $T = 80$ nm), summed up for both D_L and D_T dipolar modes (1.94 eV and 2.14 eV, respectively). Antennas are indicated by light gray color. For both antennas, the values $r_B = 55$ nm and $r_S = 50$ nm were used.

of 20 nm is already sufficient for the appearance of two well-distinguished peaks belonging to the longitudinal (D_L) and transverse (D_T) plasmon modes. As the crescent gets thinner, the former peak red shifts rapidly from 2.1 eV to 1.5 eV while the shift of the latter peak is not monotonous and not so prominent (between 2.05 eV and 2.15 eV). Interestingly, the intensity of the transverse loss peak for the inner edge excitation is strongly suppressed for a certain range of crescent thicknesses. This is caused by a quasisymmetric distribution of the mode polarization with respect to the position IE of the excitation beam (as for the longitudinal mode at the mirror plane of symmetry). It should be noted that this effect is manifested in our experimental spectra as a low intensity of the D_T mode at the IE beam spot. The multimodal *MA* peak at 2.4 eV is not well visible in the simulated energy loss spectra and does not exhibit any pronounced shift. A similar symmetry reduction (from cylindric to three-fold rotation symmetry) has been recently studied by Schmidt et *al* [48].

Figure 6 shows the maps of the energy loss intensity for the dipolar mode in the disc-shaped antenna and the sum of the longitudinal and transverse dipolar modes in the crescent-shaped

#235070 - $15.00 USD Received 23 Feb 2015; revised 7 Apr 2015; accepted 9 Apr 2015; published 27 Apr 2015

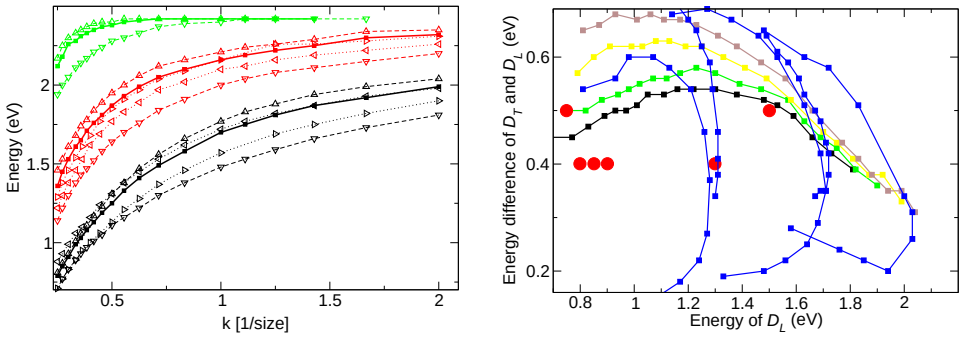

Fig. 7. Left: Simulated energies of the modes D_L (black symbols), D_T (red symbols), and *MA* (green symbols) as functions of "effective *k*", defined as inversely proportional to the characteristic lateral dimension of an antenna. The thick solid lines and squares correspond to the reference crescent-shaped antenna ($r_B = 55$ nm, $r_S = 50$ nm, $c = 45$ nm, $h = 30$ nm). The dashed lines correspond to the antennas with a height of 15 nm (down-pointing triangle) and 40 nm (up-pointing triangle). The dotted lines correspond to the antennas with modified lateral aspect ratios (*LAR*, see text for details) of 0.67 (left-pointing triangle) and 1.50 (right-pointing triangle). Right: Energies of the two plasmonic dipolar modes (D_L, D_T) in gold crescent antennas of various dimensions plotted as the D_T-D_L energy difference vs. the energy of the D_L mode. The simulated data are displayed by squares. The lines serving as guides for the eye connect the points corresponding to *LAR* scaling (blue lines) and *k* scaling for the antenna heights 15 nm (black line), 20 nm (green line), 30 nm (yellow line), and 40 nm (brown line). For comparison, the experimental data are displayed by large red circles.

antenna. The enhancement of the loss intensity in the vicinity of the sharp features (i.e., tips) of the latter antenna is clearly observed and attributed to the corresponding enhancement of local electric field.

Next, the dependence of the mode energies on the particular antenna shape is explored. Left panel of Fig. 7 shows the energies of the three distinct spectral features (D_L, D_T, and *MA*) as functions of "effective *k*" of the antenna. This quantity is defined as that one inversely proportional to the characteristic lateral dimension of the antenna (equal to r_B of the antenna except for the *LAR* scaling where it is equal to r_B of the antenna before the scaling), with the unit value corresponding to the reference crescent with $r_B = 55$ nm, $r_S = 50$ nm, $c = 45$ nm. In *k*-scaling both lateral dimensions (longitudinal and transverse) are scaled by the same factor (to which the value of *k* is inversely proportional). The energies of all the modes increase with *k* and converge to an asymptotic value of about 2.4 eV, which corresponds to the onset of the interband absorption in gold. For the *k*-interval from 0.25 to 2 and the antennas with $h = 30$ nm the energy of the D_L mode varies between 0.79 and 1.99 eV and the energy of the D_T mode varies between 1.36 and 2.32 eV (black and red thick solid lines in the left panel of 7). When the height of the antennas is increased, the energies of the plasmonic modes increase as a result of the weakened coupling between the lower and upper antenna boundary. The *k*-dependences of the antennas with $h = 15$ nm and 40 nm are shown in Fig. 7(left) by the dashed lines. The energy interval for this height range and $k = 1$ is $1.48-1.77$ eV for the D_L mode and $2.00-2.21$ eV for the D_T mode. The common feature of both *k*-scaling and varying the height is preserving the lateral shape of the antennas so the energies of different modes shift in the same direction by similar magnitudes. A mutual shift of the energies is possible by changing the thickness of the antenna (as shown in Fig. 6) or by scaling the longitudinal and transverse dimensions by factors

#235070 - $15.00 USD Received 23 Feb 2015; revised 7 Apr 2015; accepted 9 Apr 2015; published 27 Apr 2015

F and $1/F$, respectively, so that the lateral area is preserved. We define the lateral aspect ratio $LAR = F^2$ (higher than one when the longitudinal tip-to-tip distance is increased) and show the k-dependences for $LAR = 0.67$ and 1.5 in Fig. 7(left) by the dotted lines.

By combining the above mentioned scalings, independent and wide-range tuning of the plasmonic mode energies is possible. Right panel of Fig. 7 shows the energies of the D_L and D_T modes so that the horizontal axis corresponds to the energy of the D_L mode and the vertical axis corresponds to the energy difference between the D_T and D_L mode. The results of simulations (squares) show the possibility of the independent tuning of the energy of the D_L mode in the range of 0.8–2.0 eV and the D_T-D_L energy difference in the range of $0.2-0.7$ eV. Note that the *LAR*-scaling (represented by the blue lines) allows to change the energy difference with only minor changes in the energy of the D_L mode. Our experimental results [large red circles in Fig. 7(right)] cover the D_L mode energy range of $0.7-1.5$ eV for the D_T-D_L energy difference around 0.45 eV. Notably, the larger structures exhibit the D_L resonance between 0.80 and 0.95 eV, covering the infrared telecommunication wavelengths of 1.3 and 1.55 μm (0.95 and 0.80 eV).

Conclusion

We have studied the plasmonic modes in gold crescent-shaped plasmonic antennas using electron energy loss spectroscopy, determined their energies and mapped the spatial distribution of their excitation efficiency. From boundary element simulations we have assigned the observed peaks to particular plasmon resonances and obtained additional attributes such as field distributions. We have demonstrated the existence of two dipolar modes with the mutually perpendicular polarization in all studied structures, as well as the presence of a multimodal assembly at the energy corresponding to the onset of interband absorption in gold. In large structures, two additional modes of a prevailing quadrupolar character have been resolved. In extended calculations, we have demonstrated the broad-range tunability of the energies of plasmon resonances by scaling the dimensions of the antennas, and the compatibility with the infrared telecommunication technology.

Acknowledgment

We acknowledge the support by the Grant Agency of the Czech Republic (grant No. P102/12/1881), European Regional Development Fund (project No. CZ.1.05/1.1.00/02.0068), EU 7th Framework Programme (Contract No. 286154 – SYLICA and 280566 – UnivSEM), and Technology Agency of the Czech Republic (grant No. TE01020233). V. K. was supported by European Social Fund, grant No. CZ.1.07/2.3.00/30.0005.

#235070 - $15.00 USD Received 23 Feb 2015; revised 7 Apr 2015; accepted 9 Apr 2015; published 27 Apr 2015

O Comparative study of plasmonic antennas fabricated by electron beam and focused ion beam lithography

SCIENTIFIC REPORTS

OPEN

Comparative study of plasmonic antennas fabricated by electron beam and focused ion beam lithography

Received: 18 April 2018
Accepted: 14 June 2018
Published online: 25 June 2018

Michal Horák[1], Kristýna Bukvišová[2], Vojtěch Švarc[1,2], Jiří Jaskowiec[2], Vlastimil Křápek[1,2] & Tomáš Šikola[1,2]

We present a comparative study of plasmonic antennas fabricated by electron beam lithography and direct focused ion beam milling. We have investigated optical and structural properties and chemical composition of gold disc-shaped plasmonic antennas on a silicon nitride membrane fabricated by both methods to identify their advantages and disadvantages. Plasmonic antennas were characterized using transmission electron microscopy including electron energy loss spectroscopy and energy dispersive X-ray spectroscopy, and atomic force microscopy. We have found stronger plasmonic response with better field confinement in the antennas fabricated by electron beam lithography, which is attributed to their better structural quality, homogeneous thickness, and only moderate contamination mostly of organic nature. Plasmonic antennas fabricated by focused ion beam lithography feature weaker plasmonic response, lower structural quality with pronounced thickness fluctuations, and strong contamination, both organic and inorganic, including implanted ions from the focused beam. While both techniques are suitable for the fabrication of plasmonic antennas, electron beam lithography shall be prioritized over focused ion beam lithography due to better quality and performance of its products.

Localized surface plasmons (LSP) are collective oscillations of free electrons in metallic nanostructures (plasmonic antennas) coupled to the local electromagnetic field. A characteristic feature of LSP is a strong enhancement of electromagnetic field within the surrounding dielectric together with its confinement on the subwavelength scale. It can be utilized to control various optical processes in the visible and near infrared spectral region even below the free space diffraction limit[1]. This feature is utilized in numerous applications[2,3]. Properties of LSP can be tuned via engineering the size and shape of plasmonic antennas, or dielectric environment surrounding antennas[4]. Mapping of LSP resonances in metallic nanostructures with high spatial and energy resolution is necessary to understand their optical properties. Electron energy loss spectroscopy (EELS) is a technique utilizing an electron beam that interacts with the metallic nanoparticle and excites the LSP resonances[5–7]. In consequence, the energy of some electrons decreases by the characteristic energy of a plasmon resonance, which is then observable in the energy-dispersed spectra of transmitted electrons. Spatially-resolved EEL spectra further provide (relative) intensity of the near electric field of a LSP resonance projected to the trajectory of the electron beam. EELS tomography then provides a three-dimensional reconstruction of the plasmonic near field[8,9]. Additionally, EELS allows to determine the thickness of the sample[10,11].

Plasmonic antennas are often fabricated by electron beam lithography (EBL)[12] or using focused ion beam (FIB) lithography[13]. The EBL process consists of following steps: (i) deposition of a resist sensitive to electron beam on the substrate, (ii) exposition of the resists to the electron beam and development of the resist (removal of exposed or unexposed regions of the resist), (iii) deposition of a thin layer of metal, and (iv) removal of the remaining resist covered by the redundant metal (lift-off) and final cleaning of the sample. FIB lithography is more straightforward, consisting of two steps: (i) deposition of a thin layer of metal and (ii) exposition to a

[1]Central European Institute of Technology, Brno University of Technology, Purkyňova 123, 612 00, Brno, Czech Republic. [2]Institute of Physical Engineering, Brno University of Technology, Technická 2, 616 69, Brno, Czech Republic. Correspondence and requests for materials should be addressed to M.H. (email: michal.horak2@ceitec.vutbr.cz)

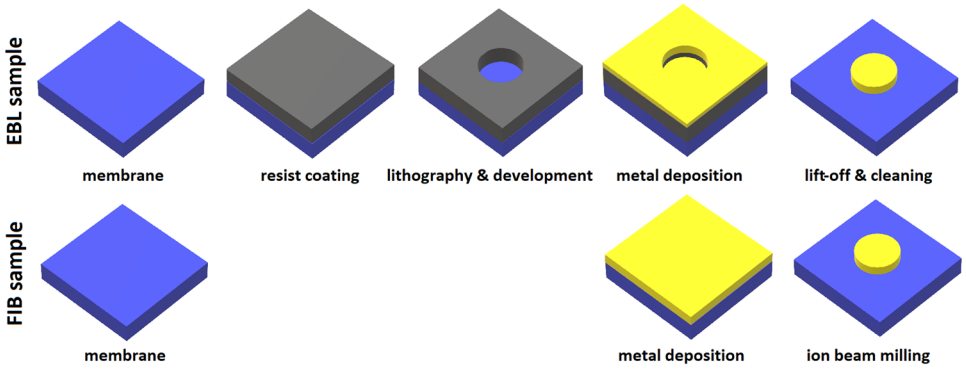

Figure 1. Schematic overview of individual steps in the fabrication process of the EBL and the FIB antennas.

focused ion beam that locally sputters off the metal (see Fig. 1). Both the EBL process and the FIB milling are capable to create sub-10-nm structures[14,15].

Naturally, both fabrication techniques have their advantages and disadvantages. In EBL, final structures can be contaminated by the residual resist or solvents. Lift-off can exert a pronounced mechanical force that can damage the fabricated structure or even the substrate, which is particularly dangerous for thin membranes used as the substrate. In FIB, large-area mechanical effects are absent but the focused ion beam can damage the sample locally. Redeposition of sputtered-off metal atoms can reduce the quality of products of the technique. There are no chemicals involved in the process but the ions in the milling beam and atoms sputtered from the metal and substrate can still contaminate the fabricated structures. EBL consists of more steps but is more suitable for large area lithography as the exposition, the only local process, is considerably faster than for FIB. On the other hand, FIB is faster when only single antenna or a small field of antennas is being fabricated. For example, considering optimal parameters for FIB and EBL (see the Methods section), FIB milling of one antenna inside a $2 \times 2\ \mu m^2$ metal-free square takes typically 2 minutes. Array of 50×50 antennas is fabricated in 84 hours (3.5 days). On the other hand, in EBL the length of chemical processes (resist coating, development, and lift off) is independent on the number of fabricated antennas and takes typically 6 hours. Electron beam exposition of one antenna lasts far below 1 second; the array of 50×50 antennas is exposed in 5 seconds. FIB enables fabrication of single crystalline plasmonic antennas when a chemically grown single crystal gold flake transferred onto a substrate is used as the pristine material instead of sputtered or evaporated polycrystalline thin film[16,17]. The quality of lithographically fabricated plasmonic antennas can be further enhanced by annealing which enlarges the grains and accordingly reduces the number of grain boundaries so the behavior of nanostructures is closer to a single crystal[18,19]. It is clear that suitability of both methods depends on specific task and experimental comparison of the structures fabricated by both methods is of high importance for the judicious selection of the optimal method. We note that the subject is relevant for a wide range of nanostructures beyond plasmonic antennas, such as biosensors[20] or metasurfaces[21].

In our contribution, we present a comparative study of gold plasmonic disc-shaped antennas fabricated by EBL and FIB lithography with gallium ions. Fabricated antennas were characterized using the transmission electron microscopy (TEM) including chemical analysis by energy dispersive X-ray spectroscopy (EDS) and characterization of LSP resonances and thickness measurement by EELS, and using the atomic force microscopy (AFM) to complement information about the morphology of the structures. Spectral and spatial characteristics of LSP resonances obtained from experiment were compared with numerical simulations with the MNPBEM toolbox[22] which relies on the boundary element method (BEM) approach[23,24].

Results

We have studied in detail four individual disc-shaped gold plasmonic antennas: two series prepared by both EBL and FIB consisting of antennas with the designed diameter of 120 and 140 nm and with the designed height of 25 nm. After their fabrication, several characterization methods have been applied. Some of those methods can modify the samples. In particular, a hydrocarbon contamination is developing during measurements in electron microscopes using high beam current (i.e., EELS and EDS)[25,26]. For this reason, the characterization methods have been applied in specific order for all investigated antennas: EELS, EDS, AFM. As we consider possible contamination to be a part of PA functionality, no specific cleaning steps have been applied between individual measurements. In particular, no plasma cleaning has been applied prior to EELS measurements, although it is often used to remove the hydrocarbon contamination.

The three-dimensional (3D) morphology of the antennas measured by EELS in terms of relative thickness is shown in Fig. 2. The average relative thickness is (0.23 ± 0.05) for 120-nm EBL antenna, (0.20 ± 0.07) for 120-nm FIB antenna, (0.23 ± 0.05) for 140-nm EBL antenna, and (0.20 ± 0.06) for 140-nm FIB antenna, see also Fig. 3d. The relative thickness is proportional to the absolute thickness of the antenna with the inelastic mean free path (IMFP) as the constant of proportionality. The IMFP in gold for the actual parameters of the electron beam (electron energy of 300 keV and collection semi-angle of 20.5 mrad) calculated using the software package EELSTools by D. Mitchell[27] applying the algorithm of K. Iakoubovskii *et al.*[11] equals to 113 nm. Consequently, the absolute thickness of the antennas is (23 ± 7) nm for FIB antennas and about (26 ± 6) nm for EBL antennas, which is in a good agreement with the desired value of 25 nm. Diameters of fabricated antennas measured from TEM

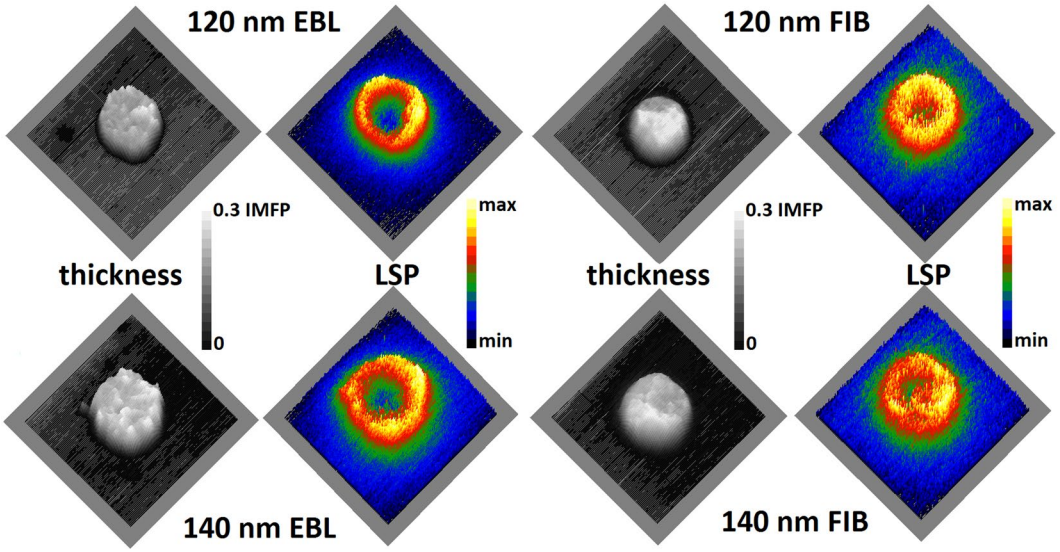

Figure 2. Thickness and LSP resonance mapping by EELS. 3D morphology of the antennas represented by the relative thickness (thickness in units of inelastic mean free path, IMFP) measured by EELS (left, grayscale) and EEL intensity maps showing the spatial distribution of LSP resonance at (1.60 ± 0.05) eV for 120 nm antennas and (1.40 ± 0.05) eV for 140 nm antennas (right, color scale). The size of all micrographs is 300×300 nm^2.

micrographs indicate good agreement between the designed and actual value. They read (125 ± 5) nm for 120-nm EBL antenna, (122 ± 6) nm for 120-nm FIB antenna, (140 ± 6) nm for 140-nm EBL antenna, and (142 ± 7) nm for 140-nm FIB antenna.

There is a clear structural difference between EBL and FIB antennas. EBL antennas have an irregular shape and their thickness varies rapidly with the position as the gold layer is polycrystalline with the grain size of about 20 nm. FIB antennas are seemingly more uniform in the thickness and their edges are smooth and featureless. Nevertheless, a closer inspection (see Fig. 3d) reveals even more pronounced (i.e. with larger amplitude) but smoother (i.e. with reduced slope) variations of the thickness with the magnitude of nearly 10 nm. The flat boundary is mainly caused by two reasons. First, the metallic layer is deposited on the flat substrate for FIB but on the patterned resist for EBL forming a flat layer in the former case and frayed edges in the latter case. Second, the ion beam has a Gaussian-like profile which leads to smoothing of the edges. Additionally, the ion beam may result into amorphization and recrystallization of gold, smoothening its surface[28]. Finally, redeposition of sputtered-off gold may contribute to the smoothness of the gold surface and might be also partially responsible for the large magnitude of the thickness variation.

Next, EEL spectra were processed to obtain the loss probability related to LSP resonances. This included zero-loss peak (ZLP) and background subtraction. The process is illustrated in Fig. 3a showing the unprocessed low-loss part of EEL spectrum decomposed into the contribution of ZLP and background, and signal corresponding to the LSP resonance for the 120-nm EBL antenna. Extracted EEL signal corresponding to the LSP resonance is shown in Fig. 3b for 120-nm antennas and in Fig. 3c for 140-nm antennas. Within the spectra we resolve single broad peak corresponding to the dipole LSP mode. This assignment is further supported by the results of numeric simulation, also shown in Fig. 3b,c. It is also in agreement with prior investigations of plasmonic disc-shaped antennas[29]. The second peak in the calculated spectra corresponds to the quadrupole LSP mode. Due to its low intensity and instrumental broadening, related to the energy width of the impinging electron beam with the full-width at half-maximum (FWHM) of about 0.18 eV, this mode is not resolvable in the experimental data. The simulation predicts the energy of the dipole LSP mode of 1.66 eV for 120-nm antennas and 1.59 eV for 140-nm antennas. Measured LSP resonance energy is (1.56 ± 0.09) eV for 120-nm EBL antenna, (1.62 ± 0.09) eV for 120-nm FIB antenna, (1.43 ± 0.09) eV for 140-nm EBL antenna, and (1.41 ± 0.09) eV for 140-nm FIB antenna. The measured energies are thus systematically red-shifted from the calculated energies, although the magnitude of the shift is rather minor and ranges between 0.04 eV and 0.18 eV. Such a red-shift can be attributed to the deviations of the actual antenna shape from the ideal disc, inhomogeneous thickness of antennas, modification of the dielectric function of gold due to grain boundaries and polycrystallinity of the antennas[30,31], or effects induced by the contamination[32] and Ti adhesion layer[33,34].

If we compare EBL and FIB antennas, we observe more intense peak for EBL antennas. Figure 2 shows the spatial distribution of the LSP resonance in the form of intensity maps at the energy of (1.60 ± 0.05) eV for 120-nm antennas and (1.40 ± 0.05) eV for 140-nm antennas. The radial dependences of the intensities averaged over the polar coordinate are shown in Fig. 3(e,f). The maximal intensity of LSP resonance is confined to sharp features on the edges of EBL antennas. In the case of FIB antennas, LSP resonance is less confined to the edges of the structures and the EEL intensity maps are blurred, which can be caused, for example, by thickness fluctuation or contamination.

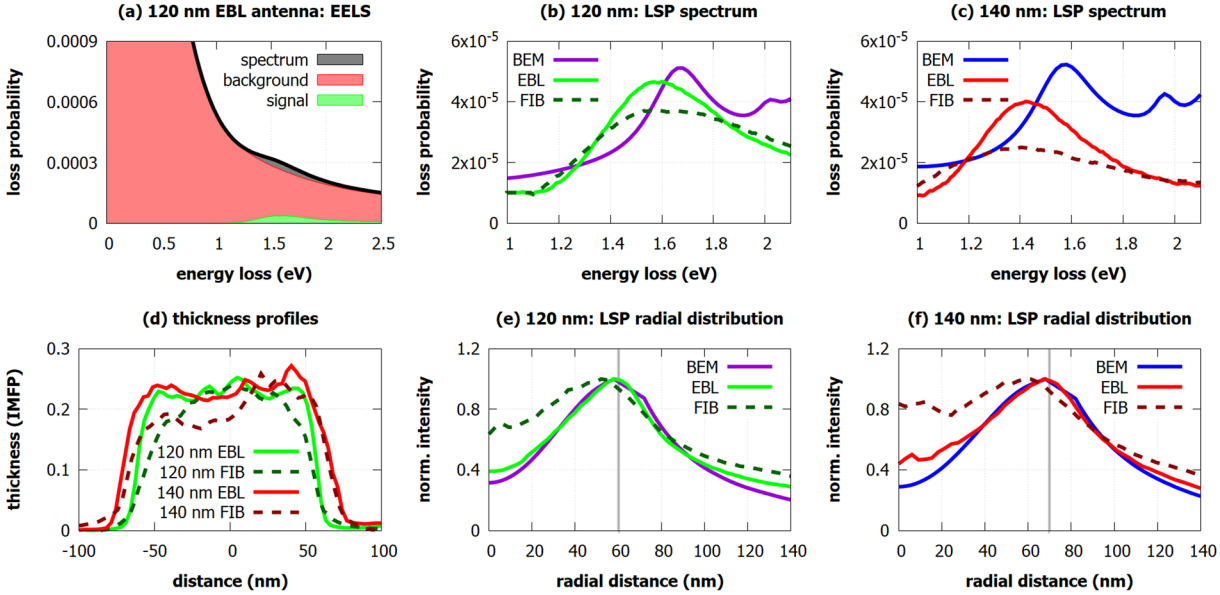

Figure 3. EELS measurement of LSP resonances. (**a**) Typical raw low-loss EEL spectrum (black) decomposed into background including zero-loss peak (red) and the signal corresponding to the LSP resonance (green) for the 120-nm EBL antenna. (**b**,**c**) Loss probability related to LSP measured by EELS in the EBL and the FIB antennas together with the calculated values obtained by BEM for 120-nm (**b**) and 140-nm (**c**) antennas. (**d**) Thickness profiles (thickness in units of inelastic mean free path, IMFP) of the antennas determined by EELS. We note that EBL antennas have slightly sharper edges. (**e**,**f**) The radial distribution of the LSP-related loss probability (at the energy of its maximum) for 120-nm (**e**) and 140-nm (**f**) antennas measured by EELS for EBL and FIB antennas and calculated by BEM. Antennas have their center at 0 nm and the edge of antennas is marked by the grey line.

Following the EELS measurements we have analyzed the chemical composition of the antennas, including their possible contamination. To this end we performed EDS analysis, which enables detection of all elements heavier than Be in one measurement. We have detected and further focused on the following chemical elements: Si and N constituting the membrane, Au and Ti constituting the antenna and the adhesion layer, respectively, Ga that forms the ion beam in FIB and can be implanted into the sample, C and O as frequent contaminants. Spatial distribution of the intensity of characteristic X-ray radiation for these elements is shown in Fig. 4 for both FIB and EBL antennas with the diameter of 140 nm together with the bright field TEM and high-angle annular dark field (HAADF) micrographs. We distinguish in total three areas with different chemical composition, denoted as Area 1 to 3 in the following. Area 1 corresponds to the antenna and Areas 2 and 3 to its surrounding exposed and unexposed to the electron beam during EELS measurements. We note that the composition of Areas 2 and 3 is almost identical with the exception of carbon, which has a stronger presence in the Area 2 (exposed to the electron beam) in the case of FIB antenna (see intense red square in Fig. 4). The distribution of individual elements within each Area is homogeneous. The average relative atomic rate of each element for each Area is given in Table 1. As the thickness of different Areas is not identical, we note that the atomic rates between different Areas are not directly comparable but have to be rescaled to the same thickness.

Both Si and N exhibit almost identical X-ray intensity over all Areas for both FIB and EBL antennas. Slightly increased intensity of Si below the antennas (Area 1) is an artifact related to the secondary emission of X-rays in the silicon-based EDS detector associated with larger thickness and density of this Area. Average stoichiometry of SiN_x membrane (neglecting Area 1) reads $Si(3)N(2.0 \pm 0.6)$. Verification measurement by EELS resulted into average stoichiometry $Si(3)N(1.8 \pm 0.3)$ which is in a very good agreement with EDS. Gold is present only at the antennas (Area 1), underpinning reliability of both fabrication techniques. In general, EDS is not accurate enough to assess the thickness of the gold layer. It is nevertheless illustrative to provide a rough estimate. The atomic rate of Au is 0.18 ± 0.03 and 0.16 ± 0.03 in the EBL and FIB antenna, respectively. These values are equal within the experimental error. The atomic rates of Si and N are listed in Table 1. We now rescale the atomic rates to the volume rates using covalent radii of N, Si, and Au reading 71 pm, 116 pm, and 124 pm[35]. Considering the thickness of the SiN_x membrane of 50 nm, we obtain rough estimates of the thickness of the gold layer of 28 nm and 27 nm for the EBL and FIB antenna, respectively, in a good agreement with the designed thickness of 25 nm and EELS measurements of 23–26 nm.

Ti is present in the Area 1 for EBL antenna but in all Areas for FIB antenna. Apparently, FIB lithography was unable to fully remove Ti from the desired Areas as the sputter rate of Ti is much smaller than that of Au. Estimated thickness of the Ti contamination layer is 1–2 nm. Ga ions have been implanted to the Areas 2 and 3 (i.e. into the antenna surrounding) for FIB antennas. The atomic rate of Ga reads 0.03 ± 0.01. Importantly, no Ga contamination is found directly above or inside antennas (i.e. in Area 1), suggesting its rather limited influence on the plasmonic response of the antennas.

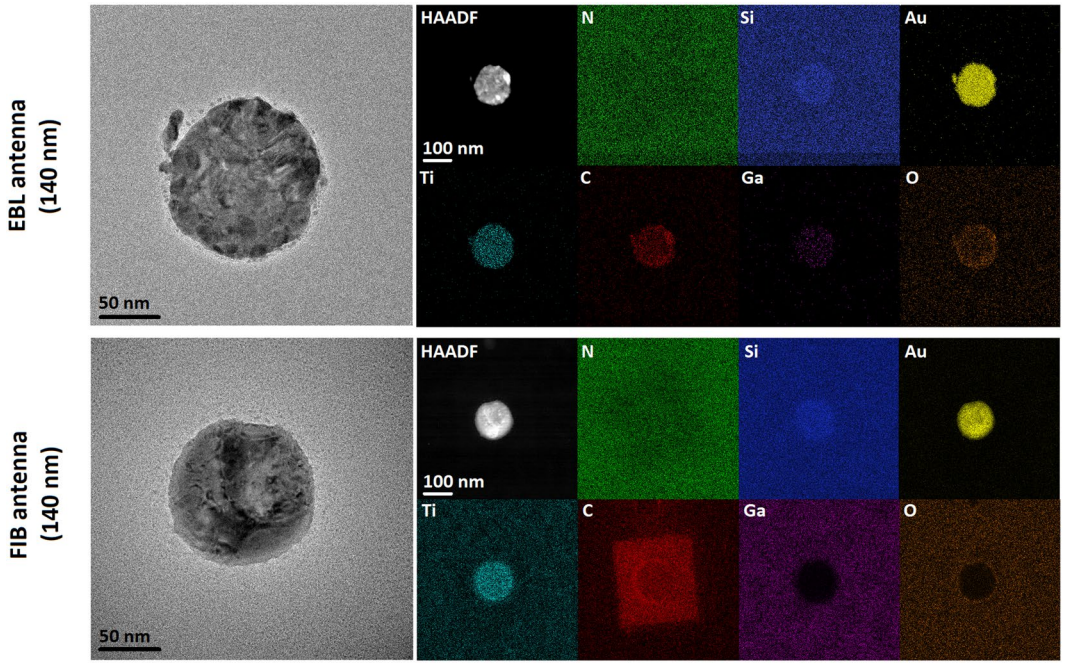

Figure 4. TEM micrographs and elemental maps showing chemical composition of 140-nm antennas. Left: TEM bright field micrographs of 140-nm EBL and FIB antennas. Right: HAADF image of the antennas presenting the distribution of heavy elements and spatial maps of element-specific X-ray intensity obtained from EDS for N, Si, Au, Ti, C, Ga, and O.

	EBL antenna			FIB antenna		
	Area 1	Area 2	Area 3	Area 1	Area 2	Area 3
Au	(18 ± 3)%	below 1%	below 1%	(16 ± 3)%	below 1%	below 1%
Ti	(4 ± 1)%	below 1%	below 1%	(4 ± 1)%	(2 ± 1)%	(2 ± 1)%
Si	(35 ± 5)%	(55 ± 5)%	(55 ± 5)%	(32 ± 5)%	(40 ± 5)%	(45 ± 5)%
N	(20 ± 3)%	(35 ± 5)%	(35 ± 5)%	(17 ± 3)%	(25 ± 5)%	(33 ± 5)%
C	(13 ± 3)%	(4 ± 2)%	(4 ± 2)%	(25 ± 5)%	(25 ± 5)%	(8 ± 3)%
O	(6 ± 2)%	(4 ± 2)%	(4 ± 2)%	(5 ± 2)%	(7 ± 2)%	(7 ± 2)%
Ga	below 1%	below 1%	below 1%	below 1%	(3 ± 1)%	(3 ± 1)%

Table 1. Chemical composition of the membranes with EBL and FIB antenna in atomic percents determined by EDS after the EELS measurement. The composition is averaged over one of three areas with homogeneous chemical compositions: Area 1 corresponds to the antenna, while Areas 2 and 3 corresponds to their surrounding exposed and unexposed to the electron beam during EELS measurements, respectively.

Finally, C and O are present as usual contaminants due to several reasons. EBL antenna indicates larger contamination in Area 1 (i.e., at the position of the antenna) where the atomic rate of C reads 0.13 ± 0.03 and the atomic rate of O is 0.06 ± 0.02. This is probably the result of incomplete resist removal during the development of lithographic pattern. Antenna surrounding (Areas 2 and 3) indicates low level of C and O contamination with the atomic rate of both elements of 0.04 ± 0.02. Such low level of contamination refers to usual contamination of the sample when it is exposed to air. FIB antenna indicates much higher C and O contamination. The sample has been contaminated by organic residues present in the FIB chamber. C is particularly strongly present in areas exposed to the electron beam during the EELS measurement[25,26] (Areas 1 and 2, intense red square in Fig. 4) and its atomic rate reads 0.25 ± 0.05. Area 3 then exhibits the atomic rate of C of 0.08 ± 0.03 which is higher value than for EBL antenna. The atomic rate of O reads 0.05 ± 0.02 in Area 1 and 0.07 ± 0.02 in Areas 2 and 3 (i.e., in the antenna surroundings) which may indicate that Ti and Ga contaminants present in the surroundings are partially oxidized.

It is impossible to determine the thickness of hydrocarbon contamination layer on the FIB antennas using EELS because the contamination would further evolve during the measurement. Therefore, we have characterized surface topography of antennas by AFM measurement. Figure 5 compares the thickness of the 140-nm FIB antenna measured by EELS (assuming low hydrocarbon contamination) and surface topography measured by AFM after the EELS measurements (with hydrocarbon contamination being fully developed). The thickness of the hydrocarbon contamination layer is uniform over the whole area of EELS measurement (Areas 1 and 2) with the average thickness of (18 ± 5) nm determined as the height difference between Areas 2 and 3.

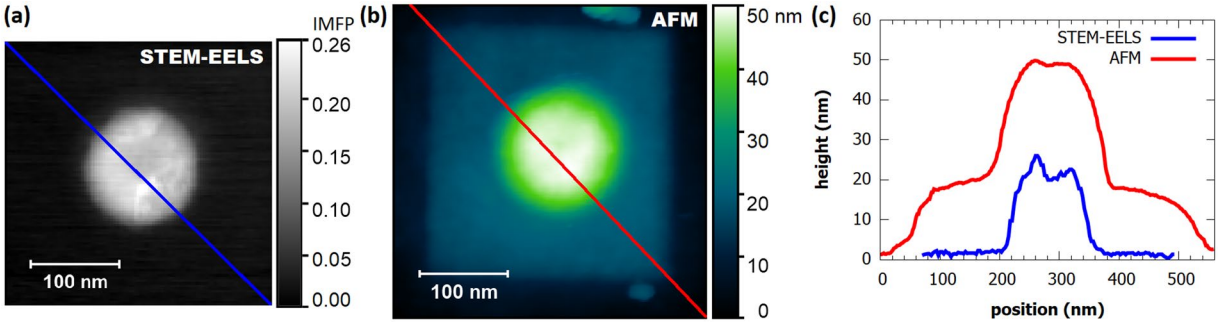

Figure 5. Thickness profile of a 140-nm FIB antenna and the hydrocarbon contamination on its surface. (**a**) Relative thickness (thickness in terms of IMFP) of the antenna retrieved by EELS. (**b**) Topography of the antenna including the hydrocarbon contamination measured by AFM. (**c**) Linear cross-sections of thickness profiles along the lines shown in (**a**) and (**b**). Relative thickness is recalculated to absolute thickness using the IMFP in gold of 113 nm. Blue line shows the thickness profile of the antenna determined by EELS, red line shows the thickness profile of the antenna and the contamination layer determined by AFM.

Discussion

The choice of preferred fabrication technique should also consider the time and potential risks of the fabrication process. FIB preparation is simple and more straightforward as no chemistry is used and fast for individual antennas or small series of antennas. Moreover, FIB lithography exerts low mechanical strain and thus enables processing of pristine materials with low adhesion to the substrate such as chemically grown single-crystalline gold flakes. EBL preparation provides generally antennas with higher quality, but the lithographic process induces potential risks of damaging the sample as the wet chemistry is used. EBL is more time consuming than FIB if a small number of antennas is prepared, but much faster if a large array of antennas is fabricated. In such case, the volume of material to be removed by FIB is too large. Therefore, either of the techniques is suitable for a different class of targeted nanostructures. In general, when no specific issues apply, EBL shall be prioritized over FIB as it produces antennas with stronger plasmonic response and low contamination.

In conclusion, we have performed the comparative study of plasmonic antennas fabricated by EBL and FIB. We have demonstrated that the EBL antennas have better quality. First, they have rather homogeneous thickness profile with decent thickness fluctuation, and sharper edges. Second, they are cleaner, with a moderate contamination of organic origin evidenced by the presence of carbon and oxygen atoms with the total rate up to 20%. On the other hand, plasmonic antennas fabricated by FIB lithography have slightly dull edges and exhibit pronounced thickness fluctuation. They are also strongly contaminated not only by organic contaminants forming a continuous layer of the thickness of about 18 nm, but also by residues of FIB milling including implanted milling ions and atoms of the titanium adhesion layer, possibly oxidized. In consequence, the plasmonic response of the antennas characterized by EELS is considerably stronger and slightly better localized for the antennas fabricated by EBL than for the antennas fabricated by FIB. To conclude, while both techniques are suitable for the fabrication of plasmonic antennas, EBL shall be prioritized over FIB lithography due to better quality of the resulting antennas.

Methods

Membranes. We used standard 50-nm-thick silicon nitride membranes for TEM with the window size of $250 \times 250\ \mu m^2$ and frame thickness of 200 μm by Silson Ltd, UK.

Electron beam lithography (EBL). As the resist, we used a 70 nm thick layer of poly(methyl methacrylate) 679.02 all-resist dissolved in ethyl acetate. Exposition has been performed within Tescan MIRA3/RAITH SEM operated at 30 kV with the electron beam current of 100 pA and the dose of 320 $\mu C/cm^2$. Exposed samples were developed in the developer AR 600-56 all-resist for 3 minutes, as the stopper we used isopropyl alcohol for 30 seconds. Afterwards, the sample was cleaned by demineralized water for 30 seconds. Lift-off was performed by 4-hour acetone bath applying mega sound for 1 hour finished by acetone stream wash. Finally, the sample was cleaned by isopropyl alcohol for 30 seconds, followed by cleaning using ethanol for 30 seconds and demineralized water for 30 seconds. To prevent the collective interaction of the antennas we fabricated individual isolated antennas with the distance between two nearby antennas of 3 μm.

Metal deposition. We used electron beam evaporator BESTEC. Pressure during the deposition was in the order of 10^{-5} Pa and voltage was set to 8 kV. We deposited 5 nm Ti adhesion layer with the deposition speed of 0.05 nm/s and 25 nm Au with the deposition speed of 0.02 nm/s. Metal pellets were purchased from Kurt J. Lesker Company. Samples were rotated at 10 rounds per minute to ensure the homogeneity of the layers. Both samples were deposited during one session to have exactly the same metallic layer on both of them. During the deposition, the thickness of the layer was measured *in situ* by quartz crystal microbalance monitor.

Focused ion beam (FIB) lithography. We used dual beam FIB/SEM microscope FEI Helios using gallium ions with the energy of 30 keV and ion beam current of 2.4 pA. We note that the energy (the highest available) and the current (the lowest available) are optimized for the best spatial resolution of the milling. The antennas were

situated in the middle of a $2 \times 2\ \mu m^2$ metal-free square, which is perfectly sufficient to prevent their interaction with the surrounding metallic frame[36].

Electron energy loss spectroscopy (EELS). EELS measurements were performed with TEM FEI Titan equipped with GIF Quantum spectrometer operated in monochromated scanning regime at 300 kV. Beam current was set to 0.8 nA and the FWHM of the ZLP was around 0.18 eV. We set convergence angle to 10 mrad, collection angle to 20.5 mrad, and dispersion of the spectrometer to 0.01 eV/pixel. We recorded EELS spectrum images with the size of $300 \times 300\ nm^2$ (100×100 pixels with the pixel size of 3 nm). Every pixel consists of 30 cross-correlated EEL spectra with the total pixel time of 20 ms. EEL spectra in Fig. 3 were integrated over the ring-shaped areas around the disc edge where the LSP resonance is significant (inner diameter about 50 nm, outer diameter about 200 nm) and divided by the integral intensity of the whole spectrum to transform measured counts to a quantity proportional to the loss probability. EEL maps were calculated by dividing the map of integrated intensity at the plasmon peak energy with the energy window of 0.1 eV by the map of the integral intensity of the zero-loss peak. Radial distributions of LSP resonances were calculated from the EEL maps by rotational averaging followed by the background subtraction (base level of the intensity in the EEL maps far away from the antennas).

Energy dispersive X-ray spectroscopy (EDS). EDS measurement was performed on TEM FEI Titan equipped with Super-X spectrometer operated in the scanning regime at 300 kV. Beam current was set to 2 nA. We recorded EDS spectrum images with the size of $600 \times 600\ nm^2$ (300×300 pixels with the pixel size of 2 nm). We integrated 100 images with the acquisition time of 10 µs per pixel. Spectrum images were post processed in Velox software. EDS maps in Fig. 4 show the net intensity (i.e. background subtracted and artifact corrected intensity). Table 1 shows the EDS quantification in atomic percents performed in Velox software using parabolic background model and Brown-Powell ionization cross-section model.

Atomic force microscopy (AFM). AFM measurement was performed using Scanning Probe Microscope Bruker Dimension Icon in the PeakForce Tapping mode, which enables larger control over applied force to prevent damaging the membrane[37]. The peak force setpoint was set to 5 nN, the scanning window was $400 \times 400\ nm^2$ (256×256 pixels with the pixel size of 1.6 nm).

Simulations. Numerical simulations of EELS spectra were performed using the MNPBEM toolbox[22] based on the boundary element method (BEM)[23,24]. The dielectric function of evaporated gold was taken from Olmon *et al.*[38] and the dielectric function of the silicon nitride membrane was set to 4[39]. The titanium adhesion layer has been neglected in the simulations. For the calculations of spectra the electron beam was positioned 2 nm from the outer side of the antenna. Obtained loss probability density was recalculated to loss probability at 0.01 eV energy intervals (corresponding to the dispersion of the spectrometer in the experiment).

Data availability. The datasets generated during and/or analyzed during the current study are available from the corresponding author on reasonable request.

References

1. Schuller, J. A. *et al.* Plasmonics for extreme light concentration and manipulation. *Nat. Mater.* **9**, 193–204, https://doi.org/10.1038/nmat2630 (2010).
2. Stockman, M. I. Nanoplasmonics: The physics behind the applications. *Phys. Today* **64**, 39–44, https://doi.org/10.1063/1.3554315 (2011).
3. Amendola, V., Pilot, R., Frasconi, M., Maragò, O. M. & Iatì, M. A. Surface plasmon resonance in gold nanoparticles: a review. *J. Phys.: Condens. Matter* **29**, 203002, https://doi.org/10.1088/1361-648X/aa60f3 (2017).
4. Kelly, K. L., Coronado, E., Zhao, L. L. & Schatz, G. C. The optical properties of metal nanoparticles: the influence of size, shape, and dielectric environment. *J. Phys. Chem. B* **107**, 668–677, https://doi.org/10.1021/jp026731y (2003).
5. García de Abajo, F. J. Optical excitations in electron microscopy. *Rev. Mod. Phys.* **82**, 209–275, https://doi.org/10.1103/RevModPhys.82.209 (2010).
6. Colliex, C., Kociak, M. & Stéphan, O. Electron energy loss spectrometry imaging of surface plasmons at the nanometer scale. *Ultramicroscopy* **162**, A1–A24, https://doi.org/10.1016/j.ultramic.2015.11.012 (2016).
7. Wu, Y., Li, G. & Camden, J. P. Probing nanoparticle plasmon with electron energy loss spectroscopy. *Chem. Rev.* **118**, 2994–3031, https://doi.org/10.1021/acs.chemrev.7b00354 (2018).
8. Hörl, A., Trügler, A. & Hohenester, U. Tomography of particle plasmon fields from electron energy loss spectroscopy. *Phys. Rev. Lett.* **111**, 086801, https://doi.org/10.1103/PhysRevLett.111.076801 (2013).
9. Hörl, A. *et al.* Tomographic imaging of the photonic environment of plasmonic nanoparticles. *Nat. Commun.* **8**, 37, https://doi.org/10.1038/s41467-017-00051-3 (2017).
10. Egerton, R. F. Electron Energy-Loss Spectroscopy in the Electron Microscope. Springer US, https://doi.org/10.1007/978-1-4419-9583-4 (2011).
11. Iakoubovskii, K., Mitsuishi, K., Nakayama, Y. & Furuya, K. Thickness measurements with electron energy loss spectroscopy. *Microsc. Res. Tech.* **71**, 626–631, https://doi.org/10.1002/jemt.20597 (2008).
12. Vieu, C. *et al.* Electron beam lithography: resolution limits and applications. *Appl. Surf. Sci.* **164**, 111–117, https://doi.org/10.1016/S0169-4332(00)00352-4 (2000).
13. Joshi-Imre, A. & Bauerdick, S. Direct-write ion beam lithography. *J. Nanotechnol.* **2014**, 170415, https://doi.org/10.1155/2014/170415 (2014).
14. Duan, H. *et al.* Metrology for electron-beam lithography and resist contrast at the sub-10 nm scale. *J. Vac. Sci. Technol. B* **28**, C6H11, https://doi.org/10.1116/1.3501359 (2010).
15. Kollmann, H. *et al.* Toward plasmonics with nanometer precision: nonlinear optics of helium-ion milled gold nanoantennas. *Nano Lett.* **14**, 4778–4784, https://doi.org/10.1021/nl5019589 (2014).
16. Huang, J. S. *et al.* Atomically flat single-crystalline gold nanostructures for plasmonic nanocircuitry. *Nat. Commun.* **1**, 150, https://doi.org/10.1038/ncomms1143 (2010).
17. Wang, X. *et al.* Vapor-phase preparation of single-crystalline thin gold microplates using $HAuCl_4$ as the precursor for plasmonic applications. *RSC Adv.* **6**, 74937–74943, https://doi.org/10.1039/C6RA15909E (2016).

18. Tinguely, J. C. *et al*. Gold nanoparticles for plasmonic biosensing: the role of metal crystallinity and nanoscale roughness. *NioNanoSci.* **1**, 128–135, https://doi.org/10.1007/s12668-011-0015-4 (2011).
19. Bosman, M. *et al*. Encapsulated annealing: enhancing the plasmon quality factor in lithographically-defined nanostructures. *Sci. Rep.* **4**, 5537, https://doi.org/10.1038/srep05537 (2014).
20. Crick, C. R. *et al*. Low-noise plasmonic nanopore biosensors for single molecule detection at elevated temperatures. *ACS Photonics* **4**, 2835–2842, https://doi.org/10.1021/acsphotonics.7b00825 (2017).
21. Babocký, J. *et al*. Quantitative 3D phase imaging of plasmonic metasurfaces. *ACS Photonics* **4**, 1389–1397, https://doi.org/10.1021/acsphotonics.7b00022 (2017).
22. Waxenegger, J., Trügler, A. & Hohenester, U. Plasmonics simulations with the MNPBEM toolbox: consideration of substrates and layer structures. *Comput. Phys. Commun.* **193**, 138–150, https://doi.org/10.1016/j.cpc.2015.03.023 (2015).
23. García de Abajo, F. J. & Howie, A. Relativistic electron energy loss and electron-induced photon emission in inhomogeneous dielectrics. *Phys. Rev. Lett.* **80**, 5180–5183, https://doi.org/10.1103/PhysRevLett.80.5180 (1998).
24. García de Abajo, F. J. & Howie, A. Retarded field calculation of electron energy loss in inhomogeneous dielectrics. *Phys. Rev. B* **65**, 115418, https://doi.org/10.1103/PhysRevB.65.115418 (2002).
25. Postek, M. T. An approach to the reduction of hydrocarbon contamination in the scanning electron microscope. *Scanning* **18**, 269–274, https://doi.org/10.1002/sca.1996.4950180402 (1996).
26. Egerton, R. F., Li, P. & Malac, M. Radiation damage in the TEM and SEM. *Micron* **35**, 399–409, https://doi.org/10.1016/j.micron.2004.02.003 (2004).
27. Mitchell, D. R. G. Determination of mean free path for energy loss and surface oxide film thickness using convergent beam electron diffraction and thickness mapping: a case study using Si and P91 steel. *J. Microscopy* **224**, 187–196, https://doi.org/10.1111/j.1365-2818.2006.01690.x (2006).
28. Michael, J. R. Focused ion beam induced microstructural alterations: texture development, grain growth, and intermetallic formation. *Microsc. Microanal.* **17**, 386–397, https://doi.org/10.1017/S1431927611000171 (2011).
29. Schmidt, F. P. *et al*. Dark plasmonic breathing modes in silver nanodisks. *Nano Lett.* **12**, 5780–5783, https://doi.org/10.1021/nl3030938 (2012).
30. Rodríguez-Fernández, J. *et al*. The effect of surface roughness on the plasmonic response of individual sub-micron gold spheres. *Phys. Chem. Chem. Phys.* **11**, 5909–5914, https://doi.org/10.1039/B905200N (2009).
31. Trügler, A., Tinguely, J. C., Krenn, J. R., Hohenau, A. & Hohenester, U. Influence of surface roughness on the optical properties of plasmonic nanoparticles. *Phys. Rev. B* **83**, 081412, https://doi.org/10.1103/PhysRevB.83.081412 (2011).
32. Koh, A. L. *et al*. Electron energy-loss spectroscopy (EELS) of surface plasmons in single silver nanoparticles and dimers: influence of beam damage and mapping of dark modes. *ACS Nano* **3**, 3015–3022, https://doi.org/10.1021/nn900922z (2009).
33. Madsen, S. J., Esfandyarpour, M., Brongersma, M. L. & Sinclair, R. Observing plasmon damping due to adhesion layers in gold nanostructures using electron energy loss spectroscopy. *ACS Photonics* **4**, 268–274, https://doi.org/10.1021/acsphotonics.6b00525 (2017).
34. Habteyes, T. G. *et al*. Metallic adhesion layer induced plasmon damping and molecular linker as a nondamping alternative. *ACS Nano* **6**, 5702–5709, https://doi.org/10.1021/nn301885u (2012).
35. Pyykkö, P. & Atsumi, M. Molecular single-bond covalent radii for elements 1–118. *Chem. Eur. J.* **15**, 186–197, https://doi.org/10.1002/chem.200800987 (2009).
36. Křápek, V. *et al*. Spatially resolved electron energy loss spectroscopy of crescent-shaped plasmonic antennas. *Opt. Express* **23**, 11855, https://doi.org/10.1364/OE.23.011855 (2015).
37. Walczyk, W., Schön, P. M. & Schönherr, H. The effect of PeakForce tapping mode AFM imaging on the apparent shape of surface nanobubbles. *J. Phys. Condens. Matter* **25**, 1–11, https://doi.org/10.1088/0953-8984/25/18/184005 (2013).
38. Olmon, R. L. *et al*. Optical dielectric function of gold. *Phys. Rev. B* **86**, 235147, https://doi.org/10.1103/PhysRevB.86.235147 (2012).
39. Schmidt, F. P., Ditlbacher, H., Hofer, F., Krenn, J. R. & Hohenester, U. Morphing a plasmonic nanodisk into a nanotriangle. *Nano Lett.* **14**, 4810–4815, https://doi.org/10.1021/nl502027r (2014).

Acknowledgements

This work has been supported by Czech Science Foundation (grant No. 17-25799 S), Ministry of Education, Youth and Sports of the Czech Republic under the projects CEITEC Nano Research Infrastructure (project No. LM2015041, 2016-2019) and CEITEC 2020 (project No. LQ1601), and Brno University of Technology (grant No. FSI/STI-J-17-4623).

Author Contributions

M.H. and T.S. initiated the idea. M.H. designed the experiment and performed the FIB fabrication and all characterization in TEM. V.S. performed EBL fabrication. J.J. and K.B. performed AFM measurement. M.H., K.B., and V.K. performed the analysis of results. All authors contributed to the scientific discussion and revision of the article.

Additional Information

Competing Interests: The authors declare no competing interests.

Publisher's note: Springer Nature remains neutral with regard to jurisdictional claims in published maps and institutional affiliations.